Analysis of the performance and stability of an axial compressor operating under inlet flow distortion

Alberto Baretter

HESAM UNIVERSITÉ

Arts et Métiers Sciences et Technologies

ÉCOLE DOCTORALE SCIENCES DES MÉTIERS DE L'INGÉNIEUR
[LMFL – Campus de Lille]

THÈSE

présentée par : **Alberto BARETTER**

soutenue le : **13 octobre 2022**

pour obtenir le grade de : **Docteur d'HESAM Université**

préparée à : **École Nationale Supérieure d'Arts et Métiers**

Spécialité : **Mécanique-matériaux**

Analysis of the performance and stability of an axial compressor operating under inlet flow distortion

THÈSE dirigée par :
[M. DAZIN Antoine]

et co-encadrée par :
[M. PIERRIC Joseph]
[M. ROUSSETTE Olivier]

Jury

M.Sofiane KHELLADI, Professeur, LIFSE, ENSAM Paris	Président
M. Xavier OTTAVY, Directeur de recherche CNRS, LMFA, Centrale Lyon	Rapporteur
M. Nicolas BINDER, Professeur, DAEP, ISAE-SUPAERO	Rapporteur
M. Julien MARTY, Ingénieur de recherche, ONERA Meudon	Examinateur
Mme. Melanie VOGES, Ingénieur de recherche, DLR Cologne	Examinatrice
M. Antoine DAZIN, Professeur, LMFL, ENSAM Lille	Examinateur
M. Pierric JOSEPH, Maître de conférences, LMFL, ENSAM Lille	Examinateur
M. Olivier ROUSSETTE, Ingénieur de recherche, LMFL, ENSAM Lille	Examinateur

THÈSE

Acknowledgments

First of all I would like to thank **Antoine Dazin**, the director of this thesis, for his support throughout the development of this work, for his scientific guidance but also for his kind character and special care to people, which is very important to create a peaceful and productive environment.
I would also like to thank **Pierric Joseph**, co-supervisor, for his advice and help on the experimental aspects and sometimes even hands-on involvement during the setup of experiments.
In addition, I thank **Olivier Roussette**, co-supervisor, for his assistance on more technical aspects and for the replacement of a bearing, which allowed the continuation of the experimental work.
I want to thank **Francesco Romanò** (for all purposes another co-supervisor) for his help especially on the theoretical side. Our discussions about experimental results have contributed a great deal to this work.
Thanks also to **Gerard Bois** for finding time, when he was in Lille, to have a look at my progress and offer his advice.
I would like to thank the technicians, namely **Patrick Olivier** and **Claude Lamaz,** that acted on the test bench allowing its operation during the experimental campaigns.

Thanks to **Christophe Cuvier**, **Pierre Braganca** from Centrale Lille and **Jean-Claude Monnier** from ONERA for their assistance in the preparation of the Particle Image Velocimetry campaign.

Thanks finally to **Raphael Barrier** and **Benjamin Godard** of ONERA for the exchanges and guidance in the context of the SUBLIME project.

Contents

NOMENCLATURE **7**

GENERAL CONTEXT **9**

1 INTRODUCTION **11**

1.1 WORKING OF TURBOFAN AND COMPRESSORS 11
1.2 FLOW DISTORTION 14

2 LITERATURE REVIEW **19**

2.1 INLET DISTORTION 19
2.1.1 ROOTS OF THE PARALLEL COMPRESSOR *19*
2.1.2 THE PARALLEL COMPRESSOR *21*
2.1.3 WEAKNESSES OF THE PARALLEL COMPRESSOR: FLOW INERTIA *22*
2.1.4 THE CRITICAL ANGLE OF DISTORTION AND THE DC60 INDEX *25*
2.1.5 HYNES GREITZER MODEL *28*
2.1.6 THE ADVENT OF CFD *30*
2.1.7 RECENT EXPERIMENTAL INVESTIGATIONS *31*
2.1.8 APPLIED INVESTIGATIONS ON BLI *32*
2.2 ROTATING STALL 32
2.2.1 MODAL AND SPIKE STALL *33*
2.2.2 MATHEMATICAL MODELS AND EXPERIMENTAL INVESTIGATIONS *34*
2.2.3 CFD AND RECENT DEVELOPEMENTS *35*
2.3 DISTORTION GENERATORS 36
2.3.1 DISTORTION GRIDS *36*
2.4 CONCLUSIONS 40

3 EXPERIMENTAL MEANS **43**

3.1 THE COMPRESSOR CME2 43
3.2 GRID SIZING 45
3.2.1 PRELIMINARY MODEL *46*
3.2.2 MANUFACTURING AND INSTALLATION *47*
3.2.3 COMPARISON WITH MODEL *48*
3.3 PRESSURE MEASUREMENTS 49
3.4 PIV MEASUREMENTS 53

4 EFFECT OF THE DISTORTION ON THE PERFORMANCE: STALL MARGIN **61**

4.1 FOUR FLOW REGIMES 61
4.1.1 STALL MARGIN BASED ON STALLING PRESSURE RISE *63*
4.1.2 SM BASED ON STALLING MASS FLOW RATE *65*
4.1.3 SYNTHESIS : FULL PICTURE *67*
4.2 DISTORTION INDEXES 69
4.2.1 INDEX DIST *69*
4.2.2 INDEX DC60 AND DC90 ..... *70*
4.3 A NEW DISTORTION INDEX 72
4.3.1 THE SCALE $\boldsymbol{\theta int}$ *72*
4.3.2 SCALING WITH INDEX $\boldsymbol{DC\theta avg}$ *77*
4.4 LIMITATIONS OF THE SCALING WITH $\boldsymbol{DC\ \theta avg}$ 80
4.4.1 SATURATION OF THE STALL MASS FLOW (PIV FIELDS) *80*

4.4.2 SATURATION OF THE STALL MASS FLOW RATE (PRESSURE SENSORS) 87
4.5 CONCLUSIONS 89

5 TRANSITION TO ROTATING STALL 91

5.1 STALL REGIMES 91
5.1.1 BEFORE THE ONSET OF ROTATING STALL 93
5.1.2 AFTER THE ONSET OF ROTATING STALL 94
5.1.3 SYNTHESIS: GENERAL PICTURE 95
5.2 MORE FEATURES OF STALL 101
5.2.1 ANALYSIS TOOLS FOR UNSTEADY PRESSURE SIGNALS 101
5.2.2 DEVELOPED ROTATING STALL 103
5.2.3 SPEED AND AMPLITUDE OF THE PERTURBATION INSIDE AND OUTSIDE THE DISTORTED REGION 105
5.2.4 CRITICAL AMPLITUDE 106
5.3 CONCLUSIONS 107

6 DETAILED FLOW DESCRIPTION OF 2 REGIMES 109

6.1 REGIME 2 : GRID 120° POROSITY 0.5 110
6.1.1 CHARACTERISTIC CURVE AND ϕ AND ψ VS θ 111
6.1.2 COMPARISON WITH MODEL 112
6.1.3 FLOW FIELDS IN THE BLADE CHANNELS 114
6.1.4 UNSTEADY ENERGY CONTENT 118
6.2 REGIME 3 : GRID 120° POROSITY 0.23 120
6.2.1 CHARACTERISTIC CURVE AND ϕ AND ψ VS θ 120
6.2.2 COMPARISON WITH MODEL 122
6.2.3 FLOW FIELDS IN THE BLADE CHANNELS 123
6.2.4 UNSTEADY ENERGY CONTENT 125
6.2.5 3D FLOW 128
6.3 CONCLUSIONS 129

7 CONCLUSIONS AND FUTURE PERSPECTIVES 131

REFERENCES 137

APPENDIX A: CHARACTERISTIC CURVES 143

APPENDIX B: RELATIONSHIP BETWEEN $\Delta\alpha$ AND $\Delta\phi$ 149

NOMENCLATURE

Latin

a	Compressor characteristic curve curvature [-]
c	Chord length [m]
c_x	Axial chord length [m]
C_L	Lift coefficient [-]
C_D	Drag coefficient [-]
F	Force [N]
f	Frequency [Hz]
$f_{rot} = 53\ Hz$	Rotor Frequency at 3200 rpm [Hz]
$i = \beta - \beta_{blade}$	Incidence angle [°]
$k = \min(p_{t_{rakes}})/(\frac{1}{2}\rho v^2)$	Grid loss coefficient [-]
k_M	Correcting coefficient of grid loss (Idelchik, 1986) for Mach number effects
M	Mach number [-]
$\dot{m}$	Mass flow rate [kg/s]
N	Revolutions per minute [rpm]
P	Power [W]
POD	Proper Orthogonal Decomposition
p	Static pressure [Pa]
p_{atm}	Atmospheric pressure [Pa]
p_t	Total pressure [Pa]
p_{t_rakes}	Total pressure measured by the rakes [Pa]
r	Radius [m]
r_p	Pressure ratio [-]
SM	Stall margin [-]
s	Screen solidity [-]
T	Static temperature [K]
T_t	Total temperature [K]
t	Time [s]
$U = \Omega r$	Blade speed [m/s]
v	Absolute velocity [m/s]
v_x	Axial component of velocity [m/s]
v_θ	Tangential component of velocity [m/s]
w	Relative velocity [m/s]

Greek

α	Absolute flow angle [°]
β	Relative flow angle [°]
β_{blade}	Inlet blade metal angle [°]
γ	Stagger angle [°]
Δp_{t-s}	Compressor total to static pressure rise [Pa]
$\Delta p_{grid} = \min(p_{t_{rakes}})$	Grid pressure drop [Pa]
$\Delta\mathrm{SM}$	Loss in stall margin [-]
η_{t-s}	Total to static efficiency [-]
λ	Inertial parameter in Hynes Greitzer (1987) [-]
ξ	Grid porosity [-]
ρ	Density [kg/m^3]
θ	Compressor annulus coordinate [°]
θ_g	Grid angular extension [°]
θ_{int}	Interaction length scale [°]
θ_{crit}	Critical angle [°]
$\phi = v_x/\Omega r$	Flow coefficient [-]
ϕ_s	Flow coefficient at last stable point [-]
ϕ_n	Flow coefficient at the nominal point [-]
$\psi_{t-s} = \Delta p_{t-s}/(\frac{1}{2}\rho U^2)$	Pressure rise coefficient [-]
$\psi_{grid} = \Delta p_{grid}/(\frac{1}{2}\rho U^2)$	Non dimensional grid pressure drop [-]
Ω	Compressor rotational speed [rad/s]

GENERAL CONTEXT

Among the new technologies identified by CORAC (Conseil pour la Recherche Aéronautique Civile) as promising for a reduction of civil airplane fuel consumption is Boundary Layer Ingestion (BLI). The technology is based on the ingestion of the fuselage boundary layer into the jet engine and different studies show that a reduction between 5% and 10% of the fuel consumption is theoretically possible (Kawai et al., 2006), (Geiselhart et al. 2003), (Ochs et al. 2017). On the other hand, the ingestion of a boundary layer is particularly challenging for the turbomachines inside the engine, especially the fan and the compressor. It is known that the performance and the stall margin of fans and compressors are badly affected in the presence of inlet flow distortion (as the one created by an ingested boundary layer). The phenomena leading to the loss of performance, and especially to rotating stall and surge, are still not known in sufficient detail by engine manufacturers to allow the production and operation of BLI engines. Another challenge is represented by the highly unsteady aerodynamic loads which fan blades have to withstand in such distorted flows; the coupling between the aerodynamic loads and the elastic structural behaviour of the blades can sometimes lead to resonance effect and failure of the blades. Led by the possible gains in fuel consumption, the last decade has seen an increase of interest in the BLI technology, and many actors like NASA have pushed research to develop know-how on the subject (Cousins et al. 2017). In France, ONERA is currently leading (from 2018) the research project SUBLIME (SUpport BLI, Méthodes et Expérimentations) financed by DGAC (Direction Générale de l'Aviation Civile) to increase knowledge on four big axes of research: the aerodynamic performance of the airplane with BLI engines, the fan and compressor stall margin in BLI environments, the type of flow created by the inlet of BLI airframes, and the aeroelastic behaviour of blades in BLI. The present work is a part of this project. It aims to increase knowledge about the phenomena that degrade the performance and stall margin of compressors in distorted flows, doing so by providing an experimental dataset of measurements in an axial compressor operated in distorted flow. The experiments have been performed on the axial flow low speed compressor CME2 operated in the Laboratoire de Mécanique des Fluides de Lille Kampé de Fériet (LMFL).

A number of distortion grids of different porosities and angular extensions intended to represent very different types of inlet flow nonuniformities have been designed and mounted at the inlet of the compressor to influence its performance. Total pressure and static pressure measurements have been performed to identify the loss of performance, and unsteady pressure measurements and Particle Image Velocimetry (PIV) have been used to investigate in more detail the flow features, with a focus on the stability limit of the compressor. The acquired experimental data should provide a source of validation of CFD simulations developed in parallel by ONERA and a consolidation and enrichment of current knowledge in distorted flow operation in axial compressors.

1 INTRODUCTION

In this opening short chapter, the topic of inlet flow distortion will be presented; in order to introduce the subject, a brief description of a turbofan will first be given, with a focus on the working principle of an axial flow compressor in a uniform flow, as in conventional engines. After this, non-uniform inlet flow operation, referred as inlet distortion, will be introduced as a general problem in turbomachinery. Some aspects that have not been fully investigated up to today are discussed and the organisation of the manuscript is presented.

1.1 WORKING OF TURBOFAN AND COMPRESSORS

In a turbofan (figure 1-1), the air entrained in the engine. It first enters into the fan, which accelerate the air creating thrust. After the fan, part of the air (called the bypass flow rate) is directly sent to the exit, and part is sent through the hot section where fuel is burned and added to it before the air reaches the exit. The ratio of the two flow rates is called bypass ratio. In the hot section, air first enters the axial compressor and its pressure and temperature are increased. In the following combustion chamber, the heat released from the combustion adds energy to the flow, increasing further the enthalpy of the gas. The turbine extracts part of the energy, transforming it into shaft work to run the compressor which requires work to compress the air; the remaining energy of the flow is used to generate thrust by an expansion in the nozzle, where enthalpy is transformed into kinetic energy.

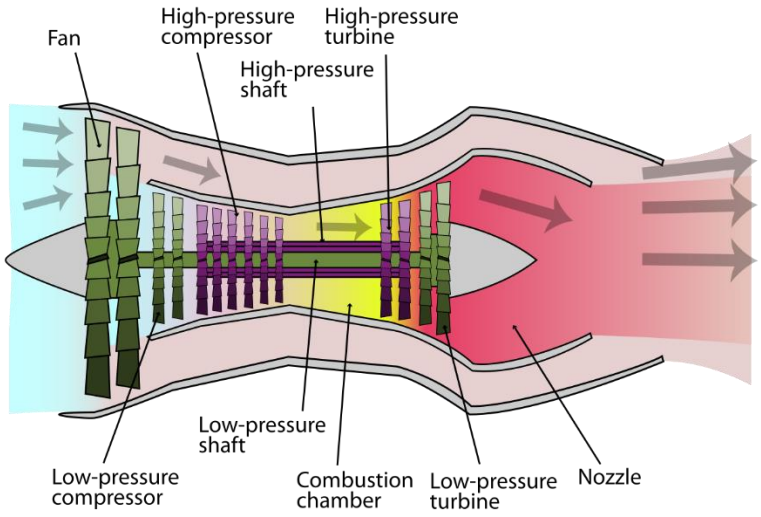

Figure 1-1 : scheme of a turbofan elements (source: https://www.Militarypedia.it)

The pressure ratio of a compressor (typically 40:1), is distributed in multiple stages of compression. In figure 1-2a the cascade of a compressor stage operating at design conditions is schematically represented. Each compression stage is comprised of a row of rotating blades (rotor) and a row of fixed blades (stator), and has limited compression capabilities, usually 1.15:1 to 1.6:1 (Cumpsty and Heyes 2015). The work done by the turning rotor blades imparts a variation of moment of momentum to the flow, generating a tangential

component of velocity $v_{\theta 2}$ at the outlet of the rotor; at the same time, an increase of pressure is achieved. The values of mass flow rate and pressure rise determine the operating point in the so called compressor characteristics (figure 1-2c). If the mass flow rate of the incoming flow is lower (figure 1-2b), the turning imparted by blades and the pressure rise increase, leading to a different point in the compressor curve (figure 1-2d).

The amount of turning a blade can provide however is limited. The flow, in the relative frame, is decelerated and encounters an adverse pressure gradient which can promote boundary layer detachment. When the inlet flow is further reduced from the point in blue in figure 1-2d, the flow can no longer withstand the amount of turning forced by the blades, and the blade stalls; unsteady phenomena as rotating stall and surge are triggered The blue point is thus called the stability limit, or last stable point of operation. A rotating stall transient is schematically represented in figure 1-2d in the red line. After the transient, the compressor works in rotating stall (red point) characterised by a reduced pressure rise and a low mass flow rate. More details about the phenomenon will be given in following chapters. In jet engines, rotating stall usually leads to surge, characterised by a breakdown of the axial flow, causing violent oscillations of the flow, and in the worst cases flow reversal can take place, sucking the flame out of the combustion chamber (figure 1-3). Since rotating stall and surge represent a hazard for engine safety, the manufacturers design engines to run with sufficient margin before the stalling pressure rise, a margin that is high enough to compensate for the lack of knowledge on the very complicated aerodynamic phenomena involved in triggering rotating stall and to prevent the stall arising due to an unexpected event modifying the machine operating conditions.

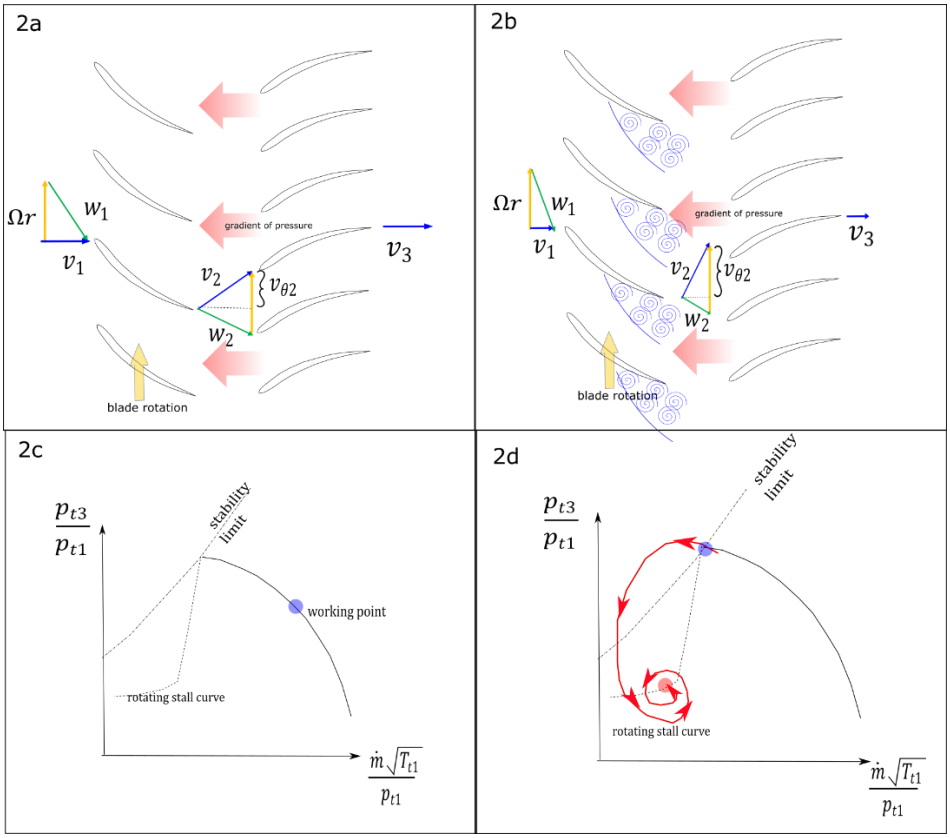

Figure 1-2. a) scheme of compressor stage working in design conditions; b) scheme of compressor stage working close to stall; c) compressor characteristic curve with nominal working point d) compressor characteristic curve with working point close to stall (blue point) and transient towards rotating stall (red line and red point).

In figure 1-4, the compressor curve at different rotating speeds is represented, operating on a line with a safety margin with respect to the stability limit. This safety margin is referred as stall margin and it is based

on the difference in pressure rise between the stability limit and the operating line. Different events can push the operating point towards the stability limit, for example the engine acceleration. During acceleration of the engine, more fuel is injected into the combustion chamber, making pressure and temperature rise more quickly than the mass flow rate entrained by the accelerating turbomachines. Thus, the pressure rise seen by the compressor rises closer to the stability limit. Other events leading to operation closer to the stability limit are rapid decelerations, ingestion of objects (birds, ice on the nacelle, debris on the runway) or inflow distortion conditions. During engine operation, the safety margin is guaranteed by anti-stall systems like bleed valves or variable stator vanes (VSV) (Rolls Royce 2015). All of the systems provide a change of the operating point to restore safe operation.

Figure 1-3: compressor surge leading to a flameout (source: El-Sayed A.F 2015)

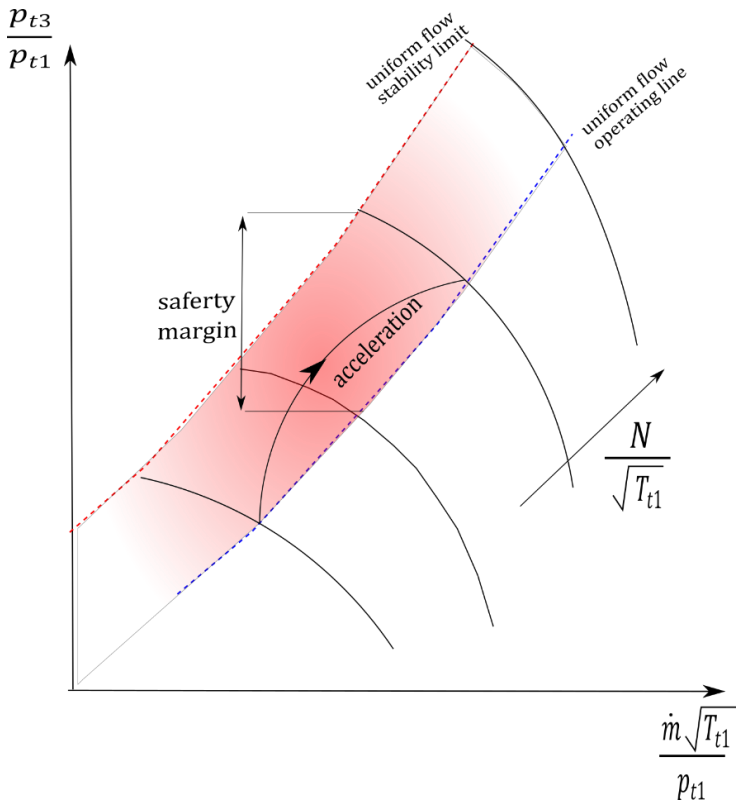

Figure 1-4 : compressor characteristic curve in uniform flow; operating line and stability limit line

The presence of a safety margin of course further represents a limitation to the pressure rise with which a stage can operate. Therefore, it must be compensated for by the introduction of additional stages if a higher pressure rise is wanted, with a consequent increase in size and weight of the engine. Having high compressor pressure ratios is highly desirable especially in civil engines, since they imply a higher efficiency of the thermodynamic cycle and thus a lower fuel consumption.

1.2 FLOW DISTORTION

Among the sources that represent a cause of rotating stall and surge, inlet flow distortion has been mentioned. Inlet distortion generally refers to a non-uniformity of the flow at the engine inlet; there can be different types of inlet distortions: total pressure and swirl distortions are the most common, but total temperature distortion also appears especially in military aircrafts and in general in transonic turbomachines. The causes for the existence of distortions can be many: the shape of the airframe and its interaction with the engine, or particular flight conditions, during take-off or during turns. In conventional jet engines however, distortion is mostly a temporary condition. That being said, in the last decades, engine design has changed in order to meet stricter polluting criteria. Higher bypass ratio engines are more desirable from this point of view. To avoid the weight penalty due to the increase of diameter of engines, short inlet ducts are used with a consequent decreased ability to attenuate inlet distortions. Other engine designs, for example boundary layer ingestion (BLI), require engines working permanently in non-uniform conditions (figure 1-5). In BLI configurations, engines are integrated in the fuselage and ingest the low speed boundary layer which develops on it. A typical total pressure pattern seen by the fan is shown in figure 1-5 on the right. A part of the inflow is almost at free stream conditions, while a part is at low total pressure and lower speed.

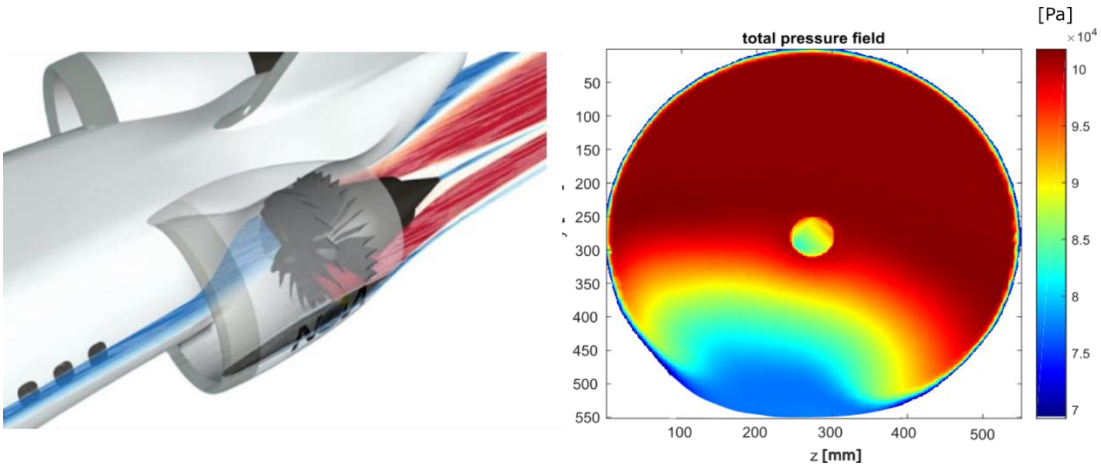

Figure 1-5 : left: boundary layer ingesting engine (source https://www.onera.fr/fr/actualites/nova-pour-une-aeronautique-plus-verte); right: typical BLI total pressure pattern (from ONERA simulations)

In simple terms, the gain in fuel consumption comes from the fact that for a given thrust force $F = \dot{m}\Delta v$, less power input must be added to a flow entering the engine at lower speed (equation 1.1).

$$P = \frac{\dot{m}}{2}(v_2^2 - v_1^2) = \frac{F}{2}(v_2 + v_1) = F(v_1 + \frac{\Delta v}{2}) \tag{1.1}$$

The power P required to create the thrust F depends on inlet engine velocity v_1 and $\Delta v = v_2 - v_1$; for a same aircraft thrust, Δv is constant, thus, a reduction of power requirement is achieved if the inlet velocity v_1 is

lower. Additionally, in the power balance of the full aircraft, BLI helps in reducing the losses associated to the wake and to the jet stream exiting the engines. Figure 1-6 schematically compares the conventional podded engines and the BLI. To balance the momentum defect in the wake, the engine produces a momentum excess. To both the wake and engine jet are associated mixing losses that reduce the efficiency of the system. In BLI, ingesting the wake and reenergize it in the engine can reduce both these mixing losses. In the limit as the wake is perfectly ingested and reenergized to the free stream velocity (figure 1-6 bottom panel) the mixing losses tend to zero.

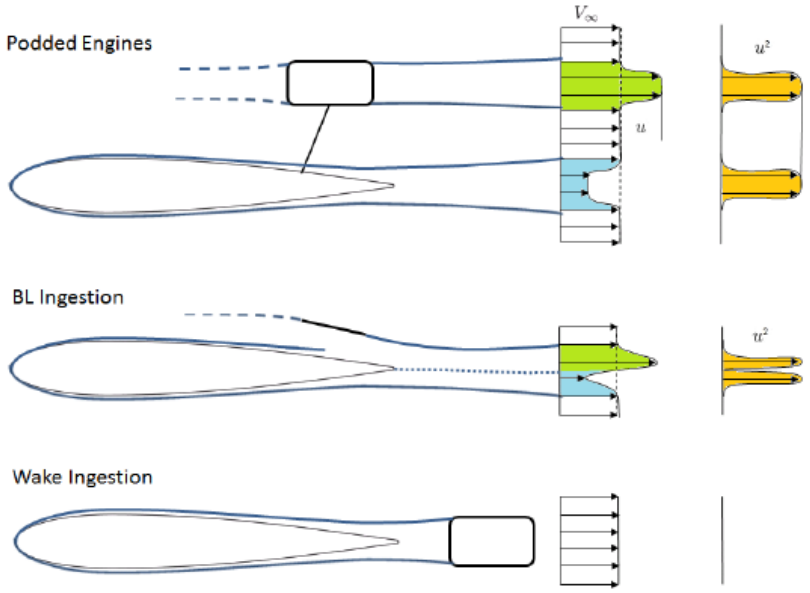

Figure 1-6 comparison of classical podded engines and BLI ; source (Arntz et al. 2014)

For BLI, some studies indicate a possible fuel reduction in the range 5-10% (Geiselhart et al. 2003), (Ochs et al. 2017).

Qualitatively, the consequences of a generic total pressure distortion on the compressor performance are shown in figure 1-7. The characteristic curve of a compressor working with inlet distortion is schematically represented. The distortion not only causes a reduction of the pressure rise, but also triggers rotating stall and surge at higher flow rates (loss of stall margin), forcing the engine to operate at lower pressure rise.
Until today, the effect of different types of distortion on the performance, especially on the stall point, is not yet properly understood and changes from compressor to compressor. In fact, the onset of rotating stall is generally caused by complex three dimensional flows concentrated in specific regions of the blade channel depending on the compressor design. These flow mechanisms are still under investigation for uniform flow condition (Pullan et al., 2015), and are surely altered by the complex non-uniform flow in distorted environments (Perovic et al., 2015). The investigation of these mechanisms is challenging experimentally, and in the past, most of the research has been focused on the identification of the stall limit, trying to link it to the intensity of various distortion types and patterns (Reid 1969), (Burstadt et al., 1971). Most of these works, described in the following chapter, were using distortion grids to reproduce a distortion of the flow. However, these studies were not entering into much detail about the actual features of the stall mechanism and of the flow field in the bladed regions at the onset of the instability. These aspects have become progressively easier to investigate in the last twenty years thanks to the development of high response pressure sensors but also to CFD. CFD in fact allows to extract information about flow quantities in regions where experimental measurements are a challenge, as in between rotor blades. An experimental technique which can provide high spatial resolution measurement in challenging regions of the flow is Particle Image Velocimetry (PIV) which has been developed since the beginning of the 80s, but still is not fully exploited in distortion studies. Even if in the last decades distortion studies have been focusing on the particular

application to BLI, grid distortion is still studied (Ewan J. Gunn et al. 2013) as it can provide many information on the physics of distortion which are still not clear.

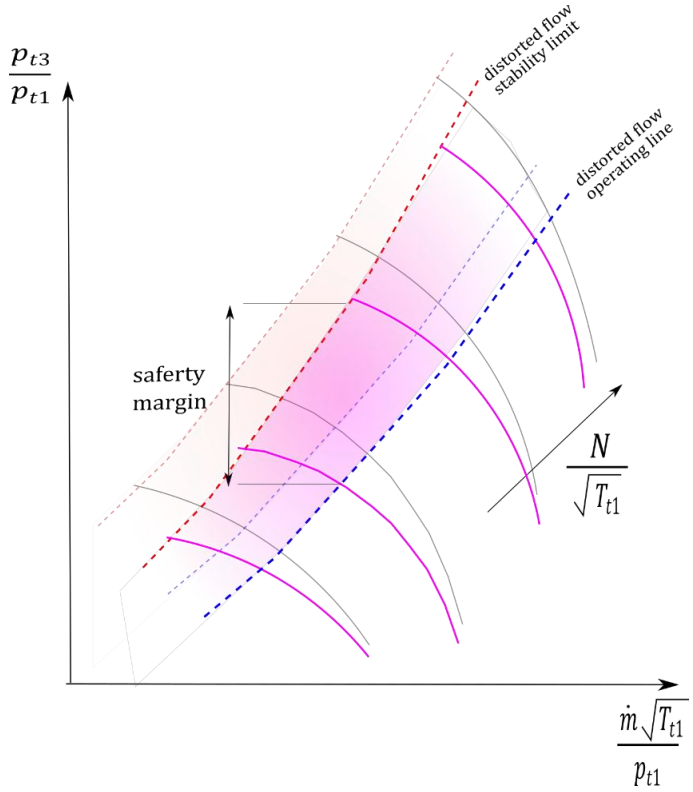

Figure 1-7: compressor characteristic curve in distorted flow; operating line and stability limit line

The use of grids is particularly cheap and simple to implement, and allows to generate distortions with simple geometrical patterns that can be characterized by different parameters as the pressure loss, the angular or radial extension. The simplicity and cost effectiveness is the main reason why the method has been so popular in distortion studies. However, it has limitations. For example, for the specific application of distortion due to boundary layer ingestion, it is clear that grids can just be partly representative of a boundary layer on the fuselage. They can reproduce the total pressure drop effect, but the turbulent flow field is very different, especially because the grids introduce in the flow scales which are characteristic of the geometry of the grids (hole size, distance between holes..). Grids are more adapted to study the general properties of distortions, in particular in parametric studies that need a simple characterisation of the grid. In this work, with the aim of investigating more the physics of a generic distortion, a study of grid distortion on an axial flow compressor is performed, with a focus on circumferential patterns. The aim of the study is to investigate further some aspects which are not very developed in literature, in particular:

- the link between the stalling point in different distorted conditions and the detailed features of the onset of the instability.
- the type of flow in the blade channels just before the onset of instability.

To address the two topics, a set of distortion grids of different angular extensions and porosities has been tested, to create a very broad range of distortions; unsteady pressure measurements during the stall transient and PIV at the last stable point have been combined to the classical distortion performance measurements.
This work is structured in the following way: in chapter 2, previous studies on inlet distortion are summarized, introducing concepts that are useful to interpret the experimental results and discussions presented in the manuscript. In chapter 3, the choice and design of the distortion grids is discussed; the test bench CME2 is

described, with details on the instrumentations and the measurement techniques that have been used to address the research goal. Chapter 4 first presents experimental results: the stall margin of the various distortion patterns tested are compared to one another. It will be shown that the set of distortion features observed in the experiments can be reduced to four flow regimes. A new scaling of the stall margin will be introduced, based on physical arguments, unlike the existing ones which have been based on empirical evidence and which need to be adapted from one compressor to another. In chapter 5, the stall margin is linked to the transient to rotating stall, analysed in more detail using unsteady pressure signals. It will be shown that the stall mechanism in the various distorted cases, fits very well in the classification in four flow regimes developed in chapter 4. Chapter 6 presents PIV fields of two particular distortion cases, belonging to two of the four regimes, to highlight the features of the flow in the blade passages, in particular before the arise of stall.

2 LITERATURE REVIEW

2.1 INLET DISTORTION

In this chapter, some of the past works concerning inlet distortion are cited, especially to introduce the physics and the concepts that are necessary to interpret the experimental results presented in this manuscript.

2.1.1 ROOTS OF THE PARALLEL COMPRESSOR

During the 50s, when the turbojet engine was becoming a widely spread technology, researchers started to investigate some phenomena faced during engine operation, especially inlet flow distortion and the arise of instabilities such as rotating stall and surge. Since the beginning, experiments dealing with non-uniform inlet flow were conducted introducing grids in the flow upstream of the compressor, to block a part of the annulus (Conrad and Sobolewski, 1950). During these first experiments a decrease of the stage pressure rise was observed, as well as a tendency to trigger rotating stall and surge at higher mass flow rates with respect to the operation with uniform flow. A special attention was paid to the propagation of the distortion through the various stages of the compressor. It was in fact observed that the grid perturbation becomes weaker and weaker when traversing the stages of the compressor, meaning that the first stages of the compressor appear to be the most critical for stability and performance issues.
Pearson and McKenzie (1959), in their note, laid down some elements to explain the weakening of the perturbation in the mid and rear stages, and by doing that, they first introduced the idea of a parallel compressor which has had a lot of impact in all of the subsequent literature.

Pearson and McKenzie considered a velocity distortion far upstream of the compressor where static pressure is undisturbed and uniform. This distortion, when convected to the compressor inlet, must be modified by the upstream influence of the compressor. Specifically, the compressor acts to reduce the velocity distortion by compensating for it with a static pressure distortion such that the upstream total pressure distortion is preserved. To demonstrate this, they imagined the full compressor as divided into two parallel compressors working with two different inlet total pressures, A and B (figure 2-1).

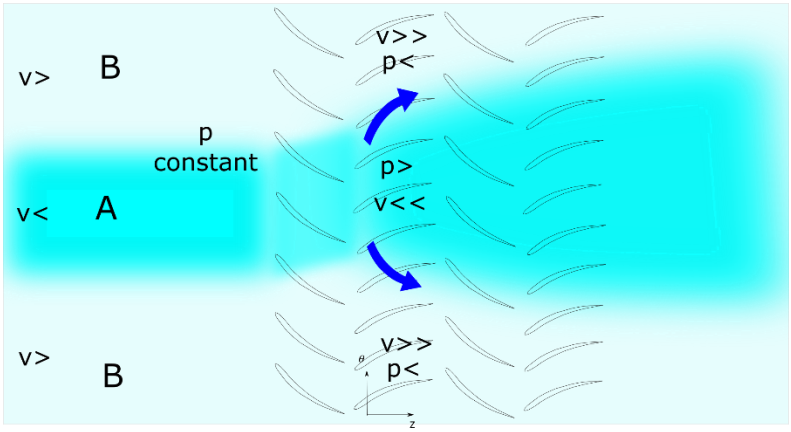

Figure 2-1 : scheme representing an inconsistent physical argument to explain the weakening of distortion through the compressor; v represents velocity of the flow and p the pressure.

With reference to the scheme, far upstream of the compressors, two flows have constant static pressure but one flow has a low velocity region (A). The compressor in A works in this low velocity region while compressor in B works outside of it. Since in A the velocity is lower, the static pressure rise developed by the compressor in A is higher than the one developed by in B. Thus, if static pressure is believed to be constant at the inlet, the downstream static pressure is higher in A than in B. However, this situation is not self-consistent. In this case in fact, flow moves from A to B from higher pressure to lower pressure, decelerating further in the central wake A and accelerating further in the surrounding flow B, leading to an even higher static pressure non-uniformity downstream. The flow description is thus inconsistent and the hypothesis of a constant static pressure at the inlet of the compressor is not valid.

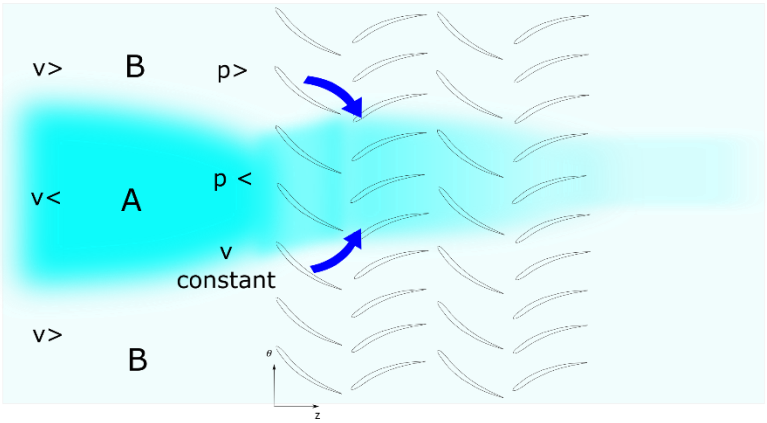

Figure 2-2 scheme representing a consistent physical argument to explain the weakening of distortion through the compressor; v represents velocity of the flow and p the pressure.

Instead, Pearson McKenzie state that, at the inlet of the compressor, velocities are almost the same and inlet static pressure is non-uniform, with low static pressure in A and a higher static pressure in B in the surrounding flow (figure 2-2). The compressor in A still creates a higher pressure rise than in B, but starting from a lower value of pressure at the inlet so that the outlet pressures in the two regions re-equilibrate through the compressor until a uniform static pressure is reached at the outlet. Streamline curvature causes acceleration of the wake and deceleration of the surrounding flow to restore uniform velocity. This is coherent with the experimental evidence.

This phenomenon of upstream redistribution was treated mathematically in some early works (Sears, 1953), (Ehrich, 1957), (Rannie and Marble, 1957), (Yeh, 1959)**.** These first works aimed to build a physical model to predict the weakening of the distortion downstream of the stage, and to gain physical insight. They were all based on a similar approach (small-perturbation theory) but were mainly differing in the hypothesis used to simplify the problem. The PhD thesis of Katz (1958) summarises some of these works and provides another similar model.

The mathematical solution of these models is particularly instructive. It consists of a superposition of a rotational convected perturbation (the distortion introduced far upstream) and an irrotational perturbation (of velocity and static pressure) which is the reaction of the compressor to the rotational upstream perturbation. The solution is thus coherent with the physical argument of Pearson and McKenzie. Mathematical expressions for the propagation of pressure and velocity distortions are found, and they predict the downstream weakening of the distortion with reasonable accuracy compared to experiments. The mathematical model also predicts that the strength of this potential effect and the downstream weakening are controlled by the compressor slope, and that they are stronger when the slope is more negative (thus at higher ϕ). When approaching the stability limit at lower flow rates, on the contrary, the effects are less strong. Another very important feature results from these models: the static pressure perturbation is closely related to a tangential velocity perturbation, which is 90° out of phase with respect to

the axial velocity and pressure perturbations. In figure 2-3 the profiles of velocity and pressure and the corresponding velocity triangles are schematically represented, as can be predicted by the models.

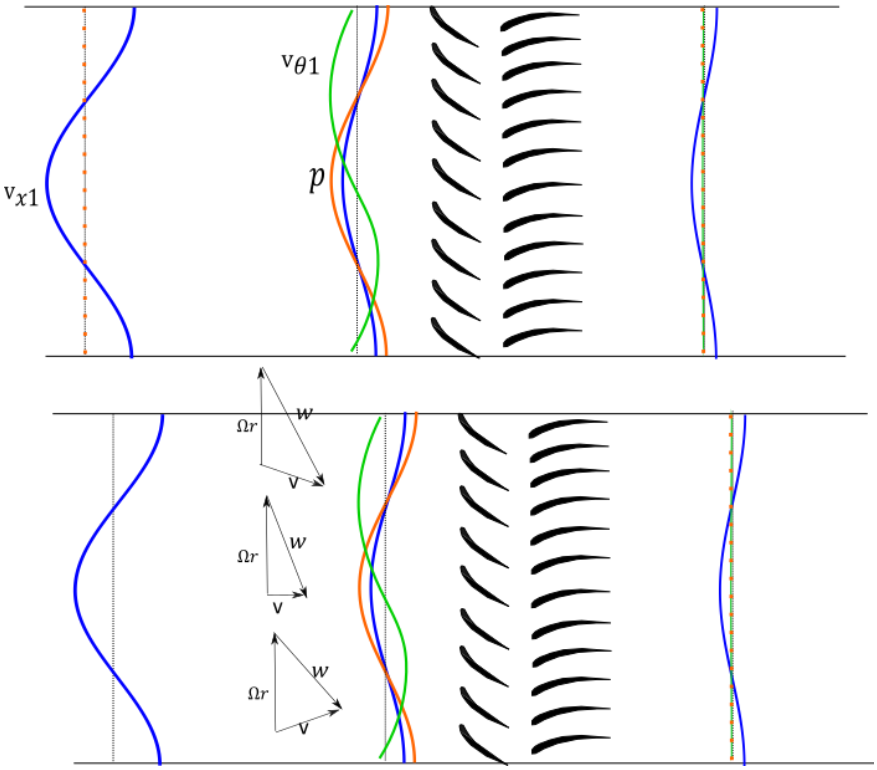

Figure 2-3 : scheme representing the weakening of the velocity distortion at the inlet of the compressor, being compensated by the rise of static pressure and tangential velocity distortions, the last being responsible of modifying the incidence on the sides of the distorted region

The perturbation of tangential velocity is modifying the velocity triangles, tilting the flow towards the centre of the distortion region. The effect is closely related to the static pressure perturbation since the static pressure gradient between the distorted and undistorted flow drives the flow towards the distorted region, generating tangential flow. A region of increased incidence is thus present where blades exit the distortion region and a region of decreased incidence where blades enter the distortion region. It will become evident in chapter 6 that PIV flow fields on the CME2 compressor are clearly capturing this pattern.

2.1.2 THE PARALLEL COMPRESSOR

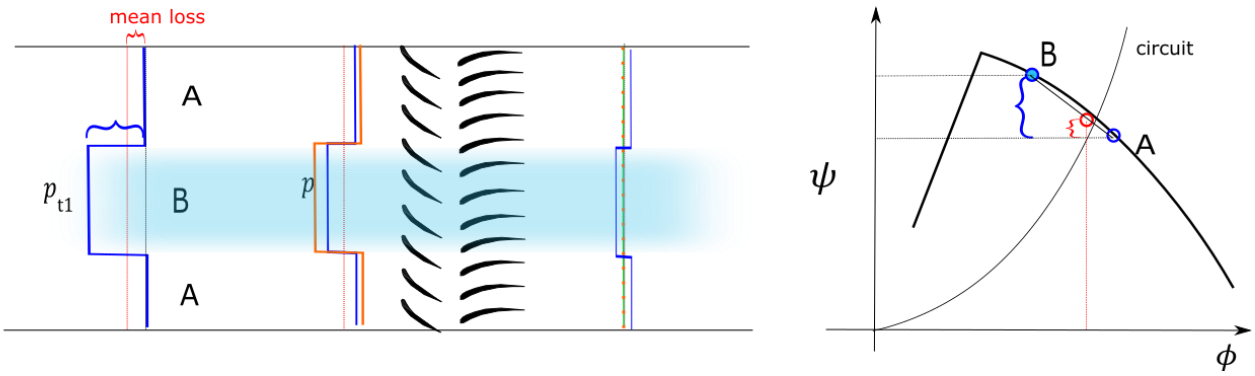

Figure 2-4 : scheme representing the principle of the parallel compressor

The parallel compressor model as stated in Braitwhaite et al., (1971), states that the overall compressor performance is the average of two compressors working at two different operating points, one in A in the

undistorted region, developing the same pressure ratio as in uniform flow, and one in B in the distorted region, developing a higher pressure ratio closer to the stall limit (figure 2-4). The overall compressor performance is determined by the weighted average of the two points A and B. As far as stability is concerned, in the parallel compressor model, the stalling point is assumed to be reached when the pressure rise of the sub-compressor in the distorted region equals the stalling pressure rise in usual non distorted operation. The first sub-compressor reaching the last stable point determines the global last stable point.

2.1.3 WEAKNESSES OF THE PARALLEL COMPRESSOR: FLOW INERTIA

An interesting observation was added by Plourde et al., (1968) which brought the parallel compressor model into discussion. A campaign of experiments was conducted in which the number of stages, the chord lengths of the blades and vanes, and the rotor stagger were changed. Plourde et al. found out that increasing rotor chord length increased the distortion tolerance, in the sense that the loss of stall margin was less serious than the one predicted by parallel compressor theory. In fact, they noticed that the stalling mass flow rate was always overpredicted by the parallel compressor model. They linked this observation to the unsteady response of blades in non-steady flow, a similar argument that was developed at the same time by Carta (1967).

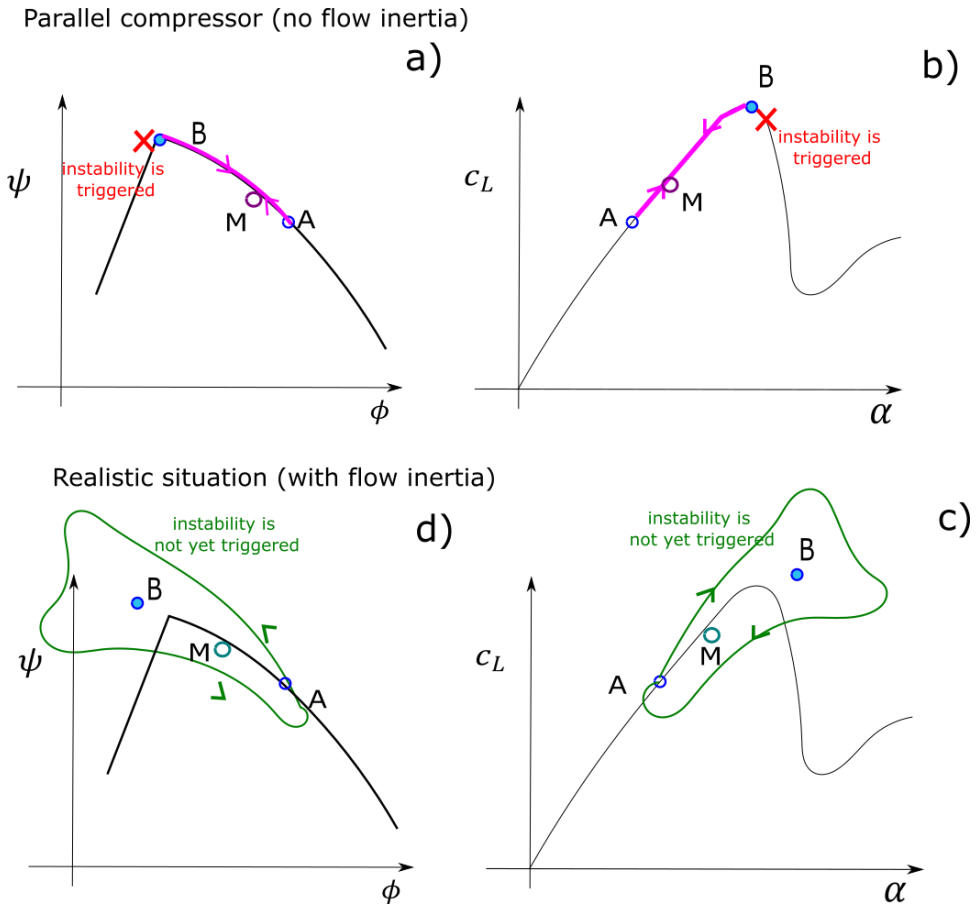

Figure 2-5 : figures a) and b) : stall point M in parallel compressor theory; A conditions far from the grid, B condition behind the grid. Figures c) and d) stall point M with flow inertia; ; A conditions far from the grid, B condition behind the grid

Carta was testing the response of aerofoils under oscillating motion and showed that the response is characterized by an hysteresis loop in the lift versus incidence curve. He noticed also that the hysteresis loop was responsible for allowing unstalled operation well beyond the static stall limit of the aerofoil. This argument was used by Plourde et al. (1968) to explain the difference between the prediction of the parallel compressor model and the experimental data. In the parallel compressor model, instability is believed to be

triggered when the blades in the distorted region (B) reach the usual stall limit (figure 2-5a). This happens approximately in the vicinity of the peak lift coefficient in the lift-incidence curve for the blades (figure 2-5b). In reality, as is suggested by Carta, the hysteresis loop in the lift incidence curve (figure 2-5c), allows the blades in the distorted region to work beyond the blade limit incidence without triggering the instability. As a result, in the compressor map, the mean flow rate at stall (point M in the figures 2-5a and 2-5d) is in general lower than the one predicted by the parallel compressor model.
According to Carta, the key parameter to estimate the importance of this unsteady effect is the following ratio of frequencies (reduced frequency).

$$\frac{f_{rot}}{1/\tau_{flow}} = \frac{f_{rot}}{2w/c} \tag{2.1}$$

In the numerator f_{rot} is the forcing frequency, coinciding with the rotational frequency in the case of the blades rotating in and out of a distortion region in the compressor, and with the pitching frequency in the case of an aerofoil. The denominator is the characteristic frequency of the flow, defined as the inverse of the flow time, the time it takes to a particle to traverse the compressor. This flow time is defined as the half of the chord length divided by the relative velocity of the flow. When this reduced frequency is high, it means that the flow time is higher than the forcing characteristic time, and thus the blade response is slower then forcing and the inertial forces delay the full development of stall.
As it was clear in the experiments by Plourde et al. (1968), the chord length plays a key role in the dynamics. A higher chord length increases the reduced frequency, and an increase of the reduced frequency, as Carta had shown, has a less detrimental effect on the stalling behaviour. An equivalent way to increase the reduced frequency is to increase the number of distorted regions per revolution. If the region of distortion is split into multiple smaller distorted regions per revolutions, the effect is an increase of the forcing frequency in the numerator. This was seen to be coherent with experimental observations, for example by Reid (1969). The concept was further developed by Melick (1973)**.** He assumed that the response of the aerofoil can be treated with a second order linear differential equation of the type:

$$\frac{d^2(\alpha_{eff}-\alpha_0)}{d\tau^2} + \left(\frac{1}{\tau_1}+\frac{1}{\tau_2}\right)\frac{d\left(\alpha_{eff}-\alpha_0\right)}{d\tau} + \frac{1}{\tau_1\tau_2}\left(\alpha_{eff}-\alpha_0\right) = \frac{1}{\tau_1\tau_2}(\alpha_{inst}-\alpha_0) \tag{2.2}$$

with τ scaled as

$$\tau = tU/c \tag{2.3}$$

The forcing is proportional to the difference between the instantaneous angle of attack α_{inst} and the angle of attack at which the perturbation of the flow occurs α_0, and the response is given in terms of an effective angle of attack α_{eff}, which accounts for the time for the flow over the aerofoil to adjust, and for boundary layer separation to occur. The two time constants $\tau_1$and τ_2 have to be determined from experiments. When such a system is forced with a sinusoid, the response is a function of the reduced frequency and the time constants and it is characterised by a reduction in amplitude and a phase lag. The function is then:

$$\frac{(\alpha_{eff}-\alpha_0)_{max}}{(\alpha_{inst}-\alpha_0)_{max}} = f(k) = \frac{1}{\sqrt{(1+4k^2\tau_1^2)(1+4k^2\tau_2^2)}} \tag{2.4}$$

This is illustrated in figure 2-6, in which the instantaneous angle cycle is in continuous line and the effective angle of attack is in dashed line. The actual response of the blade is determined by the effective angle of attack cycle, and is thus characterised by reduced amplitude. The blades are thus able to sustain higher

incidences beyond the static stall limit and correspondingly, the compressor can work locally beyond its expected stall limit.

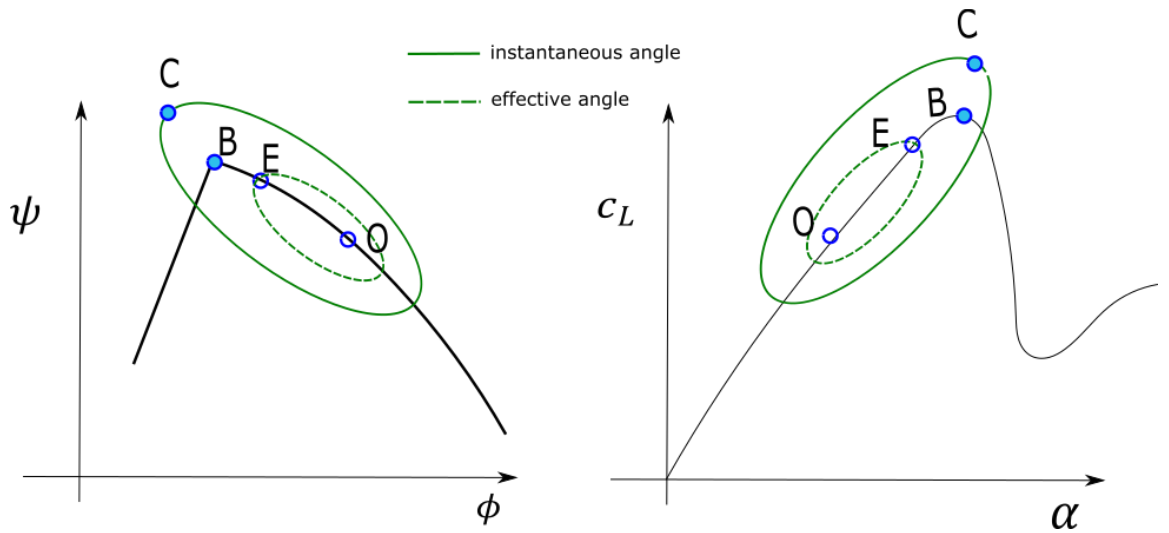

Figure 2-6 : instantaneous incidence angle and effective angle in Melick argument (adapted from Melick , 1973)

The stall point is thus expected to be reached when the blades in the distorted region are at a α_{eff}=α_{Stall} , and not the $\alpha_{inst} = \alpha_{Stall}$. For a square distortion pattern, instead of a sinusoidal one, Melick used the same approach considering all the Fourier components in determining the response in term of α_{eff}. Square patterns of different duty cycles, simulate the effect of grids occupying just an angular sector of the annulus, as the grids that were usually used in experiments (Reid 1969). For narrower grids, the high harmonic components are more important in magnitude than for a wider grid where lower harmonics dominate, and since their reduced frequency is higher (more peaks per period are present), their effect in terms of effective angle is reduced determining a smaller effective angle cycle in narrower grids than in wider grids. The loss of stall margin must thus be smaller for narrower grids than for wider grids, for a given amount of distortion. This was observed to be coherent with the experimental observations. In his analysis he then linked the pressure ratio to lift and effective angle of attack. He defined the loss in stall margin (figure 2-7) as

$$\Delta SM = \frac{(r_{pE} - r_{pO})}{r_{pO}} \tag{2.5}$$

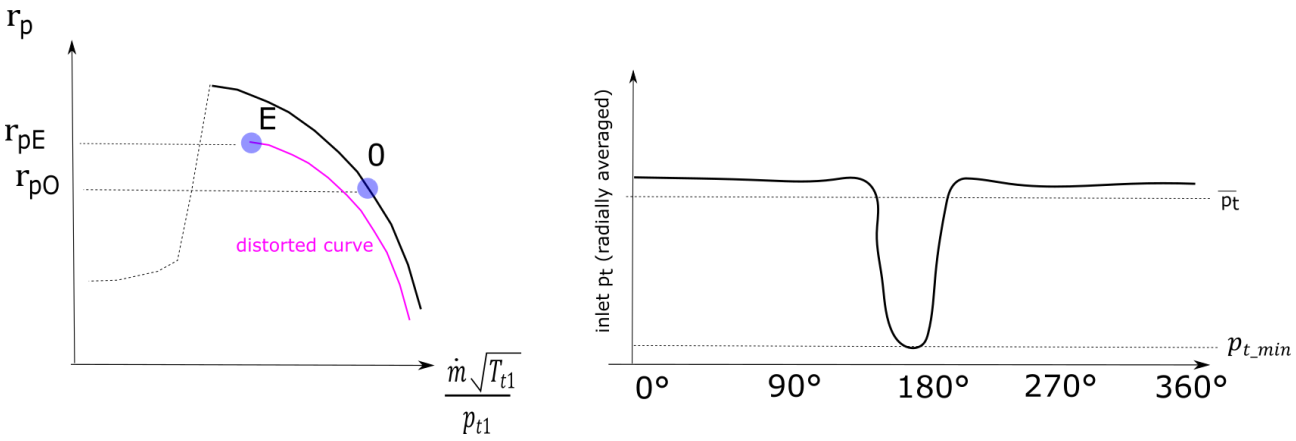

Figure 2-7 : scheme representing the quantities used in equations (2.5) and (2.6)

where r_{pE} is the stalling pressure ratio in distorted conditions and r_{p0} the nominal pressure ration in undistorted conditions. He then correlated the ΔSM with the distortion amplitude index defined as:

$$\text{Dist} = \frac{(\bar{p}_t - p_{t\,min})}{\bar{p}_t} \tag{2.6}$$

He showed the following relationship:

$$\frac{\Delta SM}{Dist} = f(k) \tag{2.7}$$

In which $f(k)$ takes the form of a low pass filter as in figure 2-8.

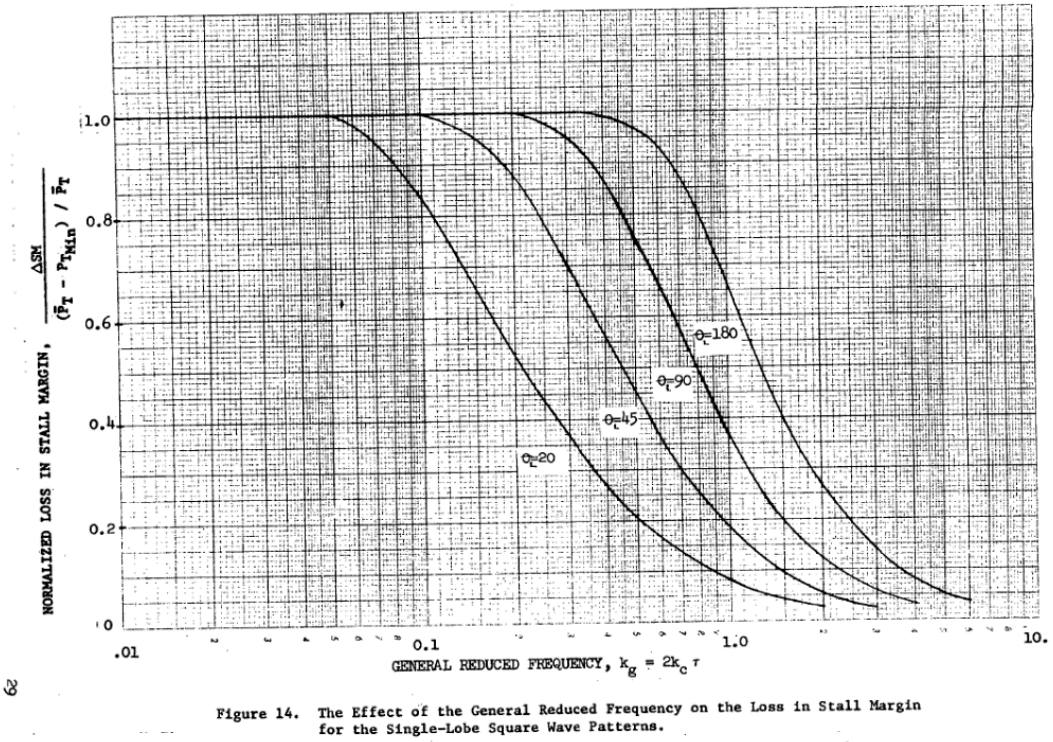

Figure 14. The Effect of the General Reduced Frequency on the Loss in Stall Margin for the Single-Lobe Square Wave Patterns.

Figure 2-8 : shape on the function f(k) for square grids of different angular extension (from H.C. Melick 1973)

The comparison between this form and their experimental results with different grids covering an angular sector of the annulus showed good agreement. Their analysis suggests that not only the amount of distortion is important, as in parallel compressor theory, but also the function f(k) determined by the response of the blades.

2.1.4 THE CRITICAL ANGLE OF DISTORTION AND THE DC60 INDEX

A wide series of experiments that are still considered as references in distortion studies were done by Reid (1969). Different grids of different distortion angle extensions were tested. The mesh of the grid was the same so that the ratio of pressures in the distorted sector p_L and outside p_H is almost the same ($p_H/p_L = const$). This last fact is true if the porosity is sufficiently high to avoid recirculation (and it is not true for all the grids that have been used for the present thesis). Reid measured surge delivery static pressure for the various grids and found that there is a critical angle of distortion above which the stall margin does not decrease further if the angle is increased (figure 2-9).

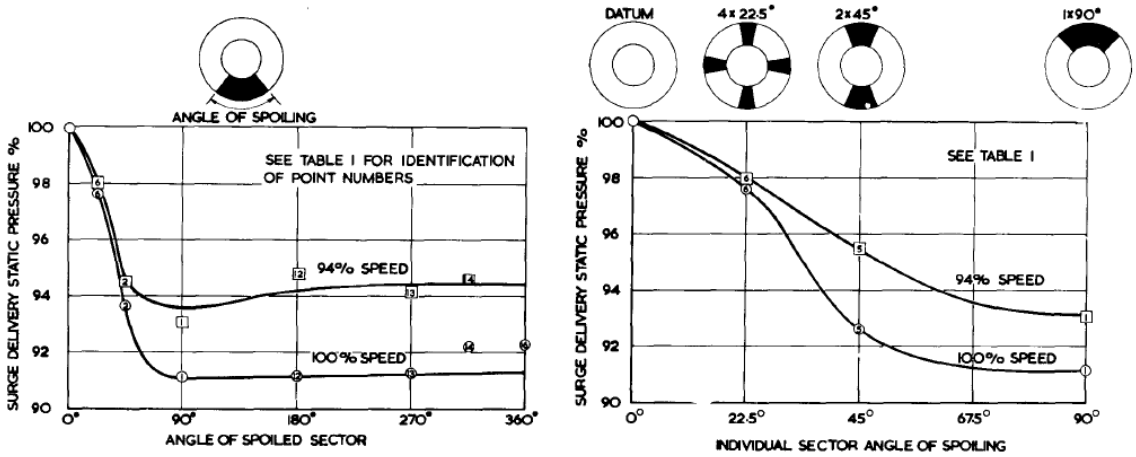

Figure 2-9 : surge static pressure versus angular extension of the distortion grids (from Reid 1969)

Since it appeared that a critical angle exists at 60°, Reid suggested the use of a new distortion index to correlate data, defined as DC60. The index is different from Dist defined in 2.6, because instead of considering the minimum total pressure in all the annulus, it considers the minimum area averaged total pressure in a window corresponding to the critical sector, p_{crit} (figure 2-10). The index is defined as

$$DC60 = \frac{\Delta p_t^*}{\bar{p}_t} \tag{2.8}$$

with

$$\Delta p_t^* = \bar{p}_t - p_{crit}$$

where $\bar{p}_t$ is the averaged total pressure calculated over the whole annulus.
It has to be noted that for angles of the grid greater than the critical angle, the area averaged total pressure in the 60° coincides with the minimum total pressure, while for lower angles, it is less than the minimum.

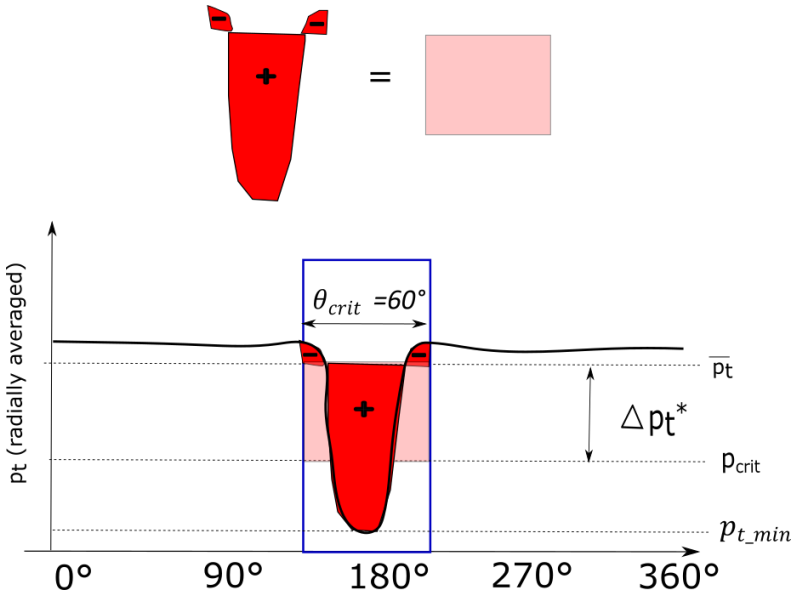

Figure 2-10 : scheme representing the estimation of DC60 index as defined in Reid (1969)

In figure 2-11 are represented the calculated values of the DC60 for perfectly square wave distortions having the same ratio of total pressure in the distorted sector and outside of it, as in Reid grids. For the calculation,

the ratio is supposed to be 1.9 just for an illustrative purpose. Its effect is to decrease the effective distortion for sectors of an angular extension less than the critical angle.

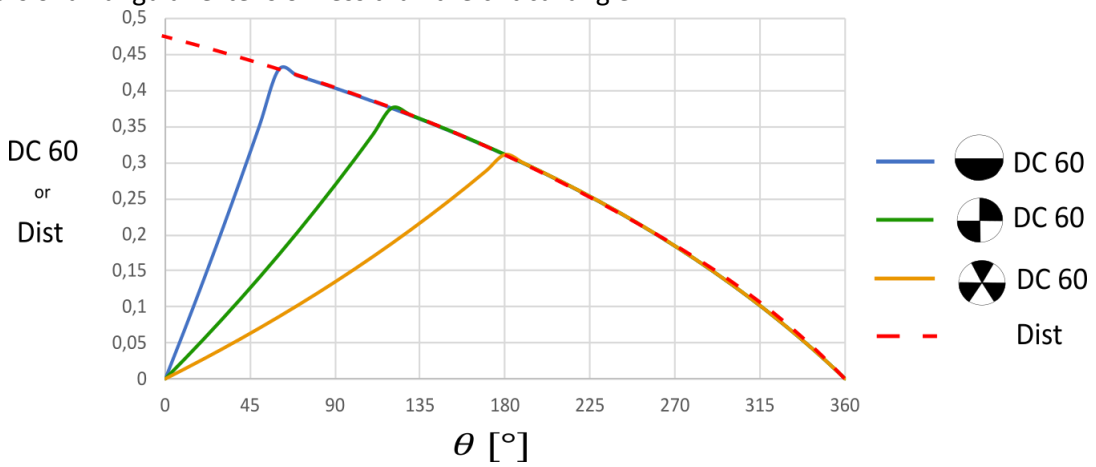

Figure 2-11 : comparison between the index Dist defined in (2.6) and DC60 defined in figure 2-10 as a function of the angular extension of square grids with the same ratio of total pressure far from and behind the grid =1.9

The index was built on purpose to have a lower effective distortion for narrower sectors in order to preserve a linear correlation between the stall margin loss and a distortion index. The physical reason behind the use of the DC60 is closely related to Melick analysis. In Reid grids, for a fixed ratio of minimum total pressure with respect to undistorted sector total pressure, the Dist index as defined in (2.6) decreases as the spoiling angle increases (figure 2-12) since the minimum pressure p_{Tmin} is closer to the mean total pressure $\overline{p_T}$ when grids are wider. Thus, looking to equation 2.7, the loss in stall margin should decrease if f(k) was a constant. f(k) however has the opposite trend and increases for wider grids. (figure 2-8). The two opposite tendencies give rise to a maximum in the stall margin loss, as qualitatively shown in figure 2-12.

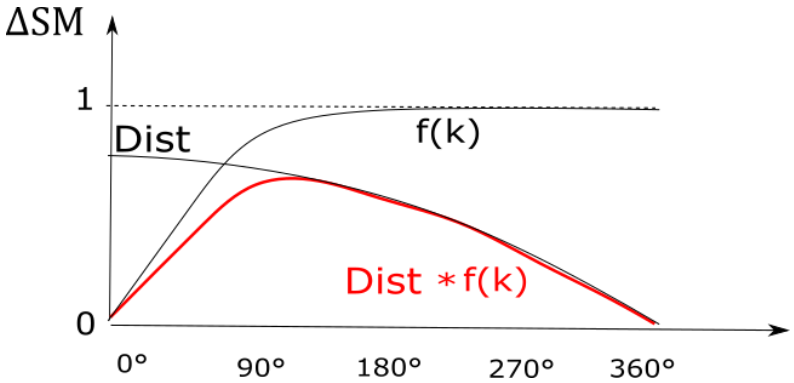

*Figure 2-12 : qualitative shape of the product Dist*f(k) for different angular extensions of square grids having the same ratio* $\frac{p_H}{pL}$

Reid tested also cases when the spoiled angle was divided into a number of smaller elements, increasing thus the distortion regions per revolutions (figure 2-9 on the right). Coherently with Melick analysis, since dividing the distortion region increases the reduced frequency, he found a less detrimental effect when the angle is divided in more sub-sectors. The definition of the DC60 automatically takes into account the effect of splitting the distortion angle (figure 2-11).

Burstadt et al. (1971) performed similar experiments on a broad set of grid circumferential and radial distortions. They found the existence of a critical angle of 60°, with similar trends compared to Reid. They concluded too that the critical angle concept is linked to a minimum blade residence time necessary to impact the compressor in a quasi-steady-state manner. They succeeded in correlating the stall margin with the distortion index.

In the late 70s and beginning of the 80s, two standards were published and then revised regularly until the last version of 2017 (AIR1419C: Inlet Total-Pressure-Distortion Considerations for Gas-Turbine Engines - SAE

International, 2017), (ARP1420: Gas Turbine Engine Inlet Flow Distortion Guidelines - SAE International, 2017). The aim is to provide information about how to determine the impact of inflow distortion on engines stability and performance. They especially describe the guidelines to testing methodologies and provide a set of distortion indexes alternatives to the DC60 which are commonly used as a metric in literature (Bissinger and Breuer, 2010). Correlations are built linking the stall margin to the distortion indexes through sensitivity coefficients. However, these sensitivity coefficients are empirical and based on data sets of tests performed on many fans and compressor. They are thus of very limited scientific interest since they don't highlight the physical mechanisms relating stall margin and distortion indexes, and are limited to existing fans and compressors designs that are part of the experimental data bases. For this reason, in the following chapters, these indexes and correlations have not been exploited to discuss the experimental results of the present study.

2.1.5 HYNES GREITZER MODEL

Following the knowledge acquired in modelling from the 60s and the evidence that the unsteady blade response is a key factor in distortion, Hynes and Greitzer, (1987) developed an extension of the well-known Greitzer model (Moore and Greitzer, 1986) to take into account the distortion. Their model is based on small perturbation theory, and treats the compressor as an actuator disk. Moreover static pressure at the outlet of the compressor is considered uniform. There are however some major differences with previous models: first the full system is modelled, including the throttle valve at the discharge; most important, the compressor and the throttle valve are modelled with their non-linear characteristics. The upstream and downstream flows are still modelled as linear small perturbations, but now, contrary to the previous parallel compressor analysis, the compressor and the throttle valve act as sources of non-linearity. They are responsible for coupling the Fourier components of the distortion. Another very important novelty in the model is the introduction of the simplified unsteady blade response, using a characteristic equation of the type (2.9) for the pressure rise of the compressor.

$$\frac{p_3 - p_{t2}(\theta)}{\rho U^2} = \psi(\phi_2) - \lambda \frac{d\phi_2}{d\theta} \tag{2.9}$$

The equation express the pressure rise of the compressor as the sum of the steady state compressor characteristic $\psi(\phi_2)$ and a term representing the unsteady response as an inertial term, characterised by the flow inertia in the blade channels λ. The term $p_{t2}(\theta)$ is the θ dependent total pressure distortion at the inlet of the compressor, and represents the effect of the grid, as input in the model.

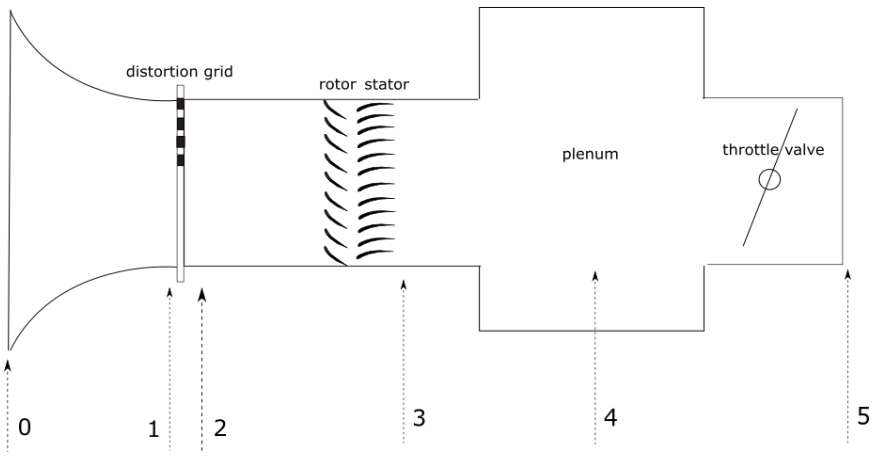

Figure 2-13 : compressor stations in Hynes Greitzer model (adapted from Hynes Greitzer, 1987).

Following the scheme in figure 2-13, Hynes Greitzer proposed a basic state of the flow defined by the following set of equations (2.10), which represent a balance circuit-turbomachine.

$$\begin{cases} \frac{p_3 - p_{t2}(\theta)}{\rho U^2} = \psi(\phi_2) - \lambda \frac{d\phi_2}{d\theta} \\ \frac{p_3 - p_5}{\rho U^2} = \frac{T}{2}\overline{\phi_2}^2 \end{cases} \tag{2.10}$$

Compared to the original Moore Greitzer model, the inertia in the upstream conduits and the unsteady accumulation of mass in the plenum (4 in figure 2-13) are not modelled, since the basic flow is assumed steady, and no surge dynamic is considered. The second equation in (2.10) represents the pressure drop of the throttle, with T being the throttle coefficient.
For an imposed pressure drop of a squared pattern, the solution for ϕ_2 has the general shape of figure 2-14. It is not simply a square pattern due to the presence of the inertial term. In Chue et al. (1989), under particular simplifying assumptions (parabolic compressor characteristic), an analytical expression is found, depending on the parameter λ/a ,in which a represents the curvature of the compressor characteristic and λ has the expression:

$$\lambda = \tau_{flow}\frac{U}{r} = \frac{c_x}{U\ (\cos\gamma)^2}\frac{U}{r} \tag{2.11}$$

and depends on the flow time τ_{flow} , the same appearing in Melick's arguments. There are two limiting cases of the solution, one dominated by inertia for high values of the ratio λ/a and one solution dominated by pressure drop when λ/a is low. In the second case, the square wave remains a square wave and the model approaches the parallel compressor. Moreover, the ratio λ/a also controls the decrease in pressure rise (figure 2-15) at stall, showing differences from parallel compressor in coherence with Melick's and Reid's arguments.

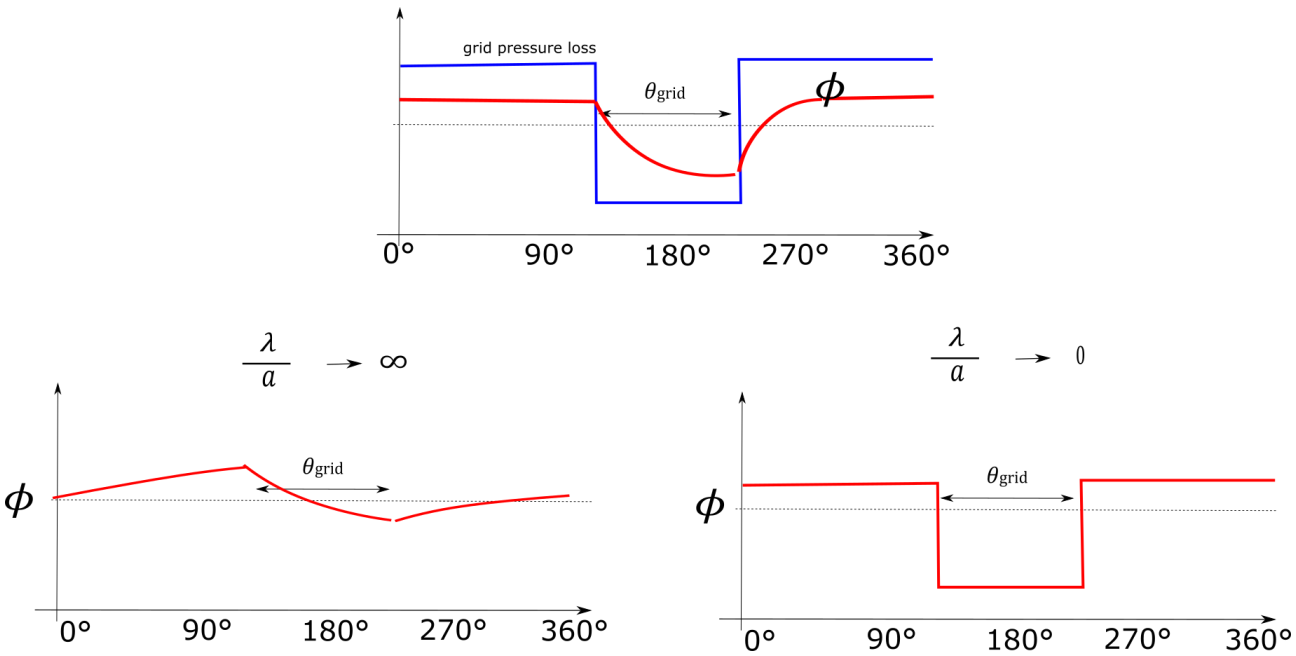

Figure 2-14 : qualitative shape of the solution of Hynes Greitzer model and two limiting cases of the solution

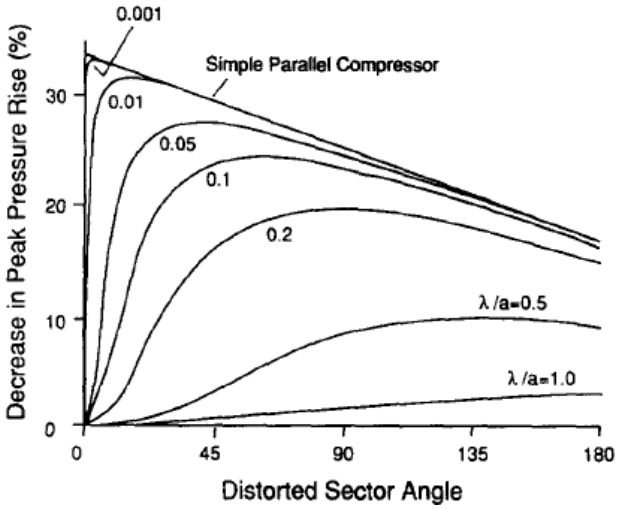

Figure 2-15 : loss in stall margin as a function of the sector angle parametric in $\frac{\lambda}{a}$ (from Hynes Greitzer, 1987)

To determine the stalling point, Hynes Greitzer model introduces on top of the basic flow a perturbation and solves an eigenvalue problem for the resulting equations. Using the model, they identified a criterion for instability defined as Integral Mean Slope (IMS) (not always valid as explained in Chue et al. (1989)). The compressor works for some portion of the annulus with a positive slope and in other portions with a negative slope (figure 2-16). Perturbations rotating in the annulus are experiencing a competition between exponential growth in the positive slope part of the annulus (in the distorted sector), and exponential decay in the negative sloped part of the annulus. When the integral under the curve defined by the local slope of the compressor on the annulus is 0, the instability is triggered. In uniform flow, in the classical Greitzer model, instability is triggered at a constant 0 slope, thus at the peak of the compressor characteristic.

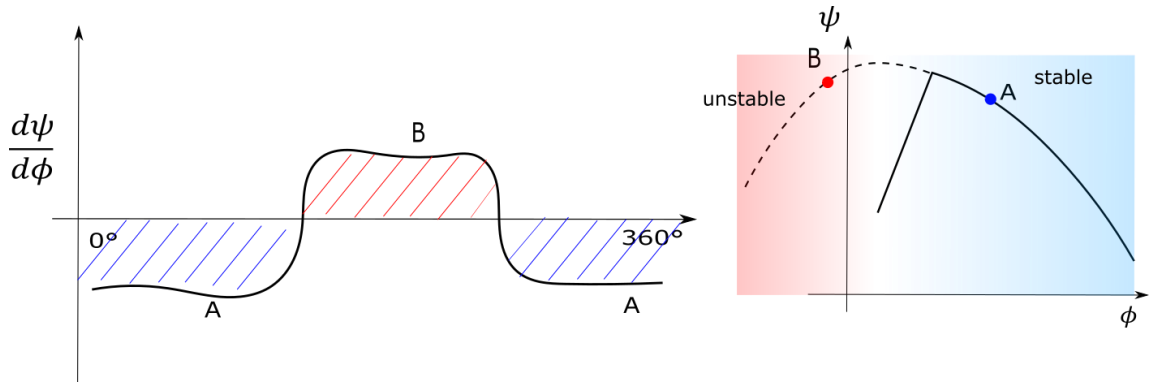

Figure 2-16 : stability criterion of the Integral Mean Square

Even if the criterion is not always valid, and in the CME2 compressor is not satisfied, the existence of perturbations growing behind the grid and decaying in the rest of the annulus has been experimentally observed in CME2 and will be discussed in chapter 5.

2.1.6 THE ADVENT OF CFD

Although very instructive to understand the physics, there are some limitations to Hynes Greitzer model to be used as a predictive tool, especially the dependence on the shape of the compressor curve, which is not known after the arise of rotating stall. It was through the advent of CFD that distortion research was pushed further. In the new millennium, the developments in computer technology have increasingly allowed to deal

with distortion problems with CFD simulations. The use of CFD has allowed to model complex cases involving coupled total temperature, total pressure and swirl distortions, and airframe-turbomachine coupling. For such complex flows and geometries, experimentally extracting information on the flow is challenging, especially because a great amount of measurements are required in a complex environment. High fidelity simulations have on the other hand allowed to have large datasets at the cost of the time required for simulation.

Yao et al., (2010) presented a RANS high fidelity CFD analysis of inlet distortion on an entire multistage fan. Their work shows that CFD is capable of predicting many of the features of distorted flows in a full turbomachine, such as total pressure and total temperature profiles transfer through the stages. Fidalgo et al., (2012) simulated inlet distortion in a transonic fan, showing that a clear effect of upstream redistribution is present and characterised by features similar of the ones predicted in the first analytical models (Katz, 1958). This upstream redistribution effect causes very different incidence angle conditions around the annulus, strongly influencing the local work input, and thus, the transfer of the distortion through the compressor. The change in axial velocity is reflected in the compressor map as an horizontal shift of mass flow while the change in incidence is responsible for modifying the effective speed of the compressor, thus shifting the operating point on different speed lines. In the first analytic models, the interaction between the distortion angle and the local work done was not modelled because in those small perturbation theories non-linear coupling of basic flow and the perturbation is not modelled. The advantage of these CFD models is that they inherently consider the full non-linearity of the problem, allowing for a more realistic description. Lesser and Niehuis (2014) analysed their simulations indicating how the various effects of distortion angle, unsteady work and velocity and static pressure distortion interact determining the transfer of the perturbation through the stage.

2.1.7 RECENT EXPERIMENTAL INVESTIGATIONS

On the side of experimental research, the competition of CFD has pushed scientists to increase the amount of instrumentation to increase spatial resolution, or to use techniques with intrinsic high spatial resolution like particle image velocimetry (PIV). Gunn et al. (2013)**,** conducted experiments with a 60° sector and performed high resolution measurements with 5 holes probes, highlighting the 3D features of the flow after the grid and in the compressor stage. They identified a region of separation close to the tip where the blades leave the distorted region (this region will be seen to be critical following PIV measurements in the present manuscript); the distortion leaving the rotor was seen to modify strongly the flow in the following stator, leading to a corner separation (Gunn and Hall, 2014). Perovic et al. (2015), performed unsteady pressure measurements on a fan, and stressed the need to investigate the detailed arise of the instability to be able to further understand the influence of distortion on the stability limit. In their paper, they state that the past research has been concentrating a lot on steady measurements, often far from the instability limit, and there is a lack of investigation of the actual unsteady onset of instability mechanisms. Part of this lack of investigation has been due to the unavailability of high response instrumentation until recently (Jahnen et al., 2014). Many recent works have clarified some mechanisms in uniform flow, as (Pullan et al., 2015), (Hewkin-Smith et al., 2019), but still, literature on distortion effects on the mechanisms of instability is restricted (Lin et al., 2005), (Page et al., 2018). This is one of the reasons why a part of this work has been devoted to unsteady measurements in various distorted conditions during the onset of rotating stall. The effort has been to present a parallel analysis of stall margin limits and the mechanism of instability for different distorted conditions.

Some of the most recent experimental research has shifted to the characterisation of the distorted flows as created by engine inlets of different shapes for BLI applications. The industrial interests in the competition for the creation of new low-consumption aircrafts have caused a revival of distortion studies. In some of these works, PIV has revealed a promising measurement technique, since it allows high resolution in space,

a necessity for complex non-uniform flows. Zachos et al. (2016) used Stereo-PIV in an S-duct inlet to characterise the effect of the curvature on the pressure and velocity fields. Similar works have been conducted by Bucalo et al. (2013), Guimarães et al. (2018) to measure distortion patterns in front of the engine. In these works, the distortion patterns have been created using recently developed methods to design distortion grids for total pressure distortion (Schneck et al., 2013) and swirl distortion (Hoopes and O'Brien, 2015). The methods aim to reproduce complex patterns of distortion similar to the ones for BLI applications. PIV methods can be also used in the bladed regions, where introducing instrumentation is challenging and can offer a valuable tool to investigate with high resolution distorted fields, compare to and validate CFD simulations. However, until today, PIV has not yet become a standard technique in distortion studies.

2.1.8 APPLIED INVESTIGATIONS ON BLI

As far as the recent development in BLI is concerned, helped by the solid support from CFD developed in the beginning of the new millennium, a very intense scientific program was conducted between MIT, Virginia Tech and Nasa during the first decade of the new millennium. The aim was to design an inlet/fan stage that can perform in a boundary layer ingestion environment. The work is briefly summarized in Cousins et al., (2017)**.** Initially, a conceptual design for an aircraft performing in a BLI was developed, the D8 (Uranga et al., 2014). URANS simulations were used to model the full inlet/fan combination, in order to have a low cost, rapid estimate of the propulsive efficiency. Experiments in wind tunnel helped then to characterise the performance on a scaled model (Ochs et al., 2017). Two key parameters for the BLI performance were seen to be the inlet loss and the fan efficiency. This conducted to a study at VirginiaTech for the development of a low loss inlet (Florea et al., 2015). A new design of the fan was finally proposed. CFD was used in the design process to observe the diffusion factor variations as blades move in the annulus, in order to control the stalling-recovery mechanism which allows a better stability. To improve the performance, the exit guide vane was design to have non uniform circumferential distribution of stators, non-circular flow path, and variable design stators in the distorted region. The project led to the first prototype of a boundary layer ingesting fan, tested successfully in the NASA Glenn 8'x6' wind tunnel.

2.2 ROTATING STALL

In the introduction, rotating stall was introduced as a phenomenon appearing at low mass flow rate, and characterised by the drop of performance of the machine. In this paragraph, more elements are added to its description, in order to ease the understanding of unsteady pressure signals shown in chapter 5.
Surge was described as a breakdown of the axial flow, with oscillations of the mass flow rate in the compressor. Rotating stall , on the other hand, consists in a disturbance of the circumferential flow pattern: one or more regions of separated flow develop in the annulus, occupying usually more than one blade channel and a more or less extended part of the blade span; these regions of separated flow, called stall cells, propagate around the compressor in the same direction as blade rotation, at a speed which is usually between 20% and 50% of the blade speed. The mechanism of propagation of the stall cell was first described in Emmons (1955). A scheme in figure 2-17 helps the interpretation.

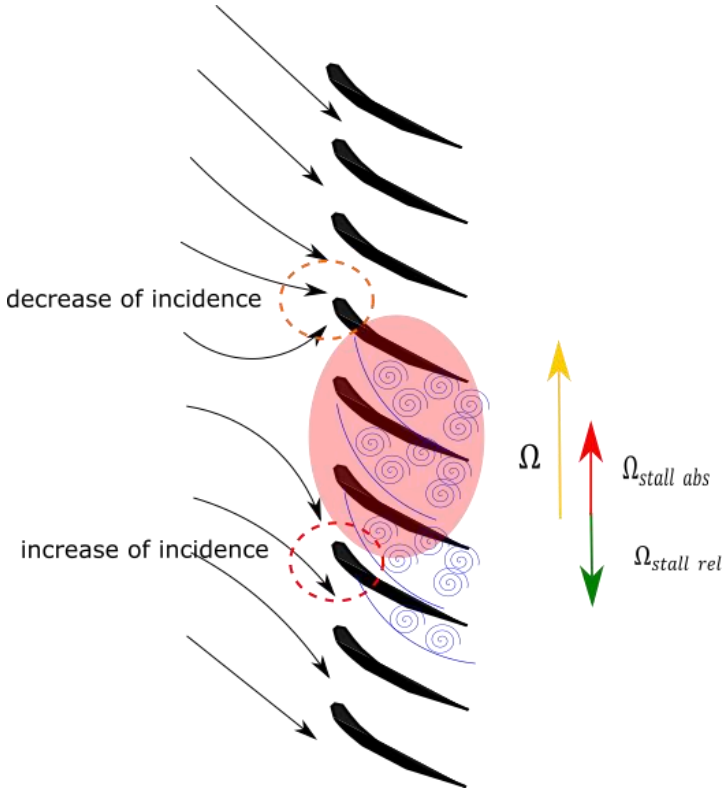

Figure 2-17 : schematic propagation mechanism for a rotating stall cell

The blockage due to the cell is responsible for deviating the flow on blades at the edges of the cell; on the lower edge in the figure 2-17 , the incidence is increased leading to stall of the next blade. In the higher edge incidence decreases leading to de-stall of the blade. In the relative frame, thus, the cell propagates in the opposite sense of the rotor rotation, so that its absolute velocity is a fraction of the rotational speed.

2.2.1 MODAL AND SPIKE STALL

Up to today, two mechanisms are known that lead to rotating stall. They are referred as “modal type stall” and “spike type stall” (Day, 1993).

Figure 2-18 : graphical representation of modal (left) and spike (right) type of stall (from Day (1993))

In the first case, the stall cells grow progressively from small perturbations of high wavelength (compared to the blade channel), as shown in figure 2-18 on the left. In the second case, cell grows from a sudden event of flow breakdown localised in the tip region, on a length scale comparable to the blade channel (figure 2-18 right). The two different mechanisms have been seen to be dependent on the type of compressor, but also on the operating conditions and are known to change when distortion is present (Perovic et al., 2015). Usually, the identification of these instabilities is done using casing pressure probes at high acquisition rates, to capture the unsteady pressure fluctuations in the tip region. The two types of stall, when captured by casing pressure probes, appear as in figure 2-19, where two casing signals acquired in the CME2 compressor are shown.

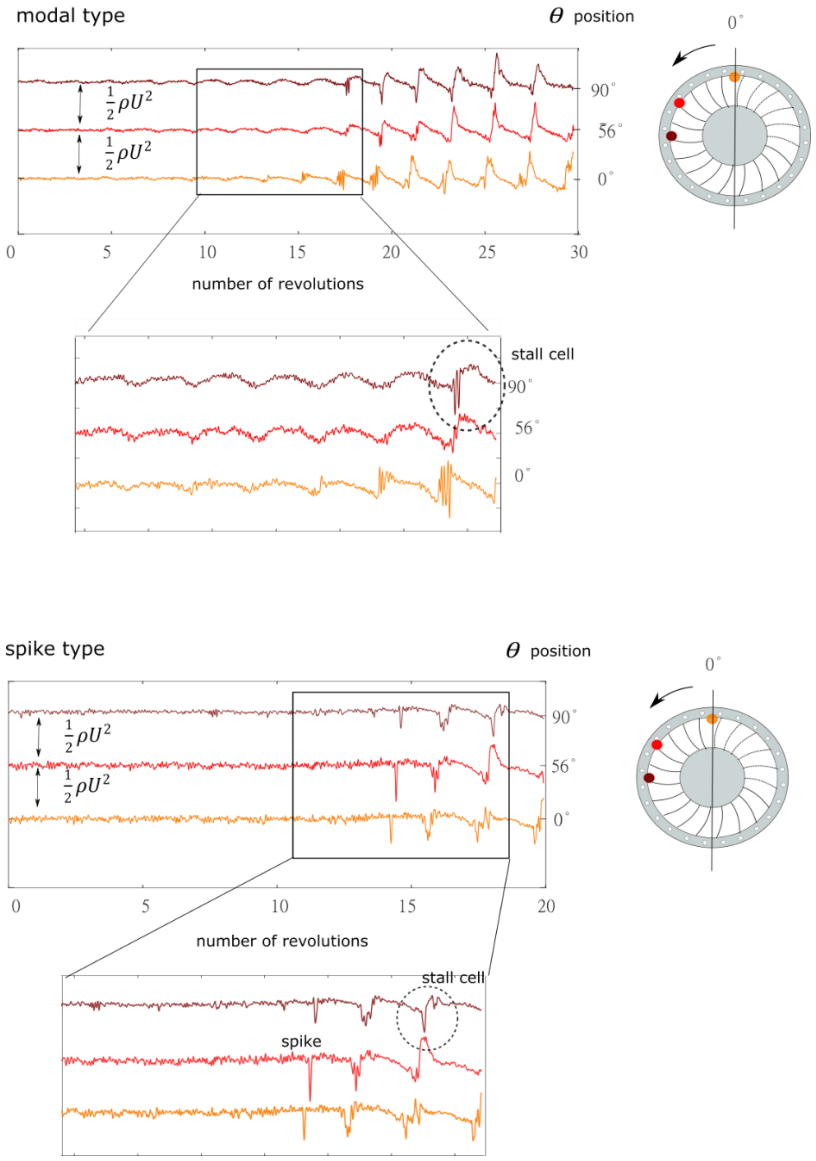

Figure 2-19 pressure signals acquired in the CME2 axial compressor, representing examples of modal and spike type of rotating stall

2.2.2 MATHEMATICAL MODELS AND EXPERIMENTAL INVESTIGATIONS

A lot of attempts to model the first type of stall have been made from the 50s (Iura and Rannie, 1953), (Sears, 1955), (Stenning and Hugh, 1955), (Stenning et al., 1959). All the models were based on small perturbation theory, and were developed in parallel and in the same framework as the first distorted flow models referred in section 2.1. The use of a small perturbation is appealing since the modes are observed to grow progressively from small oscillations of length scale bigger than the blade channel and the annulus height; this suggested that a simplified 2D modelling of the compressor as an actuator disk could capture the basic physics, without the need of modelling the complex flow in the blade passage. These first models culminated in the well-known Moore-Greitzer model, (Moore, 1984) which provides a theoretical framework for the arise of the modal perturbations at the peak of the compressor characteristic. The second type of stall, on the other hand, has been seen much more difficult to model, since it is strongly dependent on the local three dimensional flow in the blade channel. Moreover, its appearance is sudden, with a finite amplitude, and small perturbation theory is not adapted to deal with it. Based on their experiments where spike type inception was occurring always at the same incidence, Camp and Day (1998) proposed a critical incidence criterion for the appearance of the spike: when the critical incidence is reached before the peak of the compressor

characteristic, the compressor exhibits short wavelength disturbances, otherwise it will stall at the peak of the characteristics (figure 2-20).

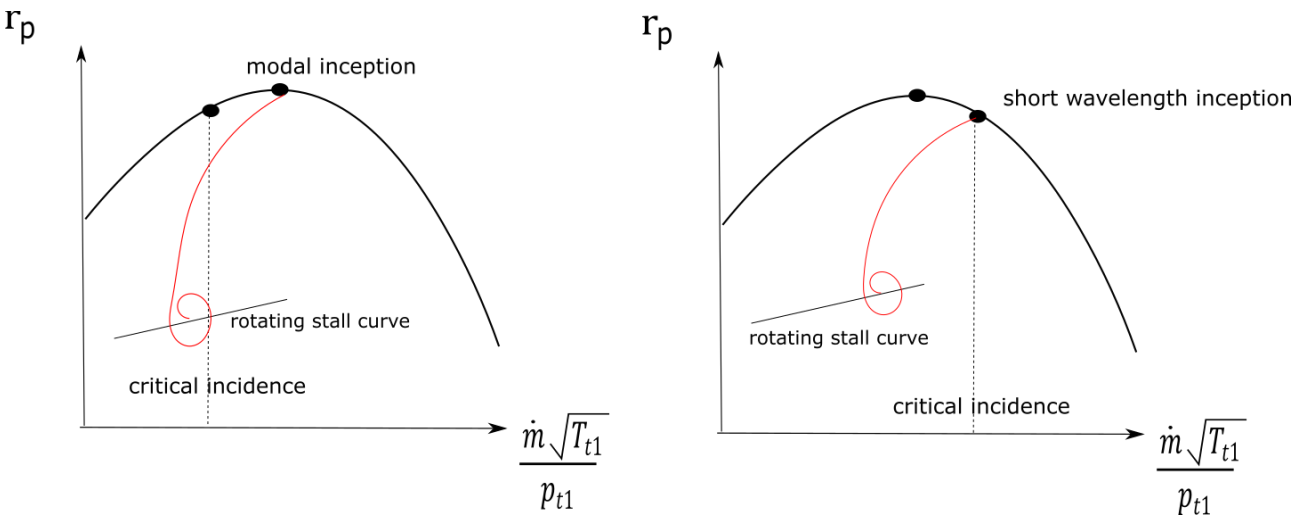

Figure 2-20 : critical incidence criterion for spike or modal type of inception

The more recent research has focused on spike instabilities, since they are the most encountered in modern jet engines (Day, 2015).

2.2.3 CFD AND RECENT DEVELOPEMENTS

Because of the difficulties in dealing analytically with spike type disturbances, during the 80s and 90s the research has especially focused on CFD methods to describe the flow structure in the blade passages (Gong, 1999), (Vo et al., 2008). Gong developed a CFD-bodyforce model of the compressor and claimed that 3D effects are necessary to describe spike inception, because in his reduced 2D body force model short wavelength instabilities cannot be sustained by the flow. Gong also reported the case of a compressor with different clearances. The same compressor with a tight clearance stalls at a ϕ =0.39 through short wavelength stall, while with a looser clearance it stalls at a ϕ = 0.42 via modal type stall. The role of tip clearance has in fact been investigated and proved to influence the stalling flow rate (Graf et al., 1998). More recently, some works have allowed a better understanding of the flow features linked to spike disturbance. A comprehensive review is given in Tan et al., (2010). The most recent works (Pullan et al., 2015), suggest the source of the spike to be flow separation near the blade leading edge on the suction surface, close to the tip. This separation creates a vortex (figure 2-21) that is able to propagate around the annulus.

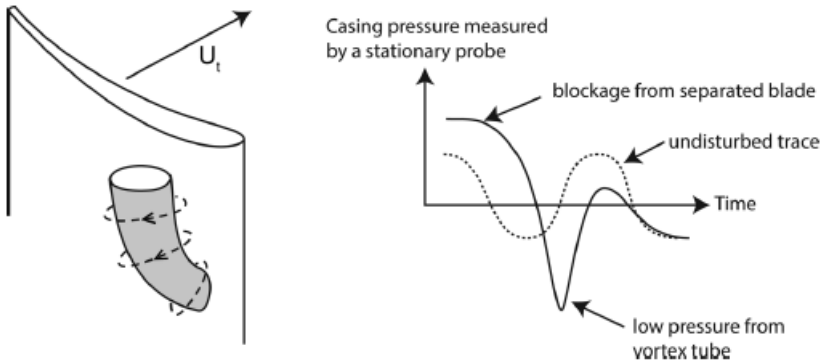

Fig. 5 The connection between spike structure and casing pressure trace

Figure 2-21 : spike instability interpretation (from Pullan et al. (2015))

In Hewkin-Smith et al. (2019) the understanding has been improved further by recognizing tip leakage and casing corner separation as two mechanisms influencing the onset of spike disturbances. However, despite the improved knowledge about the mechanisms leading to spike, no general criterion (if it exists) is known yet to predict the stalling behaviour of a compressor.
The operation of a compressor under inlet flow distortion introduces further aspects in the mechanisms leading to rotating stall. As Perovic et al. (2015) suggest, these aspects are still not much known and need more investigation. In their paper they measured unsteady casing static pressure in a BLI fan, and correlated the growth of the energy in the pressure signals in various position of the annulus to the incidence on the blades, founding a correlation. In higher incidence regions, the energy in the signals increases, indicating growth of the perturbation. Lower incidence regions, on the other hand are responsible for making the perturbations to decay. Spike perturbations are observed to grow and decay some revolutions before the onset of the instability, suggesting that the instability is triggered when the perturbations are sufficiently strong to propagate through the full annulus, without being damped by the stabilizing low incidence region.

2.3 DISTORTION GENERATORS

There exist many different ways to generate flow distortions in experimental test rigs. A first method, the most common one (Reid, 1969), (Gunn et al., 2013), is to introduce grids in the flow to generate a total pressure drop. The grids can be tailored to very different distortion patterns (Guimarães et al., 2018) and have the advantage to be a simple system to implement, and they produce highly repeatable distortion patterns. Moreover, they are passive devices without moving parts, and the risk of malfunctioning is reduced. On the other hand, grids can produce a single pattern, thus the manufacturing costs can increase in case of experimental campaigns where a broad range of distortion patterns must be studied. Moreover, in many cases, in between a test and the other, the installation must be disassembled to change the grid, thus time consuming and expensive. The grids also can produce just steady distortions, and are unable to reproduce patterns generated by turbulence or particular unsteady flight conditions. Especially to avoid the limitations regarding the steadiness of the grid produced patterns and the need to shut down engines to change grids, scientists and engineers have developed different strategies (Beale et al., 2002). One of these is the Air Jet Distortion Generators (AJDG). These air jets are mounted forward facing the flow in different radial and azimuthal positions and can inject pressurized air to create local pressure drops induced by the momentum exchange with the main flow. One application is described in Overall and Harper (1977). These systems are more flexible, since different distortions can be created without the need to manufacture single grids and can be tested easily without disassembling the rig to install the grids. On the other hand, the system is more complex and the initial investment is higher.
In our test facility, to reproduce the distortion we opted for the grid method, since it is simpler to implement and less expensive as an investment. The time needed to disassemble the rig to change grids was not a constraint, and so the limitation of dealing just with steady distortion patterns.
Since the method based on grids has been chosen, in the following the methods to design such distortion grids are presented.

2.3.1 DISTORTION GRIDS

Existent literature about grids deals mostly with grids designed to create turbulence in wind tunnels (Laws and Livesey, 1978). These are basically uniform grids so that no knowledge can be directly transferred to the design of non-uniform grids to simulate a distortion. Some studies exist that deal with non-uniform grids, with the aim to increase downstream turbulence levels with interesting applications in wind tunnels.

Some methods exist for designing decoupled pressure drop and turbulence profiles (Zheng et al., 2018). However, these grids have high porosities (>50%) to avoid recirculation, which introduces unwanted effects. The pressure drops are reduced and are not of primary concern, because the main purpose is to generate high level of turbulence. The ideal application is enhanced mixing in chemical reactions, especially in combustion. If in a wind tunnel high pressure drops represent an drawback because of higher fan power requirement, for distortion grids the pressure drop is of primary concern because it represents the amount of distortion. Up to today, a lack of investigation on distortion grids appears in the literature.

Some models of wire mesh gauzes pressure loss were first reported in Pinker and Herbert (1967). In their paper they mentioned different methods: a first method proposed by Wieghardt (1953) treated the gauze as analogous to a number of isolated cylinders placed across the flow and the loss coefficient has the form:

$$K = s/(1-s)^2 \tag{2.12}$$

The second method proposed by Pinker and Herbert (1967) themselves consists in considering the grid equivalent to an isentropic contraction followed by a sudden enlargement in which total pressure falls and static pressure rises. The expression of the loss coefficient is:

$$K = s^2/(1-s)^2 \tag{2.13}$$

s is the solidity of the grid, the inverse of ξ, the porosity.
These expressions have been tested experimentally for porosities between 0.3 and 0.7. The two models, as pointed out by Pinker have the same qualitative trend but discrepancies in the quantitative predictions. As pointed out in McCarthy (1964), performed experiments seem to suggest the use of a form similar to the one proposed by Wieghardt (1953):

$$K = cs/(1-s)^2 \tag{2.14}$$

in which the coefficient c is seen to be almost a constant of the order of 0.75 to 0.9 in turbulent regime. In (Elder, 1959), a reference to the Reynolds dependence is given in the form:

$$K = \alpha \frac{s}{Re} + K_0 \tag{2.15}$$

The K_0 term dominates for turbulent regimes and is approximately a constant. This was proved to be true for different configurations such as square mesh grids or flow normal to a bank of cylindrical tubes.
Aside from empirical correlations, some analytical treatment based on small-perturbation theory was developed by Elder (1958). In his model, the experimentally obtained expressions for the loss coefficient were supposed to hold locally for non-uniform grids. He developed a perturbation solution for the flow through a single arbitrarily shaped, non-uniform gauze; McCarthy extended the model removing some restrictive assumptions and demonstrated as particular solutions of its model the case of Elder. The model allows to link the local geometry of the grid (in terms of the solidity s) to the downstream velocity profile and pressure drop. The model was directly used by Bruce (1974) to design some distortion grids to obtain a sinusoidal downstream profile of velocity to test in distortion studies. The model of McCarthy, however, has some limitations, since it is based on simplifying assumptions:

- streamline curvature must be small, so that the model holds for grids which do not show downstream recirculation, thus for high porosity (>0.4) and generally small loss coefficients; low losses are of interest for wind tunnel applications but not necessarily for distortion.

- The model does not consider the interaction of turbulence and mean flow and the transfer of energy from the mean flow to turbulence.
- Parameters such as thickness of the grid and holes pattern are not included in the model.
- The model considers a grid spanning the full cross section

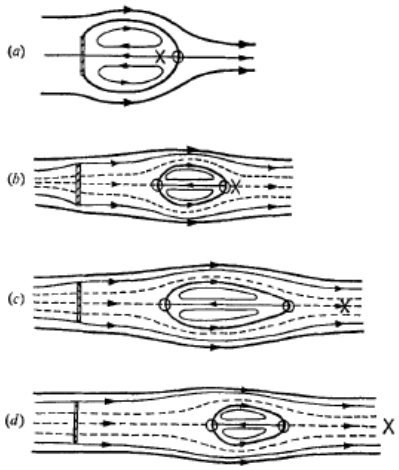

FIGURE 9. The effect of β on the near wake. ×, points of maximum turbulent intensity; – – – –, bleed air; ○, stagnation points. (a) $\beta = 0$. (b) $\beta = 0{\cdot}182$. (c) $\beta = 0{\cdot}252$. (d) $\beta = 0{\cdot}305$.

Figure 2-22 : types of flow behind a porous grid (source : Castro, 1971).

A different approach was proposed by Taylor (1963) and consists in representing the grid as a source density distribution. It was first applied to a grid in a wind tunnel free stream. The idea was further developed by Koo and James (1973) which developed a model for a uniform grid in a duct partially covering its cross sectional area. They calculated the drag coefficient and computed downstream velocities behind and outside the grid. In all cases, the models haven't been tested for low porosities below 0.3.

A lack of investigations on low porosities was partially filled by some very interesting experiments by Castro (1970) on a broad range of porosities. Castro identified mainly two regimes for the flow behind a grid, depending on its porosity: a first regime for low porosities (< 0.2/0.3) is characterized by a vortex street behind the grid (figure 2-22) and a second regime for higher porosities (>0.3) is characterised by the absence of the vortex street very likely prevented by the effect of bleed air. This vortex street is caused by the interaction between the mixing layers on the sides of the grid.

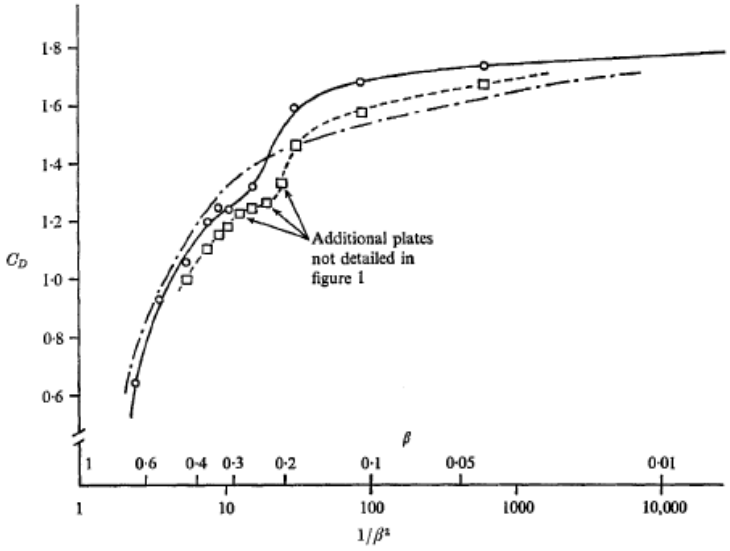

Figure 2-23 : Drag coefficient of a porous grid (source: Castro (1971)).

The limiting case is the 0 porosity, for which the wake approaches the wake of a solid body. For higher porosities, the flow exiting from the holes delays and reduces the formation of vortices and between porosities 0.2 and 0.3 there is a transition and the disappearance of the vortices. Associated to this transition a plateau exists in the drag coefficient (figure 2-23).

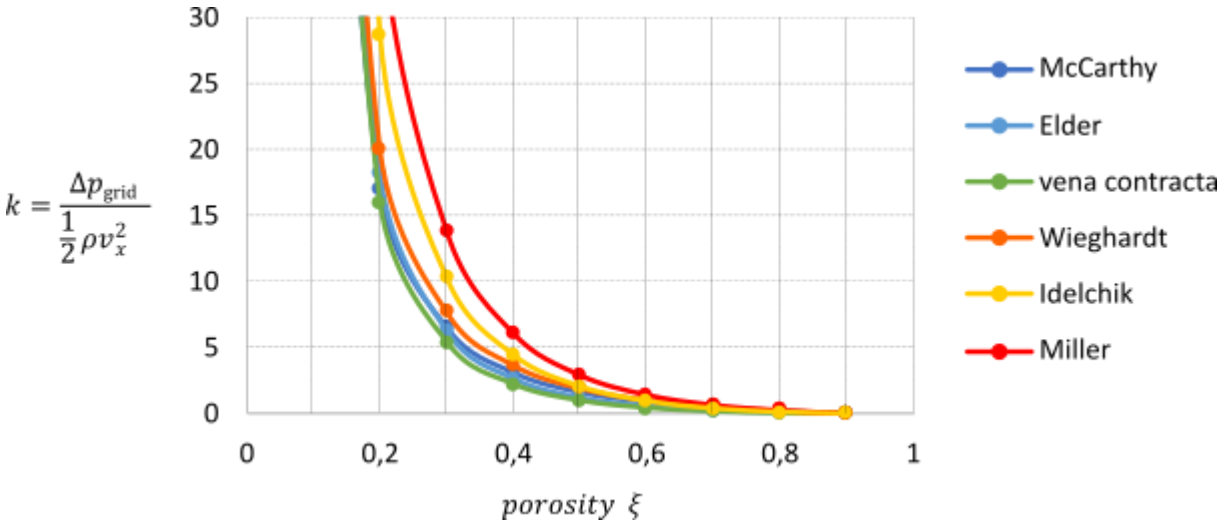

Figure 2-24: loss coefficient as a function of porosity for different correlations

Other more recent correlations specific to perforated plates are reported in Miller (1990), Idelchik (1986) and Malavasi et al. (2012). , These correlations are also plotted in figure 2-24. The more recent correlations take into account the thickness to hole diameter as an important ratio that determines the pressure loss. As it is shown in Malavasi (2012), a higher thickness to hole diameter decreases the pressure drop. In the same study it was shown that holes disposition has a negligible effect on the pressure loss. Among all the geometrical parameters, according to all the literature, the most influential is the porosity of the grid.

Recently, a model has been proposed by Schneck et al. (2013). The model consists in dividing the flow reaching the grid in many flow tubes, and solving mass and energy conservation for every tube imposing meanwhile that the sum of the upstream flow areas is equal to the duct cross section surface.

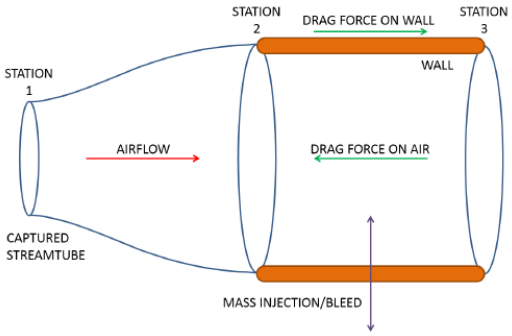

Figure 2-25: control volume of a cell of the grid (Schneck (2013))

For each cell, a control volume like the one in figure 2-25 is chosen, such that the effect of the grid wires and walls is taken into account by a drag force; for this control volume, the balance equations in figure 2-26 are formulated and solved. The output is the total pressure for each cell downstream of the grid, given the free stream velocity and total pressure at the inlet, the free area of each cell (specified as input) and given the drag coefficient of each cell (calculated for each cell using a pressure drop correlation existent in literature). A pressure drop for the grid can be specified as in equation 2.16.

$$k = \frac{\Delta p_{cell}}{\frac{1}{2}\rho v_x^2} \tag{2.16}$$

- Conservation of mass from station (1) to (2)

$$\rho A_{c_i} u_1 = \rho A_{p_i} u_{2_i} \tag{1}$$

- Conservation of momentum from station (1) to (2)

$$P_1 + \frac{\rho}{2} u_1^2 = P_{2_i} + \frac{\rho}{2} u_{2_i}^2 \tag{2}$$

- Conservation of mass from station (2) to (3)

$$\rho A_{p_i} u_{2_i} = \rho A_{p_i} u_{3_i} \tag{3}$$

- Conservation of momentum from station (2) to (3)

$$(P_{2_i} - P_3) A_{p_i} = \alpha_i C_{D_i} \frac{\rho}{2} u_{2_i}^2 A_{p_i} + \rho A_{p_i} u_{2_i} (u_{3_i} - u_{2_i}) \tag{4}$$

- Geometric constraint (the sum of the capture areas must equal the total flowpath area)

$$A_T = \sum_i A_{c_i} \tag{5}$$

- Definition of P_{03_i}

$$P_{03_i} = P_3 + \frac{\rho}{2} u_{3_i}^2 \tag{6}$$

The equations listed below can be algebraically combined to form the final, closed form solution given as

$$\frac{P_{03_i}}{P_0} = 1 - \frac{\rho u_1^2}{2P_0} \underbrace{\left(\frac{A_T}{\sum_j \frac{A_{p_j}}{\sqrt{1+\alpha_j C_{D_j}}}} \right)^2}_{\text{Area-weighted drag scaling factor}} \underbrace{\left(\frac{\alpha_i C_{D_i}}{1+\alpha_i C_{D_i}} \right)}_{\text{Local drag scaling factor}} \tag{7}$$

Figure 2-26: equations of Schneck's model (Schneck (2013))

Some methods of design have been recently developed also to create swirl distortion generators, in particular the Stream Vane Method (Hoopes and O'Brien, 2015) and have been proved interesting in the investigation of the effects of swirl distortion (Bucalo et al., 2013.). This method is not described in detail here because swirl distortion is not part of the investigation of this study.

2.4 CONCLUSIONS

Considering the existing literature, some points concerning inlet flow distortion in axial compressors appear to deserve more investigation.

First, the correlations that link the stall margin to the distortion indexes are empirical and have little connection with the physics of the flow, which still remains not well understood. The distortion indexes themselves have a very limited amount of physics in their definitions, and their use is justified by the fact that with some specific distortions and compressor designs there is empirical evidence that they work. Nevertheless, the development of more reliable indexes that can also be generalized to more types of distortions and compressor designs has to go through a better understanding of the flow physics.

Concerning this point, in this study, we have classified the various experimental distortions in four regimes based on the flow physics and we propose a new scaling of the stall margin based on a distortion index which is defined on a physical ground. This physical grounding allows also to identify the limitations of this scaling to the flow regimes that have been classified in the study and that will be described in the following chapters. As anticipated in the introduction this will be the core of chapter 4, the first one discussing the results of the study.

A second aspect that deserves more investigation is the actual mechanisms of the onset of rotating stall and the effect of the distortion on them. Rotating stall is a major factor limiting the performance of the compressor. Many works have described precisely the flow physics associated to the arising of this phenomenon in undistorted conditions. It is also clearly reported that the distortion influences the stability, and much of the studies report the loss of stall margin with various types of distortions, but not many try to associate the stall mechanisms (spike, modal, or other eventually) to the loss of stall margin in the different distorted conditions. In this work, thus, we have also classified the type of stall mechanism in four stall regimes and we show that there is coherence between the four flow regimes and four stall regimes, suggesting that there is a strong connection between the type of flow distribution upstream of the compressor and the stall mechanism. This will be the core of chapter 5, as anticipated in the introduction.

Before discussing these topics, in the following chapter 3, the experimental means and the measurement methods are introduced in detail.

3 EXPERIMENTAL MEANS

In this chapter the experimental means that have been used and developed to investigate inlet distortion in an axial compressor stage are described. First, the design of the distortion grids is discussed; then, the test bench CME2 is described, with a focus on the instrumentation and measurement techniques that have been used, mainly pressure measurements and Particle Image Velocimetry (PIV).

3.1 THE COMPRESSOR CME2

In this paragraph, the test bench, the instrumentation and the type of experiments that have been performed are described in detail. It was decided to use pressure measurements to characterise the performance of the compressor (characteristic curves) and to measure the unsteady onset of rotating stall. Particle Image Velocimetry was used to describe the flow in the blade channels in different positions of the distorted region. The use of PIV has revealed fundamental to complement the pressure measurements. The advantage of unsteady pressure sensors is that they provide easily temporally resolved data. Temporal resolution is necessary to capture unsteady or transient flow features such as spike and modes that are determinant to the stall onset. On the other hand, pressure measurements represent very localised in space information, and moreover, extracting information on other flow features as separated flow on blades is challenging. PIV on the other hand allows for spatial resolution and allows to identify other flow features as flow redistribution in the blade channels behind the grid, which are precluded using just pressure measurements.

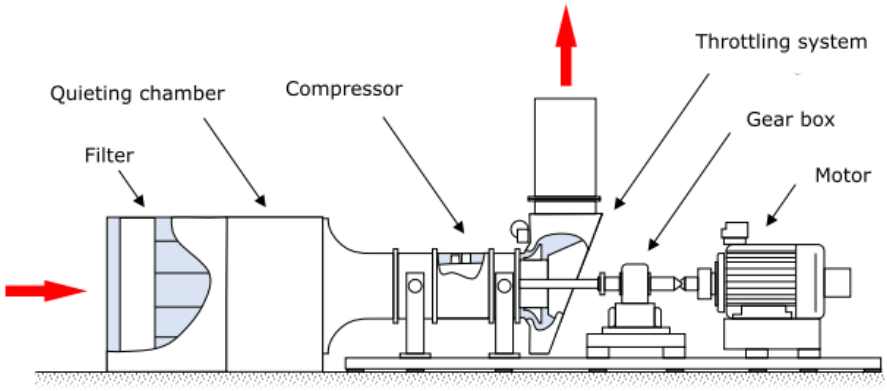

Figure 3-1: general scheme of CME2 (source Margalida, (2019))

The experiments have been performed on the test bench CME2, a low speed single stage axial flow compressor. In figure 3-1 the general scheme of the test bench is shown. The compressor is fed by an electric motor rated 200 kW nominal power. A gearbox with a ratio 2.345 completes the power transmission. It is located between the electric motor and the compressor (figure 3-1). The air circuit is open: air passes through a filter and a relaxation chamber, then through a circular converging section, which purpose is to homogenize the flow before entering the compressor. To regulate the mass flow rate, the test bench is equipped with a throttling valve system that allows to reduce the cross section of the exit volute. Downstream, air is ejected to the lab hall through a vertical duct.

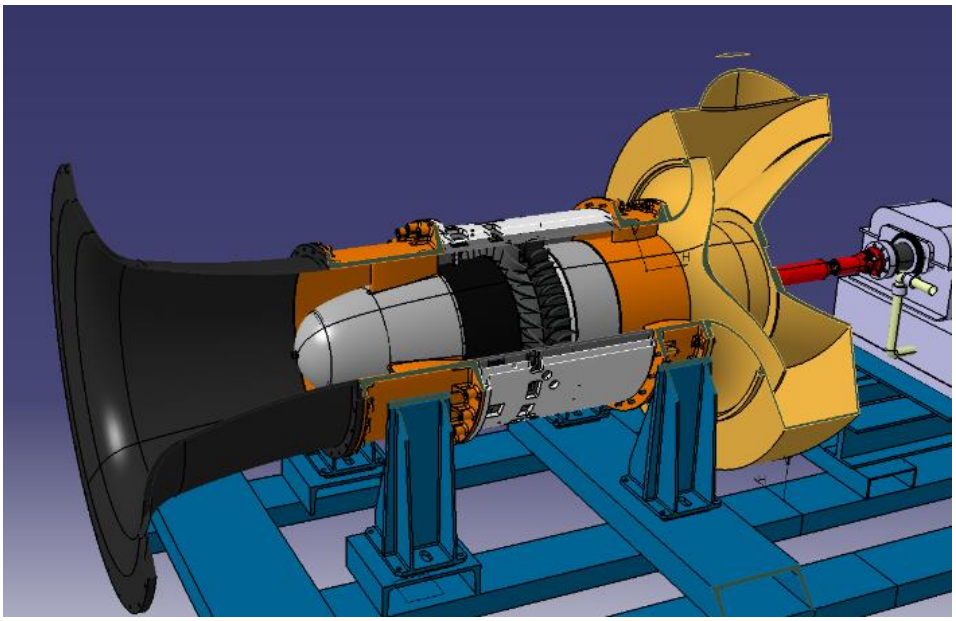

Figure 3-2: CAD images of CME2

Figure 3-2 presents a CAD picture of the machine. The compressor stage is composed of:

- Two bearings (orange in figure 3-2)
- A rotor with 30 blades and a stator of 40 blades .

This stage is enclosed into 2 casings:

- an outer carter, thicker, allows to link mechanically the stage to the bearings
- the inner carter, thinner, holds the stator. Its internal diameter is 550 mm and the hub to carter ratio varies between 0.75 at the leading edge to 0.78 at the trailing edge of the rotor. The clearance is 0.5 mm (0.6% of the rotor chord).

The set of geometrical characteristics of the compressor is shown in table 3-1.

Rotor blades	30	
Stator blades	40	
Rotor chord	84	mm
Stator chord	77	mm
Rotor stagger angle	54	°
Casing diameter	550	mm
Hub to tip ratio at rotor inlet	0.75	
Hub to tip ratio at rotor outlet	0.78	

Table 3-1 geometrical characteristics of CME2

The geometrical characteristics of the blades of the rotor and the stator are summarized in the table 3-2.

Rotor				
Height	Chord [mm]	Thickness [mm]	Stagger angle [°]	Camber angle [°]
hub	84	7.9	33.5	41.5
Mid height	84	5.6	46	23
Tip	84	2.8	54	20

Stator				
Height	Chord [mm]	Thickness [mm]	Stagger angle [°]	Camber angle [°]
hub	77	6.2	17.5	46.4

Mid height	77	6.2	15	41.5
Tip	77	6.2	12.5	36

Table 3-2 Geometrical characteristics of the blades

The throttling system (figure 3-3) is based on a worm gear mechanism: a conical element is displaced axially in the volute thanks to a system of gears and worm screws controlled by an electric motor. The system is used during the experiments to regulate the mass flow rates from high values to the stall point, in order to allow to trace the characteristic curve of the machine.

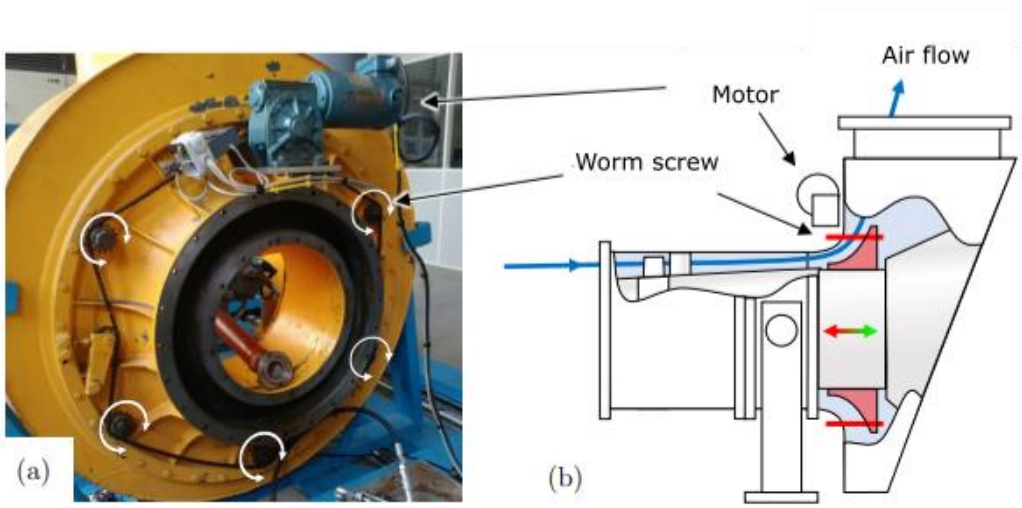

Figure 3-3 : worm gear mechanism to throttle the flow and regulate the mass flow rate (source: Margalida,2019).

At nominal operation, with pressure and temperature reference values of 101325 Pa and 15°C respectively, the compressor rotates at 6330 rpm and develops a compression pressure ratio of 1.15 for a mass flow rate of 10.5 kg/s, that corresponds to an axial speed of around 82 m/s. Table 3-3 collects these characteristics at nominal operation.

Rotational speed	6330	rpm
Mass flow rate	10.5	Kg/s
Total to total pressure ratio	1.15	
Axial velocity at tip	82	m/s
Relative velocity at tip	181	m/s
Reynolds number at tip	$1.06\ 10^6$	
Mach number at tip	0.56	

Table 3-3 flow characteristics of CME2 at nominal point

3.2 GRID SIZING

In this study, the distortion has been produced using distortion grids of different porosities (0.1, 0.23, 0.33, 0.5). The porosity is defined as the fraction of the free area over the full area of the grid. A porosity of 0.1 means thus that the free area of the grid is 10% of the grid area. The grids have been cut to cover an angular sector of the annulus (15°,30°,60°,90°,120°,150°).
In figure 3-4, on the left, four sectors of 30° with the four different porosities are represented and on the right a 60° sector is shown as it has been installed in front of the compressor.

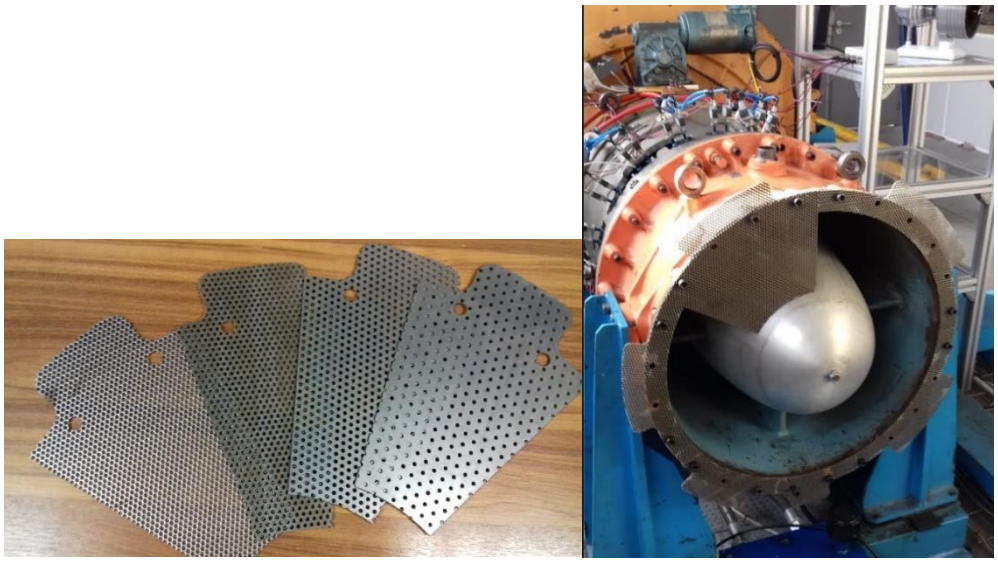

Figure 3-4 : photo of some 30° grids of different porosity used for the tests (left) and example of a 60° grid mounted in front of the axial flow compressor CME2

3.2.1 PRELIMINARY MODEL

The choice of the porosity is very important, since it controls the level of distortion and thus the effect on the compressor performance. In some literature dealing with distortion in high speed subsonic compressors (Burstadt et al.,1971), grids of high porosity are usually used. In fact, in experimental facilities operating at high subsonic Mach number, high porosity grids are sufficient to create an important effect on the performance of the compressor. The loss coefficient of a grid in a high speed flow is increased (Idelchik, 1986) with respect to the loss coefficient at low Mach numbers (figure 3-5). Thus at lower speeds, choosing high porosities grids can result in lower pressure drops and in a limited effect on the compressor performance. To determine an order of magnitude of the pressure loss of the grid before designing, a study of the correlations between grid geometrical parameters and flow quantities was thus performed, and a Matlab code was created for the design and performance prediction of the distortion grids.

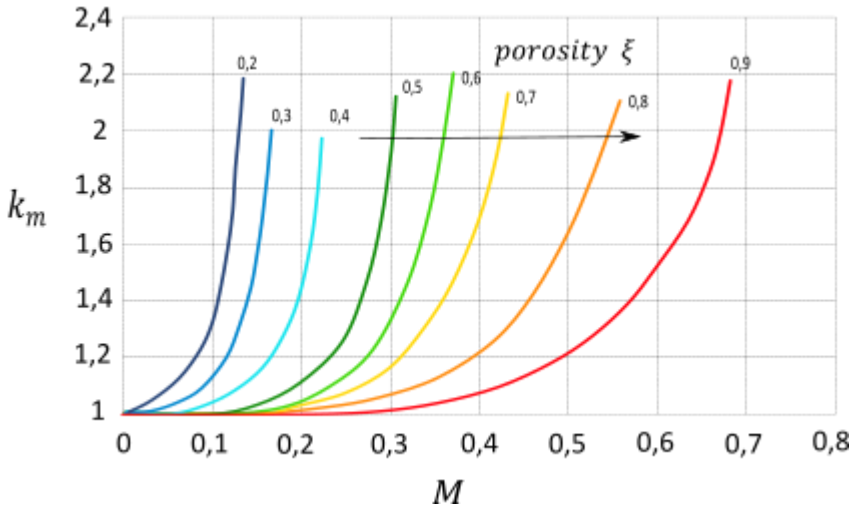

Figure 3-5: :Mach number correction (Idelchik, 1986) for the pressure loss of a perforated plate pressure loss coefficient

For the present study it was chosen to implement Schneck's model in Matlab using the Idelchik correlation. The model has been compared to the other models for non-uniform grids and seems to be the most comprehensive. What makes the model attractive is the fact that it can account for uniform , partial s or non-

uniform grids with more complicated geometries. Moreover, it can be used for design or prediction using direct or inverse calculations.
The model has the same limitations holding for McCarthy (chapter 2.3), like the fact that turbulence in the downstream field is not modelled, so that information about turbulence effects and their influence and interaction with the mean flow is precluded. Also, it is not well adapted for low porosity grids, since the correlations are not tested generally below a porosity of 0.3-0.4. But it has been used to estimate as an order of magnitude the pressure losses of different grids, in order to base their choice and design on a rational criterion. From the results which will be shown later on, it was clear that in the flow conditions (Re, Ma) of CME2, grids of high porosities (ξ >0.5) would have produced pressure losses of some percent of the dynamic pressure, and consequently the impact on the compressor would have been negligible. It was thus chosen to concentrate the design on weakly porous grids (ξ <0.5).

3.2.2 MANUFACTURING AND INSTALLATION

The grids have been cut from perforated steel plates of 2 mm thickness. In all the grids the round holes have a diameter of 3 mm, and consequently different inter-hole distance are used to create different porosities. The other parameter than can influence the total pressure drop sensibly is the ratio of the thickness to hole diameter (Malavasi, 2012). For the grids used in this study it has been kept constant in order to control the total pressure loss with the porosity. The hole distribution finally has negligible effect on the pressure drop (Malavasi, 2012).

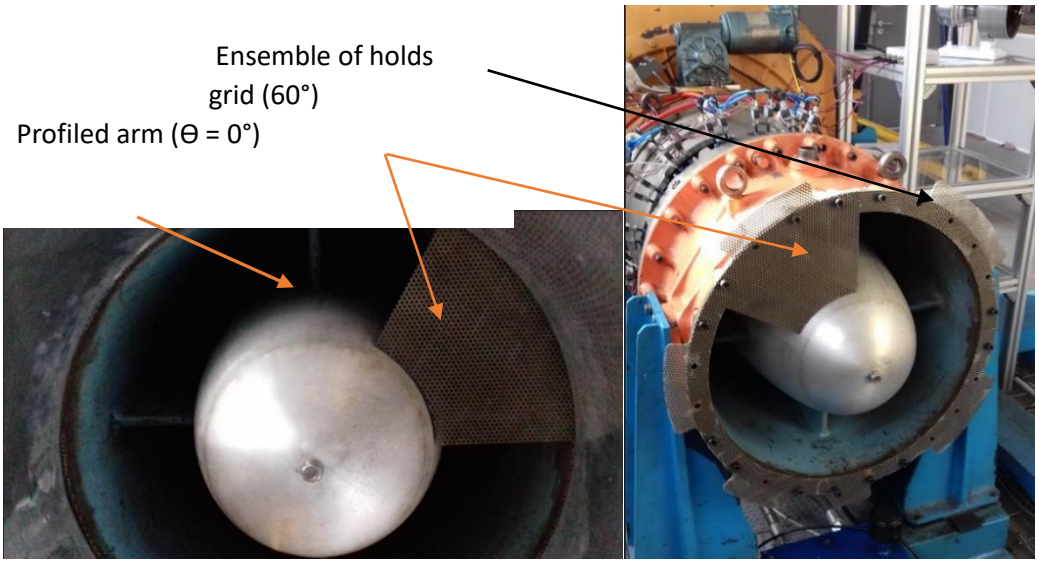

Figure 3-6: images of the installation of the grids

The grids have been mounted as in figure 3-6 at a distance of 550 mm upstream to the rotor. The distance separating the grid from the rotor is a very important parameter since it controls the flow coupling between the two elements. If the grid is too close, its effect on the flow is influenced by the compressor and it works in off design conditions. The more distant the grid, the less the coupling; however, if the grid is placed upstream of the hub of CME2 (visible in figures 3-2 and 3-4), the local annulus area is 2.3 times the area at the entrance of the rotor and thus the speed 2.3 times lower. The resultant pressure loss 5.3 times lower; thus the pressure measurements is more affected by the instrumentation uncertainty.

The distance between the grid and the compressor suggested in literature (Bobula et al., 1983), (Burstadt et al., 1971) to avoid fluid coupling between compressor and grid is one diameter in front of the compressor. In

CME2, this distance is 550 mm (cf. table 3-1). It turns out to be particularly convenient in CME2, since it coincides with position of the flange between the conduit and the bearing. This position was chosen. Figure 3-6 presents two pictures of the inlet cross section equipped with a 60° sector at two angular positions on one side and on the other of the upper vertical arm (position arbitrarily defined at Θ = 0°). On the figure on the left, the grid is fixed in another position.

3.2.3 COMPARISON WITH MODEL

The calculated pressure drops as a function of porosity are shown in figure 3-7 for different grids. The pressure drop is calculated as the difference between the uniform upstream total pressure and the minimum total pressure measured by pressure rakes between the grid and the rotor. The pressure drop is then scaled on the dynamic pressure based on the axial velocity at the inlet of the rotor. From these predictions, it was clear at the beginning of this project, that porosities higher than 0.5 and of the order of 0.7-0.9 would have given losses lower than 5% of $\frac{1}{2}\rho v^2$ with a consequent negligible impact on the compressor performance and thus it was chosen to use porosities lower than 0.5 to be sure to have important effects on the compressor performance. In the same plot, the actual pressure losses measured during the experiments are reported, using the instrumentation described in the following paragraph.

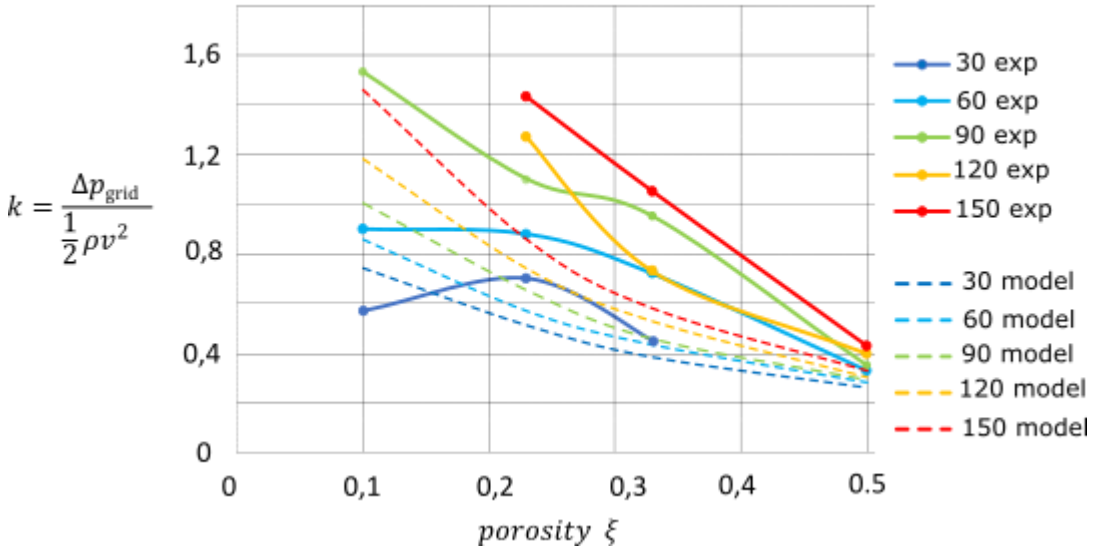

Figure 3-7: experimental pressure drop of the grids (continuous line) and numerical pressure drops calculated with Schneck's model.

The predictions of the model in figure 3-7 are good for $\xi = 0.5$, as expected, since the correlations are valid in the range of high porosities and the flow in these range (see Castro) approaches more the hypothesis of McCarthy's model. Since the correlations are not suited for the low porosity range, discrepancies are evident for lower ξ. In particular, a change is apparent between 0.23 and 0.33, where for grids of angular extension 30° and 60° the loss saturates. For 90° a phenomenon similar to the one encountered in Castro (figure 2-23 chapter 2) seems to appear between porosity 0.23 and 0.33. A possible cause is a transition from one regime characterized by the absence of recirculating vortexes and one influenced by a recirculation behind the grid. Another reason for discrepancies can also be the interaction with the compressor. Correlations are given for a flow perturbed just by the grid. The values in figure 3-7 however have been measured in the CME2 installations, where both compressor and the grids determine the flow behaviour.

The discrepancies, especially for lower porosities, suggest that very different flow conditions behind these grids must be present during operation, such as to represent a very broad range of inlet flow distortions to

be tested. It will be indeed seen in the experimental results, that very different conditions are present behind the grids.

3.3 PRESSURE MEASUREMENTS

For the study of distortion concerning the present work, the test bench has been modified to include new instrumentation and the distortion grids. In figure 3-8 are schematically represented the pressure measurements positions in CME2. In figure 3-9 are also represented the quantities used to measure the steady characteristic curves of the compressor. Test conditions are known from a manometer in the laboratory hall and a temperature probe (Pt100) at station 01 (figure 3-8) after the filters in the relaxation chamber. At the station 01 in the relaxation chamber, a Pitot tube is also installed, The static pressure is measured at the exit of the convergent at station 02. The difference of these two pressures Pconv is measured by a differential pressure sensor. Assuming an isentropic flow between the two stations 01 and 02, the sensor reads a dynamic pressure at station 02 and thus it is possible to use it to derive the mass flow rate (figure 3-9). Since the grids are creating a non-uniform upstream redistribution of the flow, it was decided to design and place eight static pressure taps at station 02 and send their mean value to the pressure sensor low port, in order to reduce the error of the measurement. It was also decided to introduce a 600 mm long conduit between the convergent and the bearing to increase the distance between the station 02 where Pconv is measured and the position of the grid; the conduit allows station 02 to be less influenced by the presence of the grid (figure 3-9).

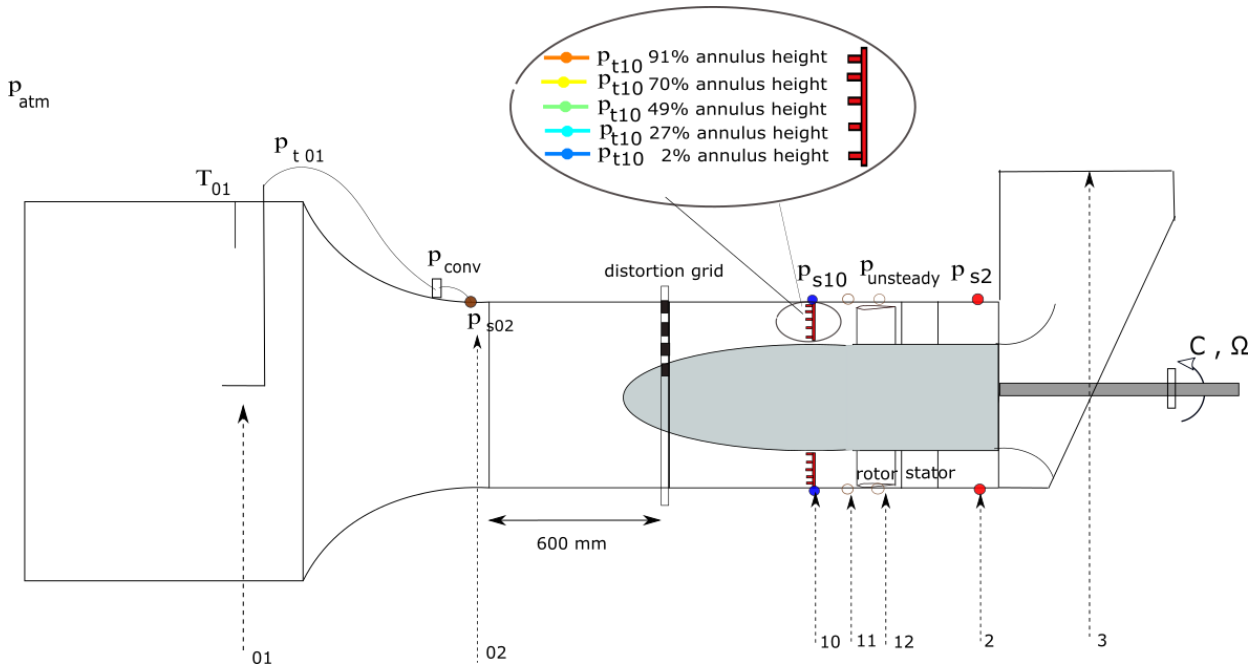

Figure 3-8 : references for pressure measurements in the CME2 compressor

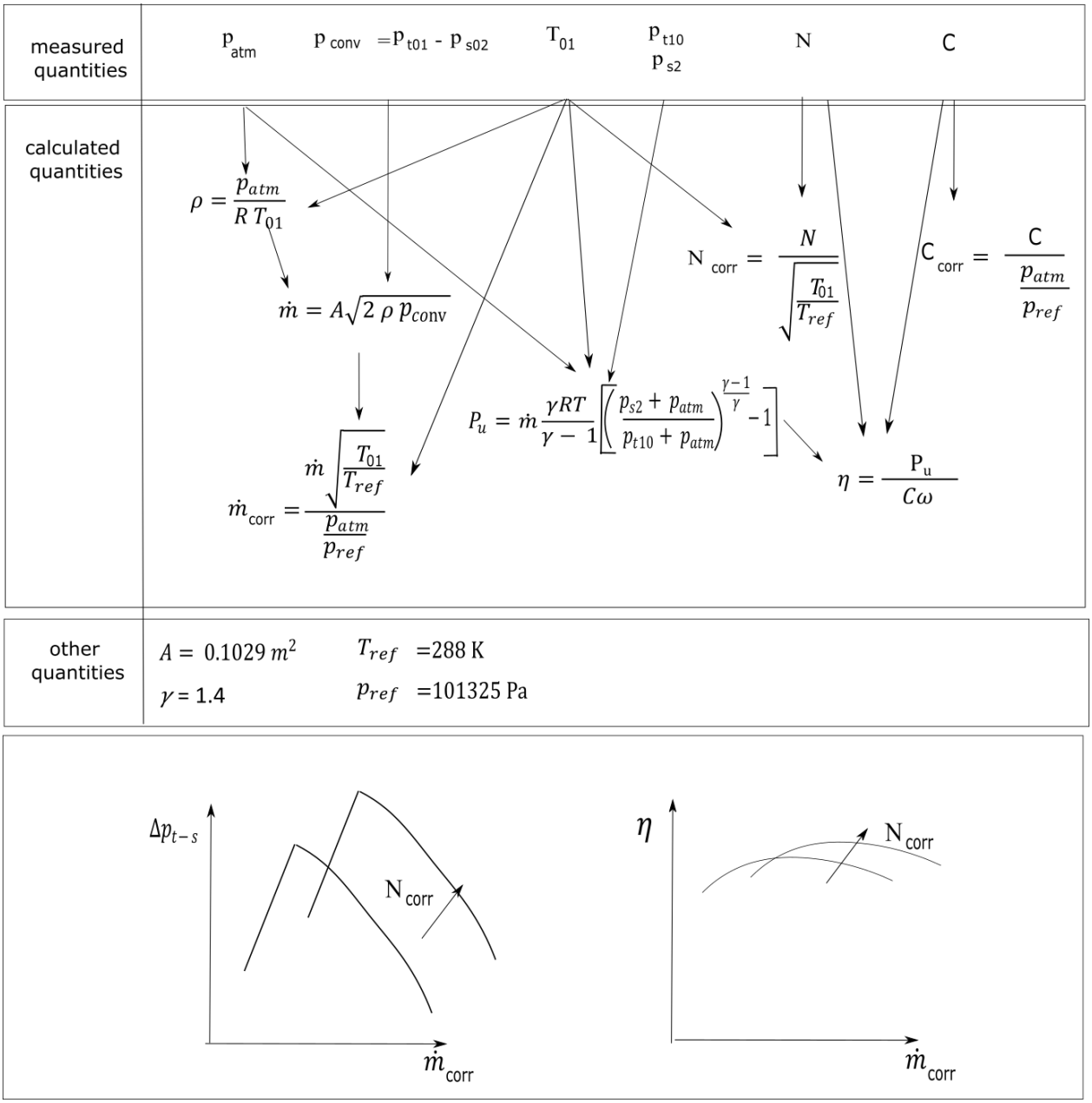

Figure 3-9 : top panel : measured and derived quantities; bottom panel: compressor performance curves

At the station 10, total pressure is measured using 8 total pressure rakes (figure 3-10). Each of these rakes has 5 Kiel probes on 5 radial positions and 2 static pressure taps (Ps10). Kiel probes were chosen because they offer a range of measurement up to 40° of incidence with respect to 2*7=14° for a Pitot tube. The radial distribution of the probes is not uniform as it is possible to see in figure 3-10, but it is such that each probe represents an annular sector equal to one fifth of the total annulus surface. This allows radial measurements to be directly comparable between them. The two static pressure taps allow to estimate the static pressure on the same axial plane defined by the Kiel probes. These measurements allow also to estimate the value of stream velocity if the hypothesis of a radially uniform static pressure is made. The realisation of the rakes was done by Vectoflow Gmbh. It's a steel 3D impression. On the top of the rake, 7 tubes are present to guide the pressure outside of the compressor to the pressure scanners. The 2 static pressures on each probes are averaged, and thus, with 8 rakes, a total of 6*8=48 tubes are to be connected to the scanners. 2 scanners DTC Series ESP-32HD were borrowed from ONERA Lille: a 32 channels scanner rated 15 psi (103500 Pa) and a 32 channels scanner rated 5 psi(34500 Pa). On the 5 psi scanner, the 4 higher radii of each probe were

connected (4*8=32). On the second scanner the total pressures of the probes at the hub (1*8=8) and the static pressures (1*8=8) were connected.

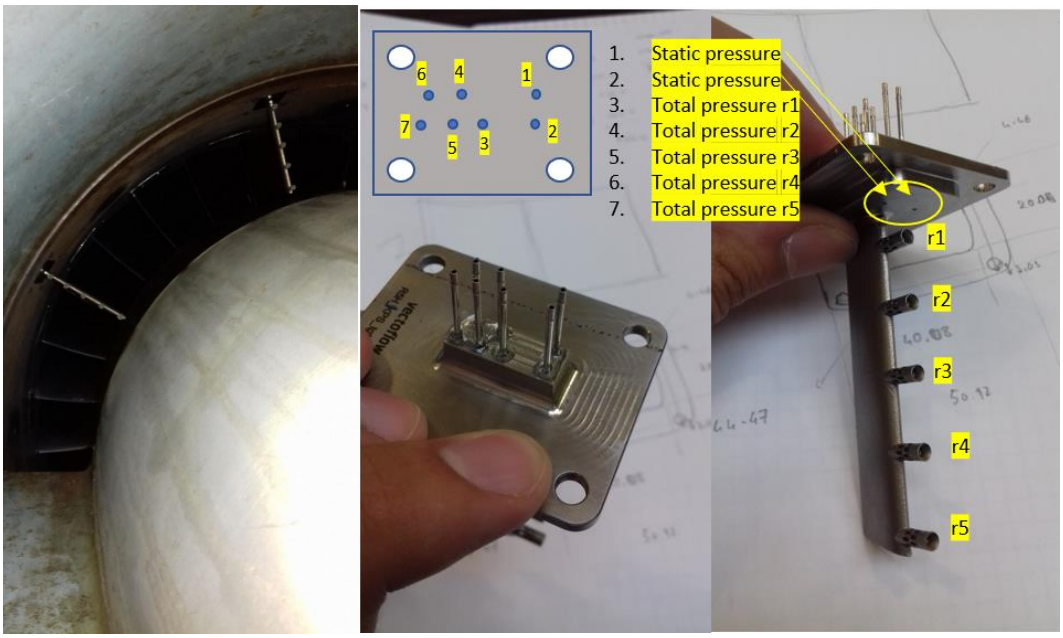

Figure 3-10 : total pressure rakes at station 10

At station 2 (figure 3-8), downstream of the stage, casing static pressure is measured at the same azimuthal positions of the rakes with eight static pressure sensors. The difference between Ps2 and Pt10 is the total to static pressure rise of the compressor, the main parameter to describe the compressor performance.
On the shaft is mounted an encoder to measure rotational speed. At the beginning of this thesis, a torquemeter was bought and installed too. The measure of torque and rotational speed allow the estimation of the real power absorbed by the compressor and the estimation of the efficiency (figure 3-9), the second main parameter for the description of the performance.

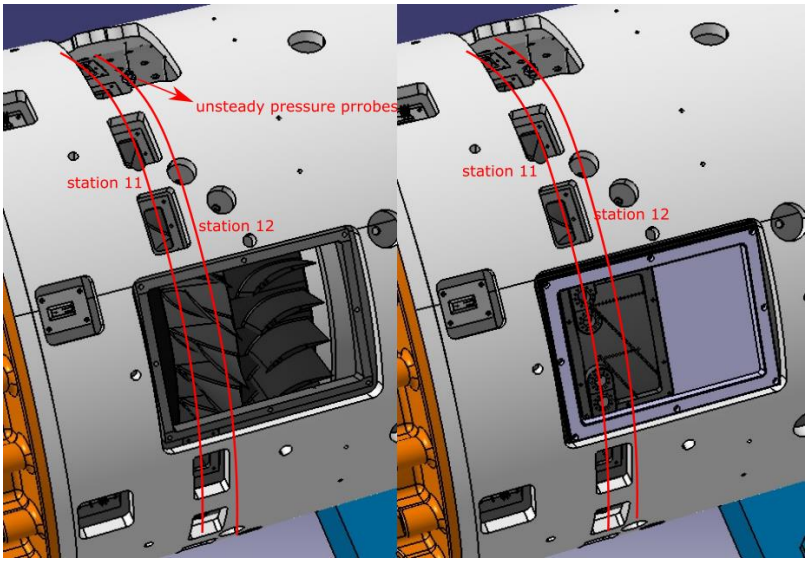

Figure 3-11: unsteady pressure probe stations 11 and 12 (figure 3-8) without instrumented window (left) and with instrumented window (right)

As far as unsteady measurements are concerned, in CME2, unsteady static pressure probes ENDEVCO can be mounted on two rings all around the carter at stations 11 and 12 (figure 3-8) and on a removable window (figure 3-11, right), offering a large choice of configurations for the measurements. In this study, two rows of

probes have been placed azimuthally at two different axial positions from the leading edge of the blades. These positions are represented graphically in figure 3-12.

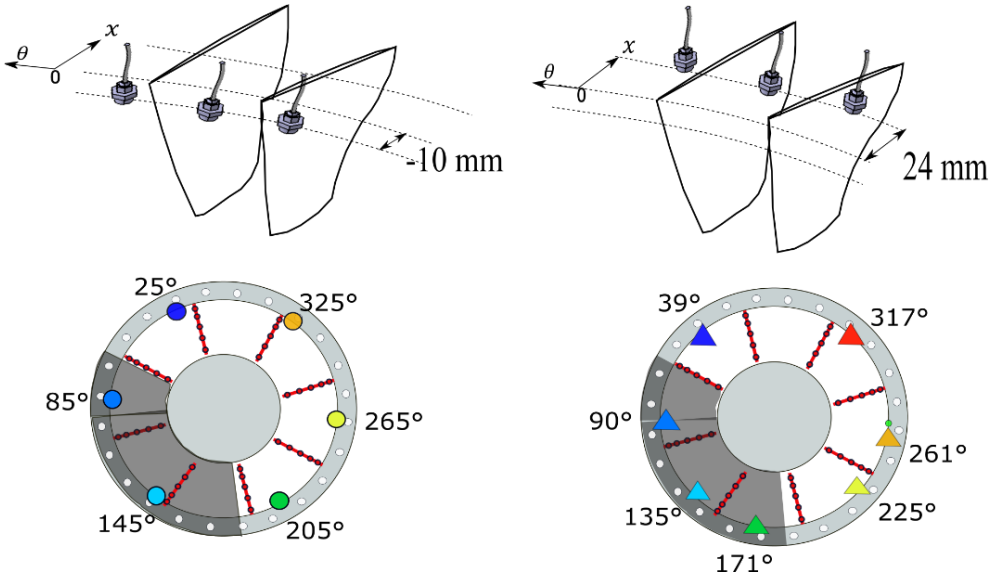

Figure 3-12 : azimuthal positions of the unsteady pressure probes. Left: station 11 in figures 3.8 and 3.11. Right: station 12 in figures 3.8 and 3.11.

These sensors have been used to acquire casing pressure during the transition to rotating stall, in order to capture the onset of the instability.
The full instrumentation and its incertitude are shown in table 3-4. More details about the uncertainty can be found in Vegliò (2015).

	Full scale (FS)	Max error
Total pressure scanners	5 psi	+/- 0.03 % FS
Downstream static pressure sensors	35 kPa	+/- 0.2 % FS
Unsteady pressure probes	6.89 kPa	+/- 0.5 % FS to +/- 1.5% FS
Mass flow rate	18.5 kg/s	+/- 0.5% FS*
Encoder	30000 rpm	+/- 0.3°

*Table 3-4 : instrumentation and its incertitude; * is an estimated value*

The compressor performance has been characterized using the steady and unsteady pressure measurements for the grids shown in table in figure 3-13a in green. Since the pressure rakes are 8, but the holes on the flange to mount grids are 24, the grids have been rotated two times to have a total of 24 pressure measurements (15° resolution as shown in figure 3-13b). In the same picture are shown the cases that have also been investigated with Particle Image Velocimetry (PIV)(figure 13-3c). A brief description of the setup for PIV experiments is given in the following. All the experiments have been performed for two mass flow rates: the nominal mass flow rate at 3200 rpm, namely 5.3 kg/s and the mass flow corresponding to the last stable point before the onset of rotating stall (around 4.2 kg/s in uniform flow and higher depending on the grid for distorted flow).

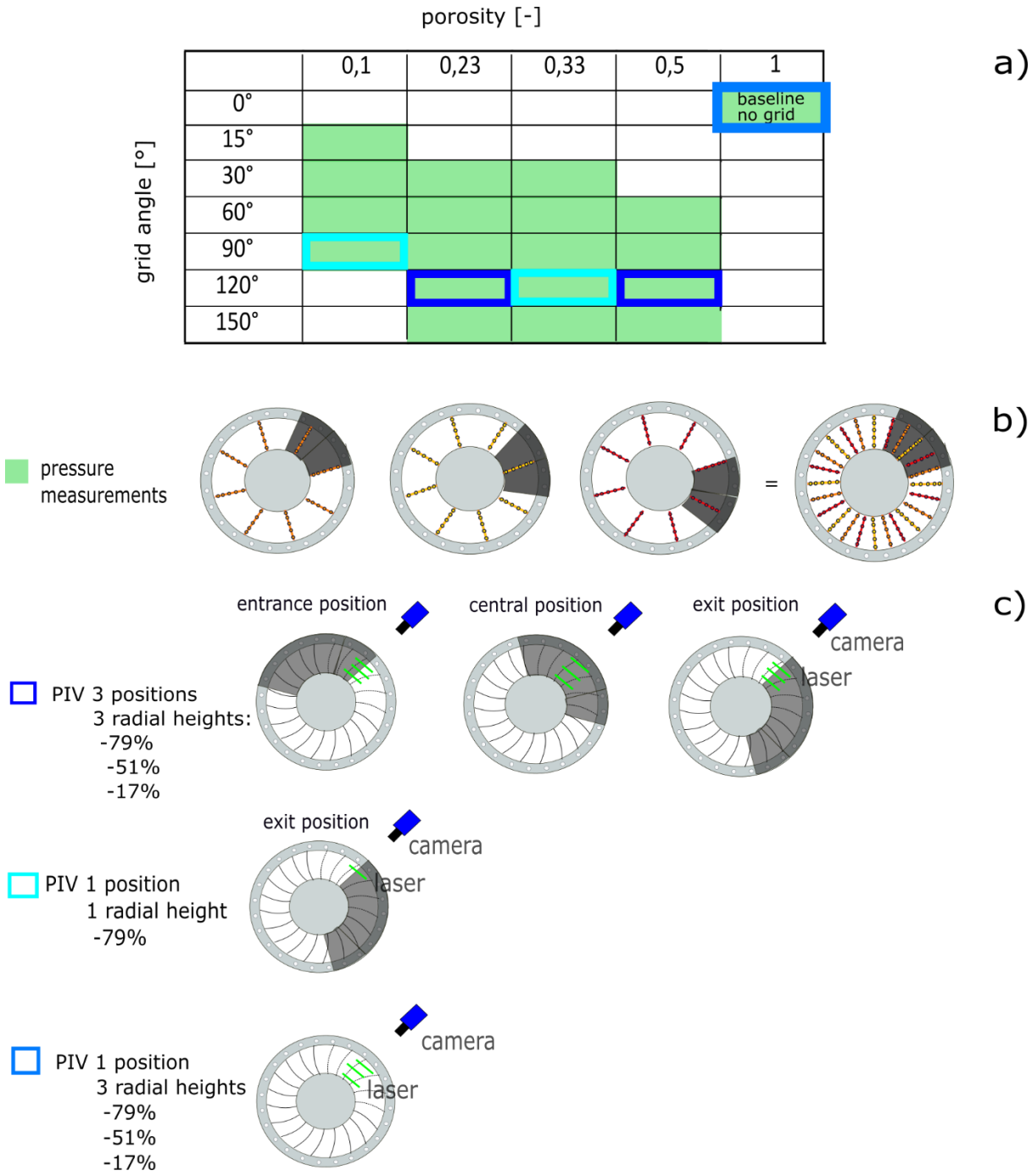

Figure 3-13 : scheme of all the experiments realised with and without grids, using pressure measurements and PIV

3.4 PIV MEASUREMENTS

The existence of the removable window (figure 3-11) has been particularly useful for Particle Image Velocimetry. This window on CME2 represents an optical access covering approximately 3 blade channels of the rotor and 4 blade channels of stator. This access has been chosen as the viewing window for PIV measurements. It was also chosen to use a blade to blade measurement plane, actually a plane tangent to a cylinder of fixed radius (figure 3-14) to have access to the main velocity components (axial and tangential). To bring the laser into the compressor, an endoscope was introduced into the casing through one of the holes created to install the pressure rakes (figure 3-14). The laser beam travels parallel to the axis of the endoscope and at its exit, a mirror turns the laser of 90° and a cylindrical lens generates the laser plane. By

varying the height of the endoscope in the annulus it is also possible to vary the height of the laser plane in the blade channel.

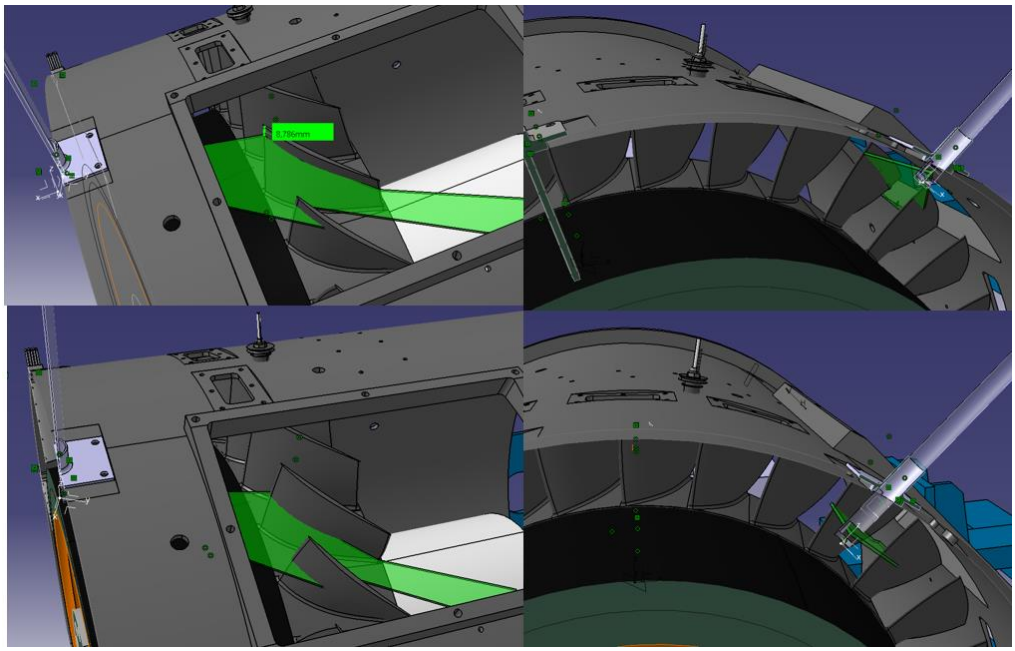

Figure 3-14: CAD representation of laser sheet view

The angular position at which the endoscope had to be introduced was chosen as a compromise in order to give a good field of view of the blade channel and at the same time to allow to translate the laser plane on most part of the blade height. In fact, different angular positions with respect to the window would not allow to view the regions closer to the tip gap, as a consequence of the casing curvature (figure 3-14).

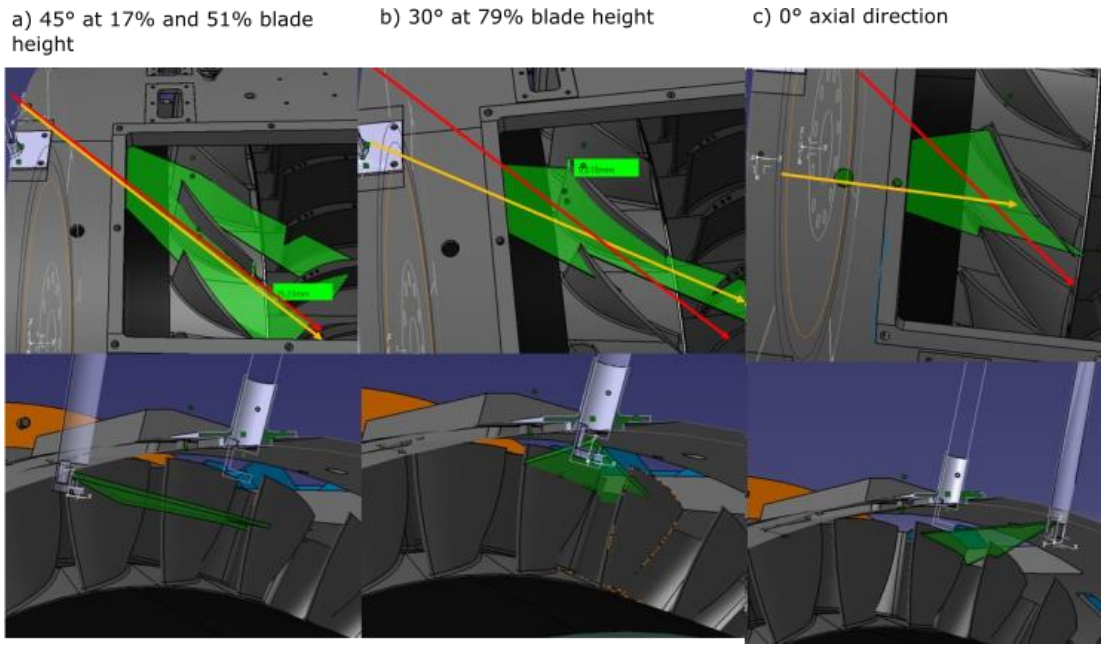

Figure 3-15: different angular positions of laser sheet. a): angle 45° (yellow line); b) angle 30° (yellow line); c) angle 0°(yellow line). In red line the stagger angle at mid chord

Three positions are represented in figure 3-15, respectively 45° (a), 30° (b) and 0° (c). The red line represents the direction of the blade chord at the mean radius, and the yellow line the direction of the laser. The laser plane illustrated in figure 3-15 on the left, enters into the channel at 45° (equal to the stagger angle at mean radius) and avoids much of the shadowing on the blade channel. In this case, the radial extent at disposal to

translate the laser plane varies between 0 and 65% of the blade height as a consequence of the cylindrical geometry (as it can be seen in figure 3-15 bottom left panel); this configuration does not allow to move the laser plane close to the blade tip, which is the most interesting part of the blade concerning the loss of stability of the compressor. The configuration with the purely axial laser (figure 3-15 right), on the other hand allows to move the laser plane up to the tip, but the view of the channel is limited because of the shadowing of the blades, especially at the trailing edge. This makes it difficult to estimate the velocity at the outlet of the rotor. The configuration with the laser plane at 30° (figure 3-15 centre) allows to translate the plane up to 79 % of the blade height, and, at the same time limits the shadowing on the channel and thus was finally chosen.

Three radial planes have been used as measurement planes: 17% , 51% and 79% of the blade height (figure 3-13), in order to see the effects of the distortion on a broader region of the blade height. To have PIV measurements in different regions behind the grids, these have been rotated in such a way that the laser plane was behind the edge of the grid (entrance or exit region in figure 3-13) or behind the centre of the grid (central region in figure 3-13). To place precisely the laser plane at the correct radial position, three base parts have been 3D printed with a geometry such as to adapt well to the hub and follow the blade channel (figure 3-16). On the top of these base parts, calibration targets were glued so that the height of the base parts plus the height of the targets is equal to the three heights used for measurements. The setting is done introducing the endoscope into the casing until the laser plane is at the level of the calibration plane. The images of the targets are then acquired and used for the PIV calibration.

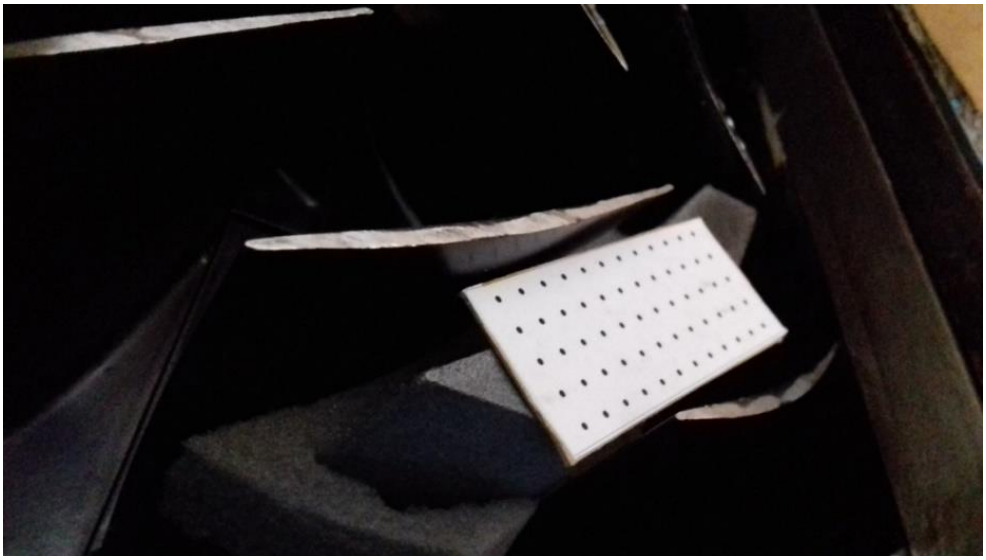

Figure 3-16 : calibration target glued on 3D printed base parts in between two rotor blades

Once the measurement planes were identified and the azimuthal position of the endoscope was determined, the major issue was to bring the laser beam from the source to the endoscope. The laser source is a double cavity Nd:Yag.(figure 3-17). A mirror arm has been then used to guide the laser beam from the laser source to the endoscope (figure 3-17). The mirror arm has 6 degrees of freedom and contains special mirrors in 5 positions to guide the laser beam with the lowest possible energy loss. Because of the high number of degrees of freedom, the alignment of the mirrors is challenging and a careful positioning of the various parts of the arm is required. Figures 3-18 and 3-19 show some details of the mounted arm, the endoscope and the camera viewing the laser plane.
The key element that allows measurement of the flow speed is the seeding. It was chosen to use droplets of a water-glycol solution, since it is less dirtying than oil droplets The solution was heated in a smoke generator and then injected in front of the inlet (station 0 in figure 3-8). The particles are about 1 µm diameter.

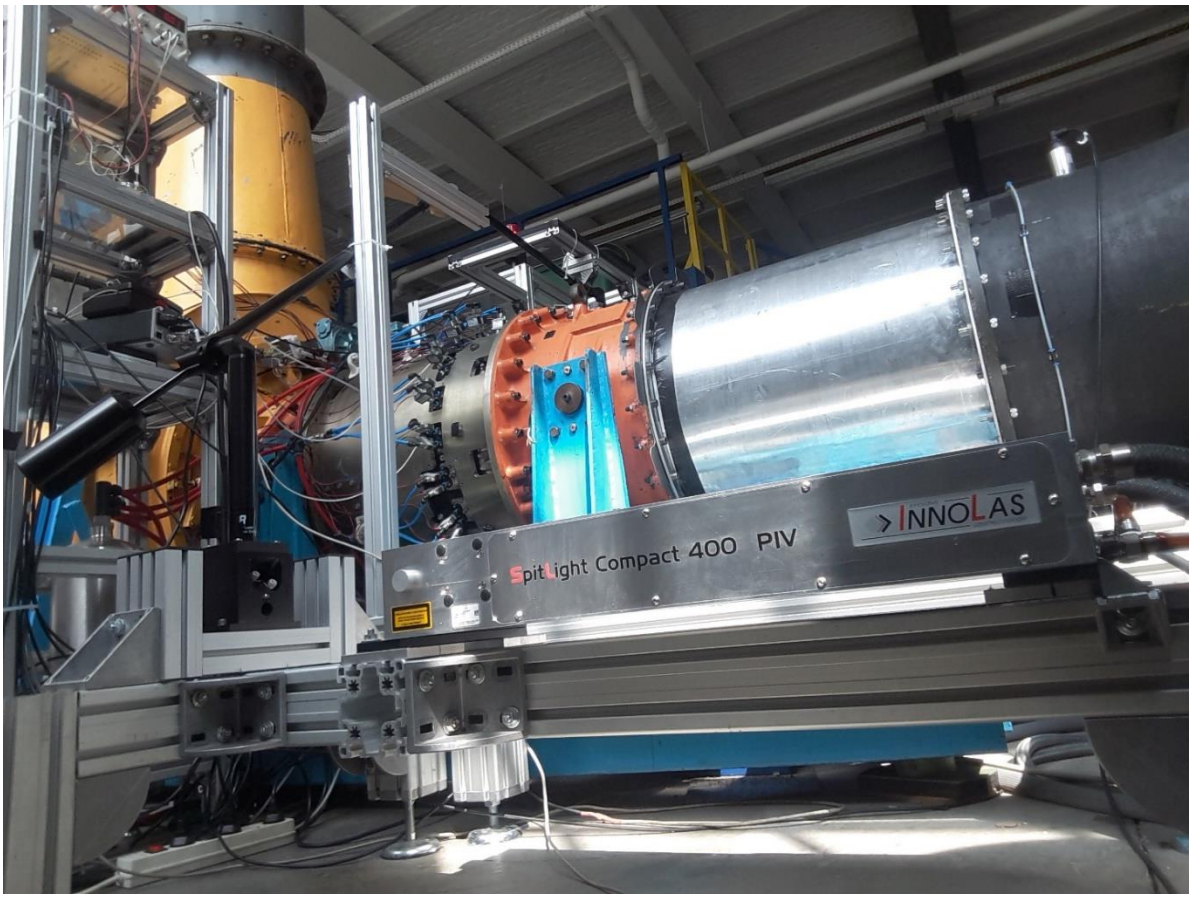

Figure 3-17 : laser and mirror arm mounted on the test bench

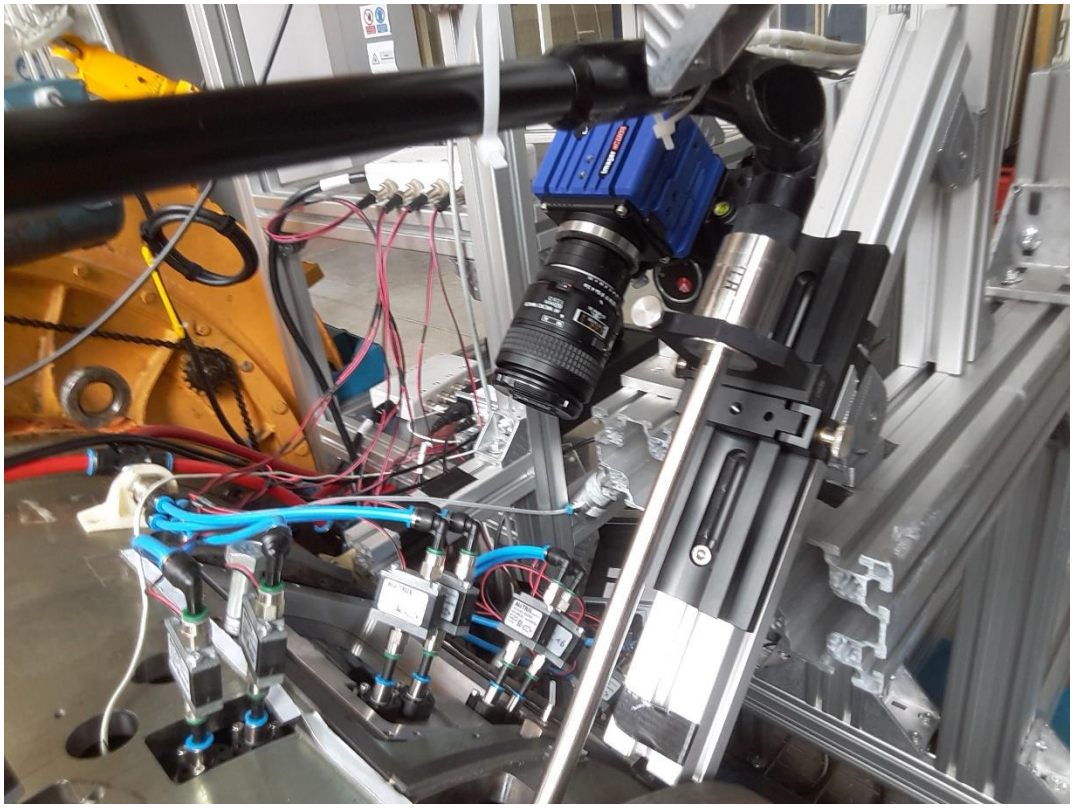

Figure 3-18 : view on the endoscope and camera

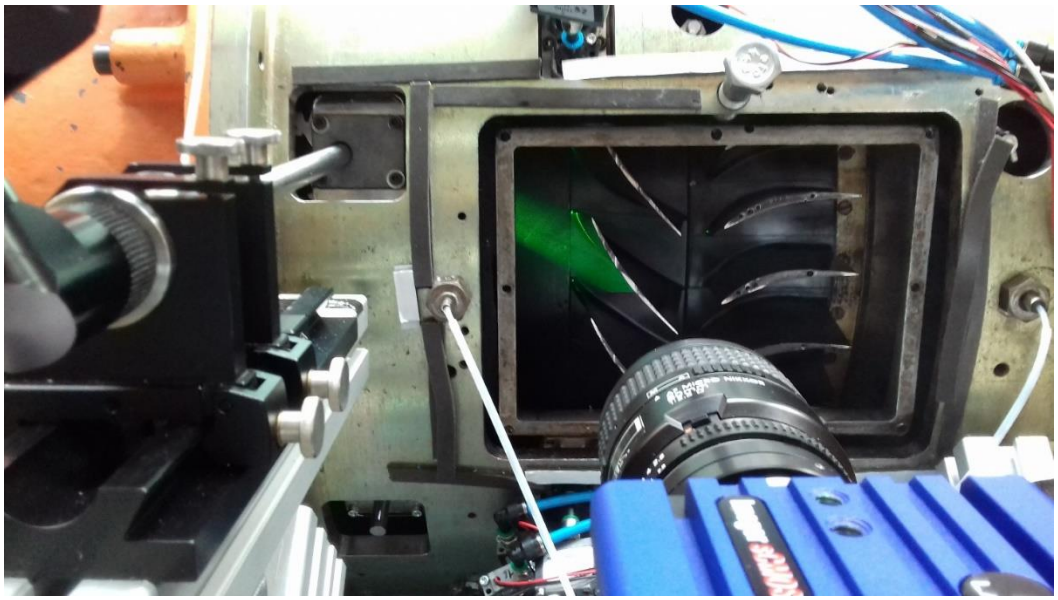

Figure 3-19 : view of endoscope and camera from a different perspective, showing also the laser plane

The camera is a Lavision sCMOS with a resolution of 2560x2160 px², with a focal length of 60 mm. Once mounted and calibrated, it allowed a field of view of 67 mm x 81 mm. The acquisition frequency was limited by the laser, that could run at 10 Hz. The PIV frequency was thus set to 5 Hz, phase locked with the rotor position. A frequency of 5 Hz corresponds approximately to a pair of images every 10 revolutions. Such a low frequency allows to analyse flow in the rotor in steady operation, but not the transient towards instability, which takes just a few revolutions to develop.
A PTU (Programmable Timing Unit) was used to synchronize camera and laser, and the software Davis8 was used for acquisition. The maximum number of images that was possible to acquire was 100, since beyond that, some particles of smoke were creating a deposit on the window and the quality of the PIV fields was strongly deteriorated. Due to the limit of the laser frequency to 10 Hz, the reduction of the active sensor field in the camera would have been of no benefit to speed up measurements; hence it was not possible to acquire more PIV samples in time before the window was polluted with seeding or condensed water.
For the post-processing, an in-house multipass algorithm has been used. In the present study, three passes with interrogation windows of 96x96, 48x48 and 32x32 with 50% overlap have been used to compute the mean flow fields starting from the 100 images. Given the camera resolution and the size of the interrogation windows, it was possible to obtain 2 vectors/mm (109 vectors/pitch, 116 vectors/blade chord).

In table 3-5 the information about the instrumentation used for PIV are resumed.

Innolas SpitLight Compact PIV 400 Nd :YAG Laser	Max Output 250 mJ/pulse pulse= 4 ns
Mirror Arm and Endoscope ILA GmbH	Max tolerated energy/pulse 80 mJ/pulse
Camera LaVision Imager sCMOS	Equipped with lenses 60 mm Exposition 15-100 µs 2560 x 2160 pixels² Acquisition rate : around 5 Hz

Table 3-5 instrumentation used for PIV experiments

In figure 3-20b, 3-20c a pair of images acquired by the camera during a test without distortion at nominal conditions is shown, on the plane at 51% of the blade height. The time interval between the two images was set 6 μs so that the displacement of the same particle between one image and the following is 8 px, corresponding to the 25% of the interrogation window of 32x32 pixels. The average diameter of the particle images in pixel is 2.5. A mask (figure 3-20c) was used during postprocessing to remove the laser reflections from the PIV analysis. Two regions of reflection appear; the first one appears in A in figure 3-20b, where the laser plane hits the rotor leading edge and also because of a reflection where the blade hits the hub, at its

root. A second region forms in B where the laser plane intersects the suction surface of the blade. The mask follows thus the suction surface until C where the laser plane is hidden because of the twisting of the blade (visible in the CAD figure 3-20a). In D the mask continues on the right until the right edge of the field of view of the camera.

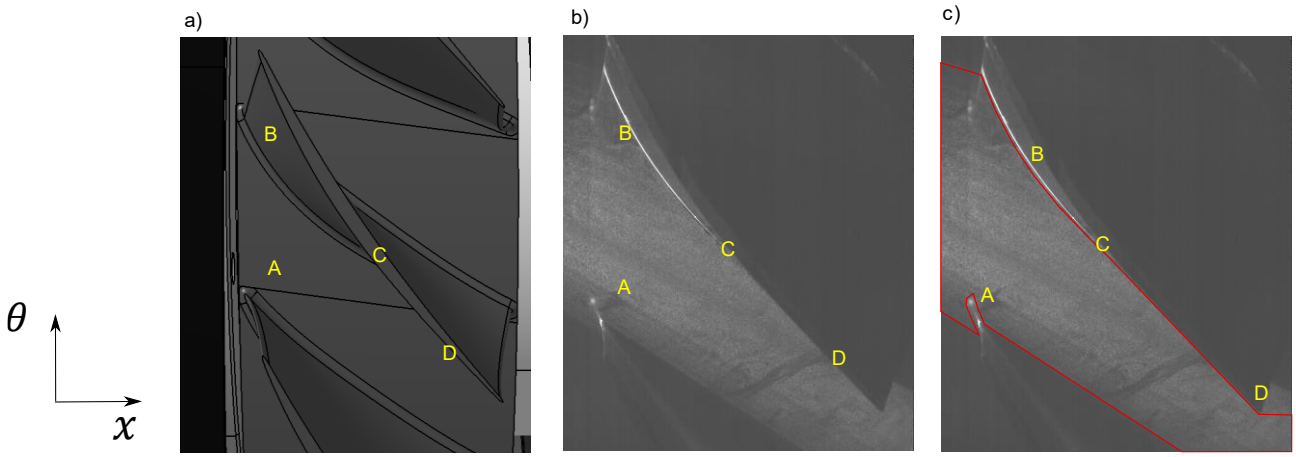

Figure 3-20 : CAD of the field of view (a) ; (b) and (c) : pair of images of the particles acquired by the camera and particular points of reflexions ; in (c) also the masque is shown.

In figure 3-21 is represented the velocity field superposed on one of the images of the camera. The tip of the blade is highlighted in black. All the PIV fields shown in the following correspond to measurements performed in that position inside the blade channel.

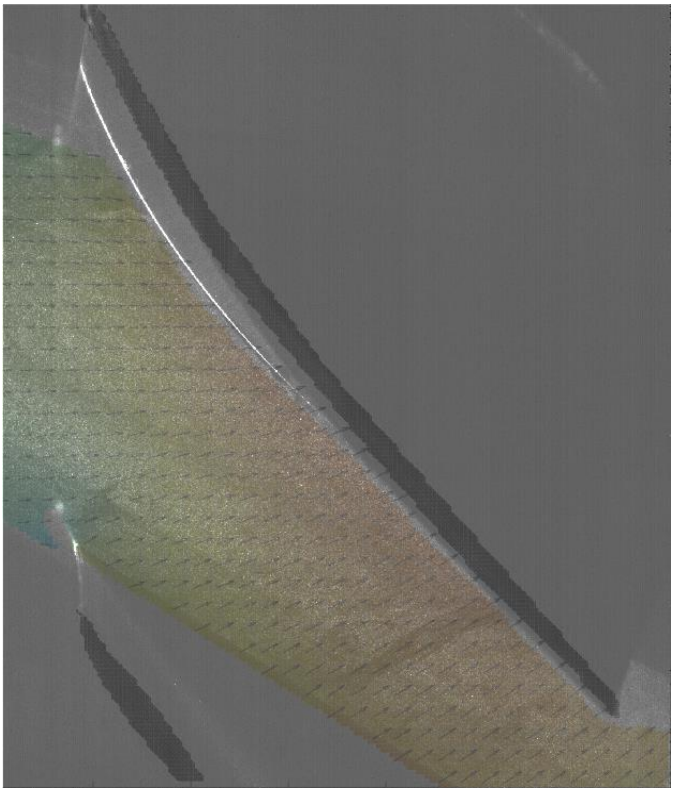

Figure 3-21 : PIV field superposed on the image particles. The tip of the blades is highlighted in black to help visualising the position of the velocity field in the blade channel

Concerning PIV uncertainty, different approaches have been developed based on Sciacchitano (2019) work. A simple method that gives a good order of magnitude is to consider the uncertainties on the various parameters that define the measurement of the velocity:

$$v = \frac{\Delta X}{M\,\Delta t}$$

The measurement on the velocity depends on:

- the displacement of the particles in the physical plane ΔX
- the magnification M that represents the factor between the physical distance on the laser sheet and the distance captured on the camera sensor
- the time between the two images of the particles used to estimate the displacement ΔX

The relative error of the measure U is thus:

$$\frac{\delta U}{U} = \sqrt{\left(\frac{U_{\Delta x}}{\Delta x}\right)^2 + \left(\frac{U_M}{M}\right)^2 + \left(\frac{U_{\Delta t}}{\Delta t}\right)^2}$$

In table 3-6 are reported the different estimated contributions to the error, which is estimated to be 3.5% and is dominated by the perspective errors on the velocities, which are discussed in the following.

$\left(\frac{U_{\Delta x}}{\Delta x}\right)$	$\left(\frac{U_M}{M}\right)$	$\left(\frac{U_{\Delta t}}{\Delta t}\right)$
-peak locking (0.1 px thus **0.3 %**) -perspective errors (**3.3%**)	- Uncertainty on dot position on calibration plane (+/- **0.1%**) - Position calibration plane with respect to measurement plane (0.5 mm thus **0.7%**) - Position camera with respect to measurement plane (0.5° thus **0.7**%)	- 10 ns (specified by laser and PTU manufacturer)
3.3%	**1%**	**0.2%**

Table 3-6 : recapitulation of different uncertainties in the PIV measurements

First of all, the camera acquires on a planar region, while the casing has some curvature. For a window of 81 mm, on the y direction (figure 3-22), the angle α created by the casing curvature is 8°. There is thus an error in the projection of v_θ and thus a deviation from v_y.

$$v_y = v_\theta cos\alpha + v_r sin\alpha$$

$$v_y = v_\theta * 0.99 + v_r * 0.14$$

The order of magnitude of the error is thus 1% in the first term and, if v_r is of the order of 10% of v_θ, then the incertitude is of the order of 1.4%. There is moreover an uncertainty due to the perspective error due to v_z component of velocity.

$$v_z = -v_\theta sin\alpha + v_r cos\alpha$$

$$v_z tan\gamma = -v_\theta sin\alpha\ tan\gamma + v_r cos\alpha\ tan\gamma$$

For a distance of 280 mm between camera and laser plane, the angle γ is 35° and thus

$$v_z tan\gamma = -v_\theta 0.14 * 0.7 \ + v_r \ 0.99 * 0.7$$

$$v_z tan\gamma = -v_\theta 0.1 \ + v_\theta \ 0.07$$

which gives the 3% of v_θ if v_r is of the order of 10% of v_θ. The estimated total error due to the two geometric errors is of the order of 3.3%.

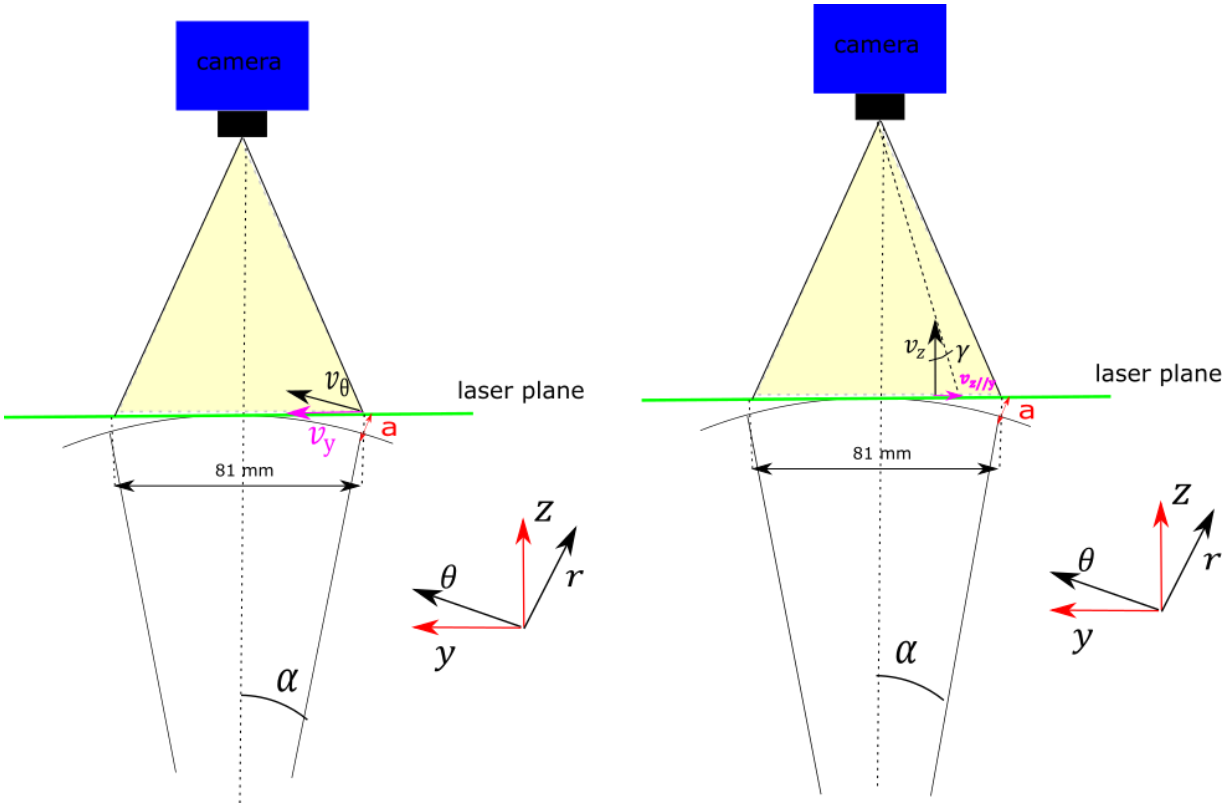

Figure 3-22 : schematic representation of the error due to the curvature casing (left) and the perspective error (right) on the estimation of the velocity components

4 EFFECT OF THE DISTORTION ON THE PERFORMANCE: STALL MARGIN

In this chapter, the distortions created with the different grids and the effect they produce on the compressor will be presented and analysed. The chapter is centred on two main results of the study which are going to be discussed: first, a classification of the various grids distortions and their effect on the compressor in four flow regimes, and second, the development of a new distortion index and its ranges of applicability and limitations.
Regarding the classification in four regimes, it will be shown that, in addition to the two well-known regimes separated by the critical angle (Reid, 1969), new regimes can be introduced. They are not described in the literature - to the knowledge of the author - because of the restricted range of porosities usually investigated. The classification that will be proposed is thus a much broader representation of the physics associated to an azimuthally distorted flow. In these four regimes, the different response of the compressor will be characterised by the stall margin, which is the most significant parameter that describes the limits of the compressor performance.
The link between the stall margin and the distortion generated by a grid is usually done through correlations that rely on the use of distortion indexes, as it was introduced in chapter 2. During the past decades, many indexes have been developed and continue to be used. Some of them, as the DC60, have been presented in the chapter 2. An effort of standardization has been proposed in AIR 1419 C (2017) which provides a guide for building a set of indexes to characterise the distortion in a compressor. The basic limitation of these indexes and the correlations based on them, however, is that they rely heavily on empirical experimental data. They are thus less useful for prediction, especially for new compressors about which no experimental data is available. The DC60 relies on the identification of a critical sector, which is not known a priori before experiments. The AIR 1419C on the other hand builds correlations based on experimentally determined sensitivities, to compensate the lack of the understanding of the physics of the distortion.
The new index that will be presented, has its roots in the physics involved in the problem, and thus on more solid grounds. It is based on the identification of a scale of the flow called θ_{int}, which captures the physics of the interaction of the undistorted and distorted regions at the edges of the grids. This index will be presented in the chapter, and the ranges of applicability with respect to the four regimes identified at the beginning of the chapter will be discussed in more detail. It will be shown that its use is limited to two regimes, but an extension to the other regimes can be hoped extending and modifying the physical arguments on which it is based on.

In the first part of the chapter (section 4.1), a panorama of the effect of the different porosities and angular extensions of the grids on the compressor performance is given, in order to introduce the classification into four flow regimes. After that, existing distortion indexes are tested on the experimental data of the study and discussed (section 4.2); the new index is then introduced (section 4.3), and its limitations discussed in the final part of the chapter (section 4.4).

4.1 FOUR FLOW REGIMES

In the following, the stall margin will be presented and its evolution discussed for the various grid distortions (porosity and angular extensions) introduced in the previous chapter. Let us first remind that a stall margin decrease can be characterised by both a loss of pressure rise and a higher stall mass flow rate at the stalling

point. The detailed characteristic curves are available in Appendix A. This chapter will focus on the effects of the grids on the stall margin.

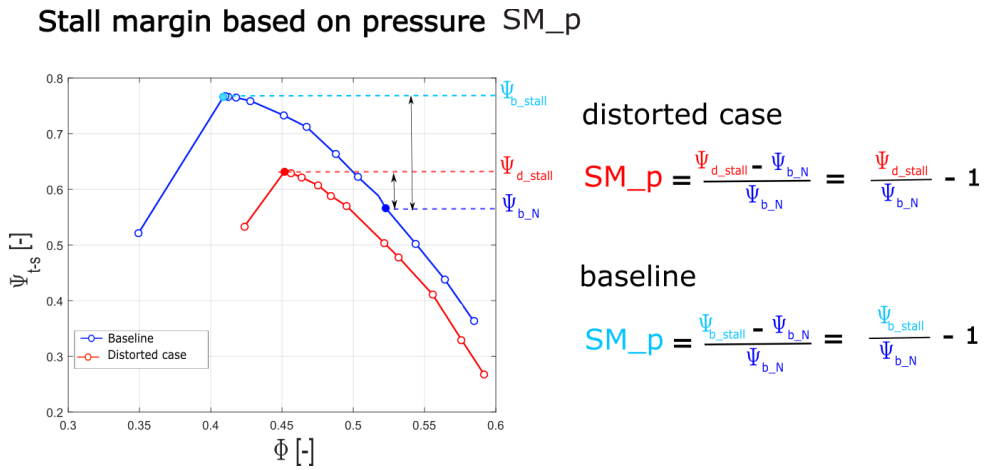

Figure 4-1 definition of stall margin based on pressure rise. In light blue the stall margin for the baseline, and in red the stall margin in the distorted case. ψ_{b_N} pressure rise coefficient for the baseline in nominal conditions ; ψ_{b_stall} pressure rise coefficient for the baseline at last stable point; ψ_{d_stall} pressure rise coefficient for the distorted curve at the last stable point

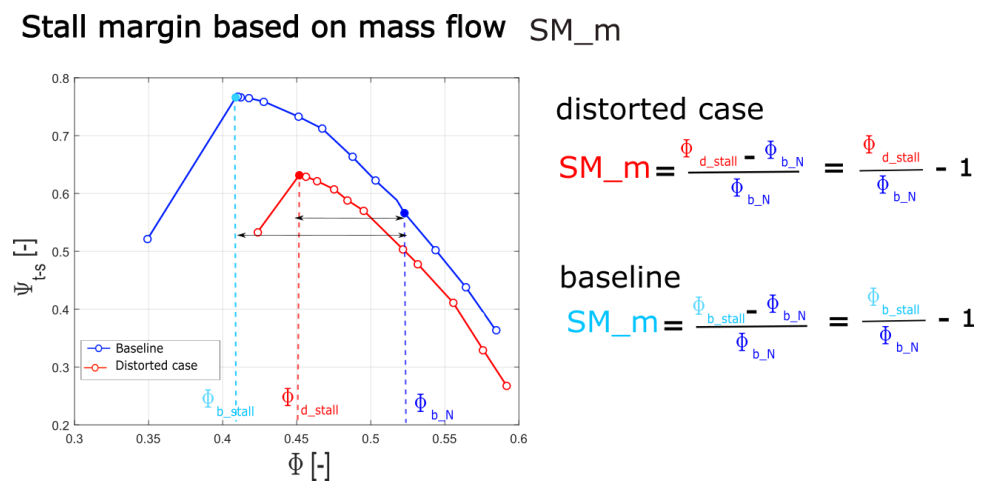

Figure 4-2 : definition of stall margin based on mass flow rate. In light blue the stall margin for the baseline, and in red the stall margin in the distorted case. ϕ_{b_N} flow coefficient for the baseline in nominal conditions ; ϕ_{b_stall} flow coefficient for the baseline at last stable point; ϕ_{d_stall} flow coefficient for the distorted curve at the last stable point

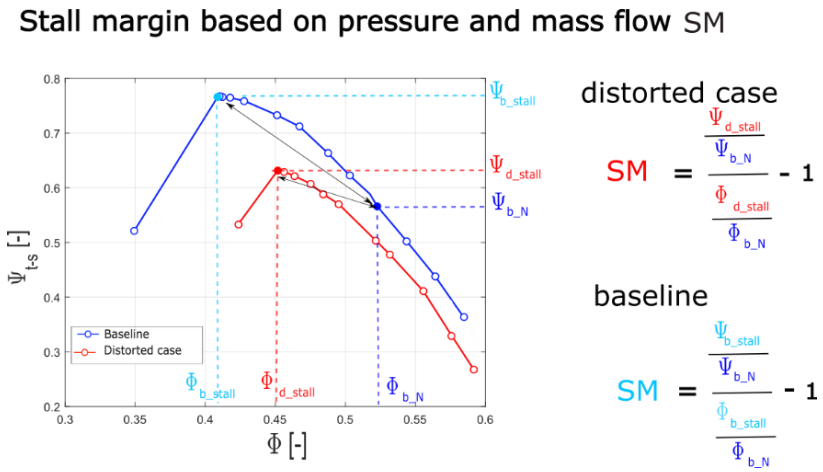

Figure 4-3 : definition of stall margin based on both mass flow rate and pressure rise. In light blue the stall margin for the baseline, and in red the stall margin in the distorted case. ψ_{b_N} and ϕ_{b_N} pressure rise coefficient and flow coefficient for the baseline in nominal conditions ; ψ_{b_stall} and ϕ_{b_stall} pressure rise coefficient and flow coefficient for the baseline at last stable point; ψ_{d_stall} and ϕ_{d_stall}pressure rise coefficient and flow coefficient for the distorted curve at the last stable point

Different definitions of stall margin can be built including one of the two aspect or both (figures 4-1, 4-2, 4-3). The first definition of stall margin, SM_p (figure 4-1) is based on the pressure rise difference between stall conditions and the nominal ones. The second definition, SM_m (figure 4-2), considers only the stalling mass flow rate difference between stall conditions and the nominal ones as an indication of the limiting range of operation. The most complete definition SM takes into account both the stalling mass flow rate and the pressure rise (figure 4-3). In what follows we focus on the SM_p (4.1.1), the SM_m (4.1.2) and section 4.1.3 will synthetize the four regimes identified in the previous sections, showing the full picture.

4.1.1 STALL MARGIN BASED ON STALLING PRESSURE RISE

The evolution of the stall margin based on the pressure rise as a function of the angular extension of the grid is first presented in figure 4-4. The plot is parametrised by the porosity of the grid, in order to see both the effects of the angular distortion and of the porosity.

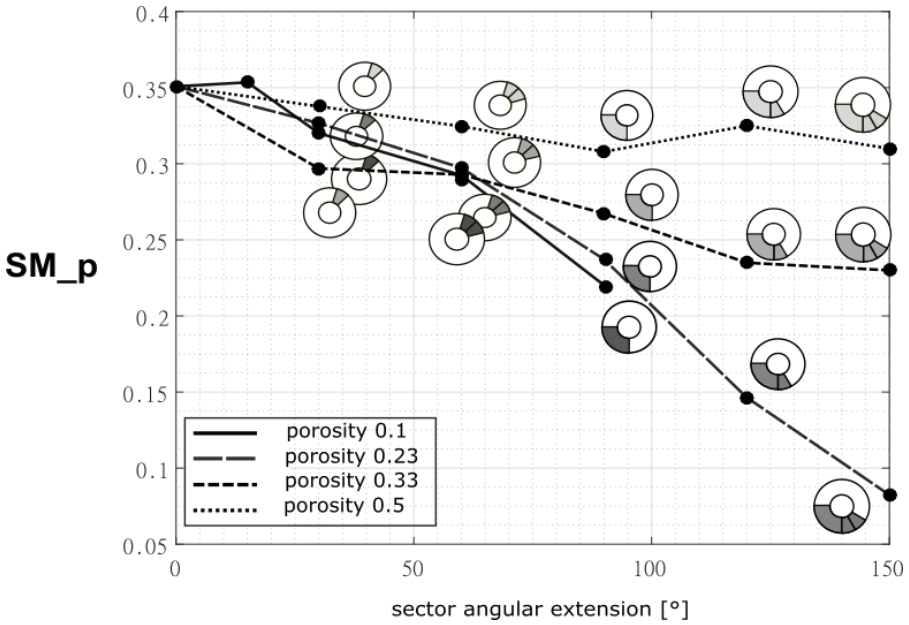

Figure 4-4 : stall margin based on pressure rise as a function of angular extension of the distortion grid.

The general tendency is a decrease of the stall margin with an increase of the angular extent of the grid. In the case of the porosity 0.5, however, a saturation of the stall margin is present when the angular extension is increased beyond 90°. This is referred as the critical angle phenomenon, as it was stated in Reid (1969). The existence of such a critical angle is not obvious, however, for porosities lower than 0.5. For lower porosities, in fact, when the angle of the sector is increased, the stalling pressure rise capability deteriorates further, not allowing to determine a critical angle in these cases.

To compare the present results with the results obtained by Reid (1969), the stalling delivery static pressure has been plotted in figure 4-5, as it was the parameter used by Reid. The tendencies are similar to the ones observed in figure 4-4, and the existence of the critical angle is not evident as it was in Reid (see chapter 2), except for the highest porosity grid.

A major difference between Reid results and the present results is the range of porosities used. Reid used grids of high porosity (0.7 -0.9) for which the ratio of the total pressure in the distorted and undistorted sector is the same whatever the angular extensions are, once the porosity is fixed. In the present study however, since low porosity grids have been used (0.1-0.5), this is not generally true, if not for porosity 0.5 as it can be seen in figure 4-6, in which the total pressure behind the grid is plotted as a function of θ, the angular coordinate for the different grid porosity.

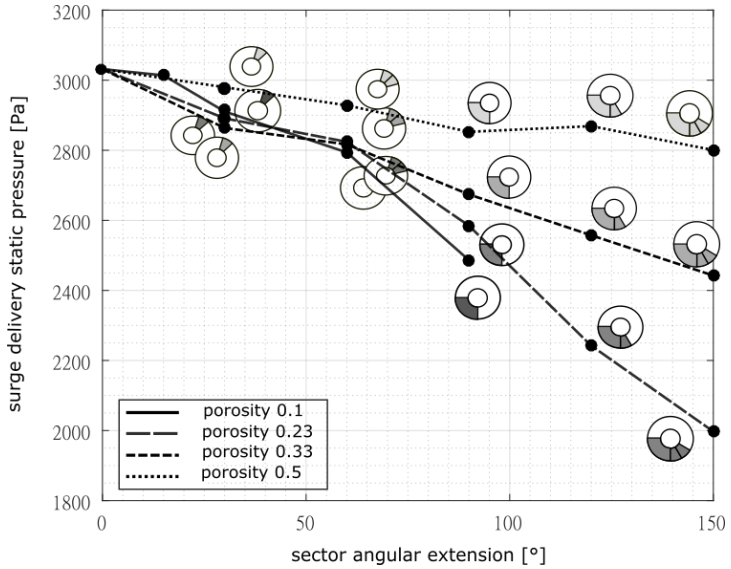

Figure 4-5 surge delivery static pressure as a function of angular extension of the distortion grid.

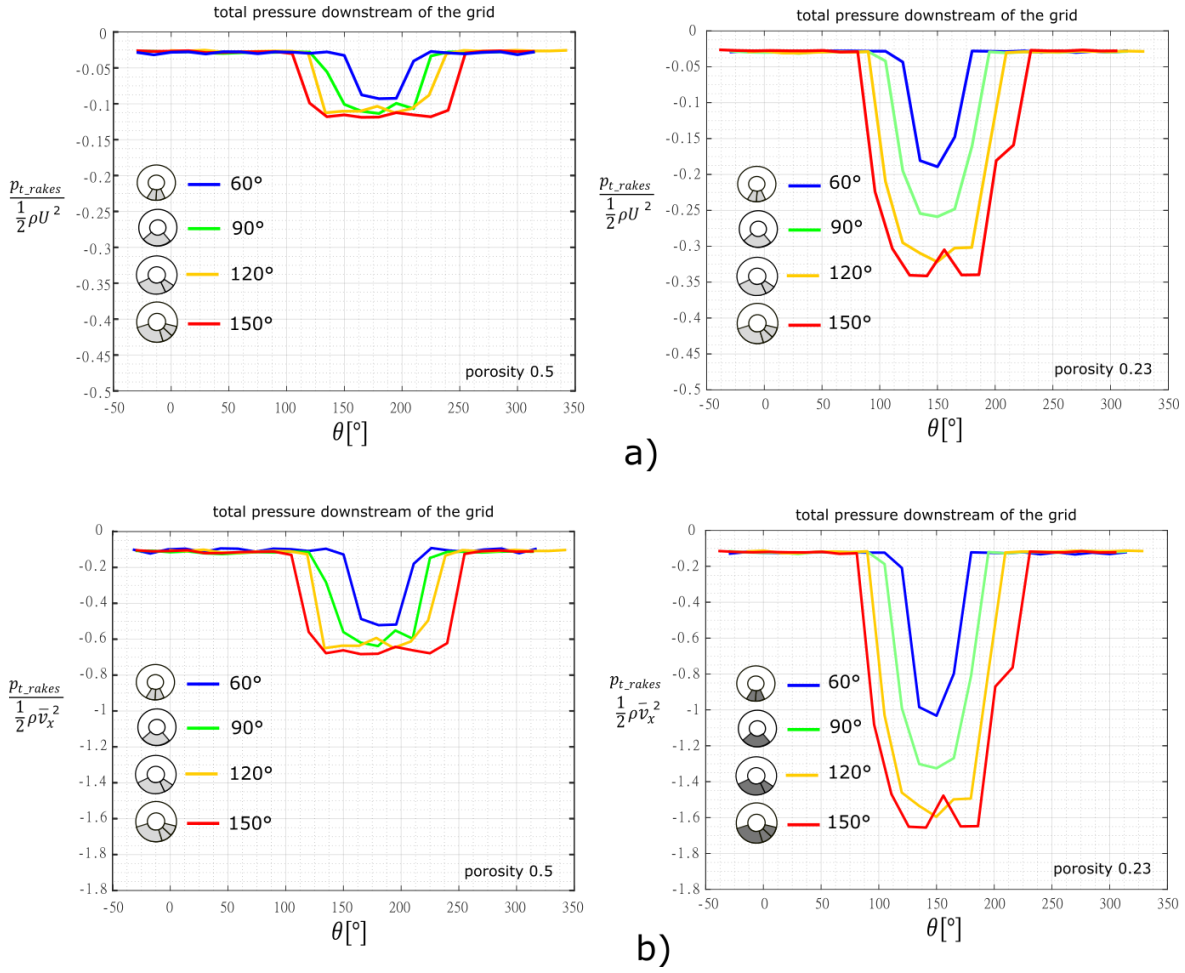

Figure 4-6 : comparison of the total pressure pattern behind the grids of different angular extensions at the last stable point ; on the left porosity 0.5 ; on the right porosity 0.23. 6a and 6b use different scaling, respectively based on U and v_x

In figure 4-6a left and right, results are presented for different angular extensions and a porosity fixed to 0.5 and 0.23 respectively. The pressure drops have been made non-dimensional with respect to $1/2\,\rho U^2$, since

this is a pressure characteristic of the compressor. However, since the last stable point is not the same for all the curves, a different way to make the pressure drop non dimensional is shown in figure 4-6b, based on the axial velocity. The difference in the trends doesn't change however. It is clear that for porosity 0.5, the grids behave as in Reid case with a similar ratio of pressure in the distorted and undistorted sector. On the other hand, grids of lower porosity do not behave this way, since the ratio of pressure behind and outside the grid increases with the angular extent.

The different behaviours can be explained, since weakly porous grids behave in between a solid body and a perfectly porous medium, the last represented by highly porous grids. More precisely, for highly porous grids, the upstream redistribution of the mass flow is small, since the blockage of the grid is small, even for high angular extensions of the grid. This explains why in figure 4-6 on the left, the low peak total pressure behind the grid is little influenced by the extension of the grid. For weakly porous grids, instead, the upstream redistribution of the mass flow is greater, similar to a solid body blockage, and depends much more on the angular extension of the grid. As a consequence, the peak minimum total pressure is controlled not only by the porosity but also by the extent of the grid. This marks a difference with Reid grids, and it is to be connected to the absence in figure 4-4 of a critical angle for porosities below 0.5.

Nevertheless, the present results capture, as in Reid experiments, a difference between wide grids (wide compared to the critical angle appearing for porosity 0.5) and narrow grids and confirm the existence of two regimes at high porosity: a regime for narrow grids where the stall margin deteriorates as the extent of the grid is increased, and a regime for wide grids where the stall margin saturates. In the two regimes, the saturation of the stall margin (figure 4-4) corresponds to a saturation of the total pressure loss (figure 4-6 on the left).

However, the present experiments include a third regime which is not captured in Reid experiments, since the porosity range in his experiments was limited to high porosities. This third regime concerns wide grids of low porosities (<0.5). These grids characterise a regime in which the total pressure loss decreases monotonically as the angular extent of the grid is increased (figure 4-6 on the right), and correspondingly the stall margin.

In the following paragraph, we will concentrate on the other aspect of the loss of performance, namely the stalling mass flow rate, and we will show how it is influenced by the porosity and angular extension of the grids.

4.1.2 SM BASED ON STALLING MASS FLOW RATE

If the shape of the total pressure drop in the annulus can be linked to the trends in the stall margin based on pressure rise, in the following it will be shown that the shape of the flow coefficient behind the grids has a connection to the stall margin based on flow rate SM_m. Figure 4.7 presents the evolution of this last parameter with the grid porosity and angular extension.

Figure 4-7 clearly shows two regions separated by an angle ideally between 60° and 90°. In the first region (grid angular extent lower than 60°), the SM decreases when the angular extent is increased, while in a second region beyond 90°, the SM remains constant. In figure 4-.8, the profiles of the flow coefficient ϕ at the last stable point are plotted as a function of the θ coordinate for different porosities.

Figure 4-8 shows that the flow coefficient behind the grids of 90° and 120° reaches an almost constant value. On the other hand, the grids of 60° do not show a clear constant ϕ and the flow in the distorted region decreases and then re increases to match the flow outside of the grid. This distinction between flows where a plateau is reached and flows without a plateau corresponds to the distinction of the two regions in figure 4-7, where the stall flow rate remains constant, and where it decreases monotonically. There is thus a clear link between the plateau in the ϕ profile and the saturation of the stall mass flow rate.

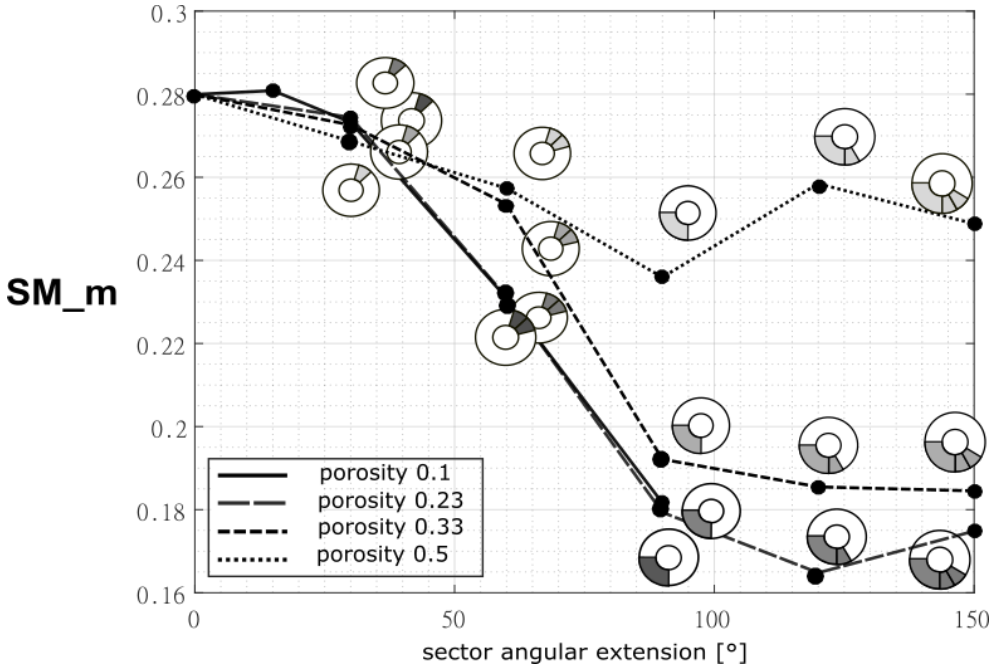

Figure 4-7 stall margin based on mass flow rate as a function of angular extension of the distortion grid.

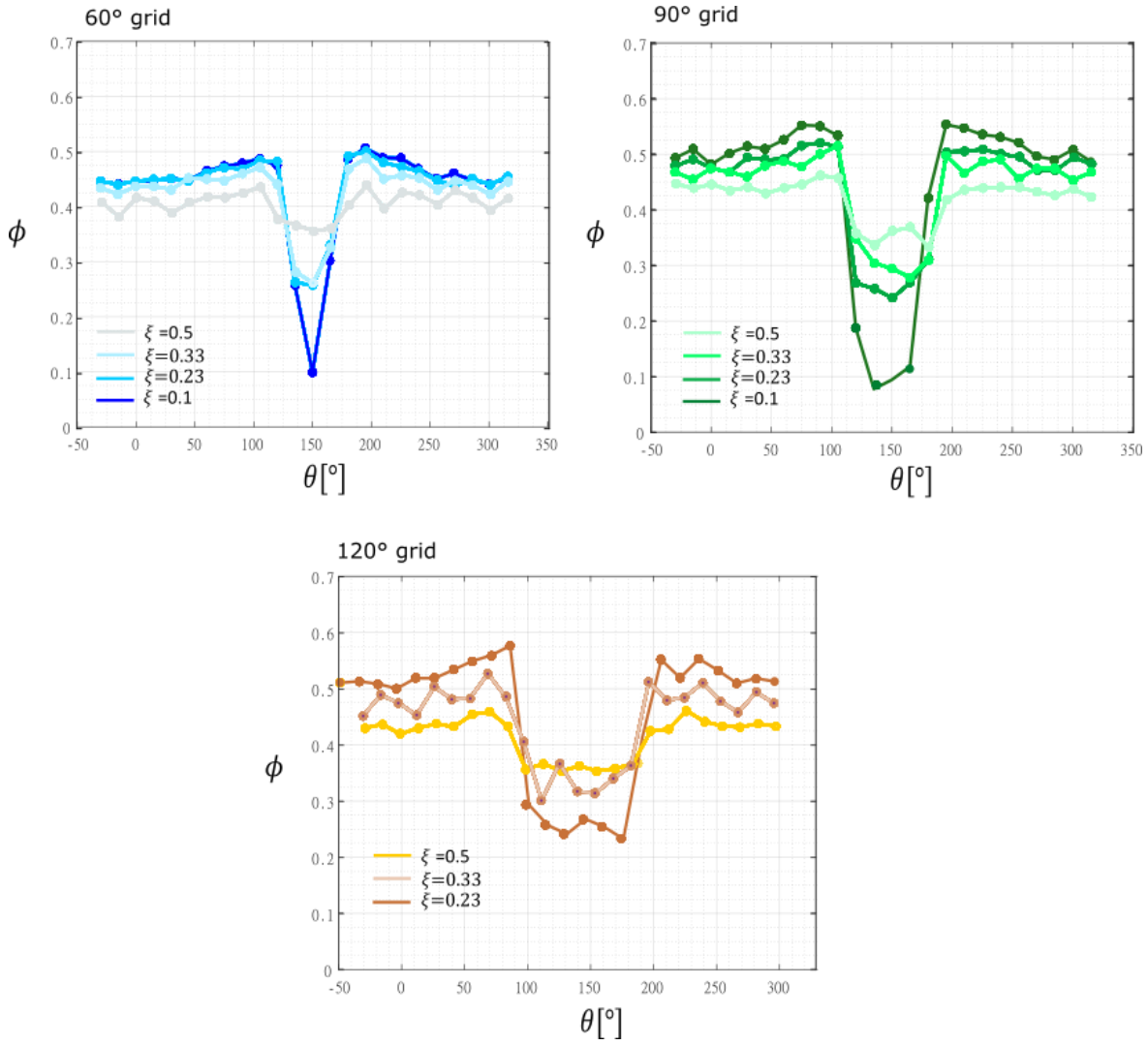

Figure 4-8: profiles of flow coefficient ϕ (measured at the last stable point) in the annulus as a function of θ. The three pictures correspond to three extensions of the grid and the colours indicate the porosity.

4.1.3 SYNTHESIS : FULL PICTURE

The previous sections have evidenced different flow behaviours depending on the grid size and porosity: the saturation of the total pressure drop (figure 4-6) and the existence of a plateau in the flow coefficient (figure 4-8). They are used to define three regimes characterising the flow behind the grids:

1. Narrow grids (<=60°) don't show neither a saturation of the pressure drop (figure 4.6) nor a plateau in the flow coefficient (figure 4-8).
2. Large grids of high porosities (0.5) show both a saturation of the pressure drop (figure 4.6) and a plateau in the flow coefficient (figure 4-8).
3. Large grids of low porosities (>0.23 and <0.5) show a plateau in the flow coefficient (figure 4.8) but no saturation of the pressure drop (figure 4-6).

In terms of stall margin, the saturation of the total pressure drop leads to a stalling pressure rise which remains constant (figure 4-4), and the existence of a plateau in the flow coefficient leads to a stall flow coefficient which remains constant (figure 4-7). A clear pattern thus appear.
The clear message that appears is that the total pressure drop induced by the grid has a visible effect in terms of stalling pressure rise and the flow redistribution upstream of the compressor (the shape of ϕ) controls the stalling mass flow rate.
Looking at figure 4-7, another aspect must be discussed that enriches the distinctions in flow regimes just shown and allows to introduce the fourth. Grids of porosity 0.1 show values of SM_m very close to the values for porosity 0.23, indicating that the stalling mass flow rate saturates for low porosities independently of the extension of the grid (at least until 90°). In the characteristic curves is clearly seen that decreasing the porosity, the stall mass flow rate changes less and less until it saturates for porosities lower than 0.23 (figure 4-9). This saturation of the stall flow rate with porosity characterizes a fourth regime for very weakly porous grids. A fourth regime has thus been introduced:

4. Grids of very low porosity (<0.23) are characterised by a saturation of the stalling mass flow rate

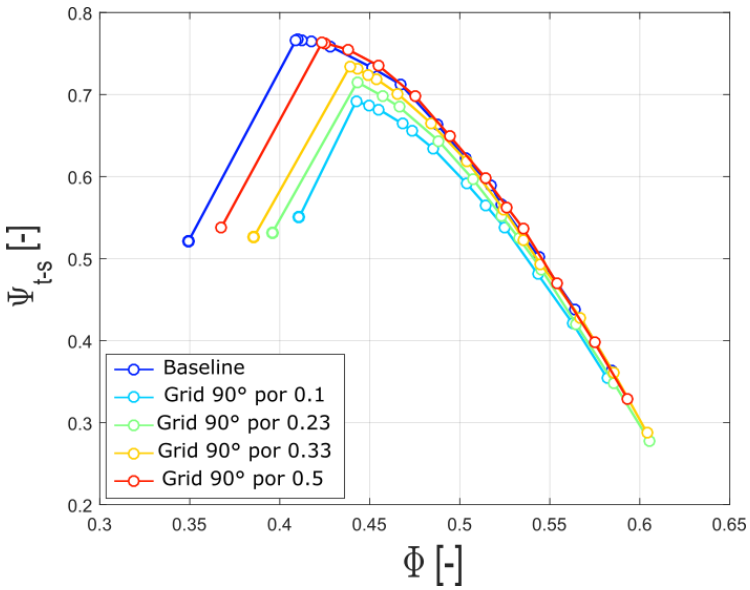

Figure 4-9 : characteristic curves with 90° grids and different porosities : saturation of the stall flow rate for low porosities

The four regimes have been summarized in figure 4-10, in the porosity-angular extension plane.

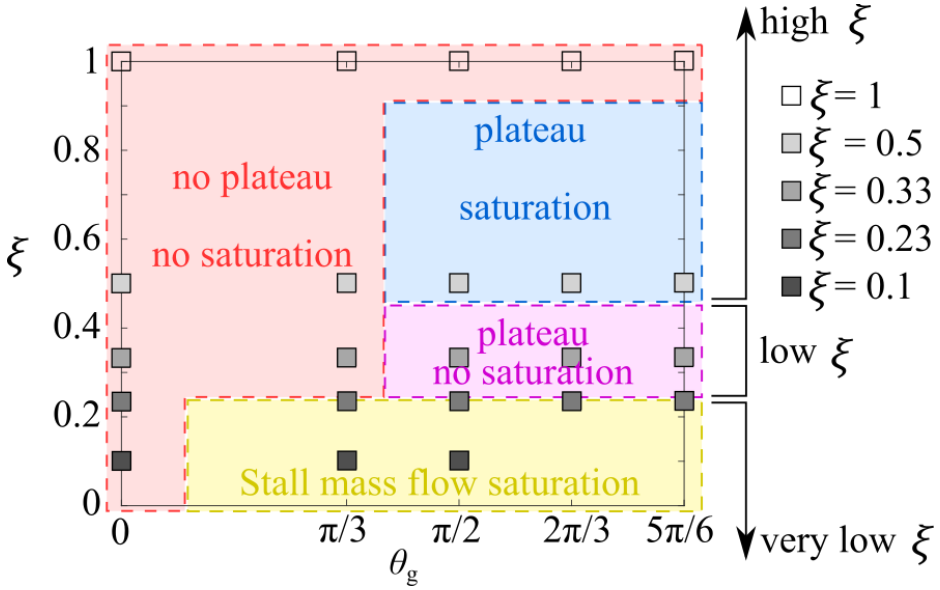

Figure 4-10 identification of four regimes for the flow behind the grids based on two criteria: the saturation of the total pressure drop and the existence of a plateau in the flow coefficient ϕ. On the x axis the extension of the grid, and on the y axis the porosity.

The most comprehensive stall margin definition SM (introduced in figure 4-3) has been used in figure 4-11 and reflects the existence of the four regimes just highlighted. The narrow grids below 60° show a monotonic decrease of stall margin. The decrease of stall margin is observed also for wide grids at lower porosities, whereas the wider grids show a saturation of SM for porosity 0.5. A particular case is for the porosity 0.1, where the SM is essentially the same as the stall margin at porosity 0.23, since the stall mass flow rate saturates.

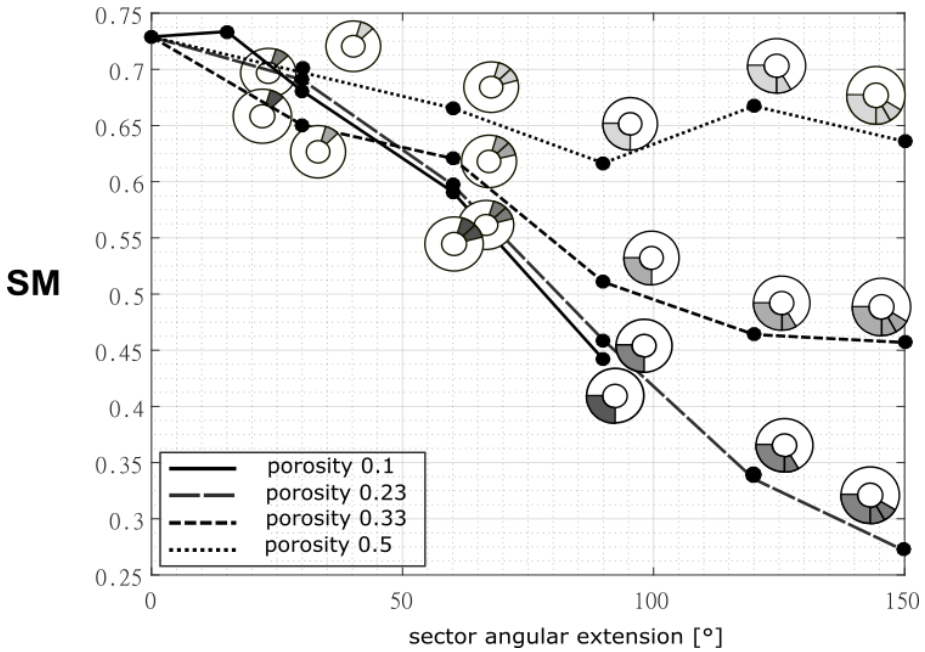

Figure 4-11 : stall margin based on mass flow rate and pressure rise as a function of angular extension of the distortion grid.

The present discussion reflects the richness of the types of flow existing behind the grids and the different effects in terms of stall margin. The different grid porosity, and not only their angular extension, influence the upstream and downstream redistribution due to the different effects of blockage and this is reflected in

the different shapes of the total pressure and flow coefficient profile. These different features of the flow in front of the compressor have a correspondence with the different behaviours of the compressor in terms of stall margin, showing that the distribution of the flow in front of the compressor is a key factor for the determination of the stall margin.
However, in the present discussion, the classification of the flow regimes is based on the porosity of the grid and it is specific for a grid and it is not adapted to a general type of distortion. What is usually done is to characterise the distortion using distortion indexes which in their definition take into account physical parameters associated to the physics of the flow. Some of these indexes will be used in the following section to build correlations of the stall margin.

4.2 DISTORTION INDEXES

In the following paragraph, two existing indexes introduced in the chapter 2 are used to build correlations with the experimental data of this study: the index Dist and the DC60. The index Dist is known to provide bad correlations but it will be used in the following because its faults clearly show the existence of the four regimes which cannot all captured by a single index. Aside from the DC60 then, a DC90 has been built and tested.

4.2.1 INDEX DIST

The simplest distortion index introduced in chapter 2, is the index Dist. We recall the definition of the index:

$$Dist = \frac{p_{t\_min} - \overline{p_t}}{\overline{p_t}}$$

In figure 4-12, the stall margin has been plotted vs this index, based on the difference between the minimum total pressure behind the grid and the average total pressure, and which is thus a measure of the intensity of the distortion. If the results exhibit a general tendency of a decrease of the SM with an increase of Dist, the data are rather scattered.

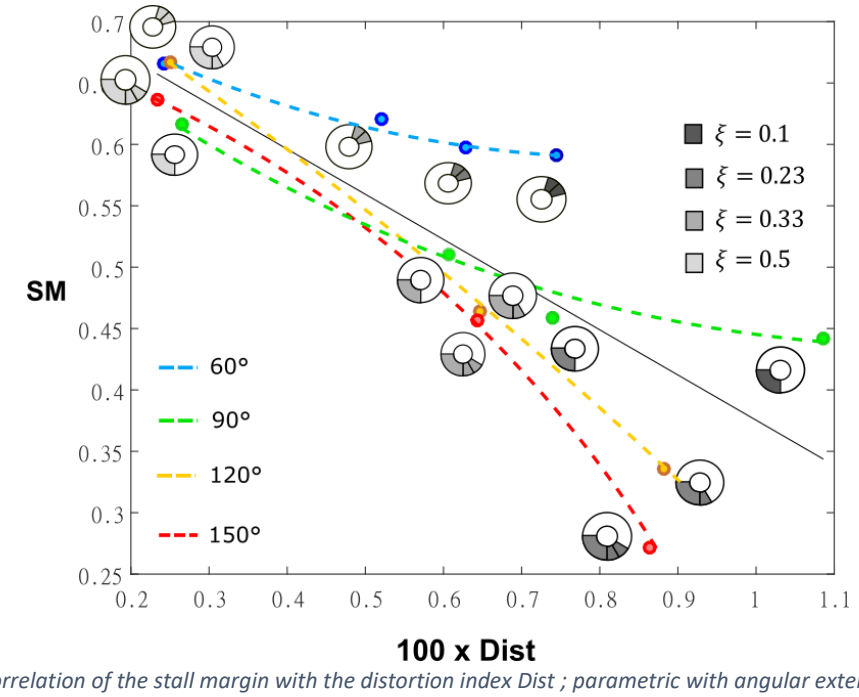

Figure 4-12 : correlation of the stall margin with the distortion index Dist ; parametric with angular extension of the grids

Grids of different width have different sensitivities to distortion. In particular, the 60° grids have a lower sensitivity than the rest of the grids. For a Dist index of 0.65 for example, the stall margins of the 90°, 120° and 150° are similar, but the stall margin of the 60° grid is higher, indicating that the impact of the same intensity of distortion (Dist index) has a weaker effect with 60° grids. This reflects the existence of regime n°1 for 60° grids clearly separated from regimes 2 and 3 and confirms that the simple pressure drop used in the Dist index does not account for the different sensitivities that exist for different angular extensions of the grids. The correlation does not work also at very low porosities, where regime number 4 is encountered. In fact, for the same stall margin of 0.45 , two 90° grids (porosity 0.23 and 0.1) have different distortion indexes since the pressure drop is very different. To account for the lower sensitivity of the 60° grids, the Dist index of the 60° grids should be reduced in order to move the corresponding points in figure 4-12 to the left, closer to the linear fit. The DC60 by Reid (1969) was developed with this scope. Instead of measuring the peak total pressure drop of the grid, it measures the average on 60° of the integral pressure drop. The average on 60° in fact is always lower than the peak pressure drop for grids of amplitude equal or below 60° and thus the distortion index is smaller.

4.2.2 INDEX DC60 AND DC90

The correlation with the DC60 is shown in figure 4-13.

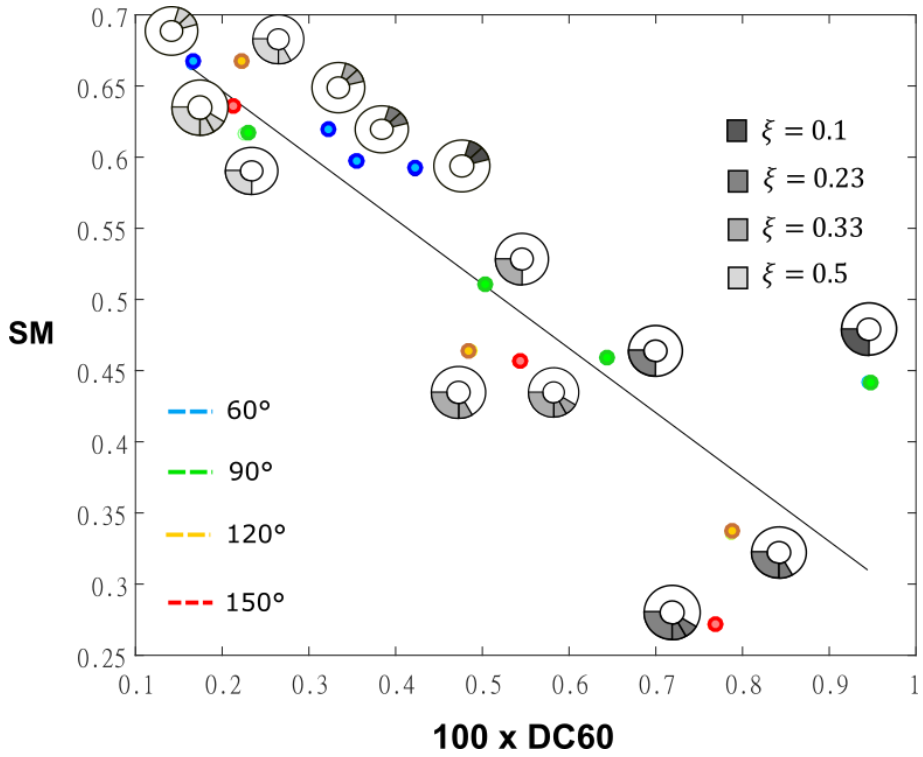

Figure 4-13 correlation of the stall margin with the distortion index DC60 ; parametric with angular extension of the grids

The DC60 improves the correlation as the results are less scattered around a linear fit. The mean square difference to the linear fit (straight line in figure 4-12) is 0.12 compared to 0.196 for the index Dist. The 60° grids are now included in the correlation since their integral averaged pressure drop is considered instead of the minimum total pressure (see chapter 2 on the definition of the DC60). The wide grids of porosity 0.23 however are still not well captured by the DC60.The DC60 is based on the assumption of a value of a critical angle equal to 60°. Different compressors however could have a different value of the critical angle. Other indices can be built on the same principle as the DC60, on the basis of a different critical angle, for example DC90 and DC120. The correlation with a DC90 for example is presented in figure 4-14. The mean square

difference to the linear fit is lower (0.056) than for DC60. A correlation with a DC120 (not presented here) was also calculated but the standard deviation is almost the same as for DC90, indicating a saturation effect. The saturation of the mean square difference to the linear fit after 90° can thus suggest a critical angle of around 90° for CME2 compressor. This would be coherent with figure 4-7, in which the stall margin based on mass flow rate is shown being almost constant for angular extensions above 90°. The deviations from the regression are shown in figure 4-15. Most of the grids have a relative deviation below 3% while especially higher angle grids have higher deviations but always below 15%.

The correlations with the DC60 or DC90 work better than the one with Dist, but some aspects need further discussion: in the definition of the indexes, for all the grids, the total pressure loss is weighted on an extent equal to the critical sector no matter the extent of the grid (see chapter 2). This procedure is not based on a solid physical argument and is instead justidied on the basis of "a posteriori" experimental evidence that it works. What is the reason why for different grids the same sector is used to weight the distortion? If the critical angle is identified to be 90°, why the losses of a grid of 30° and 90° should be weighted both on the sector of 90°? Moreover, another limitation is that DC60 relies on the identification of the critical angle, which is not known a priori, and can be identified just after having collected a sufficient amount of experimental data, which can be expensive and time consuming.

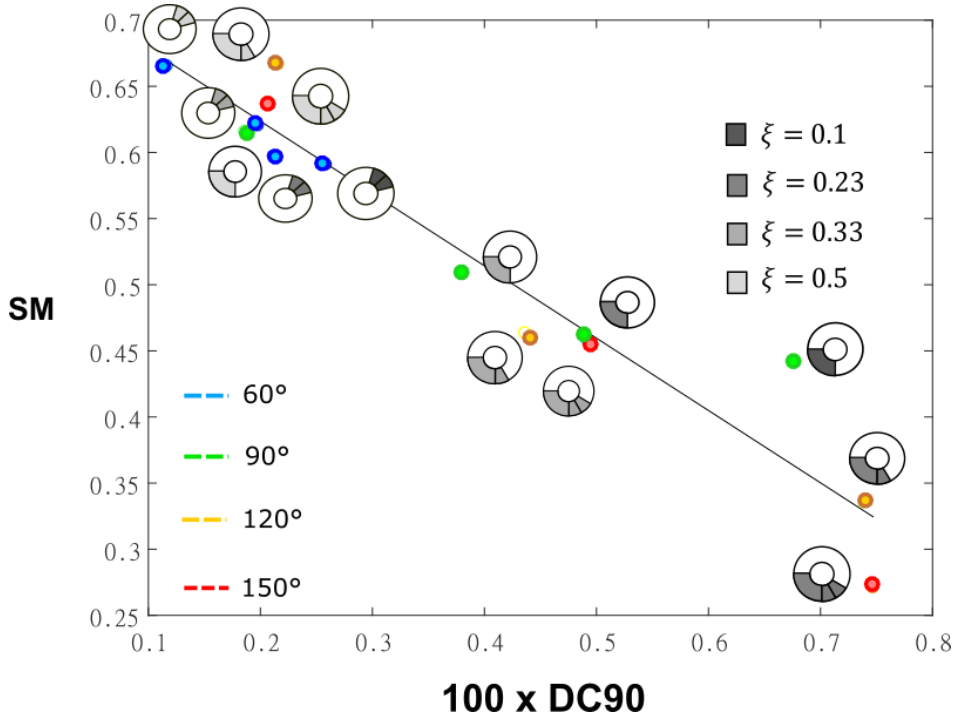

Figure 4-14 correlation of the stall margin with the distortion index DC90 ; parametric with angular extension of the grids

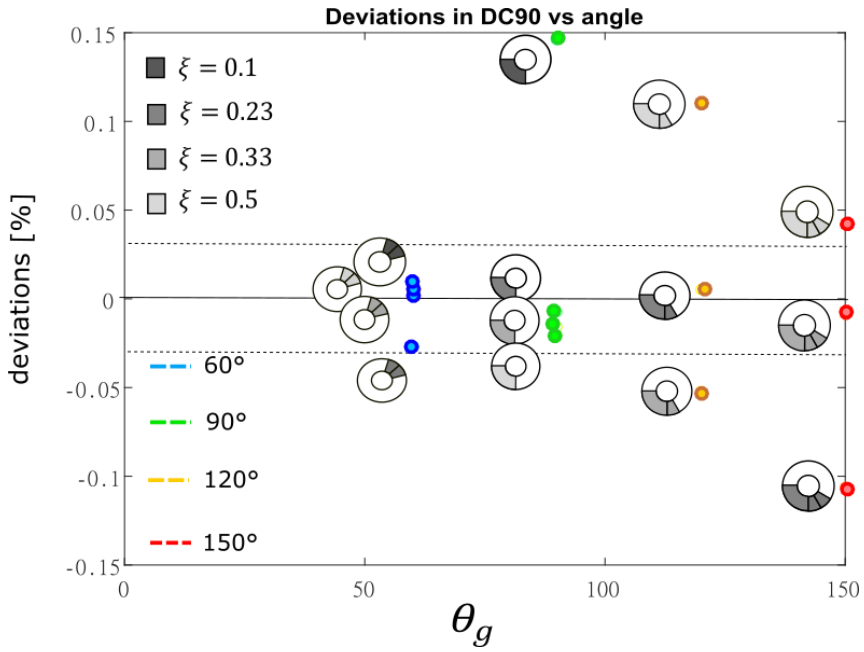

Figure 4-15 % deviations in the correlation of the stall margin with the distortion index DC90

For this reason, based on a more solid physical arguments, a new scale of the flow (θ_{int}) will now be introduced. It will provide a better identification of the sector on which averaging the total pressure loss. It will thus allow to substitute the DC60 criterion with a new criterion DCθ_{Avg}.

4.3 A NEW DISTORTION INDEX

First of all, in this section, the scale θ_{int} will be introduced (subparagraph 4.3.1.), starting from the arguments of Chue et al (1989). Some of their conclusions were reminded in chapter 2, but will be rediscussed in the following. Then, based on the θ_{int}, the new index DCθ_{Avg} will be introduced and used to provide a scaling of the stall margin (subparagraph 4.3.2). The limitations and ranges of application of this new index will be discussed in more detail in the last paragraph (4.4).

4.3.1 THE SCALE θ_{int}

This scaling is based on the on the Hynes Greitzer (1987) model and on Chue et al. (1989) work. As introduced in chapter 2, the model allows to calculate the flow coefficient profile $\phi(\theta)$ due to a total pressure distortion imposed as an input into the model. The model represents a balance circuit-turbomachine and it is based on the two equations (4.1), which have already been introduced in chapter 2.

$$\begin{cases} \frac{p_3 - p_{t2}(\theta)}{\rho U^2} = \psi(\phi_2) - \lambda \frac{d\phi_2}{d\theta} \\ \frac{p_3 - p_5}{\rho U^2} = \frac{T}{2}\overline{\phi_2}^2 \end{cases} \tag{4.1}$$

With reference to figure 4-16, the term $p_{t2}(\theta)$ represents the total pressure distortion at the compressor inlet. The compressor pressure rise, in undistorted conditions, is given by $\psi(\phi_2)$, the undistorted characteristic curve and an inertial term dependent on a geometrical parameter λ. Between stations 3 and 5 in figure 4-16 there is finally a pressure drop due to the throttle valve (throttle coefficient T in equation 4-1). The importance of the parameter λ is underlined as it is a key parameter of the interaction of the compressor

with the distorted flow. It controls the shape of the $\phi(\theta)$ and its deviations from the shape of the imposed total pressure $p_{t2}(\theta)$.

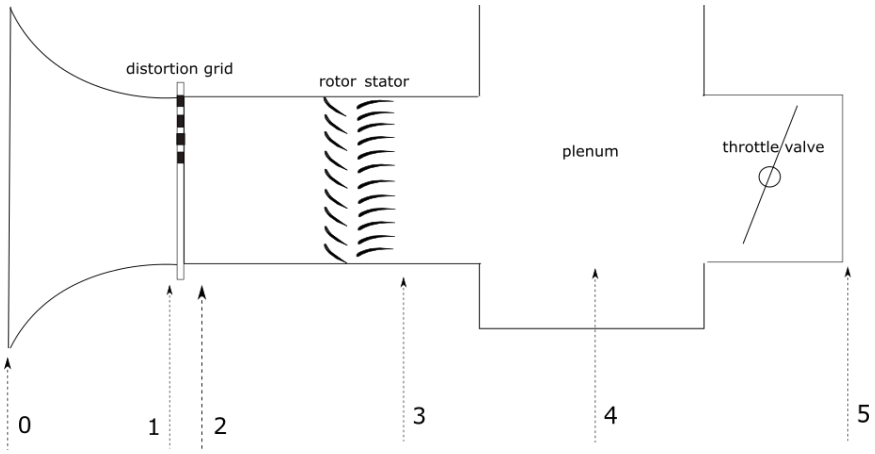

Figure 4-16 : compressor stations in Hynes Greitzer model

Based on the model, Chue et al (1989) derived an analytical solution for the ϕ coefficients in a distorted flow of the form:

$$\phi(\theta) = \begin{cases} \phi_m - \dfrac{\sqrt{R_L - \psi_m}}{a} \tan\left[\dfrac{a}{\lambda}\sqrt{R_L - \psi_m}\left(\theta - \dfrac{\theta_g}{2}\right)\right] & for\ \theta \in [0, \theta_g] \\ \phi_m - \dfrac{\sqrt{\psi_m + \psi_g - R_L}}{a} \tanh\left[\dfrac{a}{\lambda}\sqrt{\psi_m + \psi_g - R_L}\left(\pi - \theta + \dfrac{\theta_g}{2}\right)\right] & for\ \theta \notin [0, \theta_g] \end{cases} \quad (4.2)$$

This represents the flow coefficient seen by the compressor in the annulus as a function of θ. θ is the azimuthal coordinate, θ_g the amplitude of the grid sector, ψ_g is the pressure loss of the grid, R_L is the pressure rise in the total pressure sector downstream of the grid. ψ_m and ϕ_m are the values of the maximum of the compressor characteristic curve. In the model, the characteristic curve is assumed to be a parabola of curvature a. In figure 4-17 the parabolic fit of the CME2 characteristic curve is shown. It has been used in the following determination of the θ_{int}.

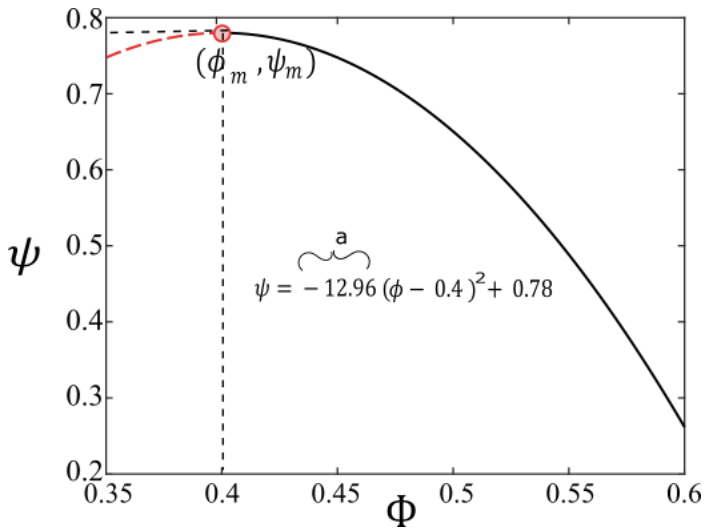

Figure 4-17: CME2 parabolic fit used in Hynes Greitzer model for the determination of the θ_{int}

The solution in (4.2) is valid in the range $\psi_m + (\pi^2\lambda^2/a^2\theta_g^2) > R_L > \psi_m$. The function hyperbolic tangent, as discussed also in chapter 2, describes the relaxation between the values of ϕ behind and outside of the grid (shape in figure 4-18). The main deviation from the simple square wave comes from a combination of the parameters λ/a, ψ_g and R_L. The boundary-induced interaction between distorted and undistorted sectors due to the fluid inertia can be estimated considering how the $\phi(\theta)$ relaxes to the square wave type $\phi(\theta)$ outside the perturbed region. The shape of the relaxation is of the form

$$\tanh\left[\frac{a}{\lambda}\sqrt{\psi_m + \psi_g - R_L}(\theta)\right] = \tanh\left(C\theta\right) \tag{4.3}$$

with

$$C = \frac{a\sqrt{\psi_m + \psi_g - R_L}}{\lambda} \tag{4.4}$$

As Chue et al. (1989) state in the paper, what is important in determining the stability of the distorted flow, is the interaction between the undistorted and distorted regions, rather than a critical residence time in the distorted sector. This interaction, can be characterized by an angle θ_{int} that we introduced as it is shown in figure 4-18. The interaction zone is highlighted in yellow, and two red markers identify its boundaries. These boundaries have been defined mathematically as the value of θ at which the hyperbolic tangent has reached the value 0.99, thus has almost relaxed to a constant value. Above the boundaries of the θ_{int} region thus, the flow coefficient ϕ is constant.

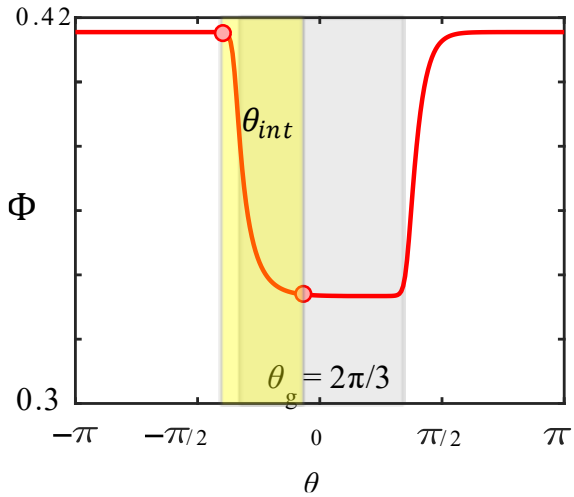

Figure 4-18: example of flow coefficient profile calculated with Hynes Greitzer model; grid 120° with A=4, B=0. In grey the region occupied by the grid, in yellow the region corresponding to θ_{int}

This condition of the relaxation of the hyperbolic tangent to 0.99 can be expressed manipulating equation 4.3. To characterize the interaction angle, we consider the condition.

$$\tanh\left(C\frac{\theta_{int}}{2}\right) \sim 1 \tag{4.5}$$

which results in, using a mathematical property of the hyperbolic tangent:

$$\theta_{int} \sim \frac{2\pi}{C} = \frac{2\pi\lambda}{a\sqrt{\psi_m + \psi_g - R_L}} \tag{4.6}$$

In figure 4-19, the interpretation of the condition is shown. If flow inertia is neglected (in the limit as λ tends to 0), the hyperbolic tangent tends to a square wave, and the interaction region to zero. On the other hand, the higher the inertia, the hyperbolic tangent relaxes more slowly and the interaction region is wider. The definition of the interaction angle θ_{int} implies a separation between a region characterised by interaction (of angular extension θ_{int}) and a region where the drop of the flow coefficient is well established and characterised by the inflow disturbance length scale, identified by θ_g, the grid angular extension. Equation 4.6 allows thus to characterise the interaction length as a function of the grid distortion.

In the following, the relationship between the θ_{int} and the ψ_g will be discussed. This is an important step to build the DCθ_{Avg} scaling which will be presented in the following sub-section. To link a value of θ_{int} to a distortion ψ_g, a parametric study was conducted using Hynes-Greitzer model. A grid of the form given in 4.7 is introduced:

$$\Delta p_{grid} = \frac{A}{2}\{1 + tanh[(\theta_g^2 - \theta^2)S + 1]\} + B \tag{4.7}$$

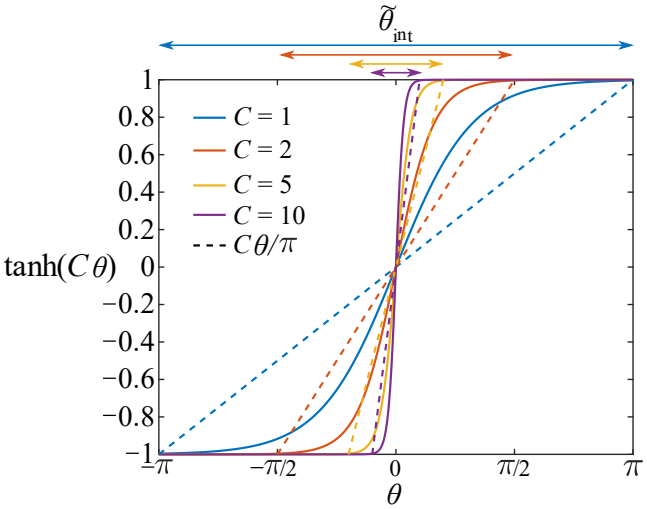

Figure 4-19 interpretation of the interaction angle describing the relaxation of the solution between the distorted and undistorted sectors.

Parameter A defines the amplitude of the perturbation and B its mean value. S is the parameter that controls the sharpness of the hyperbolic tangent (square wave for S=∞). In the present study it was fixed S=8. The compressor characteristic is the parabolic fit shown in figure 4-17. For each extension of the grid θ_g, the total pressure losses of the grid, with different amplitudes A and B, are given as input to the model, and the flow coefficient $\phi(\theta)$ is calculated. An example is shown in figure 4-20 in which B=0 . The dots in figure 4-20 mark the points where the hyperbolic tangent relaxes to a constant value, and identify thus the interaction angle θ_{int}.
The θ_{int} identified in figure 4-20 are shown in figure 4-21 as a function of A and θ_g.

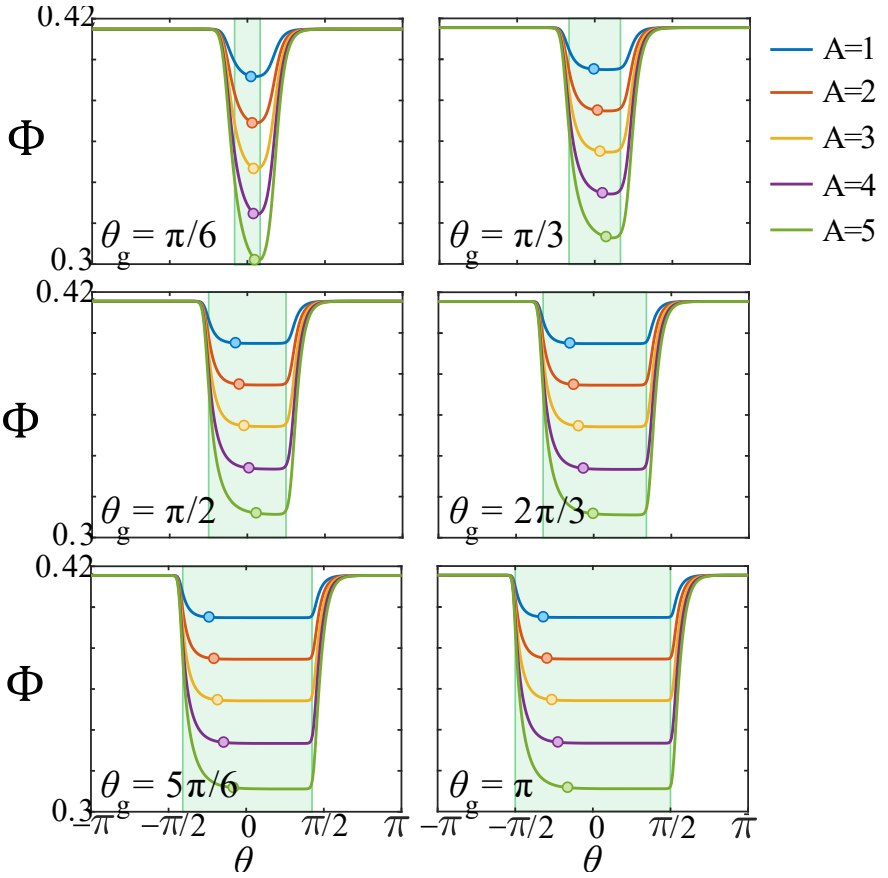

Figure 4-20 : results of Hynes Greitzer model for different grid angular extensions and amplitudes of the total pressure loss amplitude(A). In all the calculations B=0. The marker denotes the limit of the interaction region.

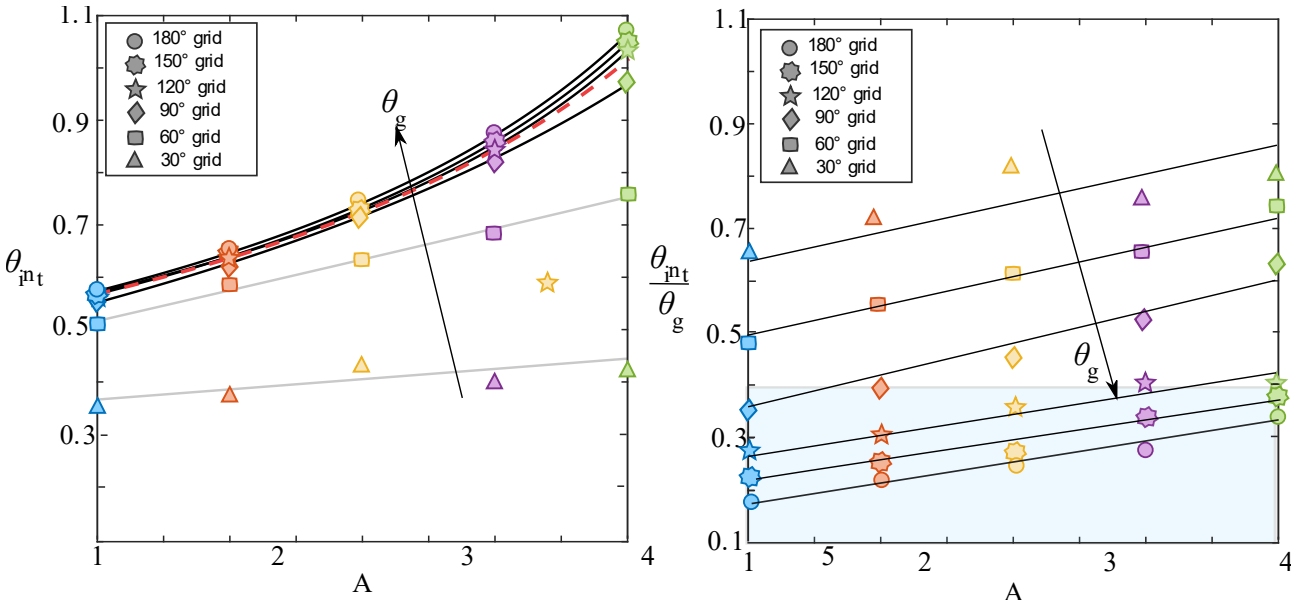

Figure 4-21 : left: correlation of θ_{int} with the amplitude of the grid perturbation; parametric in θ_g. Right: θ_{int}/θ_gas a function of A; parametric in θ_g.

Figure 4.21 (left) shows that all the curves almost collapse to a single one for wide grids (>=90°). These cases for which the curves of different grid extensions collapse, is characterised by a ratio:

$$\frac{\theta_{int}}{\theta_g} \leq 0.4 \tag{4.8}$$

as it is shown in figure 4-21 on the right. For higher ratios θ_{int}/θ_g (figure 4-21 right), thus for narrower grids, the correlation works less well (figure 4-21 left). We thus identify the ratio 0.4 as the limit of the range of the correlation.

Based on the fit in figure 4-21, θ_{int} has been calculated for the grids of this study, using the experimental values of A and B in the fit. It was seen that the value of the θ_{int} is very weakly sensitive to the term $\psi_m + \psi_g - R_L$ and is almost constant and equal to 30° for all the grids tested in this study. Thus the limit $\theta_{int}/\theta_g \leq 0.4$ becomes $\theta_g \geq 75°$. This value of 75° coincides with the boundary of regimes 1 and 2 that is usually called critical angle. The key fact is that this differentiation of the two regimes, now, instead of being linked to a supposed ''critical angle" of 60° or 90°, it is connected and derived from the scale θ_{int}. Some additional words have to be said about this last statement.

When the DC60 or DC90 indexes weight the integral pressure loss of narrow grids (below the critical angle) on a sector corresponding to the critical angle, they reduce the actual distortion to a decreased "equivalent distortion". The hidden physical mechanism is flow inertia (chapter 2) but it is not clear why the effects are captured by considering a critical angle as a reference for all the grids. The θ_{int} has the advantage that intrinsically considers flow inertia, on a physical basis, without the need to introduce a critical angle. If the flow inertia of the compressor is weaker (lower λ), the θ_{int} is automatically lower (equation 4.6) and the correlation will extend possibly to 60° grids, since now $\theta\_int/\theta\_g < 0.4$ can be satisfied with lower θ_g. That comes without the need of specifying a lower critical angle θ_{crit} to make the correlation work; a θ_{crit} which moreover is not known a priori. If the flow inertia on the other hand is bigger, the Hynes Greitzer model will predict higher values for θ_{int} and the scaling will restrict to wider grids automatically, as if the critical angle were higher.

4.3.2 SCALING WITH INDEX $DC\theta_{avg}$

In this paragraph the θ_{int} is used to provide a new scaling for the SM versus a corrected distortion index in the range $\theta_{int}/\theta_g \leq 0.4$. Instead of a critical angle of distortion, the flow physics captured by the model suggests a different relevant length scale. This length scale must take into account both the length scale of the grid θ_g and the interaction length scale θ_{int}. A new scaling is then introduced where the θ_{crit} in Reid is substituted by a θ_{avg} defined as:

$$\theta_{avg} = \frac{\theta_{int} + \theta_g}{2} \tag{4.9}$$

The definition in (4.9) is chosen such as the window in which the total pressure drop is integrated corresponds to an order of magnitude to the plateau of the flow coefficient ϕ itself, accounting at the same time the two scales θ_{int} and θ_g. To better explain it, we make reference to figure 4-22. It is clear that the definition in 4.9 is a good indication (we specify again "as an order of magnitude") of the distorted region where the ϕ is constant. If both the θ_{int} and θ_g have to enter into the definition and they need to provide an order of magnitude estimate of the plateau of ϕ, then the natural definition is (4.9).

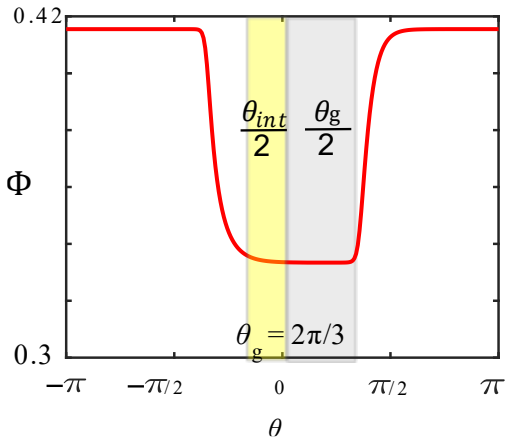

Figure 4-22: interpretation of the definition of the θ_{avg}.

A new index $DC\theta_{Avg}$ can be now introduced:

$$DC\theta_{Avg} = \frac{\Delta p_t^*}{\bar{p_t}} \tag{4.10}$$

It corresponds to the $DC60$, but the critical angle of 60° is replaced by θ_{Avg} (figure 4-23). More precisely, in this case:

$$\Delta p_t^* = \bar{p_t} - p_{crit\_avg}$$

where p_{crit_avg} is now the minimum area averaged total pressure in a window of angular extension θ_{Avg}. $\bar{p_t}$ is, similarly to the definition of DC60, the averaged total pressure calculated over the whole annulus.

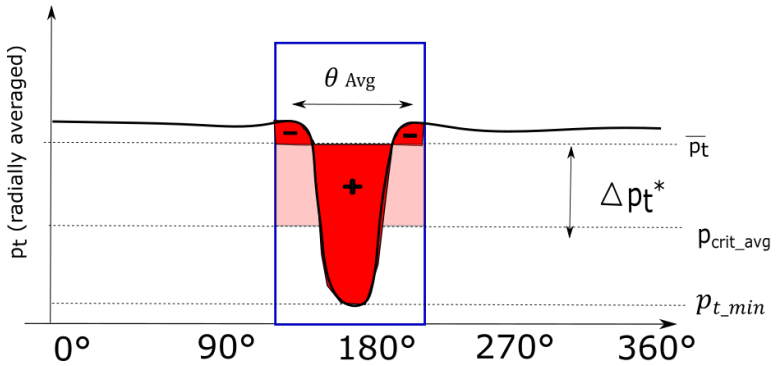

Figure 4-23 : definition of the $DC\theta_{Avg}$ corresponding to the definition in equation 4.10

The stall margin has been correlated with the new index and is shown in figure 4-24. In the figure, the 60° have been shown transparent, since they are not correlated, being outside the limit $\theta_{int}/\theta_g \leq 0.4$. On the other hand, the 90° with porosity 0.1, in the figure, has been highlighted in purple because the scaling does not work for this grid. This grid in fact, is included in a fourth regime where the stall flow rate at stall saturates, and thus the scaling is not adapted.

The correlation works well instead in the second and third regime, with a standard deviation of 0.06. In figure 4-25, the experimental ϕ measured at the rakes for different angular extensions is shown. In the same figure is represented the extension of the interaction angle θ_{int} estimated with the Hynes-Greitzer model. Its value of about 30° is a remarkably good prediction when compared to the experimental data. For grids below 60°, no plateau is present in the values of ϕ and ψ and all the region behind the grid is characterized by the interaction scale θ_{int}. The 60° grids are thus topologically different than wider grids and belong to a different regime (first regime in figure 4-10), dominated by the inertial interaction. The θ_{int} marks the difference between the first regime and the second and third regimes that are responsible for the different sensitivity of the 60° compared to the others in figure 4-12.

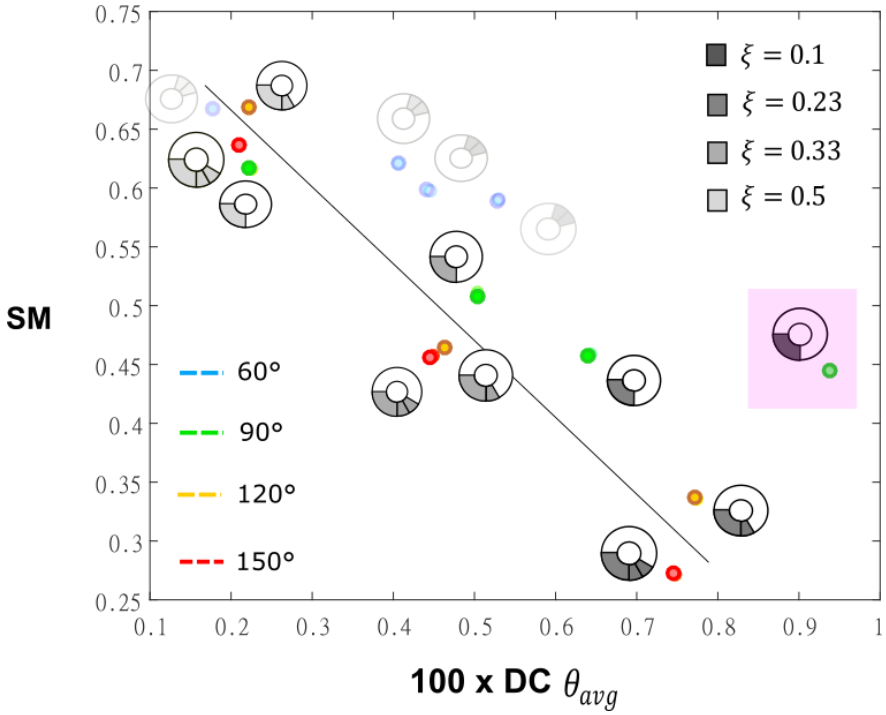

Figure 4-24 : correlation of the stall margin with the distortion index DCθavg ; parametric with angular extension of the grid

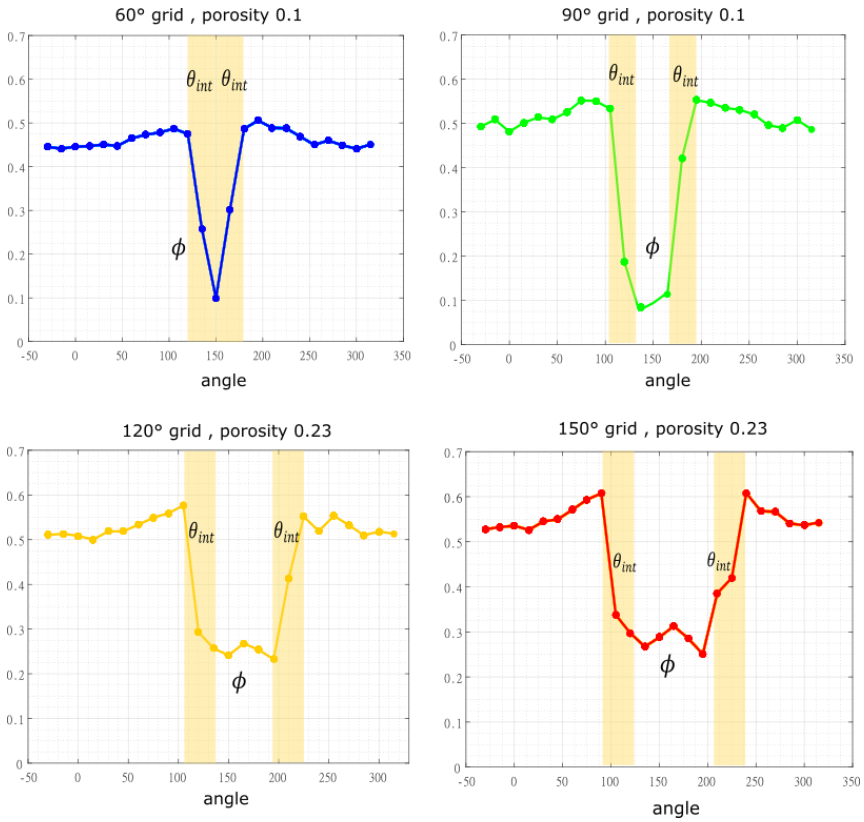

Figure 4-25 experimental ϕ and ψ measured by pressure rakes for some grids; the rectangles in yellow represent the extension of θ_{int} predicted by Hynes Greitzer model.

Once again, a clear advantage of this approach is that the correlation can be built with less experimental data, since it is not necessary to identify a critical angle, which requires a sufficient amount of tests with different angular extensions. The θ_{int} can be identified with the mathematical model, and few experiments can be sufficient to estimate the slope of the line in figure 4-24. In the remainder of the chapter, the

limitations of the index $DC\theta_{avg}$ will be discussed more in detail, especially the breakdown of the scaling in the fourth regime.

4.4 LIMITATIONS OF THE SCALING WITH $DC\ \theta_{avg}$

The scaling presented above presents nevertheless some limitations. On one side, as already discussed, the correlation is limited by the constraint imposed by equation 4.8, which limits the applicability of the correlation for low angular extension of the grids that are part of the regime characterised by complete presence of interaction between distorted and undistorted sectors. Thus the first regime identified in figure 4-10 is not included.

On the other hand, another limit has been anticipated to be the saturation of the stall margin at low porosities in regime four. From figure 4-24, the 90° grid with porosity 0.1, has an increased index of distortion compared to the 90° with porosity 0.23, but has a similar SM. The saturation of the SM is directly linked to the saturation of the stall mass flow rate between porosity 0.23 and 0.1, as it is clear in figure 4-7 and in the characteristic curves in figure 4-9. The 90° at porosity 0.1 has in fact a stalling mass flow rate equal to the 90° with porosity 0.23. A similar effect is evident for the 60° gird of porosity 0.1, whose stall margin is not significantly worse than for the 60° grid with porosity 0.23 (figure 4-4 and appendix A). These effects must be linked in some way to the very low values of porosity 0.1, which are more representative of a solid body than of a porous medium.

Some more investigation on this effect has been achieved using PIV and unsteady pressure probes measurements. The two types of measurements (shown respectively in the sub-paragraphs 4.4.1 and 4.4.2) are consistent with each other and suggest a similar conclusion, namely that the reason for this saturation caused by porosity 0.1 is likely to be a channel blockage. The flow conditions faced by the blades in different parts of the annulus, in fact, vary a lot due to the presence of the grid in the flow, and lead to flow separation, especially at the outlet of the distorted region. Similarly, the flow rate for the 120° grid and 150° grid with porosity 0.23 is particularly low behind the grid and is expected to lead to flow separation. Through the use of PIV data on the 120° grids, we want to show that indeed a separation is encountered and it becomes stronger as the porosity is reduced, until channel blockage is encountered. It will be shown that the trace of such increase of the intensification of the separation is captured also in unsteady probes, in consistency. The presentation of PIV results and unsteady pressure constitutes the remainder of the chapter.

4.4.1 SATURATION OF THE STALL MASS FLOW (PIV FIELDS)

Since the separation regions introduce unsteadiness in the flow, in order to capture the main features of the 100 flow fields of which a PIV acquisition consists of in a concise way, a proper orthogonal decomposition (POD) has been performed on the fields, to extract the most significant modes. With 100 PIV samples measured in unsteady flow, the RMS values of the velocity components have not converged yet. This would be the case for at least 500-1000 recorded images. On the other hand the mean velocity converges fast, after 20-50 images, so that the POD analysis provides a good estimate of the first modes and the energy content. In the following paragraph 4.4.1, the POD modes of 120° grids of different porosities will be compared. In figure 4-26, the POD has been applied to the baseline (the undistorted case) at the last stable point before the onset of rotating stall. This is equivalent to a 120° grid with porosity 1 and represents the starting point of the discussion. Then, the POD modes for the 120° grid with porosities 0.5 , 0.33, 0.23 will be shown to highlight the increase of the separation region.

In figure 4-26, just the first four modes of the POD are shown, namely the most energetic. The fields are calculated at 79% of the blade span and show the relative velocity in the blade channels. The first mode corresponds to the average on the 100 instantaneous flow fields. Higher modes represent deviations from

the mean flow. Thus the scale in the legend of figure 4-26 and following will be different for the first mode than for the others.

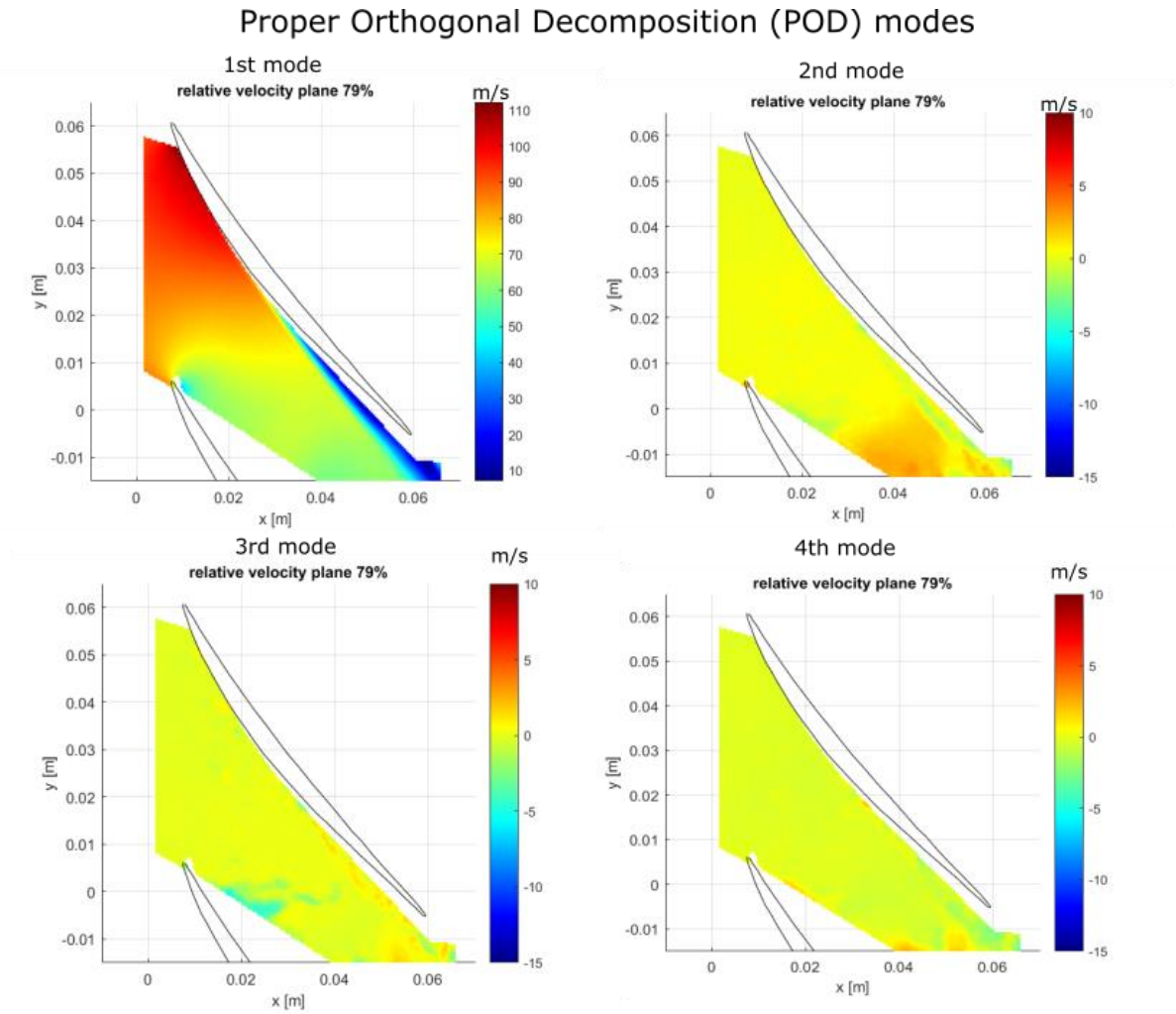

Figure 4-26 first 4 POD modes of the flow field at 79% of the blade height ; baseline without grid

The values of the normalized energy is shown in figure 4-27.

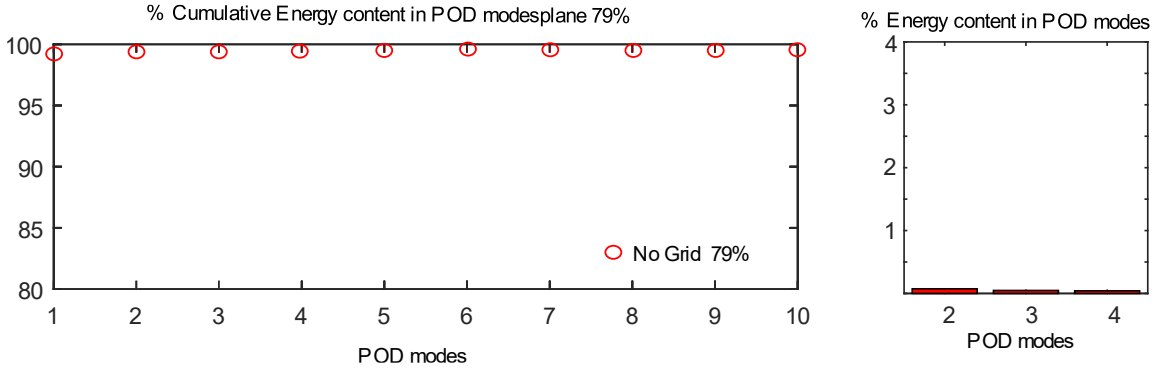

Figure 4-27 cumulative energy in the first 10 POD modes for the baseline with no grid (left) ; energy content of the second, third and fourth mode (right)

The energy distribution shows that the 99% of the energy is contained in the first POD mode, which coincides with the mean flow field. A separation region appears on the suction surface, but the unsteadiness is very low. In fact, the other modes, which represent deviations from the mean flow, do not exhibit particular

patterns, consistently with their negligible energy content. When the 120° grid with porosity 0.5 is analysed, the separation region has increased compared to the baseline (first mode in figure 4-28).

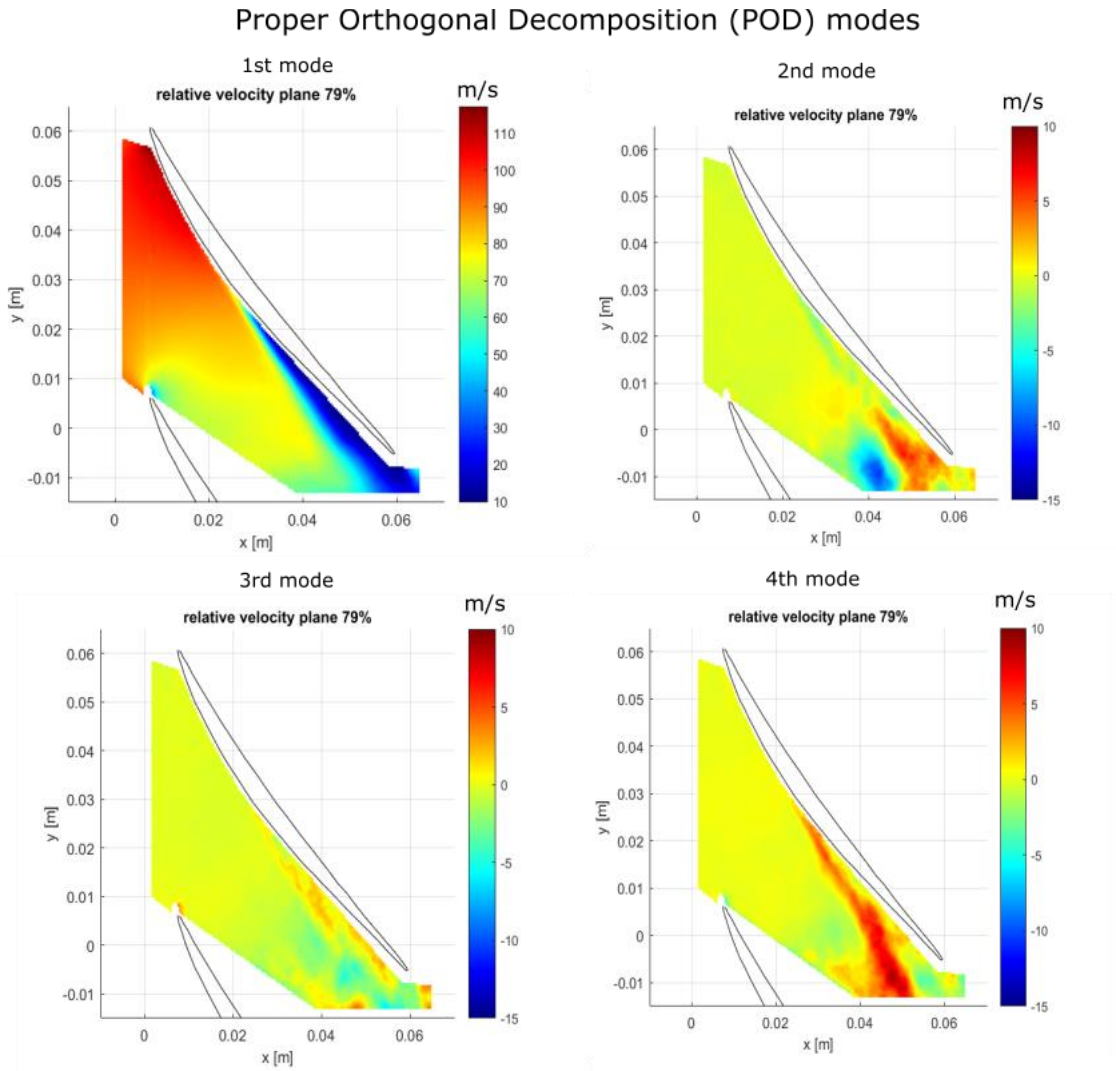

Figure 4-28 first 4 POD modes of the flow field at the exit of the distortion region at 79% of the blade height ; 120° grid with porosity 0.5

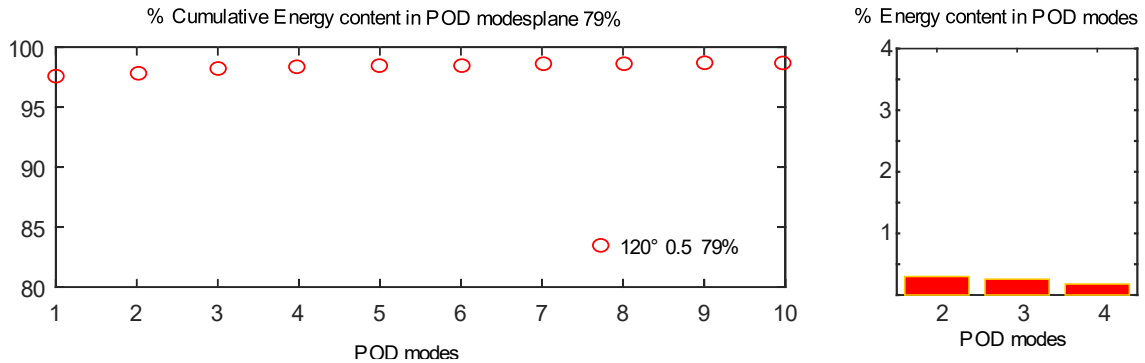

Figure 4-29 cumulative energy in the first 10 POD modes for the 120° grid with porosity 0.5 (left); energy content of the second, third and fourth mode (right)

Higher modes associated to the separation region appear more clearly (figure 4-28), and the energetic content starts spreading on higher modes (figure 4-29). The second and third mode show a similar pattern, with inversed values of velocity. Consistently, their contribution to the energy is similar (figure 4-29 on the left). The second mode shows a region of higher than zero velocity towards the trailing edge at a small

distance from the suction surface (coordinates x=0.05, y=-0.005). In the third mode, this same region has a negative velocity. Further into the channel (coordinates x=0.04, y=-0.01) the second mode exhibits a negative velocity region, which in the third mode is positive. The flow thus oscillates between the two modes, indicating that the unsteadiness of the flow has increased.

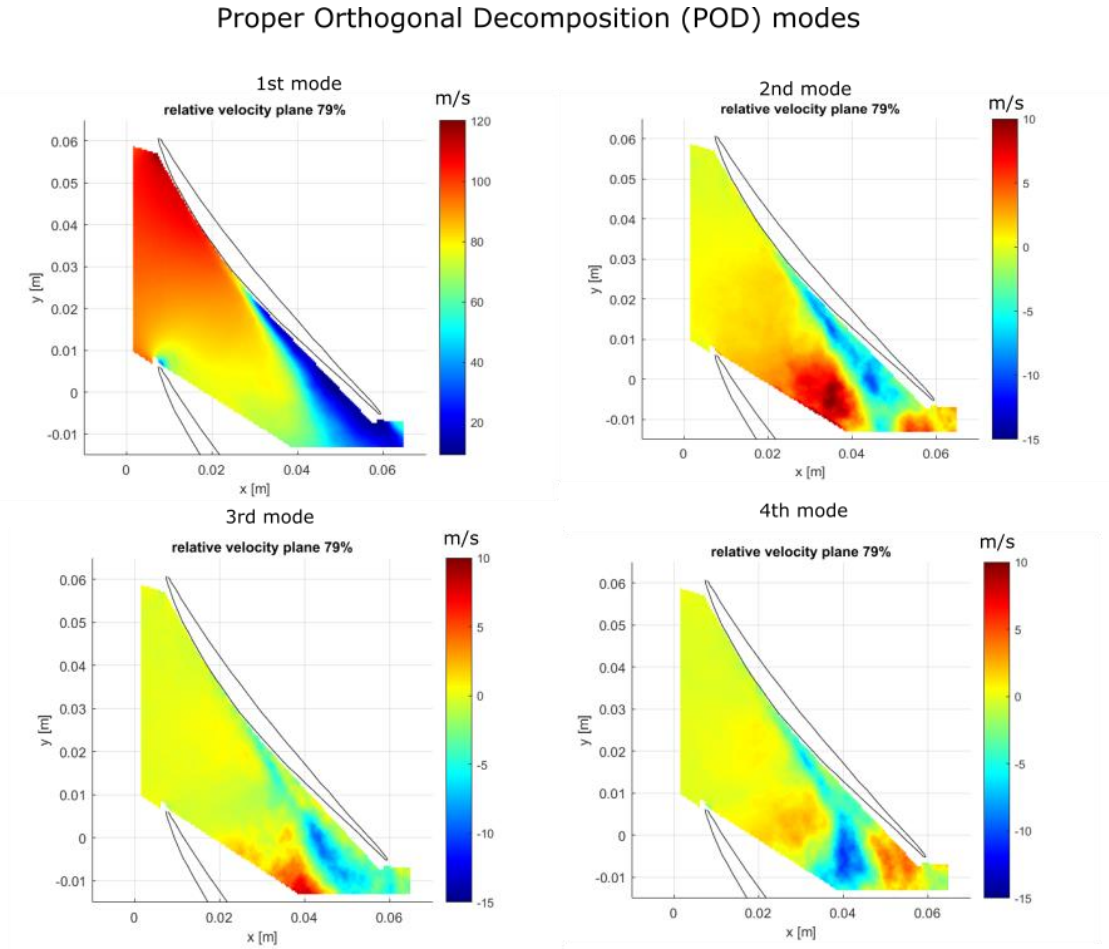

Figure 4-30 first 4 POD modes of the flow field at the exit of the distortion region at 79% of the blade height ; 120° grid with porosity 0.33

The fourth mode is associated to the mixing layer between the separated region and the clean flow and contributes less in terms of energy (figure 4-29 on the left). Even if the unsteadiness of the flow is higher than without the grid, still 97% of the energy is contained in the first mode.

In figure 4-30 are shown the modes for the 120° grid with porosity 0.33. The separation region has further increased in size, and correspondingly, the energy content in the first mode has decreased to 94% (figure 4-31), indicating an increased level of unsteadiness. The two oscillating modes which in figure 4-28 were the second and third more energetic, have now become the third and the fourth and the second more energetic mode has become the one associated to the shear layer.

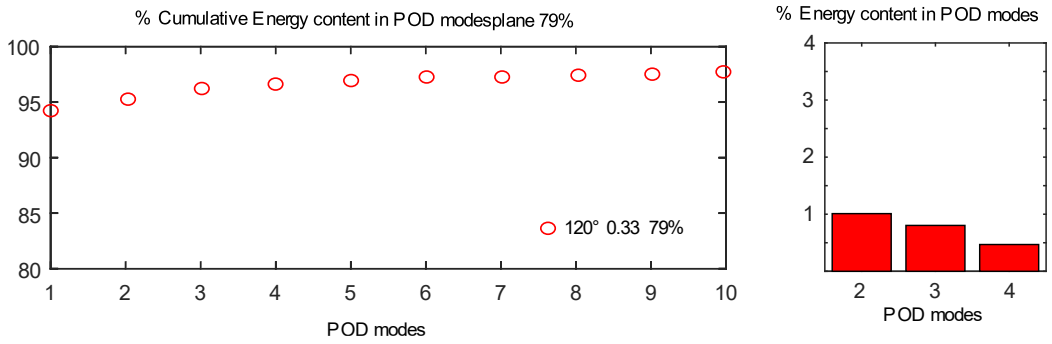

Figure 4-31 cumulative energy in the first 10 POD modes for the 120° grid porosity 0.33 (left) ; energy content of the second, third and fourth mode (right)

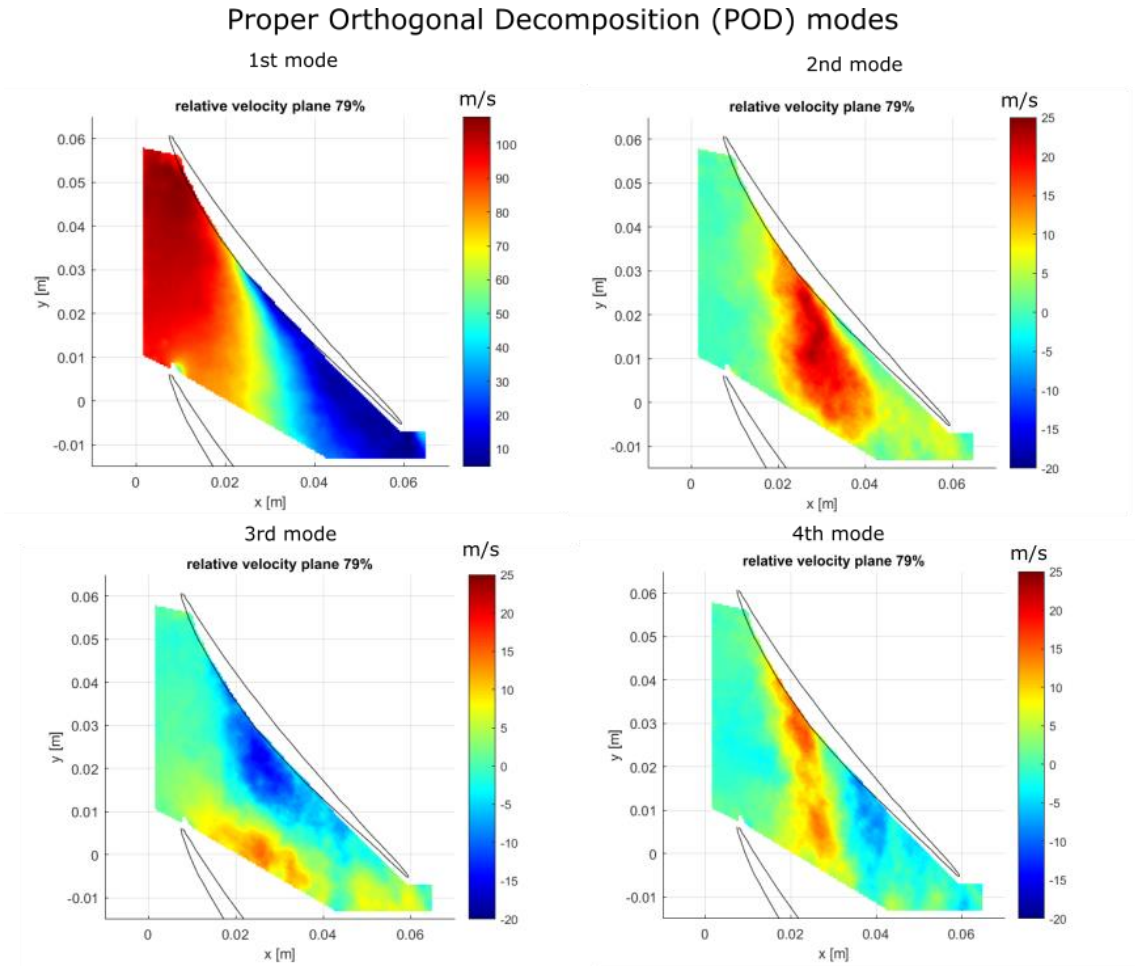

Figure 4-32 first 4 POD modes of the flow field at the exit of the distortion region at 79% of the blade height ; 120° grid with porosity 0.23

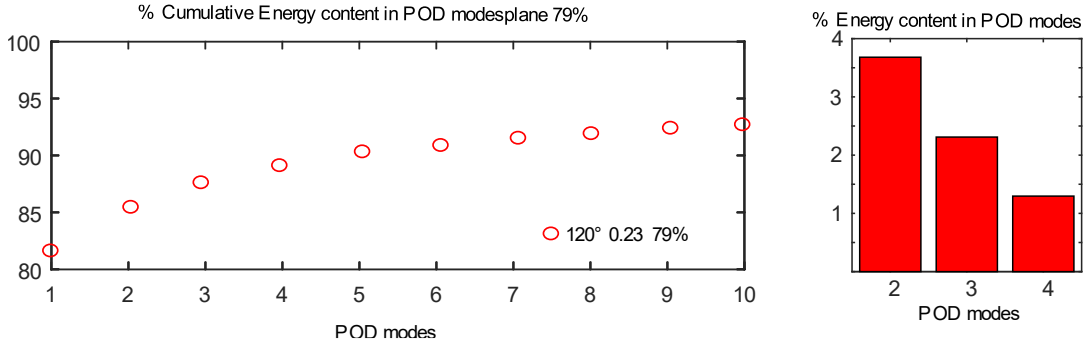

Figure 4-33 cumulative energy in the first 10 POD modes for the 120° grid porosity 0.23 (left) ; energy content of the second, third and fourth mode (right)

When the porosity is further decreased to 0.23, the separation region appears much bigger (figure 4-32). The second mode associated to the shear layer is the most energetic after the first, and its contribution to the energy stands out more clearly (figure 4-33 on the left) than for the case with porosity 0.33 (figure 4-31 on the left). The first mode now contains only 82% of the total energy. The third and fourth modes are still complementary, showing alternating regions of high and low velocity but they are no more confined to the trailing edge region, but have moved forward in the channel, which now appears blocked.
The distribution of the energy in the modes thus changes when porosity is decreased: a mode linked to the shear layer progressively grows in energy and stands out in the energy distribution, indicating that a strong separation of the flow forms in the channel, causing a local blockage. It is expected that similar grids creating channel blockage have a similar energy distribution of the modes, and this is confirmed by the 90° with porosity 0.1 (figure 4-34 and 4-35).

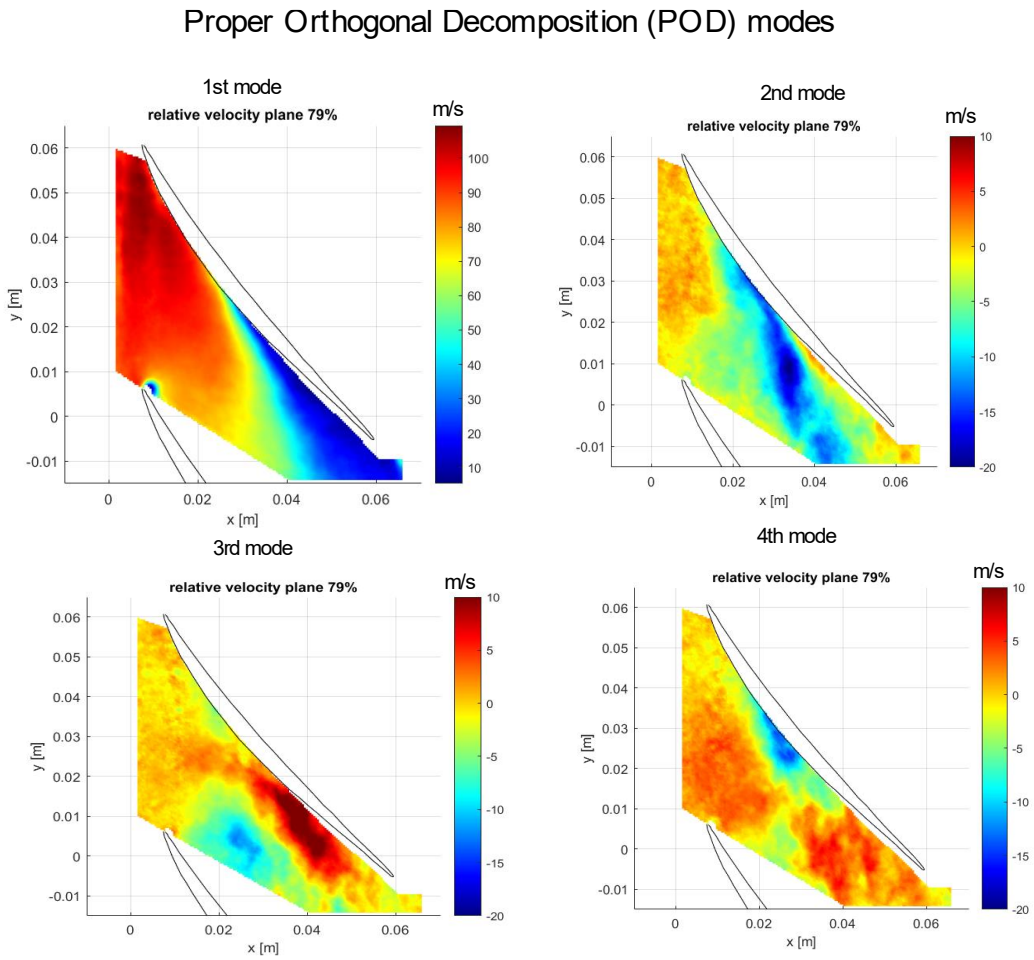

Figure 4-34 : first 4 POD modes of the flow field at the exit of the distortion region at 79% of the blade height ; 90° grid with porosity 0.1

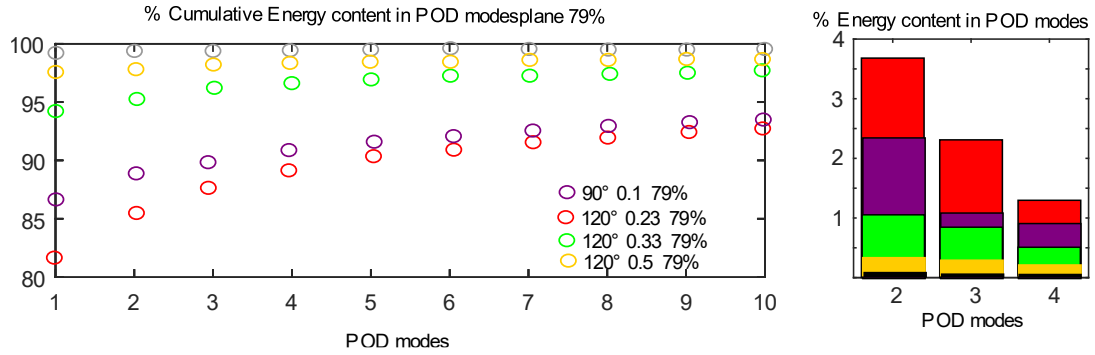

Figure 4-35 cumulative energy in the first 10 POD modes for the 120° grids with porosities 0.23, 0.33, 0.5 and for the 90° grid with porosity 0.1 (left); energy content of the second, third and fourth mode (right)

A full comparison between the previous cases is done in figure 4-35. Grids 90° with porosity 0.1 and 120° with porosity 0.23 show a similar distribution of energy, with the mode linked to the mixing layer being the most energetic, and standing out clearly with respect to the other modes. The similar distribution of energy and the very similar form and energies of the modes suggest that further decreasing the porosity below 0.23 does not contribute significantly to the channel flow. This is true if locally the channel are blocked already at porosity 0.23, and the flow bypasses the occluded channels as schematically represented in figure 4-36; if the channels are bypassed, reducing further the porosity does not change the local flow redistribution and the fact that the channels are bypassed, since blocked.

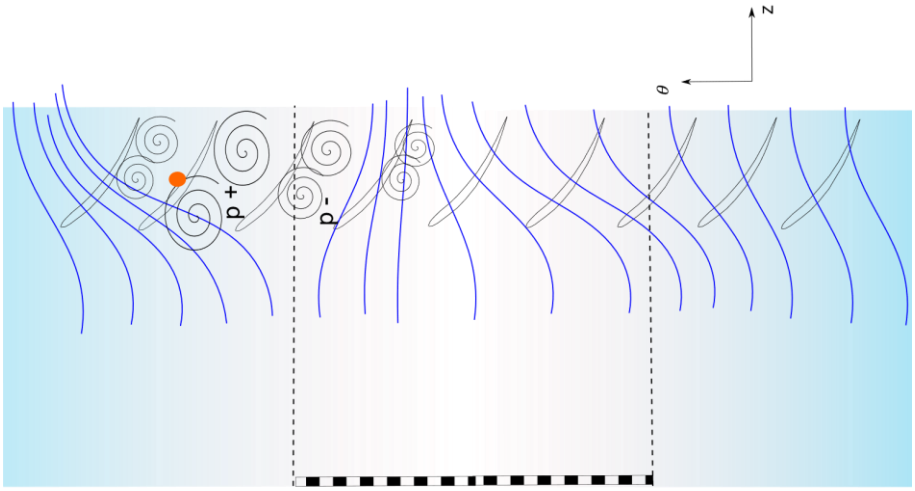

Figure 4-36 : scheme representing flow deviation caused by channel blockage at the exit of the distorted region. The probe indicated in the figure is corresponding to the probe in figure 33

From the point of view of the compressor performance, channel blockage is relevant. In fact, the interaction scale θ_{int} relevant in the scaling, results from the interaction between the compressor (parameter λ , a) in equation 4.6 and the grid (ψ_g). The mechanism of interaction between a grid and the compressor is upstream redistribution, which depends on both compressor and grid parameters and makes the compressor to provide a higher work done on the fluid where the ϕ is lower. In the limit when ϕ is 0 and channels are blocked, the effect of upstream redistribution saturates because ϕ can't be lower and the compressor is not working locally. The interaction between compressor and grid described by θ_{int} is expected thus to be no more valid and the scaling to breakdown. If the porosity of the grid is reduced, the local flow must be topologically similar, determined by the blockage of the channels. If the upstream redistribution is saturated for porosities lower than 0.23, then it is reasonable to expect that the stalling flow rates are similar (as it was observed in figure 4-7 for porosities 0.1 and 0.23). The saturation of the upstream redistribution thus leads to a saturation of the stalling flow rate. In the following paragraph it will be shown that a similar pattern of

growth of the separation is captured in pressure signals, and that a saturation of the upstream redistribution appears as well.

4.4.2 SATURATION OF THE STALL MASS FLOW RATE (PRESSURE SENSORS)

The signs of a flow separation are also obvious from the casing unsteady pressure signals acquired during the experiments. Figure 4-37 presents unsteady casing pressure signals acquired in different parts of the annulus at the last stable point. A region of strong perturbation of pressure appears at the outlet of the distorted region, between 171° and 261°, thus where blade exit the distorted region. The position at 171° is approximately the position where PIV fields in figure 4-34 are extracted. These strong pressure oscillations reflect the existence of a flow separation that is thus consistent with PIV.

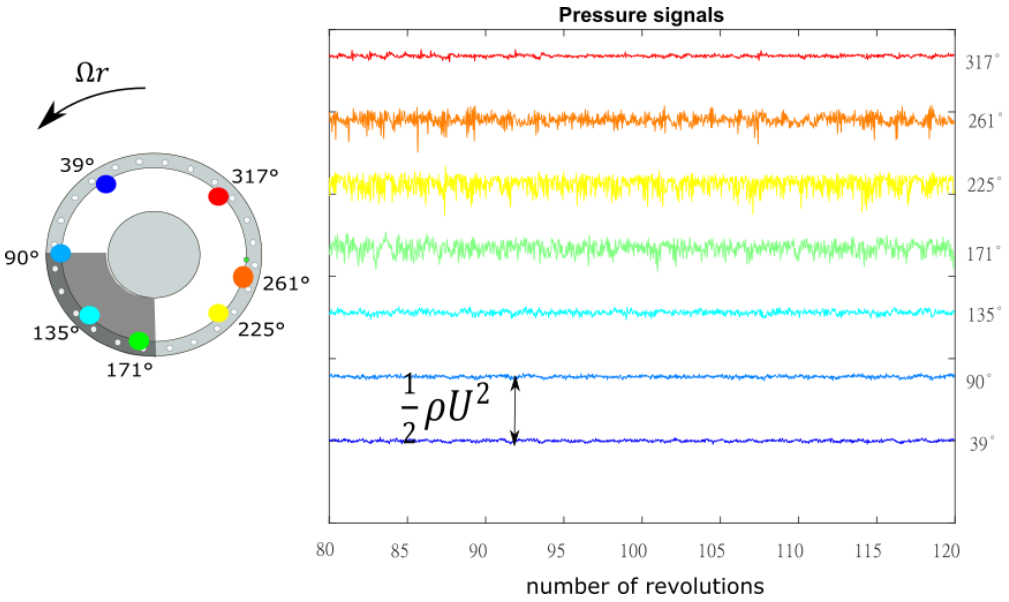

Figure 4-37:unsteady casing pressure signals acquired during the beginning of the transient towards rotating stall; grid 90° porosity 0.1; the angles are numbered in the sense of rotation of the compressor

To extract more information from the signals, a Fourier analysis has been performed to identify the pressure amplitude and energy (square of the pressure amplitude) of the various frequencies in the Fourier spectrum. The signal of figure 4-37 on which the analysis is performed is the orange at 261°, sufficiently far from the interaction region at 171° but not too far to miss the oscillations due to flow separation. Its position is also shown schematically in figure 4-36. The analysis has been performed with the same probe in the same position but with different porosities of the 90° grid, to see the differences in the energies. In figure 4-38, the cumulative energy of the Fourier spectrum is represented for the signal at 261° as a function of the frequency for all the porosities of the 90° grid. To the cumulative energy has been subtracted the energy of the average (frequency 0) to compare just the energy associated to oscillatory phenomena. This is why in figure 4-38 the cumulative energy starts from 0. The values of energy have been then scaled to a reference quantity to allow the comparison of different signals; this reference quantity is $(1/2\,\rho U^2)^2 \Delta f$, where $(1/2\,\rho U^2)^2$ represents the energy density of the characteristic reference pressure $1/2\,\rho U^2$ and Δf represents the frequency interval of the Fourier transform. Thus, the quantity $(1/2\,\rho U^2)^2 \Delta f$ represents the energy in a signal of constant amplitude $1/2\,\rho U^2$. Figure 4-38 represents thus how much energy the higher and higher Fourier harmonics add to each signal. For porosities >=0.23, the first increase in the cumulative energy from 0, corresponds to the blade passing frequency (BPF). After, the energy increases further at the BPF harmonics. Starting from porosity 0.33, some energy is present at frequencies lower than the BPF. This energy is thus not linked to useful work and reflect the presence of the separation which grows in size as the energy between $3f_{rot}$ and the BPF grows. This is consistent with the tendencies described using the POD. The

interpretation of this energy as associated to a separation region is consistent also with the broad range of frequencies on which the energy is distributed (3$f_{rot}$to BPF). In fact, the different phases of growth, separation and shedding of vortexes from the blades are expected to introduce different frequencies in the flow.

The general tendency is a growth of the energy in the signal when porosity is reduced, but the growth is slower and slower until a saturation is encountered between porosity 0.23 and 0.1. This saturation is consistent with the argument of a channel blockage, because the flow being blocked below porosity 0.23, the energy should be locally the same.

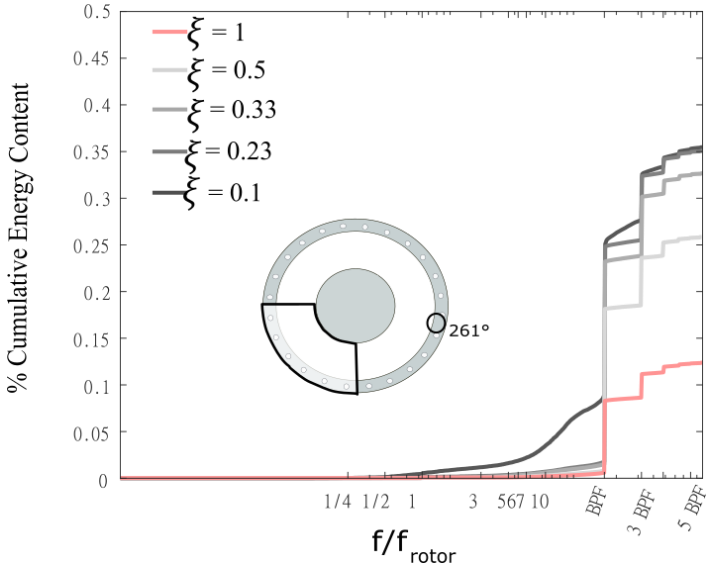

Figure 4-38: cumulative energy in the Fourier spectrum in the signal at 261° for grids of 90° and different porosities

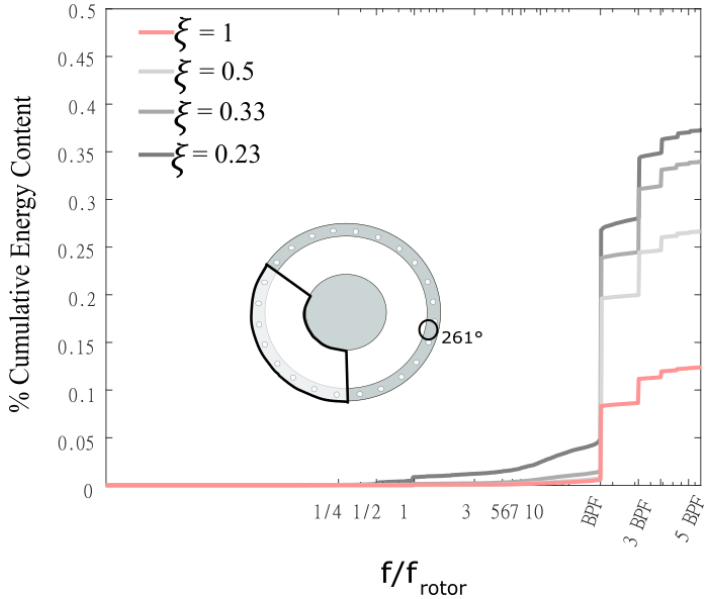

Figure 4-39 cumulative energy in the Fourier spectrum in the signal at 261° for grids of 120° and different porosities

A similar tendency of growth of the energy with a decrease of the porosity is encountered in signals acquired with the 120° grids of different porosities (figure 4-39). The probe is always the same in the same position. In this case however, no saturation is encountered, indicating that no blockage is reached before the porosity 0.23. These results reinforce thus the argument that a channel blockage saturates locally the flow distribution upstream of the compressor, and this is very likely the reason why the stalling mass flow rate saturates and the scaling breaks down.

To conclude, the scaling based on the $DC\theta_{Avg}$ performs well for cases where a plateau in the flow coefficient is observed and for which the scales θ_{int} and θ_g can be distinguished, thus in the regimes 2 and 3. These conditions are not met in two situations in the present results:

- When the region behind the grid is fully dominated by the interaction scale θ_{int} (60° grids) and no plateau in the flow coefficient is reached.
- When flow separation in blade channels causes an upstream redistribution which is determined by channel blockage, such that the stall mass flow rate saturates.

4.5 CONCLUSIONS

In this chapter, the compressor performance in the different grid distorted conditions has been compared in terms of stall margin. A first comparison of the stall margin for different grid porosities and angular extensions has allowed to identify four different flow regimes which are connected to the flow redistribution between the grid and the compressor. Two of these regimes are encountered at low porosities and are not seen in classical distortion studies (Reid, 1969) which concentrate on highly porous grids. The stall margins have been then compared using different distortion indexes as DC60 to provide a correlation. Some weaknesses of the indexes have been discussed, and a new index $DC\theta_{avg}$ based on a characteristic interaction angle θ_{int} is proposed to correlate data. θ_{int} flow scale, intrinsically takes into account the flow inertia and distinguishes two of the four regimes characterised by a different sensitivity to distortion. This is a better identification of the two regimes compared to the critical angle, which has to be identified by performing time consuming experiments. The θ_{int} can be estimated using mathematical models (Hynes Greitzer) and allows to limit the number of experiments to perform in order to build the scaling for a compressor. When the grid extension is narrower than twice θ_{int}, the flow is fully dominated by the inertial interaction and no plateau of ϕ is reached. On the other hand, for wider grids, a plateau is reached, and the stall margin correlates well with the index $DC\theta_{avg}$. For narrower grids on the other hand, a different scaling must be identified. Thus the first regime identified in the beginning of the chapter is not included in the scaling. Another limit of the correlations has been discussed: when porosity is sufficiently low, the stalling mass flow rate saturates (fourth regime) and the scaling is broken. An explanation for this is suggested by PIV and unsteady pressure measurements. PIV identifies a strong separation of the flow at the outlet of the distortion region for low porosities, causing channel blockage. The blockage of channels, locally breaks the coupling between the compressor and the grid and makes the stalling point sensitive only to the mass flow.

5 TRANSITION TO ROTATING STALL

In the previous chapter, the stall margins for the different grids have been compared, especially scaling them with a distortion index $DC\ \theta_{avg}$. This scaling indicates that a key factor in determining the stall margin is the interaction between the undistorted and distorted region, characterised by the length scale θ_{int}. The 60° grids have been seen to be characterised by a flow dominated by the interaction scale θ_{int}, differently from wider grids when the interaction controls just a portion of the distorted region. This is a main cause of the different behaviours of the identified regimes. On the previous chapter however, no reference has been made to the actual mechanism that determines stall, namely the growth of an instability. This mechanism, introduced in chapter 2, is known to be of modal or spike type.
In the present chapter, unsteady pressure signals acquired during the transient towards rotating stall are investigated to classify the different grids on the basis of the stall mechanism. This classification will enrich the description of the four regimes identified in the previous chapter, completing the picture. In paragraph 5.1, two examples of unsteady pressure signals are first shown; they are representative of two different regimes. They are used in the paragraph to show how Fourier analysis has been used to capture the presence of modes before the stall onset, and the characteristic frequency of the rotating stall cell. Based on these two features, it is possible in fact to classify the grids into four stalling regimes, consistently with the four flow regimes identified in the previous chapter. In paragraph 5.2, additional stall features are identified with the help of an analysis tool based on cross correlation between the pressure signals.

5.1 STALL REGIMES

To investigate the nature of the instability onset, the unsteady probes on the casing have been used to acquire unsteady pressure signals during the transient towards rotating stall. The throttling valve was closed progressively, starting from the last stable point to induce rotating stall. During the transient, the 8 probes placed at different azimuthal positions were acquiring pressure signals as the ones represented in figure 5-1.

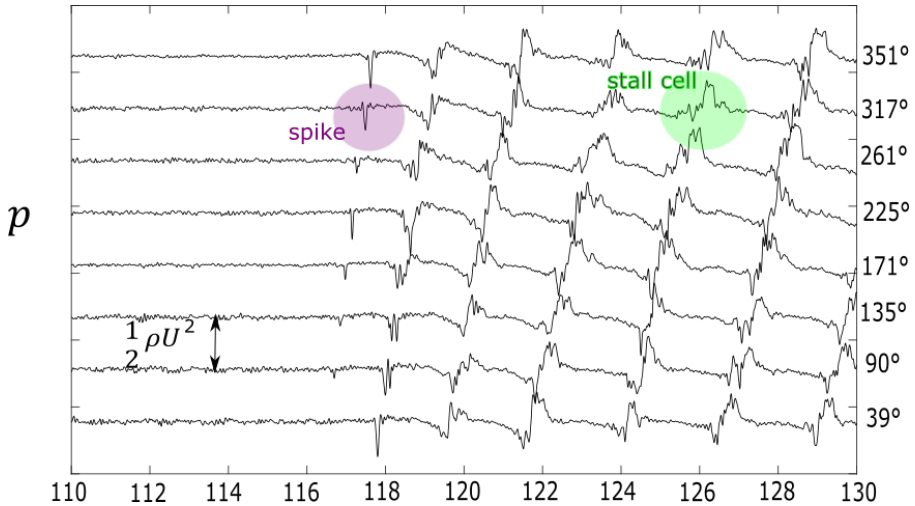

Figure 5-1 : example of transition to rotating stall in undistorted conditions ; 8 pressure probes are placed in different azimuthal positions

These signals capture the onset of the instability (spike in figure 5-1) and the subsequent development of the transient until rotating stall is developed and rotating stall cells (figure 5-1) propagate in the annulus. It has been observed in previous works (Margalida et al., 2020), (Vegliò, 2015) that the perturbation arising in CME2 is always of spike type, as it is shown in figure 5-1. The same throttling procedure to induce the transient was performed with all the grids that have been tested in this work and it was seen that different stall patterns arise from different grids. As an example, in the following, two cases corresponding to different grids (120° porosities 0.23 and 0.5) are detailed (figures 5-2 and 5-3). PIV data are available for the two grids. These two examples are used to show how useful information regarding the stall mechanism has been extracted from the signals.

Comparing figures 5-1, 5-2, 5-3, the transient to stall presents different features depending on the inlet distortion imposed. In particular, from inspection of the pressure signals, two features appear in the signals with the 0.23 porosity grid (figure 5-2) before the arise of the instability.

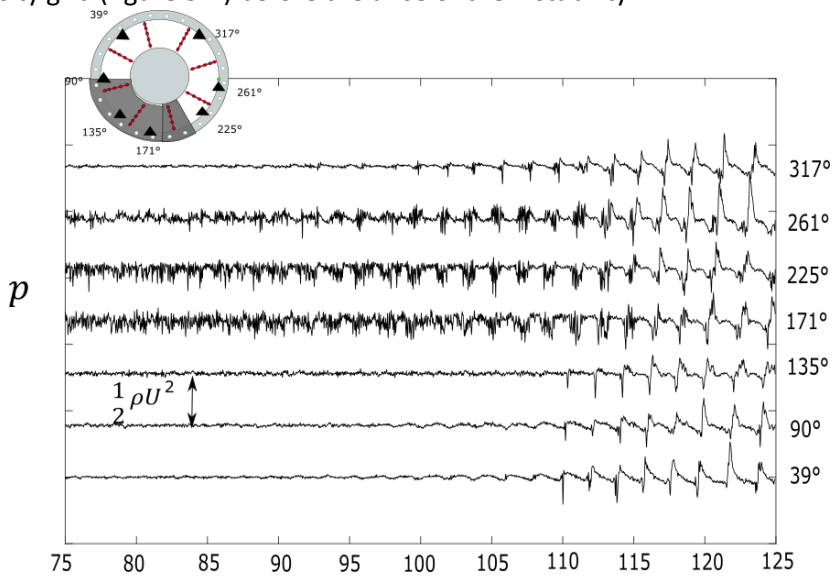

Figure 5-2 : example of transition to rotating stall with 120° grid porosity 0.23; 8 pressure probes are placed in different azimuthal positions at mid chord of the rotor

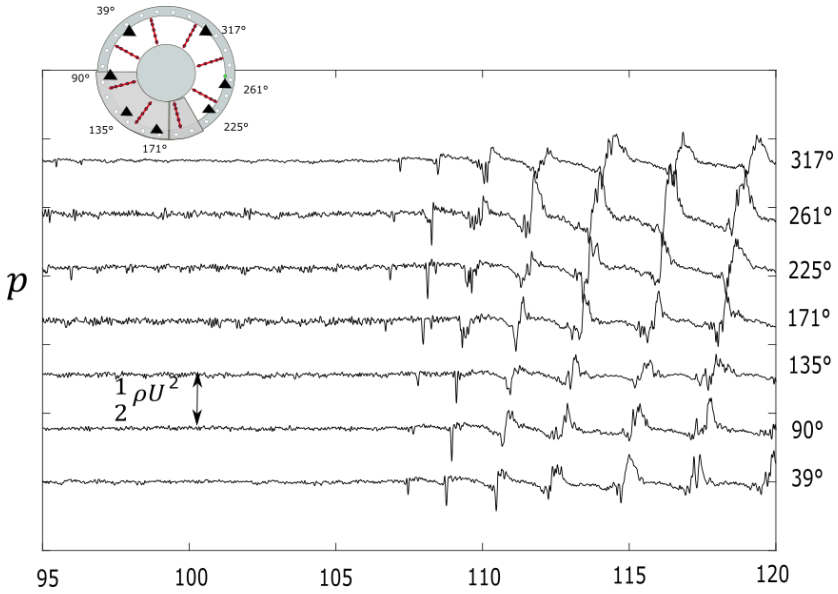

Figure 5-3 example of transition to rotating stall with 120° grid porosity 0.5; 8 pressure probes are placed in different azimuthal positions at mid chord of the rotor

First of all, some strong pressure oscillations are present at the outlet of the distortion region (171°-261°). A similar phenomenon, but with a lower amplitude is observed in the 0.5 porosity grid (figure 5-3). As it was

already mentioned in the previous chapter 4, the strong oscillations between 171° and 261° are very likely related to the secondary perturbations in the blade channels due to vortex shedding in the separation region, since they appear at the exit of the distortion region and are stronger for the porosity 0.23 than for 0.5, consistently with the energy distribution in POD modes of the PIV fields.
The second feature is the presence of some modal oscillations in the signals at 39° and 90° before the arise of rotating stall. The presence of modes is not so surprising, since the grid is forcing a pressure non uniformity in the system.
For a first characterisation of the two signals, a Fourier analysis has been performed before the arise of rotating stall (0-100 revolutions) and after the rotating stall has established (125-266 revolutions).

5.1.1 BEFORE THE ONSET OF ROTATING STALL

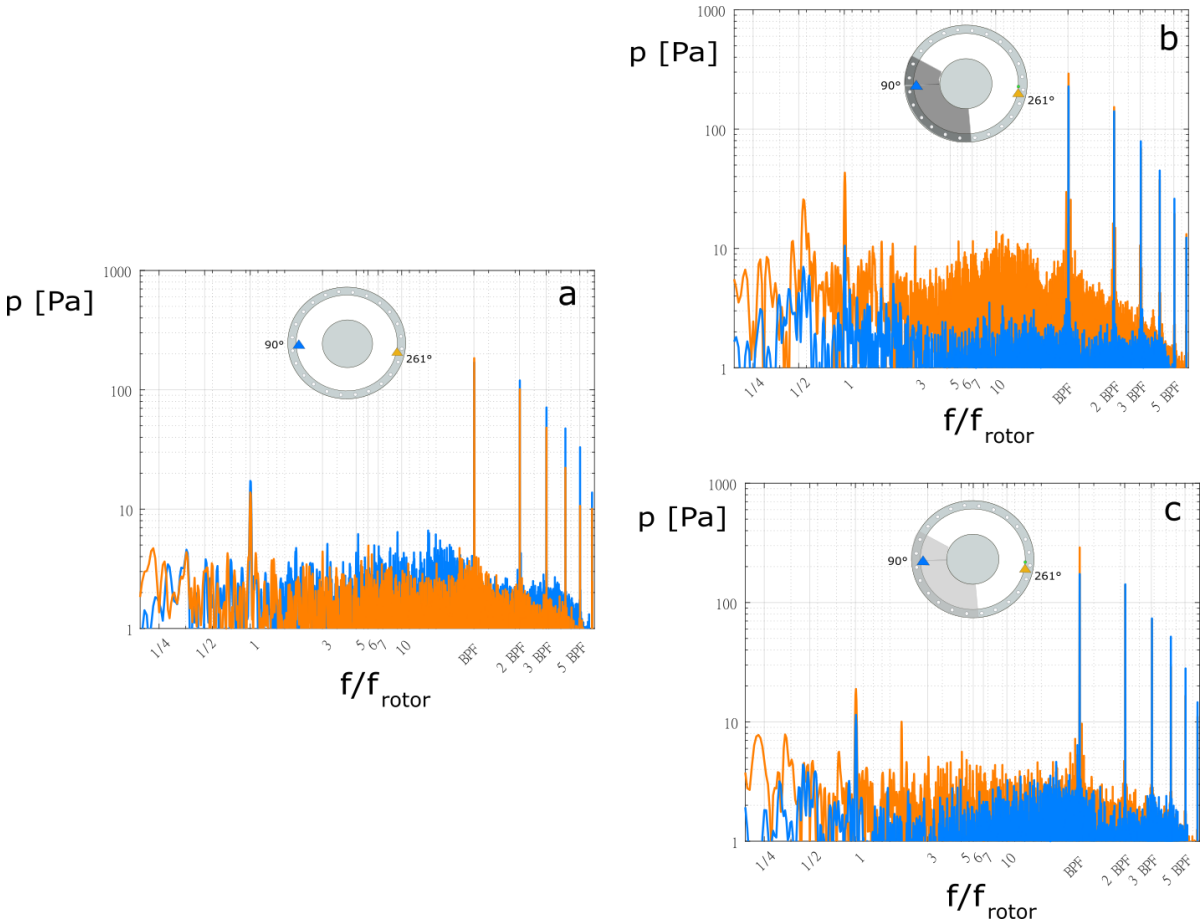

Figure 5-4. Fourier spectra before the onset of rotating stall. 4a): Fourier spectrum of the pressure signals in figure 5-1 (no grid); 4b) Fourier spectrum of the pressure signals in figure 5-2 (grid 120° porosity 0.23); 4c) Fourier spectrum of the pressure signals in figure 5-3 (120° grid porosity 0.5). f_{rot} is the rotor frequancy (53.3 Hz)

In figure 5-4, the spectra of the baseline (a), of the 120° with porosity 0.23 (b) and porosity 0.5 (c) are compared. They contain information before the onset of stall (0-100 revolutions). For the cases with the grid, the intensity of the noise for signals between 171° and 261° is higher than for the other signals, and this is linked to the secondary perturbation identified in PIV fields. Fourier spectra also show the existence of a peak in frequency approximately at $f_{rotor}/2$ (figure 5-4b, 5-4c) before the onset of rotating stall. This suggests on the other hand a mode of the system, also because this frequency is present in all the signals at different azimuthal positions. Both in the frequencies in the range of $f_{rotor}/2$ and the general increase in intensity in the full frequency range are not present in the signals without the grid (figure 5-4a). For the grid with porosity 0.5 (figure 5-4c), signals don't show a substantial increase of the intensity in the positions 171°-261°, since

unsteadiness of separation is reduced, but still show low frequencies around $f_{rotor}/2$, indicating that a mode is present. The mode however has a reduced amplitude and is not clearly visible in the time signals in figure 5-3.

5.1.2 AFTER THE ONSET OF ROTATING STALL

After the rotating stall development, other features appear. The spectra are presented in figure 5-5 for the baseline (a), the 120° with porosity 0.23 (b) and porosity 0.5 (c). It can be seen that the main low frequency peak corresponding to the rotation frequency of stall cells is different with the grid or without it (figure 5-5a and 5-5b). To ease the comparison, a dashed line has been traced corresponding to $f_{rotor}/2$ in the x-axis. The presence of the grid thus modifies the propagating speed of rotating stall cells when rotating stall is established. For the 120° grid with porosity 0.23 the first low frequency peak has a relative frequency (0.488) higher than the frequency without grid (0.407). On the other hand, for the 120° grid with porosity 0.5, the first low frequency peak has a relative frequency (0.415) slightly different from the frequency without grid, indicating a lower influence of the grid on the propagation of stall cells.

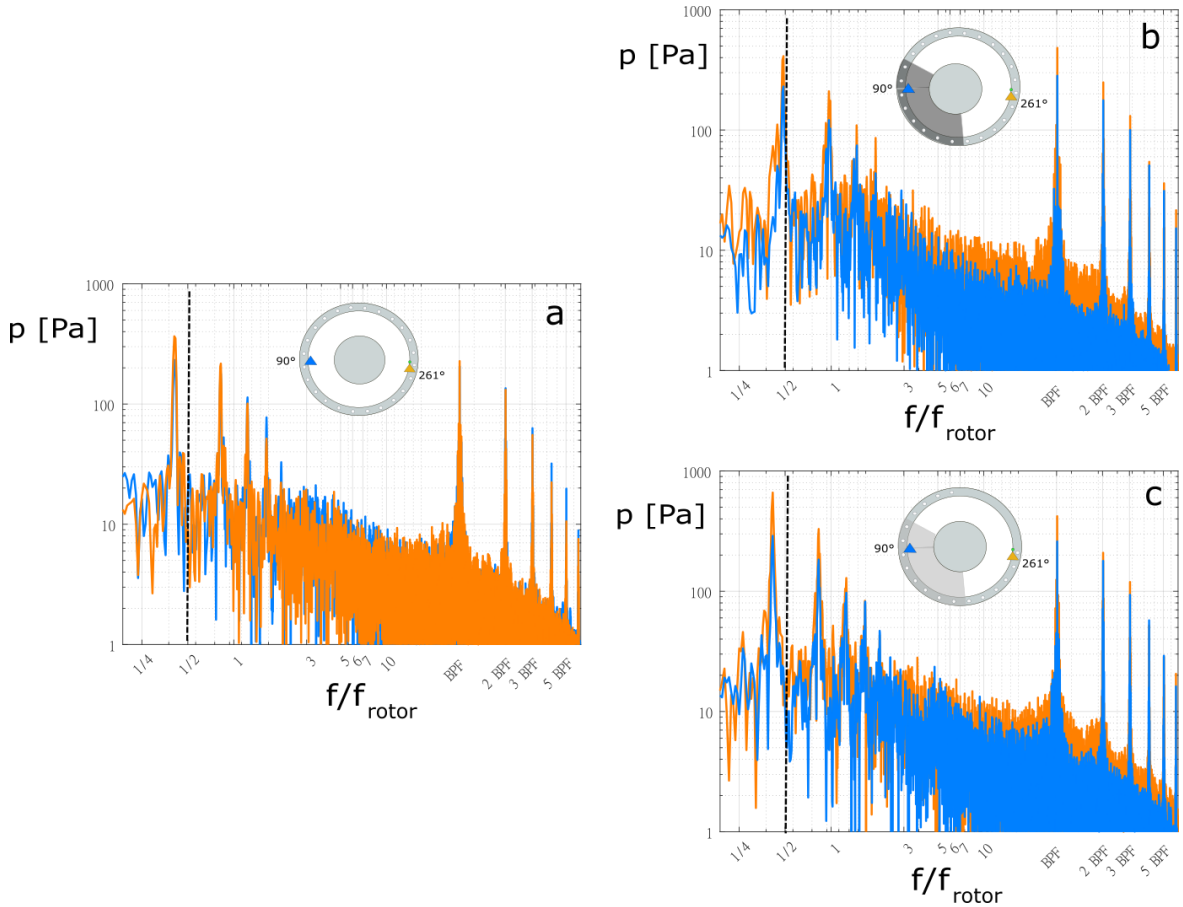

Figure 5-5 Fourier spectra after the onset of rotating stall. 4a): Fourier spectrum of the pressure signals in figure 5-1 (no grid); 4b) Fourier spectrum of the pressure signals in figure 5-2 (grid 120° porosity 0.23); 4c) Fourier spectrum of the pressure signals in figure 5-3 (grid 120° porosity 0.23);. f_{rot} is the rotor frequancy (53.3 Hz)

To summarize, the grid with porosity 0.23 exhibits a clear mode before the onset of rotating stall, also visible inspecting the signals. After rotating stall has established, the stall cell frequency is higher than without the grid. For the more porous grid, a mode is still captured before stall, even if less evident in the signal, and after rotating stall has established, the speed of rotating stall cells is almost the same as in the undistorted case. It is clear thus that different intensities of distortions have different influence on the onset of modes and on

the final state when rotating stall has established. The results suggest that a stronger distortion leads to modal stall. This will be confirmed in the following paragraph: the same Fourier analysis to identify modes prior to stall and the rotating stall cell frequency has been performed on the signals acquired during tests with the other grids and the results are summarized, for all the cases at once.

5.1.3 SYNTHESIS: GENERAL PICTURE

The same analysis of the Fourier spectra has been performed for all the grids, before and after the arise of rotating stall. In figure 5-6 the low peak frequencies captured in the part of the signal before and after the arise of rotating stall are represented as a function of the distortion index.

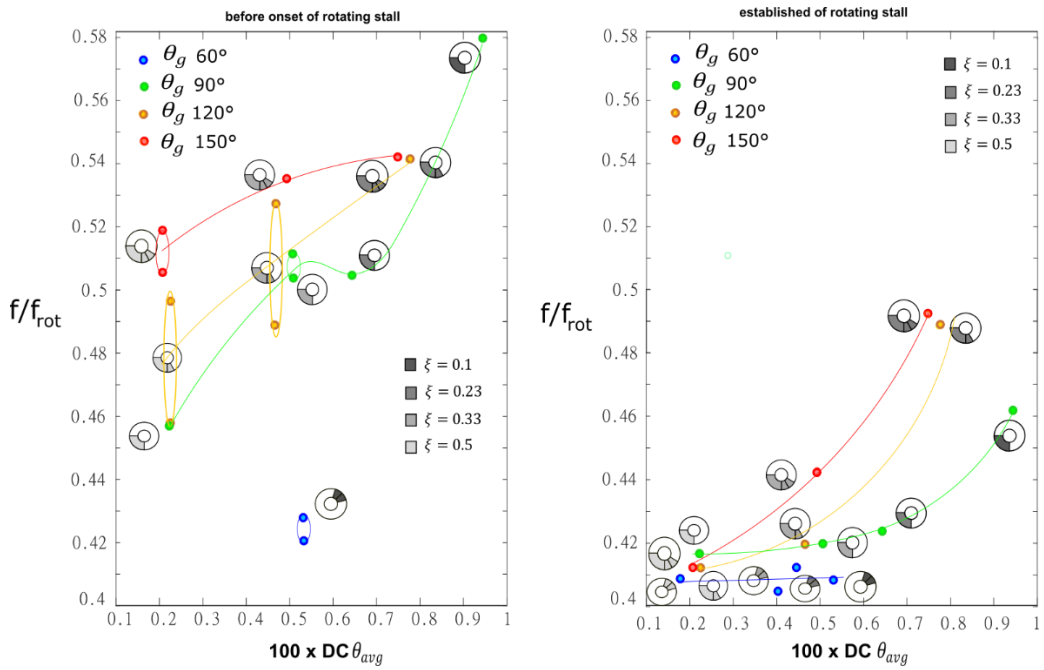

Figure 5-6: on the left : low frequency in the Fourier spectrum before the onset of rotating stall; on the right: low frequency in the Fourier spectrum after the onset of rotating stal. f_{rot} is the rotor frequancy (53.3 Hz)

A clear difference appears between grids below 60° and the rest. Below 60°, grids don't substantially alter the low frequency peak in developed rotating stall (aka the rotating cell speed) with respect to the baseline case no matter the amount of distortion; also, no low frequencies appear before rotating stall, except for the 60° with porosity 0.1. The amplitude associated to the frequency in this last case is however reduced. Above grid angles of 90°, for the stronger distortions, modes are forced in the signal before the stall onset and influence the final rotating stall frequency. The more porous grids (0.5) of extension from 90° to 150° show an in between behaviour: some modes appear before rotating stall, but the final stall cell frequency is close to the frequency for 60° grids and the non-distorted case, as it was seen just in the above discussion for the 120° grid with porosity 0.5.
We can thus identify three cases:

1. $\theta_g < 2\theta_{int}$ =60° : no modes before stall and final cell speed as in undistorted case
2. $\theta_g > 2\theta_{int}$ =60° high porosity: modes before stall and final cell speed almost as in undistorted case
3. $\theta_g > 2\theta_{int}$ =60°low porosity : modes before stall and final cell speed higher than in undistorted case

In the following, figure 5-7, some pressure signals corresponding to these cases are shown. For the grid of 60°, in the signals, the first spike is clearly recognisable (5-7d), and the stall transient looks very similar to the one without grid.

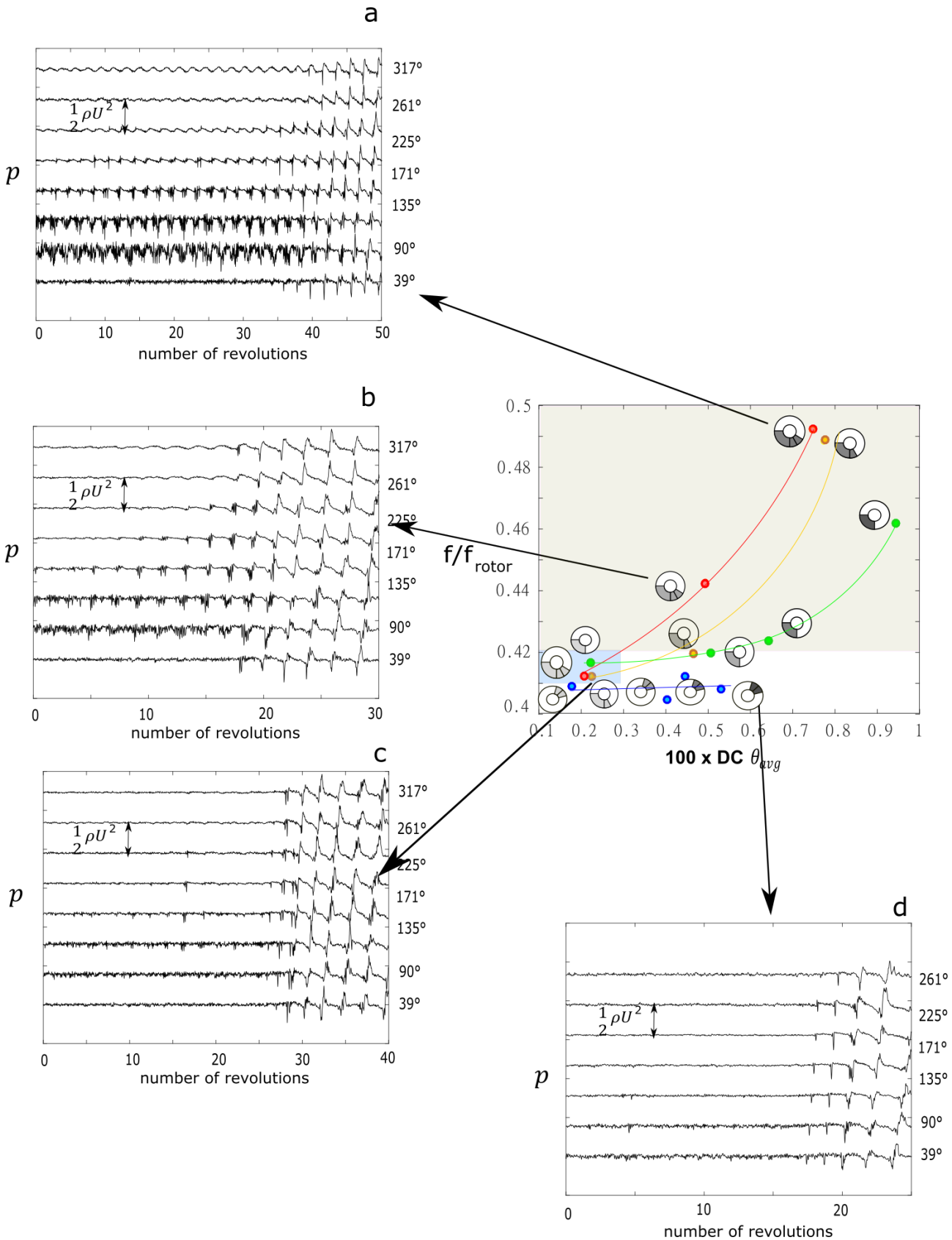

Figure 5-7: unsteady signals during transition to stall. 7a) 150° grid porosity 0.23; 7b) 150° grid porosity 0.33; 7c) 120° grid porosity 0.5; 7d) 60° grid porosity 0.1

This suggests that the stall mechanism for the first case is of spike type. However, in signals for grids above 60°, modes of increasing amplitudes at the moment of the arise of the instability are present. For example,

for the grid 150° with porosity 0.33 (b), modes are visible and no clear spike is clearly recognisable as it is for the 120° grid with porosity 0.5 (c). In the case of the grid 150° with porosity 0.23 (a), the modes are clearly identified and a modal stall is recognisable. On the other hand, there is no clear presence of a spike.
Since the general pattern appearing reminds of a competition between spike and modal stall, in order to better identify the competition, Lin's model (Lin et al., 2017), an extension of Hynes Greitzer model (Hynes et al., 1987) capable of modelling modal stall has been implemented and run. The model can be particularly useful in the present case, as it is able to predict modal perturbations but not spike perturbations, thus discrepancies between the model and the experimental results can be interpreted as a modal or a spike type stall prevailing over the other. Lin's model is a stability approach based on the original Hynes Greitzer model. It calculates the stability of the basic flow. The first step was to calculate this one with the Hynes Greitzer model approach. The input to the Hynes Greitzer model are the fitted characteristic curve of the compressor, and the pressure drop of the grids. The compressor characteristic curve of CME2 has been fitted with a cubic function, since during the calculations with the model it was seen that the cubic function makes the code numerically more stable. The fit is shown in figure 5-8 .

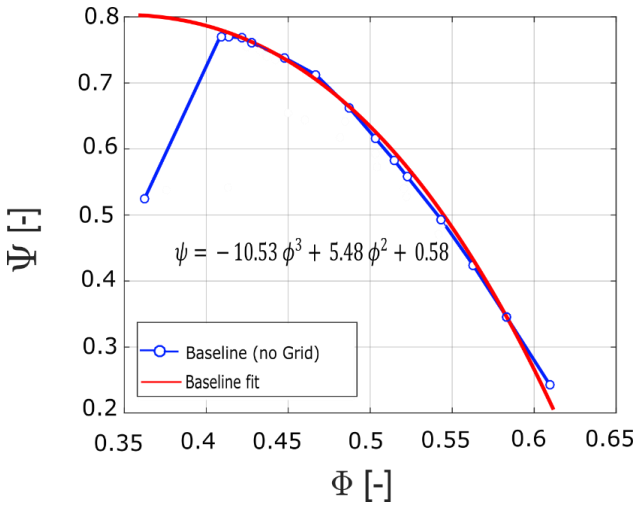

Figure 5-8 CME2 experimental characteristic curve and cubic fit used as input in Hynes Greitzer model

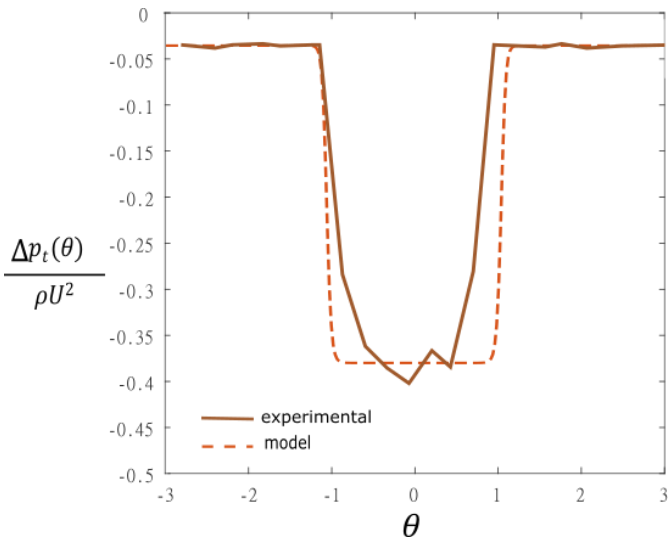

Figure 5-9: experimental total pressure profile downstream of the 120° grid with porosity 0.23 and matched square wave profile used as input in Hynes Greitzer model

The pressure drop of the grids input to the model is modelled using the hyperbolic tangent function described in the previous chapter, of the form:

$$\Delta p_{grid} = \frac{A}{2}\{1 + tanh[(\theta_g^2 - \theta^2)S + 1]\} + B \tag{5.1}$$

A and B are extracted from experimental measurements obtained with the pressure rakes to match the experimental pressure drop profile. An example for the 120° grid with porosity 0.23 is shown in figure 5-9. Finally, for the calculation of the basic state, $\lambda = 0.5$ is specified, as it correspond to the value in CME2. Once the basic flow is calculated, Lin's model is used to calculate the stability. Its inputs are shown in table 5-1. For their meaning we remind (Hynes et al., 1987), (Lin et al., 2017).

Unsteady blade response parameter	μ	1.03 [-]
Non-dimensional compressor length	l_C	1.5 [-]
Blade speed	U	80.7 [m/s]
Mean radius	R	0.2415 [m]
Greitzer parameter	B	0.208 [-]
Number of modes	N	40 [-]

Table 5-1: setting of the parameters used in input to Lin's model; more details in Hynes et al. (1987), Lin et al., (2017).

In output, the model calculates the stalling point with the various grids. In figure 5-10, the experimental curves are shown, together with the stalling flow coefficient measured with Lin's model.

The following observations can be made when looking at figure 5-10:

- For $\theta\_int/\theta\_g < 0.4$ (grids of 90°, 120°, 150°), the modal prediction is good for porosities 0.23 and 0.33. On the other hand, for porosity 0.5, the stalling point is underestimated. Grids in fact are forcing modes, especially for strong distortions, at higher flow rates than the flow rate where the incidence on the blades reaches the critical value for which the spike is triggered. When the porosity is 0.5, the forcing of modes appears at lower flow rates close or below the critical incidence flow rate and thus spike type stall tends to dominate. This is consistent with figure 5-6 showing the grids with porosities 0.5 having a mode before the onset of stall, but having a final cell frequency very close to the undistorted case controlled by spike stall. This confirms the cases 2 and 3 described previously as dominated by a spike stall (2) and modal stall(3).
- For $\theta\_int/\theta\_g > 0.4$ (60° grids), all porosities higher than 0.1 are not in agreement with the model, as modes are predicted to appear at lower flow rate than the actual stalling point where critical incidence is reached. This suggests that the spike dominates the dynamics in these cases and is consistent with figure 5-6. This is case 1 in the previous discussion observing figure 5-6.
- For all θ_int/θ_g an interesting case is the porosity 0.1: the prediction are not good; the model predicts a mode at higher flow rate than the experimental stalling flow coefficient. In fact, in experiments, the stalling flow coefficient is influenced by the saturation effect described in the previous chapter, a phenomenon that cannot be captured by Hynes Greitzer and Lin's models. These models in fact do not account for separation and channel blockage. The number of blades is infinite in the model (actuator disk) and the flow is always perfectly guided. This features that are not captured by the model make the prediction fail. This is a fourth case in which the physics is controlled by the saturation of stall flow rate.

Four stall regimes can therefore be identified. There is a certain correspondence between these stall regimes and the flow regimes that were identified in the previous chapter. In particular, a first differentiation can be done again in terms of angular extension of the grid, since 60° grids exhibit different stalling features than wider grids. The porosity, as for the flow regimes, plays also a role in the stall regimes, since higher porosity grids tend to be still dominated by spike stall, even if modal oscillations can appear, in opposition to low

porosities dominated by modal stall. In figure 5-11 the four stall regimes just identified are superposed on the phase diagram of the 4 flow regimes identified in the previous chapter.

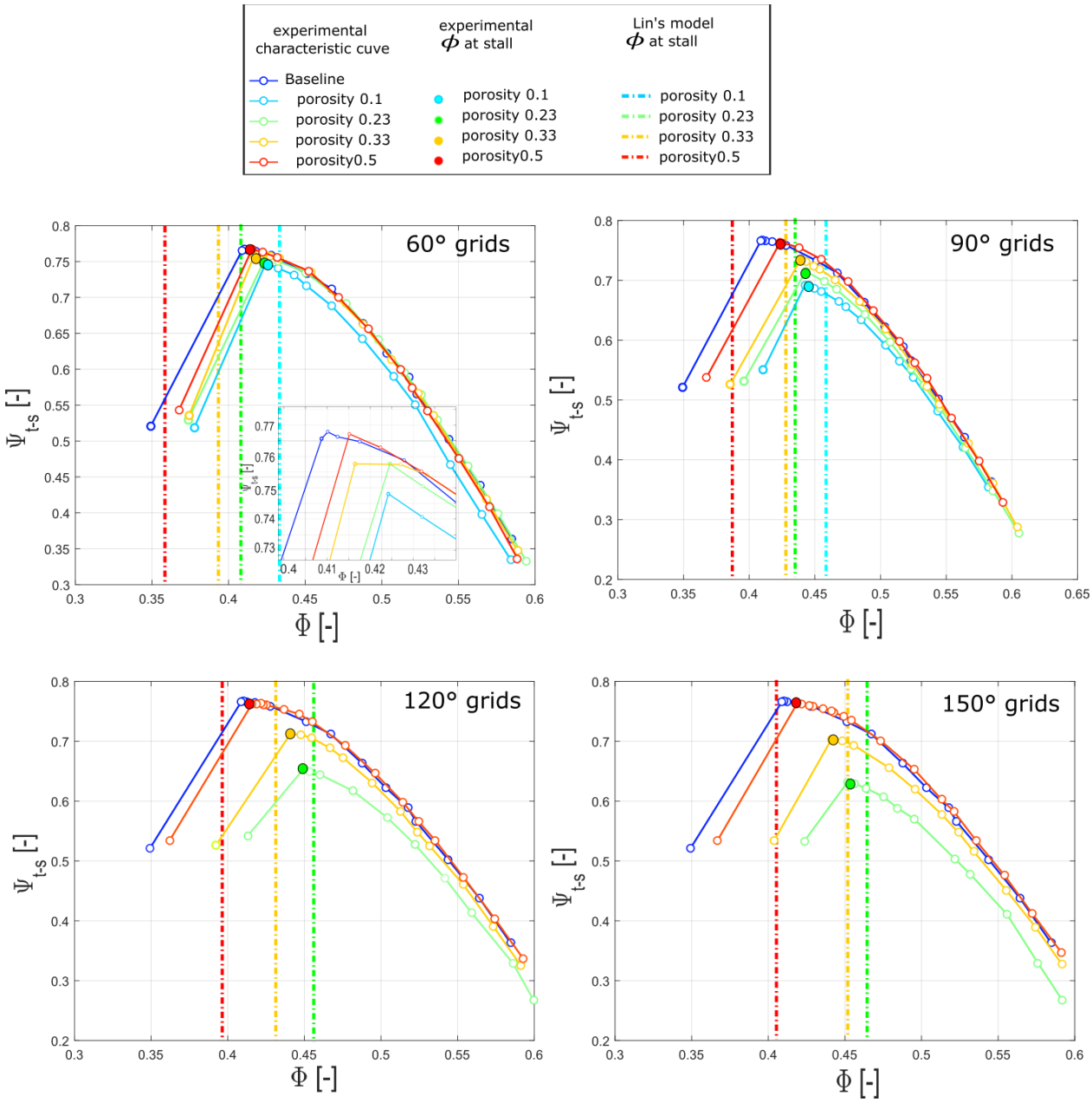

Figure 5-10: compressor characteristics for different distortions; with dotted lines are shown the ϕ at stall calculated with Lin's model.

The four stall regimes are:

1. $\theta\_int/\theta\_g > 0.4$ for high or low porosities (red), the stall is dominated by spike as in undistorted conditions
2. $\theta\_int/\theta\_g < 0.4$ for high porosities (blue) the grids introduce harmonic instability at stall, but these have negligible effect on the dynamics, which still is dominated by spike.
3. $\theta\_int/\theta\_g < 0.4$ for moderately low porosities (purple) the grids introduce harmonic instability at stall, and these have negligible effect on the dynamics, dominating it.
4. Grids at very low porosity experience a saturation of the stalling flow coefficient, and no clear mechanism is identified

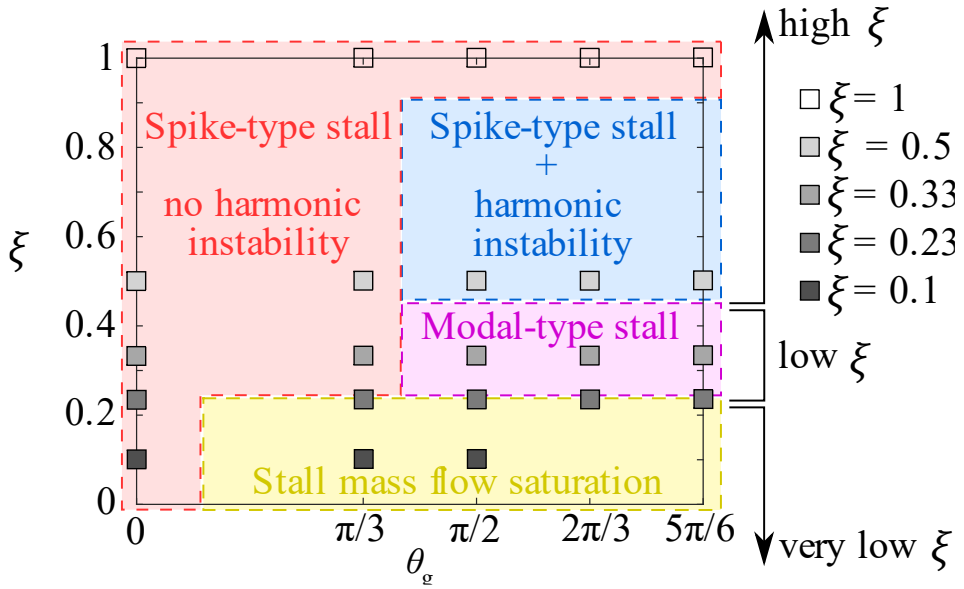

Figure 5-11: phase diagram representing the four flow regimes identified in the previous chapter with the corresponding four stall regimes identified in this chapter.

In figure 5-12 the experimental stalling ϕ (x axis) and the stalling ϕ calculated by the model (y axis) are compared in a more compact form than in figure 5-10. Also, the points in the figure have been coloured following the different regimes of figure 5-11. The purple line represents ideally $\phi_s^{model} = \phi_s^{exp}$ and indicates that points close to the curve are characterized by a modal stall. The model predictions are good even for high distortions where separation in the blade channels can be observed. The model reaches instead the limit of the prediction for very low porosities, when the separation is sufficiently strong to influence substantially the upstream flow redistribution (yellow). The blue points are outside the confidence level of the model prediction and reflect the fact that the modal oscillations observed are qualifying modal stall. The red points are finally out of the correlation and are identified with a different mechanism, namely spike stall.

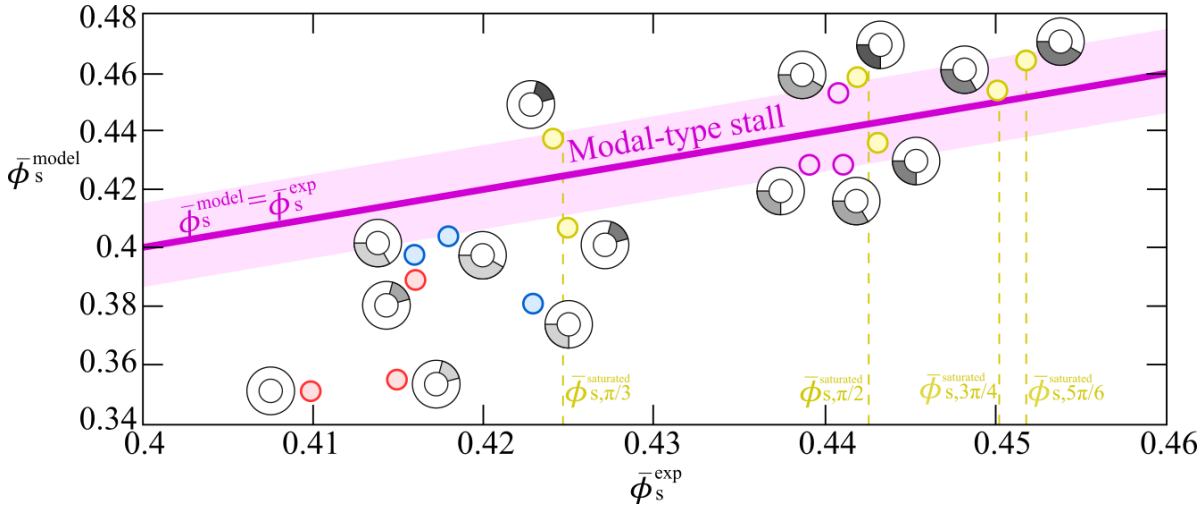

Figure 5-12: Lin's model calculated stall flow coefficient (y axis) and experimental stall flow coefficient (x axis). Purple line indicates the condition $\phi_s^{model} = \phi_s^{exp}$

This classification based on both the flow regimes behind the grid and the type of instability observed, suggests that the flow behind the grid has an influence on the stall type. Concerning this influence, one observation is interesting. For the 120° grid with porosity 0.23 it was shown thanks to PIV fields that a strong

separation exist on the upper span of the blade at the outlet of the distortion region. This separation perturbation is expected to exist also for other high distorting sectors as 150° grids of porosities 0.33 and 0.23, or 90° with porosity 0.23. This separation is not captured by simplified models (Hynes-Greitzer and Lin) but still, looking at figure 5-12, the predictions of the model are good. The predictions start failing when very low porosities are tested and the upstream redistribution saturates. This could suggest that the presence of flow separation in the channels becomes relevant to stability when it is strong enough to modify the upstream redistribution at the inlet of the compressor. Instead, moderate flow separations in the channel that don't cause a substantially different upstream flow, and are not determinant for the loss of stability.

5.2 MORE FEATURES OF STALL

In the remainder of the chapter, some more features of the stall patterns will be discussed. One more feature that appeared in the signals will be discussed in particular: in figure 5-6, it was shown that modes exist before the onset of rotating stall, forced by the presence of the grid. On the other hand, after rotating stall has established, the propagating speed of the stall cells is influenced by the grid. In the following, the unsteady signals will be analysed more in depth to provide more information on this last feature. It will be shown that this increase of rotating speed for stronger distortion is coupled to a decrease of the pressure amplitude of rotating stall cells, and it is consistent with considerations regarding the increase of drag in rotating stall.

5.2.1 ANALYSIS TOOLS FOR UNSTEADY PRESSURE SIGNALS

To further investigate pressure signals, a tool has been developed based on cross correlation and is described in the following. It allows to follow the development of the pressure amplitude and propagating speed of the perturbation during the transient from the onset of the instability to the complete development of well-established rotating stall.

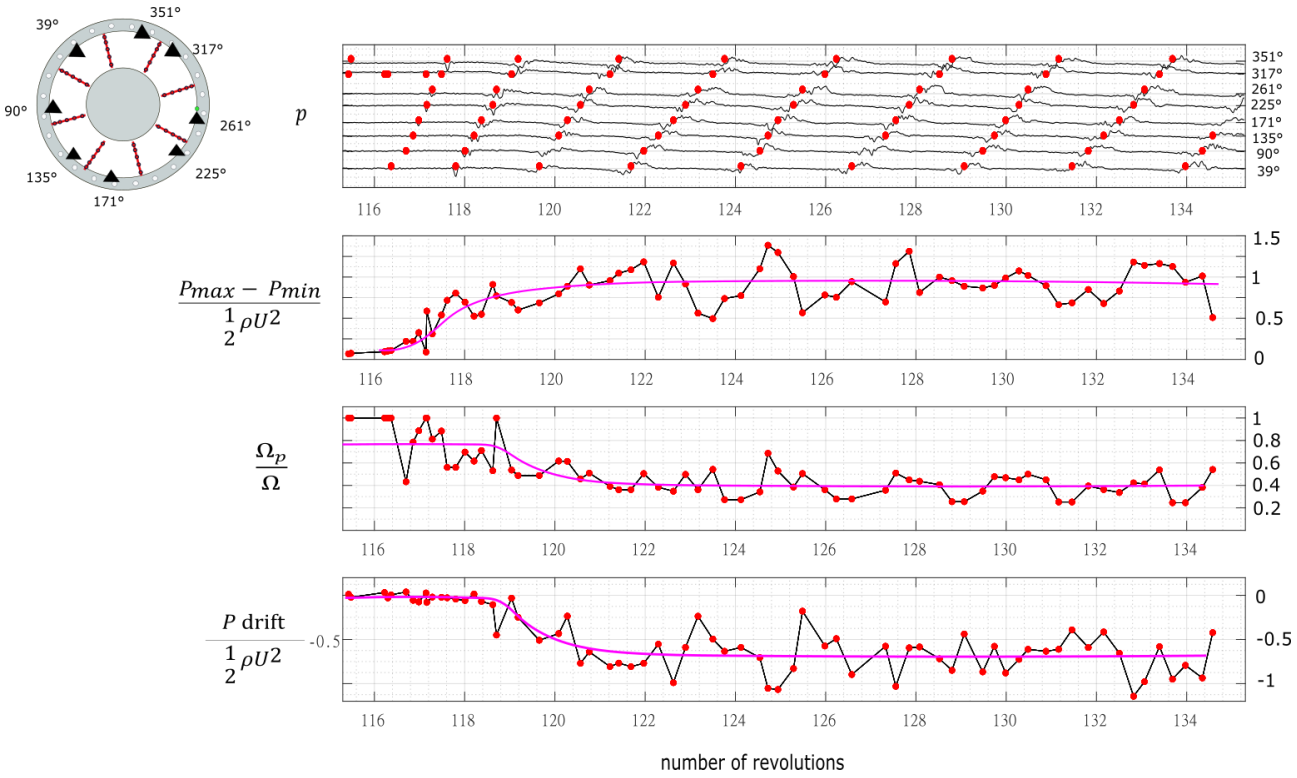

Figure 5-13 : Stall transient with no grid; on the x axis the number of revolutions, on the y axis: position of the perturbation in time and space (top panel), non-dimensional pressure amplitude (2nd panel from top), non-dimensional perturbation speed (3rd panel from top), non-dimensional drift (bottom panel).

The typical transition to stall (figure 5-1) is represented here again in figure 5-13 in the top panel. The signals have been filtered (low pass filter with cut frequency 800 Hz) to eliminate the blade passing frequency (1600 Hz).

As in figure 5-1, the 8 probes are placed at different azimuthal positions and are used to track the perturbation rotating in the annulus. The perturbation has been tracked from the first spike during the evolution until it evolves into a rotating stall cell, and is identified with a red marker in figure 5-13 in the top panel. The tracking of the perturbation has been done using cross correlation between each signal and a reference piece-wise signal composed of a typical spike, a stall cell and a transition between the two. The peaks of the correlation represent the time position of the perturbation (red dots in figure 5-13).

Once the perturbation position is located in space (the 8 angular positions of the sensors) and time (number of revolutions), a window of width 0.2 revolutions centred about the cross correlation peak is defined and peak to peak amplitude of the pressure in this window is measured. The width of 0.2 revolutions was chosen since it represents the typical perturbation size. The peak to peak amplitude is shown in the second panel from the top in figure 5-13. In figure 5-14 a scheme is represented to help the understanding: in this figure, the window is shown centred around the red dot corresponding to the local position of the perturbation in time. The maximum and minimum pressures measured in the window are subtracted to characterise the local pressure amplitude of the perturbation. Another quantity of interest measured in the window is the pressure drift, namely the difference in pressure measured at the extremes of the window (see figure 5-14). This quantity that we will call the drift in the following is shown in figure 5-13 in the 4th panel from the top during its evolution. The drift represents the difference in pressure that is responsible for driving the perturbation around the annulus. At the beginning of the transient (revolution 116 in figure 5-13), when the perturbation is still small and requires a lower tangential pressure gradient to be transported azimuthally, the drift is very small and the perturbation is convected by the mean flow. When the perturbation grows, the drift becomes negative, indicating that the azimuthal motion of the stall cell is opposed by a tangential pressure gradient.

Finally, in figure 5-13, in the third panel from the top, the speed of the perturbation is shown. It is calculated from the time position of the perturbation (top panel) and the angular distance between one probe and the other.

Coherently with the drift building up to contrast the motion of the stall cell, the speed of the perturbation diminishes from the typical speeds of 90% of Ω for the spike perturbations to 40% of Ω for developed rotating stall cells.

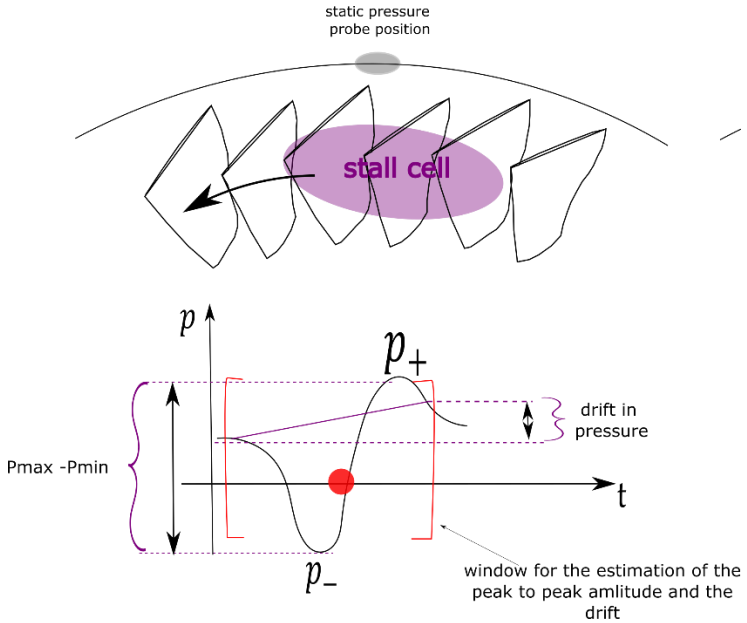

Figure 5-14: scheme for interpretation of the pressure amplitude (figure 5-13 second panel from the top) and drift (bottom panel in figure 5-13).

5.2.2 DEVELOPED ROTATING STALL

The method of analysis based on cross correlation has been applied to the signals acquired for all the grids to better highlight the phenomenon encountered in figure 5-6, namely the increase of the speed of the rotating stall cell. The instantaneous pressure amplitude and rotational speed of the developed stall cell (as in figure 5-13 in 2nd and 3rd panel) have been averaged on 60 revolutions in the region of developed stall, and have been plotted in figure 5-15 as a function of the SM. In figure 5-15, Ω_{cell} represents the average on 60 revolutions of the instantaneous values of Ω_p/Ω . A_{cell} represents the average on 60 revolutions of $(p_{max} - p_{min})/0.5\rho U^2$. $A_{cell} * \Omega_{cell}$ represents finally the product between the two previous quantities. The average in time of the quantities allows a first characterisation of the quantities for each grid.

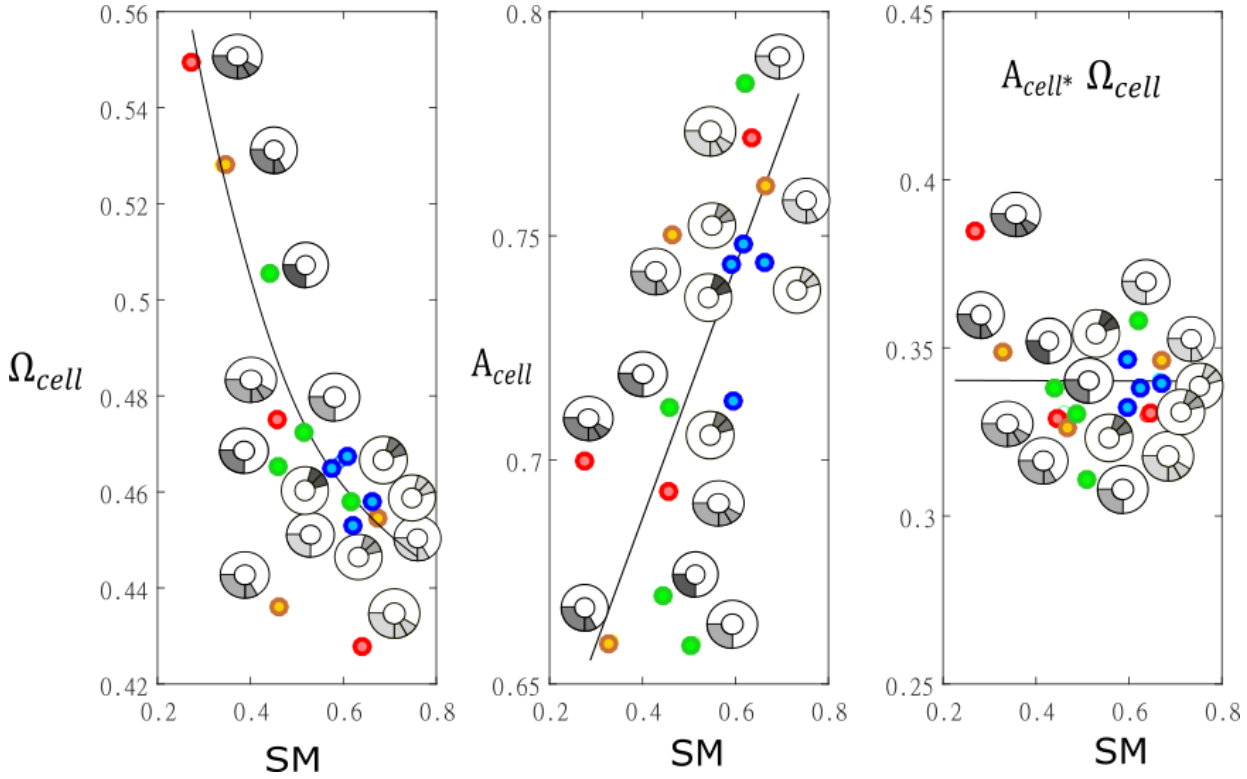

Figure 5-15: non-dimensional propagation speed of the stall cell (left), non-dimensional pressure amplitude of the stall cell (centre) and product between the two as a function of the stall margin (right).

Figure 5-15 shows that the speed of rotating stall cells increases as the stall margin deteriorates, consistently with figure 5-6. On the other hand, the pressure amplitude of the stall cell decreases in order to conserve approximately the product of the two quantities.

The physical interpretation is described in the following. In developed rotating stall, the performance drops and an increased amount of losses is produced with respect to the last stable point before the onset of stall. This increased amount of losses can be interpreted as the result of an increase of drag on the blades due to the presence of rotating stall cells rotating at a fraction of the rotational speed of the compressor. We can thus imagine a function describing a drag coefficient of the following type:

$$C_D = C_{Ds}(i)\,[1 + C1(\Omega - \Omega_s) + C2(\Omega - \Omega_{cell})^2 + \cdots] \qquad (5.2)$$

The drag coefficient depends, among other parameters, on the relative velocity of the perturbation $\Omega - \Omega_s$ with respect to the blades. If the relative velocity is 0 (small perturbation), $C_D = C_{Ds}(i)$ with $C_{Ds}(i)$ the drag coefficient at the stalling point. In stall however, the coefficient must be corrected with terms accounting for

the relative velocity of the perturbation (stall cell). Thus, the variation in drag coefficient when the conditions are moved away from the last stable point can be expressed at the leading order as

$$\Delta C_D \sim \Delta(\Omega - \Omega_{cell}) \tag{5.3}$$

The usual form of the drag coefficient for a flow over blades has the form described in Jardin (2017). The form is quadratic as a function of incidence in a broad range of incidences (up to 30°), such as to include even the strongest distortions encountered in the present study.

$$\Delta C_D \sim \Delta i^2 \tag{5.4}$$

A variation of incidence i can be however linked to a variation of the axial flow in the compressor, namely to ϕ . Considering a small variation $\Delta\phi$, it is possible to show that it must be linked to a variation of incidence $-\Delta i^2$ for the typical ranges of ϕ and i in CME2 (appendix B). Thus it is possible to say that:

$$\Delta C_D \sim \Delta i^2 \sim -\Delta\phi \tag{5.5}$$

This allows to link the relative velocity of stall cells to the flow coefficient ϕ:

$$\Delta C_D \sim \Delta(\Omega - \Omega_{cell}) \sim -\Delta\phi \tag{5.6}$$

and since the Ω is constant in all the experiments,

$$\Omega_{cell} \sim \phi_s \tag{5.7}$$

Now, recalling the definition of stall margin and its dependence on ϕ we can write

$$\Omega_{cell} \sim \phi_s \sim 1/SM \tag{5.8}$$

which is the form in figure 5-15 on the left panel. The amplitude of the stall cell A_{cell} can be on the other hand linked to the drop of pressure rise observed from the last stable point to developed stall. Imagining that this loss in pressure rise observed is linked to the amplitude in pressure of the rotating stall cells A_{cell}, we can say that:

$$\mathrm{A}_{cell} \sim \Delta\psi \tag{5.9}$$

And since the point in developed rotating stall in the characteristic curves (appendix A) is almost at the same ψ for all the grids, $\mathrm{A}_{cell} \sim \psi_s$, and once again recalling the definition of stall margin and its dependence on ψ_s,

$$\mathrm{A}_{cell} \sim \psi_s \sim SM \tag{5.10}$$

The different amounts of drag produced when passing from the last stable point to developed stall for the different grids, are thus consistent with the findings in figure 5-15. Strong distorting grids have a lower pressure rise at stall than weakly distorting grids, thus, to reach rotating stall from the last stable point, the energy to dissipate in drag is lower. This results in a smaller pressure amplitude of the rotating stall cell and a reduced relative speed $(\Omega - \Omega_{cell})$, thus a higher Ω_{cell}.
In the remainder of the chapter, two examples of the application of the cross correlation method are shown. The aim is using this method to extract more information on the stall features. This last part of the chapter

is focusing on two particular cases: a modal and a spike dominated case. For the modal case, the method is applied to a 150° grid with porosity 0.33 and for the spike case, it is applied to the 60° grid with porosity 0.33. In the following figure 5-16 the case with 150° and porosity 0.33 is shown.

5.2.3 SPEED AND AMPLITUDE OF THE PERTURBATION INSIDE AND OUTSIDE THE DISTORTED REGION

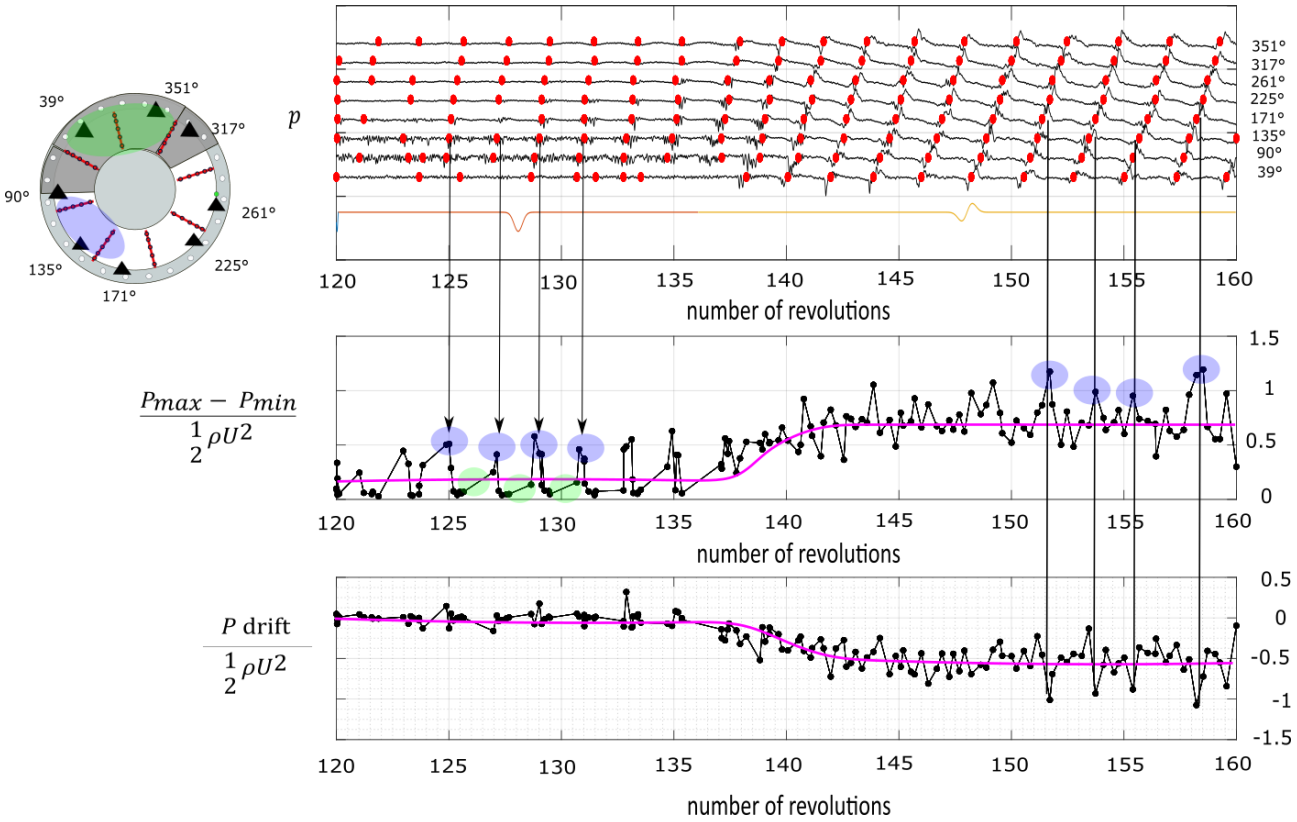

Figure 5-16 : Stall transient with 150° grid with porosity 0.33; on the x axis the number of revolutions, on the y axis: position of the perturbation in time and space (top panel), non-dimensional pressure amplitude (middle panel), non-dimensional drift (bottom panel).

In figure 5-16 are presented: the time position of the perturbation (top panel), the pressure amplitude (second panel form the top) and the drift (bottom panel). The speed has the same shape as the drift and is not shown.

Before the onset of stall around the 140th revolution, the cross correlation method captures some peaks, located especially at the exit of the distortion region. Their interpretation is not easy because in the signal are present both a mode (remember figure 5- 6) and a separation perturbation between 90° and 135°. As for figure 5-13, a first part of the transient is characterised by a zero drift (figure 5-16 bottom panel), when the perturbation is still small in amplitude. After the onset of the instability, the drift increases in magnitude consistently with the stabilisation of rotating stall cells rotating in the annulus. When the stall is developed (after 150th revolution is figure 5-16), the interpretation of the location of the perturbation (the red dots) is clearer, since it represents the position of the rotating stall cell. After revolution 150, the peaks in the pressure amplitude (central panel figure 5-16), are highlighted in purple. The peaks occur when the perturbation is located at the exit of the distortion region (135°). What is interesting is that corresponding to these peaks, the drift has its minima (bottom panel). Thus, when the perturbation reaches a maximum pressure amplitude, its propagating speed reaches a minimum.

5.2.4 CRITICAL AMPLITUDE

The case of the 60° grid with porosity 0.33 is now discussed. It is an interesting case since it allows some observations on the first part of the transient dominated by spike. When applied to narrow grids dominated by a spike mechanism, the cross correlation method suggest the existence of a critical value of the amplitude of the perturbation when instability is triggered. In particular this seems to be plausible when looking at the signals of figure 5-17.

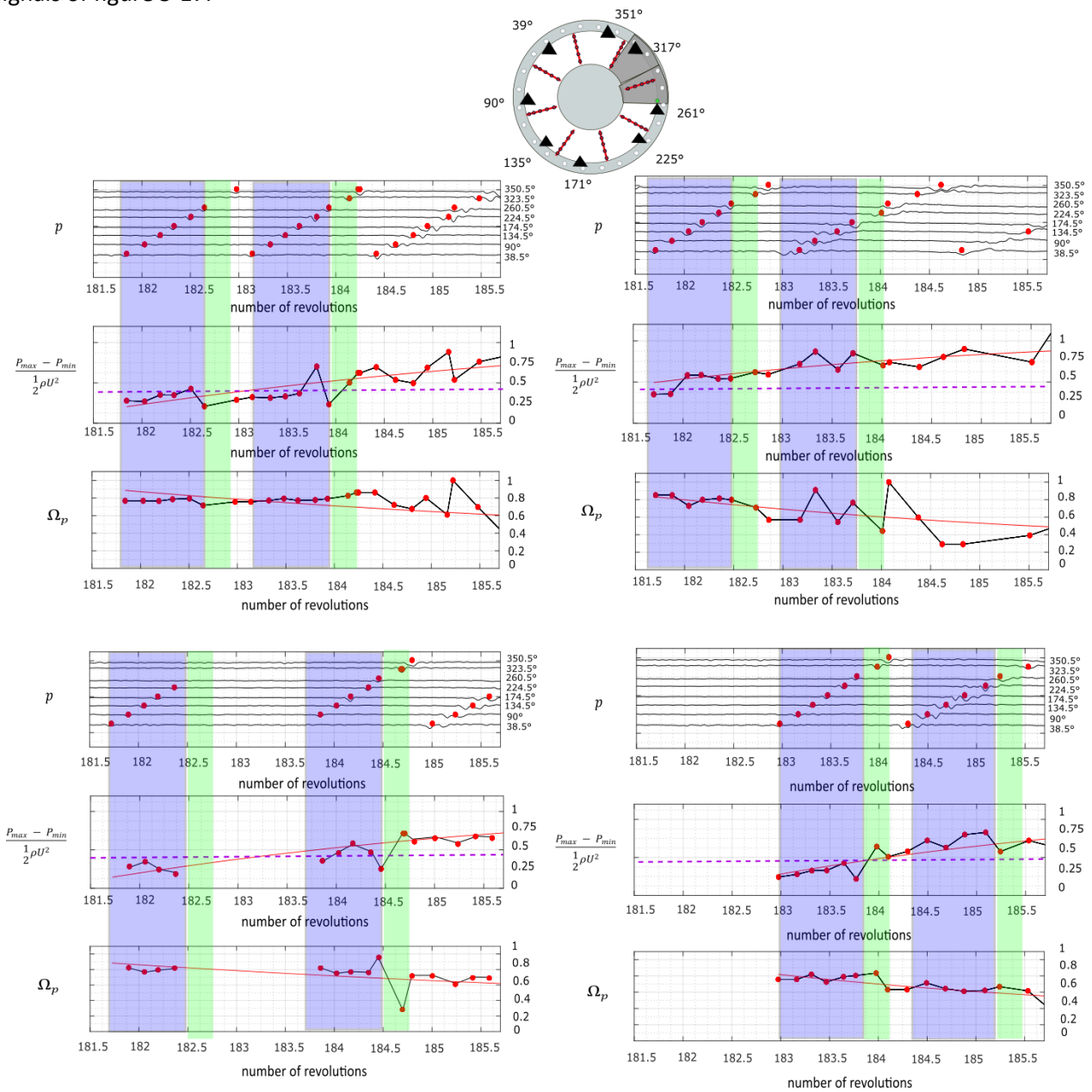

Figure 5-17 : Four repetitions of rotating stall transient with 60° grid. First panel: filtered signal; second panel: perturbation pressure amplitude; third panel: perturbation speed. Dashed violet line in the second panel: threshold for spike development; red continuous line: polynomial fit .Green background: part of the signal where the perturbation falls; blue background: part of the signal where the perturbation grows.

In figure 5-17, four repetitions of stall transient with the 60° grid are shown. Instead of showing the full transient as in figures 5-13 and 5-16, just the first revolutions are shown, since they contain information on the development of the spike. In case a, the spike is formed at revolution 181.7, and its pressure amplitude grows in the following revolution (highlighted in blue). After the blue region of growth, a sudden decrease in amplitude is encountered in the green region. In the following of the transient, the perturbation starts to grow again (2nd blue region starting at revolution 183.2), until again a jump is encountered at revolution 184,

at the same angular position around 260°. After this second jump, the perturbation evolves undisturbed and is no more shown in the figure. The position 260° corresponds to one edge of the grid. Locally, the flow is accelerated due to the side effect of the grid, and the incidence reduced, with a stabilising effect that acts against the perturbation. This could explain the local decay around 260°. However, the same phenomenon of decay of the perturbation at the angular position 260° is not encountered in all the cases. For example in b, the growth of the perturbation is rather continuous. In c on the other hand, the decay is evident and it is responsible for quenching the perturbation, until at revolution 183.8 a new spike forms. Case d is similar to case a, with the difference that in d, the decay at the revolution number 183.7 does not slow down the growth as in case a. The results shown in figure 5-17 suggest that a threshold value in the perturbation amplitude exists, above which the perturbation continues to grow. In case c, the amplitude of the first perturbation is not strong enough to allow propagation, instead in case b, already at the first appearance of the perturbation, the amplitude is big enough to allow further undisturbed growth. In case a, the first perturbation continues to propagate, but it's growth is slowed down. This threshold value is about 0.425 of the dynamic pressure based on the blade tip speed. There is thus a clear competition between the stabilizing effects of the low incidence region existing at the edge of the grid and the proper dynamic of the instability (Baretter et al., 2021).

5.3 CONCLUSIONS

In this chapter, unsteady pressure signals during the transition to stall have been analysed. A general pattern has been found experimentally, and supported theoretically using an extension of the Hynes Greitzer model. The signals allow to introduce four different regimes of stall: narrow grids always show the same type of stall, dominated by spike, as in the undistorted case. For wider grids, a difference appears following the porosity. Higher porosity grids show modal oscillations, but the dynamics is finally dominated by spike; lower porosities are instead dominated by modal stall. A fourth regime is identified at very low porosities, where the separation regions in the blade channels modify the upstream redistribution and do not allow to say which mechanism dominates the stall. These four mechanisms fit well in the four regimes identified in the previous chapter examining the flow features of the flow behind the grids. The correspondence of the flow regimes and stall regimes suggests that the type of flow is determinant for the stall mechanism observed.
Another feature has been observed in pressure signals. Other than forcing modes before rotating stall, grids also change the rotational speed of rotating stall cells. A method based on cross correlation has been developed to follow the perturbation pressure amplitude and propagating speed during the transient. The analysis shows that the increase of the rotational speed of the stall cells for stronger distortions is associated to a decrease of the pressure amplitude of the cells, so that the product of the two quantities is constant. This is explained by some considerations on the evolution of the drag of the blades close to stall. A similar inverse relationship between the pressure amplitude of the stall cell and its propagating speed is captured by the cross correlation method during time when blades cyclically enter and exit the distorted region: when blades rotate behind the grid, the perturbation grows in amplitude and its rotational speed decreases, and the reverse is true when blades rotate outside the distorted region. The cross correlation method finally shows that for the 60° grids where stall is spike dominated, a competition exists between the dynamic of the spike and the stabilising effect of the low incidence region at the entrance of the distorted region, and suggests that a critical amplitude of the perturbation determines when one of the two effects prevails over the other.

6 DETAILED FLOW DESCRIPTION OF 2 REGIMES

In the previous chapters, the stall margin and the stall mechanism have been described for the various grids, identifying four different regimes which summarize the response of the compressor with all the tested grids. In this chapter we want to use the experimental measurements to describe in more detail the flow for two cases in particular, namely two 120° grids at the extreme of the porosity range (porosity 0.5 and 0.23). The two grids are at the extremes of the scaling SM - $DC\ \theta_{avg}$ (figure 6-1) and belong to two different regimes as seen in the previous chapters. To recall, the grids with porosity 0.23 never reaches a saturation of the stall margin, and the stall inception is modal. On the other hand the grid with porosity 0.5 reaches a saturation of the stall margin and experiences spike type stall.

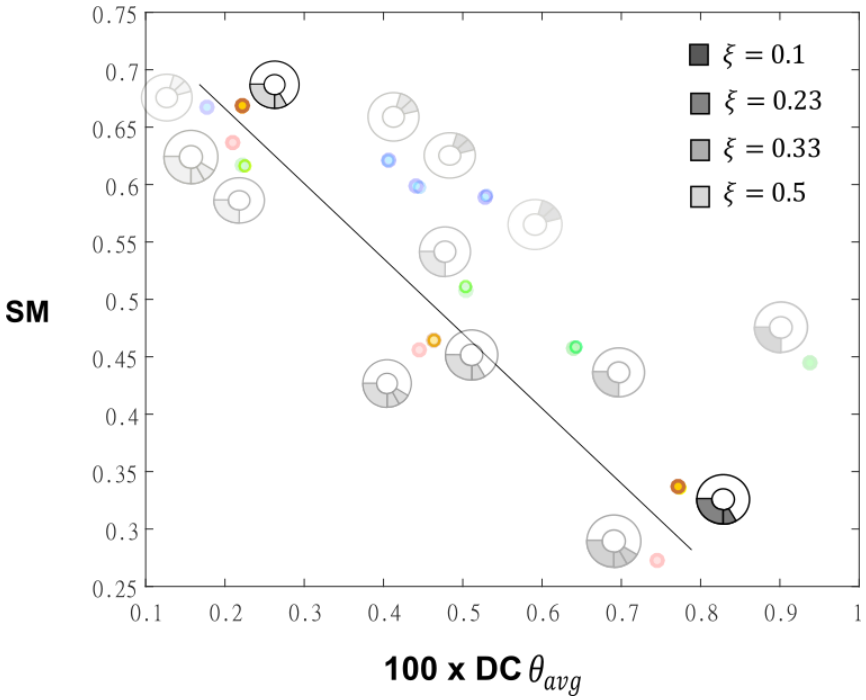

Figure 6-1: scaling SM vs $DC_{\theta avg}$. The two grids at the centre of the discussion in this chapter are highlighted.

It will be shown that the weak amount of distortion created by the more porous grid leads to a flow which does not deviate greatly from the undistorted flow, consistently with the stall margin being very similar to the undistorted case. On the other hand, the weakly porous grid introduces more complex features in the flow which makes it very different from the undistorted case. To help the interpretation of the experimental results, in the chapter, constant comparison with the Hynes Greitzer model predictions will be made. It will be seen in that the weakly porous grid breaks some hypothesis of the model. In particular the flow show separation on a substantial part of the annulus and three dimensional features; in the model, no three dimensional effects are modelled and moreover, since the compressor is modelled as an actuator disk, no blade dynamics and separated flow can be taken into account. Nevertheless the comparison with the model suggests that these features which appear in the experiments and that the model cannot capture are not of leading order for the onset of the instability, since it was already seen in the previous chapter that the model correctly captures the stalling mass flow rate.

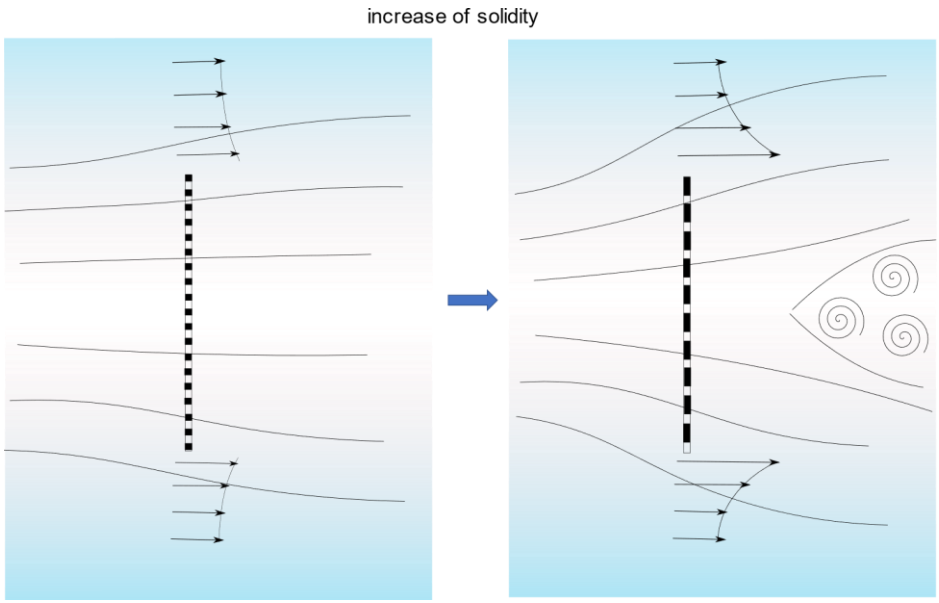

Figure 6-2: picture representing schematically the different features of the flow behind a highly porous grid (left) and a weakly porous grid (right).

The chapter is structured in the following way: first, in paragraph 6.1, the flow behind the 120° grid with porosity 0.5 is described; it is representative of the second regime defined in the previous chapter in 5.1.3. The characteristic curve and the total pressure profiles behind the grid will be presented (6.1.1) and compared to the results obtained using Hynes Greitzer model (6.1.2). PIV fields are shown in 6.1.3 to better identify some flow features and POD analysis of these fields in 6.1.4 is used to extract more information about the flow. Paragraph 6.2 follows the same scheme on the other grid, the 120° with porosity 0.23, representative of the third regime defined in 5.1.3.

The main difference between the flow behind the two grids is an effect of the very different porosities. In particular, following the discussion in chapter 2, the grid of lower porosity is expected to show flow features in between a porous medium and a solid body (figure 6-2). This redistribution is much more important than for the porosity 0.5, due to the higher blockage. The upstream redistribution was seen responsible for the increase (in magnitude) of the total pressure behind the grid, when the angular extension of the grid increases, compared to highly porous grids, where the peak total pressure saturates. This was seen a determinant feature for the saturation of the stall margin.

The flow features connected to the higher flow redistribution when porosity is decreased, approach, in the limit of zero porosity, the features of a solid body blocking the flow. An important acceleration effect is expected on the edges of the grid (figure 6-2) to counteract the strong deceleration of the flow in front of the grid. (In the chapter, the profiles confirm such a redistribution of flow in particular for the grid with porosity 0.23).

6.1 REGIME 2 : GRID 120° POROSITY 0.5

In the following, the flow features induced by the 120° grid with porosity 0.5 are described. In figure 6-3 the total pressure pattern measured by the pressure rakes in the annulus is shown. The distortion is circumferential, with negligible levels of radial distortion. The total pressure drop created by the grid is around 8% of $1/2\ \rho U^2$ and it is a weak level of distortion, creating little influence on the characteristic curve of the compressor, which is shown in figure 6-4.

6.1.1 CHARACTERISTIC CURVE AND ϕ AND ψ VS θ

In the compressor curve (figure 6-4), a point M is marked in red. It represents the last stable point before stall for the distorted curve. This point represents just the mean operating point. In reality the flow conditions vary in the annulus, in and outside of the region occupied by the grid, since the grid is forcing different levels of total pressure behind it.

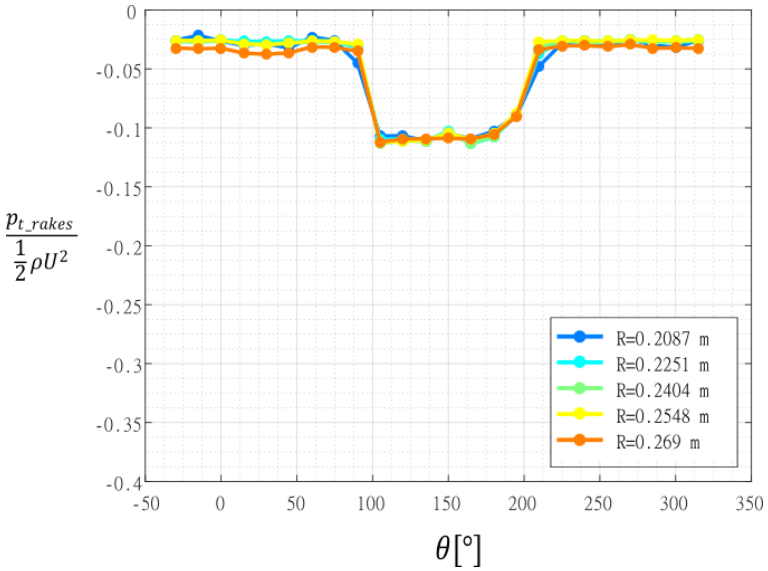

Figure 6-3: non-dimensional total pressure behind the 120° grid with porosity 0.5 as a function of the angular position in the annulus at the last stable point; parametric in the radius.

ϕ and ψ vary in the annulus and their values are shown in dashed line in figure 6-4 and as a function of the annulus coordinate θ in figure 6-5. The average of the profiles in figure 6-5, are the coordinates of point M in the compressor characteristic. The points behind the grid have been identified with letters from A to I and are shown both in figure 6-4 and 6-5.

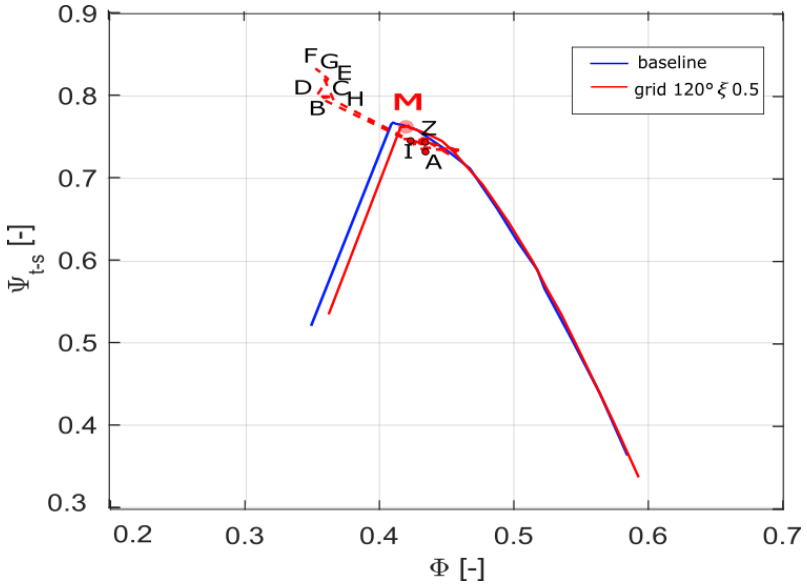

Figure 6-4: characteristic curve with the 120° porosity with 0.5. Point M represents the mean flow at the last stable point, and the dashed red line the local flow coefficient and pressure rise conditions in the annulus at the last stable point

The values of ψ are directly measured as the local total to static pressure rise, using pressure rakes and static pressure taps. The local ϕ on the other hand is first estimated at the level of the rakes plane, from the dynamic pressure measured as the difference between the total pressures and the casing static pressure. Its

value at the level of the rotor inlet is calculated using a correction factor which accounts for the convergence of the hub between the plane of the rakes and the rotor inlet (from conservation of mass). This effect is small but not negligible. The area of the annulus is decreasing of 8% between the two stations.
In reality, between these two stations (rakes and rotor inlet) upstream redistribution in front of the compressor is also acting and can change the velocity pattern, decreasing the velocity distortion seen by the compressor.

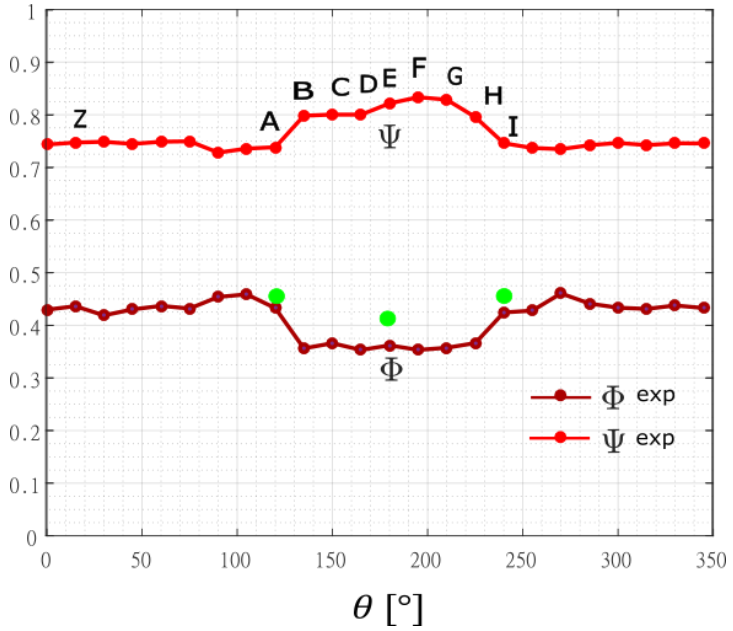

Figure 6-5: flow coefficient and pressure rise at the last stable point as a function of θ for the 120° grid with porosity 0.5; the green marker are the values of ϕ extracted from PIV fields. Point from A to I are measured behind the grid and correspond to the same points in figure 6-4.

It is expected then, that the velocity distortion measured at the rotor is slightly different than at the rakes. PIV measurements on the other hand, provide a direct measurement of the ϕ values at the inlet of the compressor. In figure 6-5, three flow rates measured with PIV for the three positions behind the grid are plotted. They have been obtained averaging the PIV velocity profiles 4 mm upstream of the leading edge.
The estimation of the ϕ by pressure rakes is closer to the value in PIV for points A and I but behind the grid in E, the ϕ measured by PIV is higher. This discrepancy is in consistency with the argument of upstream redistribution. Upstream redistribution in front of the compressor causes a lower velocity distortion seen by the compressor.
Looking at figure 6-5, the prolife of ϕ is almost a square pattern with the gradually varying ϕ at the edges of the grid, and no strong sign of acceleration at the edges is noticed, as the upstream redistribution of the grid is mild.

6.1.2 COMPARISON WITH MODEL

In figure 6- 6, the ϕ and ψ profiles have been compared to the profiles calculated with Hynes Greitzer model at the same flow rate. The comparison is interesting especially because in the model, no upstream redistribution is modelled and thus the comparison highlights clearly the effects of the edges of the grids and the redistribution on the ϕ profiles. For the calculation, the CME2 compressor curve has been modelled as a cubic with the parameters described in chapter 2. The total pressure drop matches the experimental pressure drop, in order to have the same input into the model. At the edges of the grid the flow rate is slightly higher than in the model (highlighted in yellow), and behind the grid slightly lower. The deviations are however small. ψ is smaller where the velocity is higher and bigger behind the grid. The weak effect of the

upstream redistribution makes the model to be close to the experimental values. The experimental curve (figure 6-7) and the one calculated by the model are thus very similar, and almost the same as the undistorted curve, indicating that the low level of distortion has little effect on the performance drop.

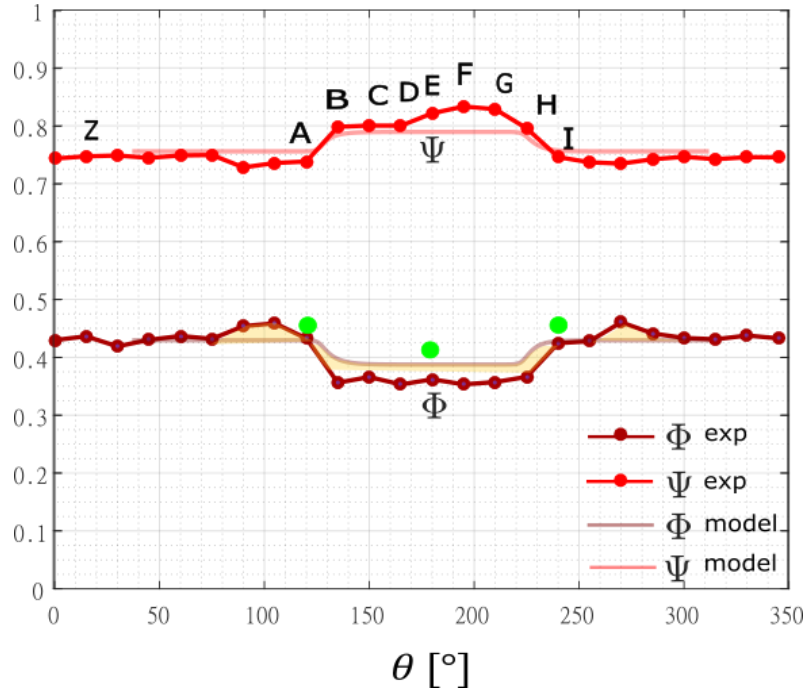

Figure 6-6: comparison between the experimental profiles and the profiles measured with Hynes Greitzer at the last stable point. In yellow are highlighted the areas marking the surplus of ϕ at the edges of the grid and the ϕ deficit behind the grid.

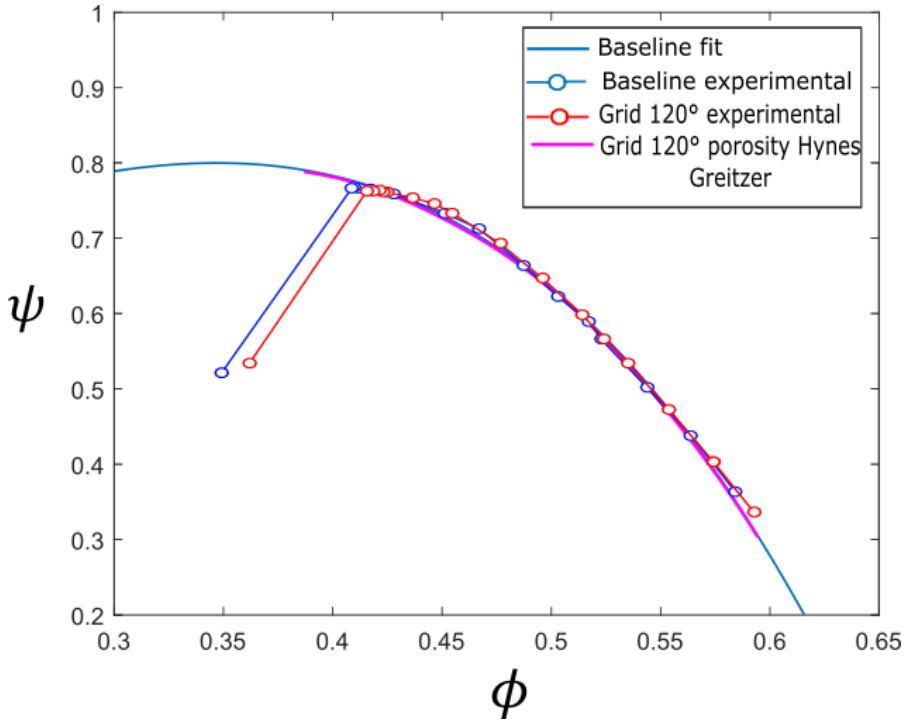

Figure 6-7: comparison of the experimental compressor curves of the baseline without the grid and the 120° with porosity 0.5 (both experimental and numerical).

Actually, the value of ϕ behind the grid measured in PIV (figure 6-6 green markers), is actually very close to the mean ϕ (point M in figure 6-4) which is also close to the mean value in undistorted flow. The non-uniformity of velocity at the inlet of the rotor is thus reduced and the flow is not expected to deviate

significantly from the uniform undistorted flow. This is confirmed by the flow fields captured by PIV measurements that are described in the following.

6.1.3 FLOW FIELDS IN THE BLADE CHANNELS

In figure 6-8, the PIV fields at the 79% of the blade height are shown for the three positions A, E, I that correspond to figure 6-5 and 6-6.
We remind that the location

- A corresponds to the entrance into the distorted region
- E corresponds to the centre of the distorted region
- I corresponds to the exit of the distorted region

On the right in figure 6-8, the flow field at the last stable point in non-distorted conditions is shown for comparison. It has to be noticed that the two cases are not exactly at the same flow rate ($\phi = 0.416$ for the case with the grid and $\phi = 0.41$ for the case without). Nevertheless the two values are very close and the comparison is possible at least qualitatively.
Looking at figure 6-8 on the left (gird 120°), a separation region appears on the suction surface of the blades, similarly to the case without the grid. This is consistent, since the local conditions are very similar to the flow rate in undistorted conditions.
However, the separation region has different features in A, E, I. The separation region is more extended in I than in E, where it is much similar to the undistorted case. In A on the other hand it is reduced compared to both I and E. One possible contribution is the effect of angle distortion at the edges of the grid. Point A and I are in fact in the interaction region, where the tangential pressure gradients move the flow towards the distortion region, creating a tangential component of velocity. The existence of this tangential component of velocity is confirmed in figure 6-9, in which the average of the velocity and absolute flow angle profiles at the leading edge are shown for the position A, E, I. In the picture, the values of the average velocities and absolute flow angle for the case without grid are also shown in dashed line, in order to allow a comparison. While in uniform flow the inflow absolute angle is small (-2°), at the exit and inlet of the distorted region, values of -8° and 6° are present. Correspondingly, tangential velocity components are present of the order of magnitude of 5 m/s. This tangential inflow in fact modifies the incidence on the blades (figure 6-10) and velocity triangles locally, as it is schematically represented in figure 6-11, where the velocity triangles for A, E, I are shown. In E in figure 6-11, at the centre of the grid, the flow is almost axial. In A on the other hand a tangential component of velocity is directed in the sense of rotation and in I it is directed opposite to the rotation. The two are connected to the tangential pressure gradient (schematized in figure 6-11 on the right).

Grid 120° porosity 0.5

No Grid

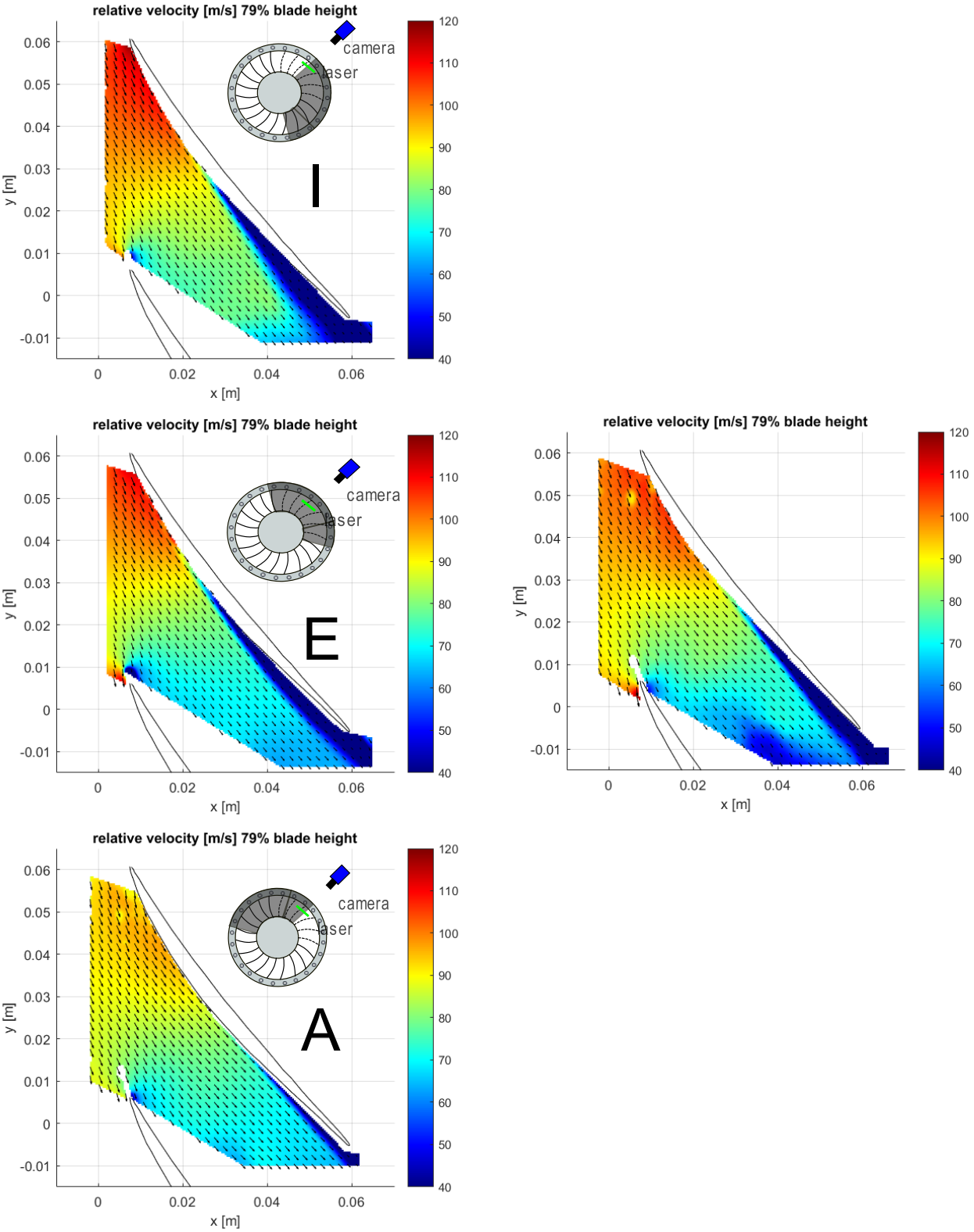

Figure 6-8: on the left PIV fields (79% blade span) in the three positions A,E,I (figure 6-6) for the 120° grid with porosity 0.5 at the last stable point; on the right PIV field (79% of the span) for the baseline at the last stable point

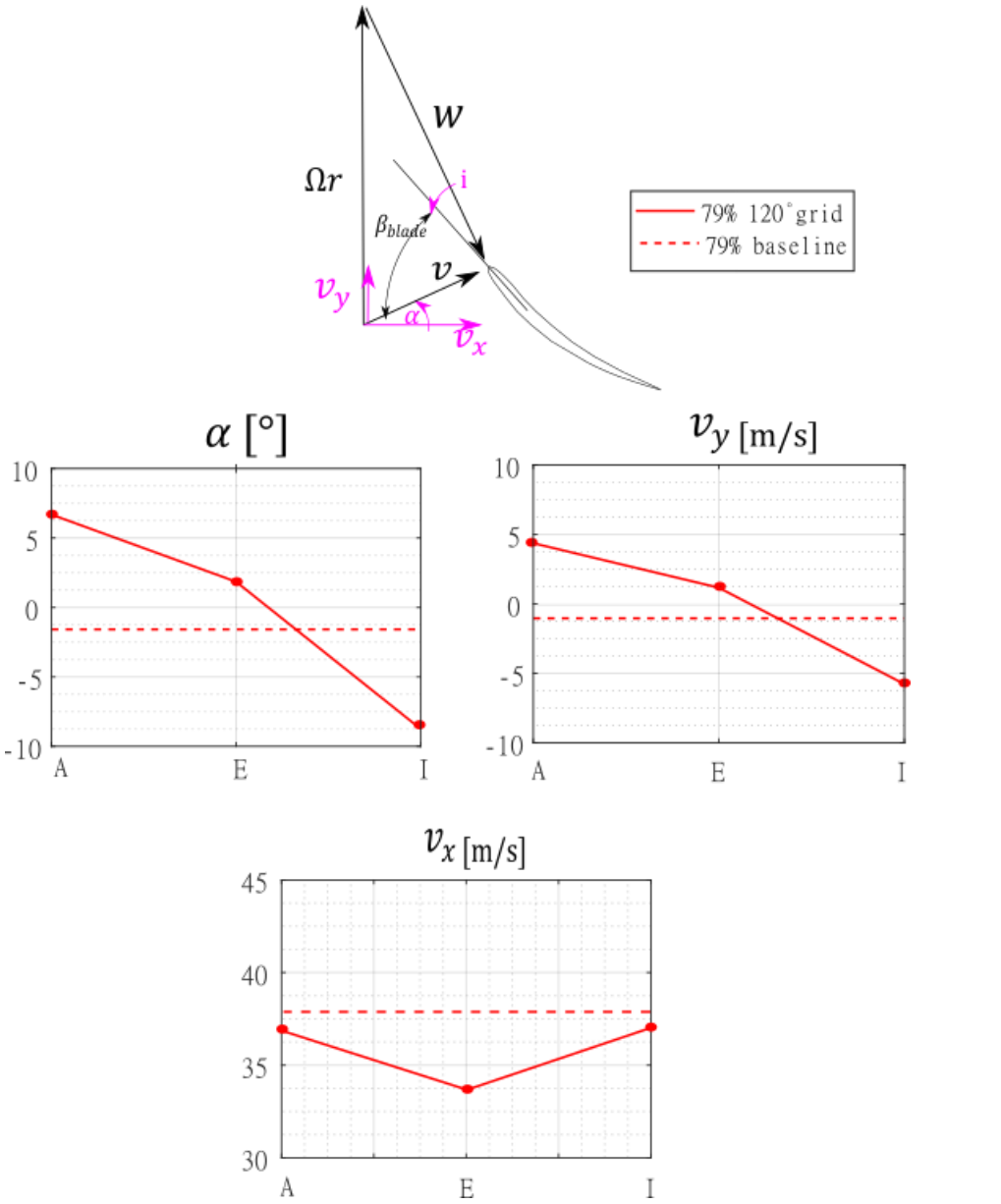

Figure 6-9 : average calculated at the leading edge of PIV fields in figure 6-8 on the left of : absolute flow angle (α), tangential component of velocity (vy), axial component of velocity (vx)

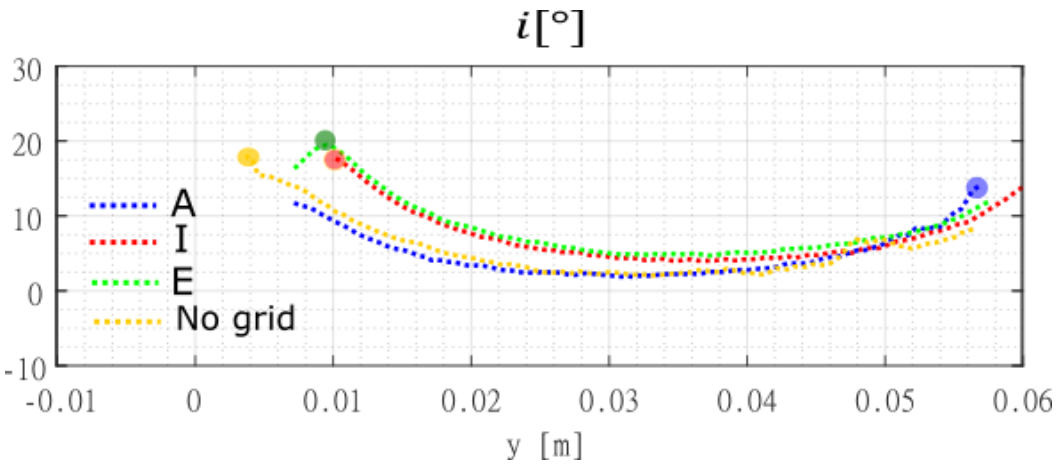

Figure 6-10: profiles of the incidence angle as a function of y extracted at the leading edge for the four PIV f fields in figure 6-8

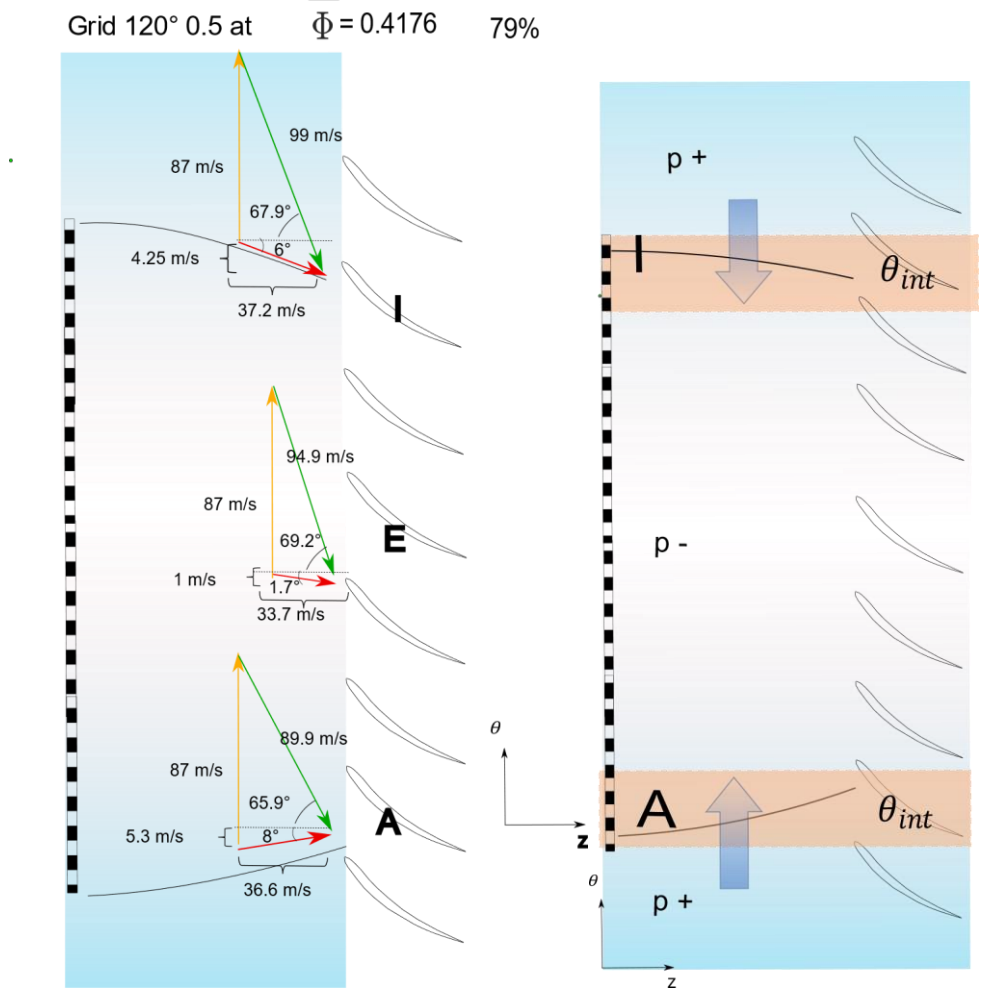

Figure 6-11 : left : velocity triangles extracted at the leading edge from PIV fields in figure 6-8 ; right scheme representing the tangential pressure gradients and their effect in the interaction region

From figure 6-11 it is clear how the tangential pressure gradient modifies locally the velocity triangles and acts on the incidence on the blades. In A, the flow is tilted towards the centre of the distortion region, so that locally blades see a reduced incidence. On the other hand, in C, the tangential pressure gradient acts to increase the incidence. The effect of the tangential gradients on incidence is clear from the profiles of incidence in figure 6-10. The incidence in A is the smallest (the blue marker indicate the maximum value at the suction surface leading edge). The reduction of incidence in A implies a reduced loading, and is consistent with the velocity field in figure 6-8, which shows a mild diffusion of the relative velocity compared to the undistorted flow, indicating locally un-loading of the blade.

For point I on the other hand, the incidence is increased, and is higher than in the undistorted flow. Moreover, incidence reaches values similar to E, where the high incidence is associated to the low axial velocity in the wake of the grid. The effect is an increase of loading and operation closer to the stalling point, as it is indicated by the separation regions appearing close to the suction surface in E and I.

In these regions operating at higher incidence, it is expected that the separation region is associated to a higher unsteadiness of the flow.

Since in figure 6-8 the average flow fields are plot, no information about the unsteadiness can be extracted, and thus, a POD analysis of the fields was performed to extract more information.

6.1.4 UNSTEADY ENERGY CONTENT

In figure 6-12 the cumulative energy with the number of modes of the POD analysis of the velocity fields obtained for positions A, E and I whose average were presented in figure 6-8, is plotted. The modes suggest that the mean flow field still contains the most of the flow energy. Nevertheless at the outlet of the distortion region, some part of the energy is contained in modes connected to the presence of the separation. The trends in figure 6-12 are consistent with the fields in figure 6-8 and with the size of a separation region. The lowest energy in the first mode is encountered in I, where the size of the separation region is bigger. The field in E and the undistorted have similar sizes of the distorted region, and consistently, in figure 6-12, the energy in the first mode is similar. On the other hand, the flow in A has negligible energy in modes higher than the first, consistently with the fact that the separation region is minimal and unsteady sources of the flow are reduced.

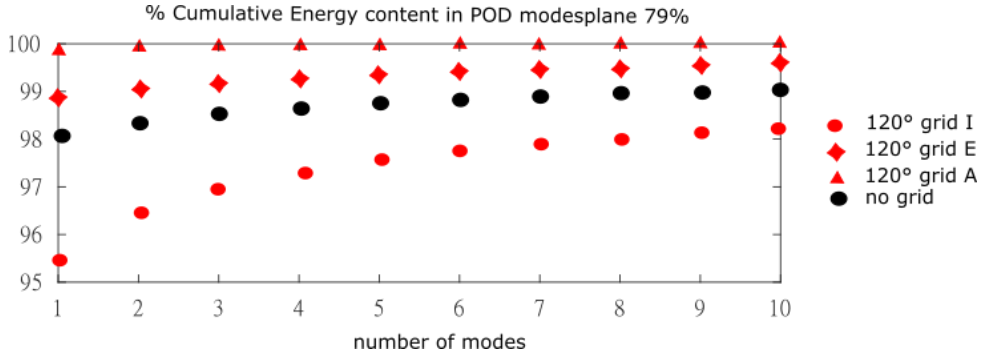

Figure 6-12 cumulative energy content in POD modes; comparison between the four fields in figure 6-8 at the last stable point.

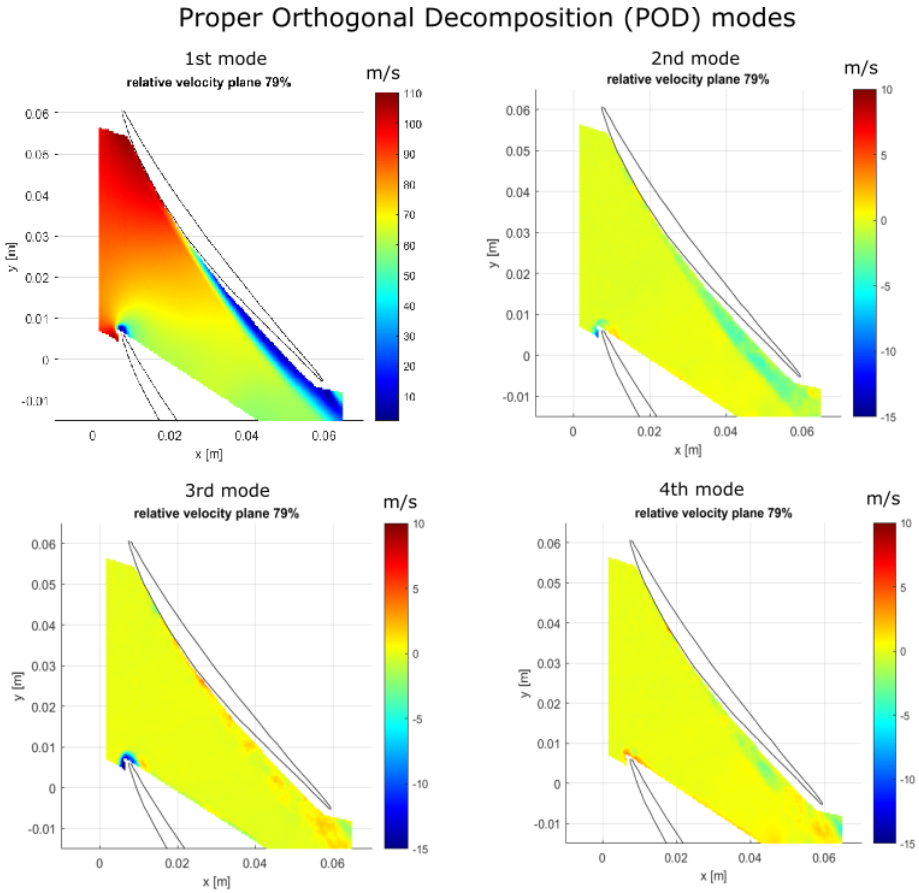

Figure 6-13 first 4 POD modes of the flow field at the centre of the distortion region (E) at 79% of the blade height ; 120° grid with porosity 0.5

In figure 6-13 the POD modes for the position E are shown. The second mode shows a non-zero velocity where the shear layer is present and the third and fourth mode are oscillatory, with regions of higher and lower than zero velocity. The effect of the separation region, however is stronger at the exit of the distortion region (figure 6-14).

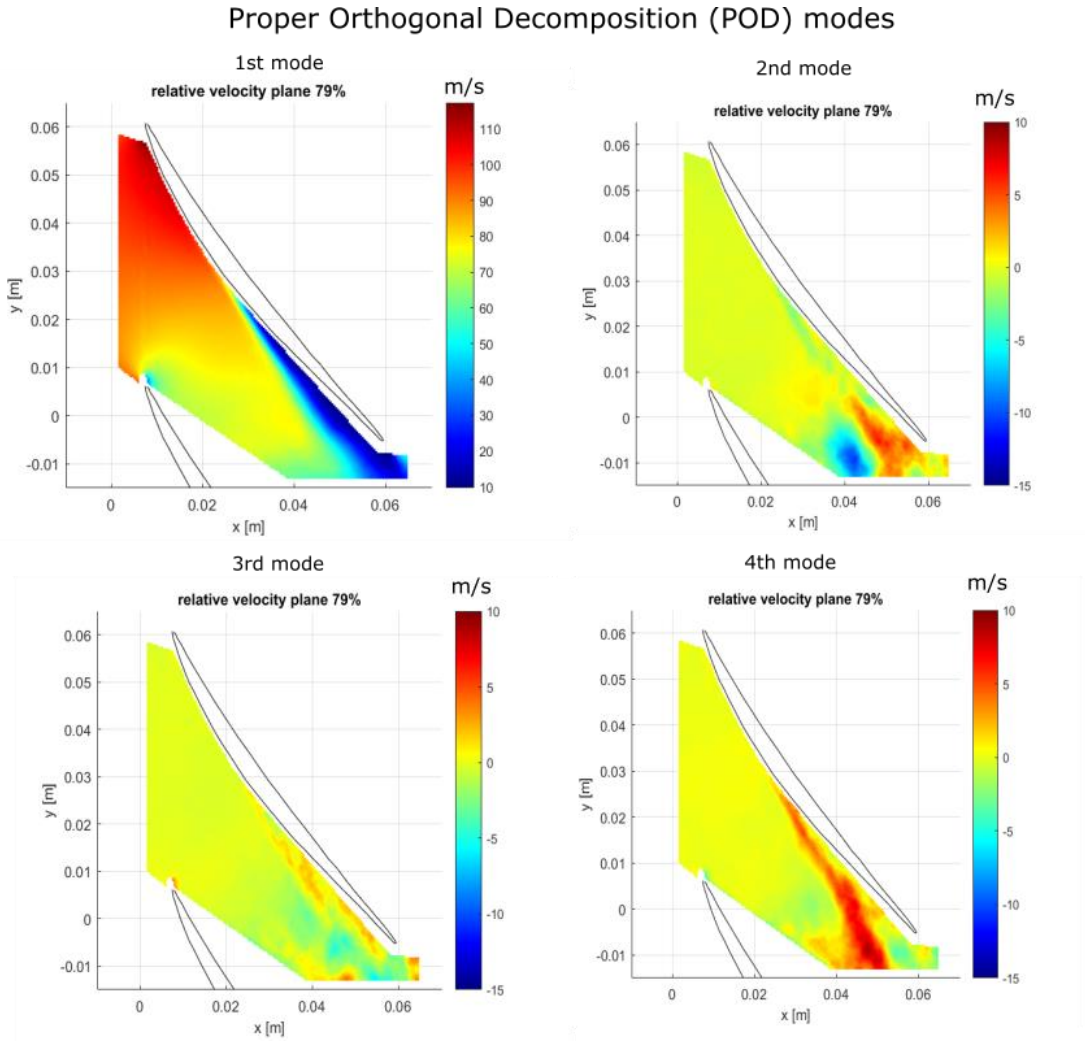

Figure 6-14 first 4 POD modes of the flow field at the exit of the distortion region (I) at 79% of the blade height ; 120° grid with porosity 0.5

To summarize, the 120° grid with porosity 0.5 produces a weak distortion, such that the velocity non uniformity at the leading edge is reduced in magnitude and the compressor works in conditions not dissimilar to the conditions at the last stable point in uniform flow. The upstream redistribution is reduced, and the ϕ profiles have the usual form behind a highly porous medium: a step behind the grid with an interaction region that matches the flow behind and outside of the distorted region. At the edges of the grid, in the interaction region, flow angle distortion, connected to the existence of tangential pressure gradients is one reason for an asymmetry of flow between A and I at the inlet and outlet of the distorted region. Nevertheless, the flow asymmetry is such that the flow conditions between A, E I varies slightly. The energy contained in the POD is also asymmetric: the region in A has very low unsteadiness, and region I is the most unsteady between the three.

6.2 REGIME 3 : GRID 120° POROSITY 0.23

In figure 6-15, the total pressure pattern measured by the pressure rakes is shown for the 120° grid with porosity 0.23.

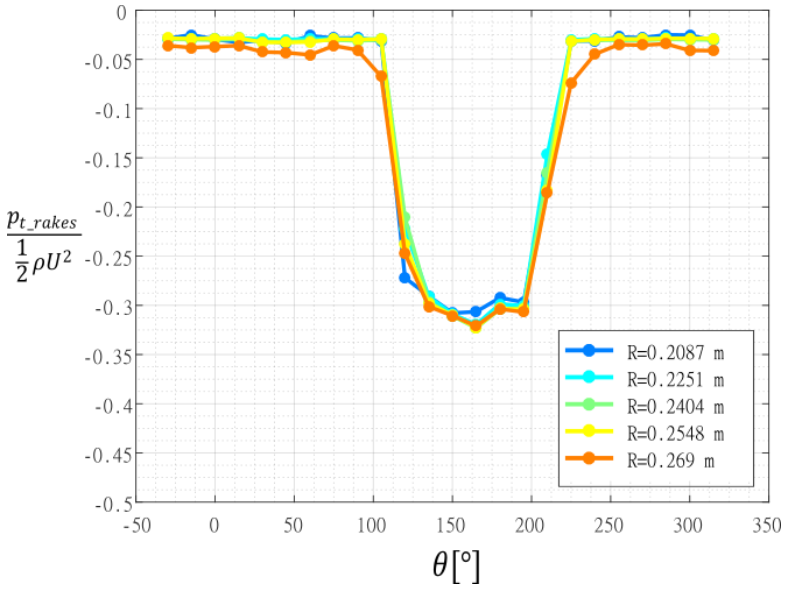

Figure 6-15 non-dimensional total pressure behind the 120° grid with porosity 0.23 as a function of the angular position in the annulus at the last stable point; parametrin in the radius.

The distortion is sensibly higher than for the porosity 0.5 (around 28% of the $1/2\,\rho U^2$ thus almost 3.5 times the loss with the grid with porosity 0.5) and is still mainly circumferential, with negligible levels of radial distortion.

6.2.1 CHARACTERISTIC CURVE AND ϕ AND ψ VS θ

The characteristic curve of the compressor is shown in figure 6-16.

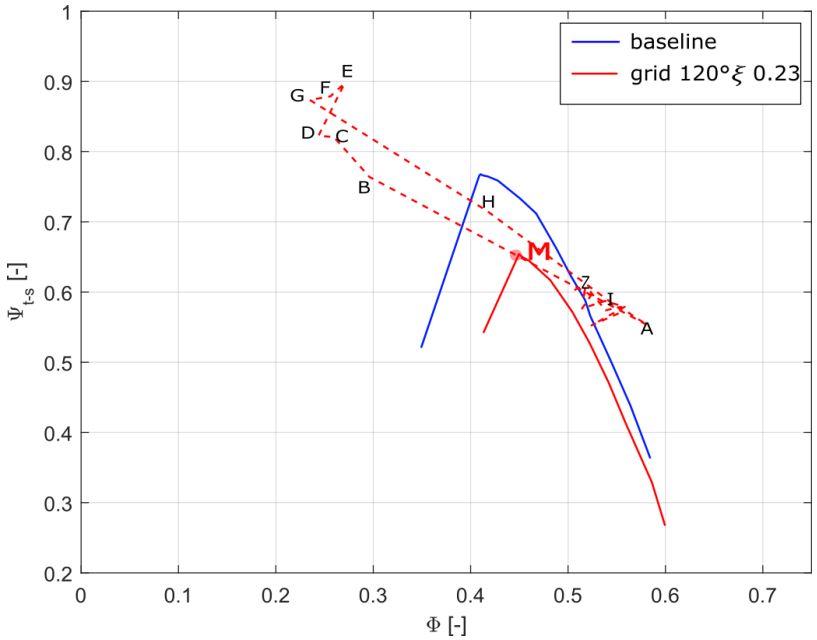

Figure 6-16: characteristic curve with the 120° porosity with 0.23. Point M represents the mean flow at the last stable point, and the dashed red line the local flow coefficient and pressure rise conditions in the annulus at the last stable point

The effects of the distortion are remarkable. As for the case with porosity 0.5, the ψ and ϕ profiles averaged on the radius are shown in figure 6-17 and the cycle they produce is represented in the characteristic curve in figure 6-16 with dashed line. The mean flow is point M. The conditions blades are facing in different parts of the annulus are now very different. The points behind the grid reach very low flow rates, where the blades are locally expected to stall. On the other hand, points outside the distorted region are working at flow rates largely higher than the average value.

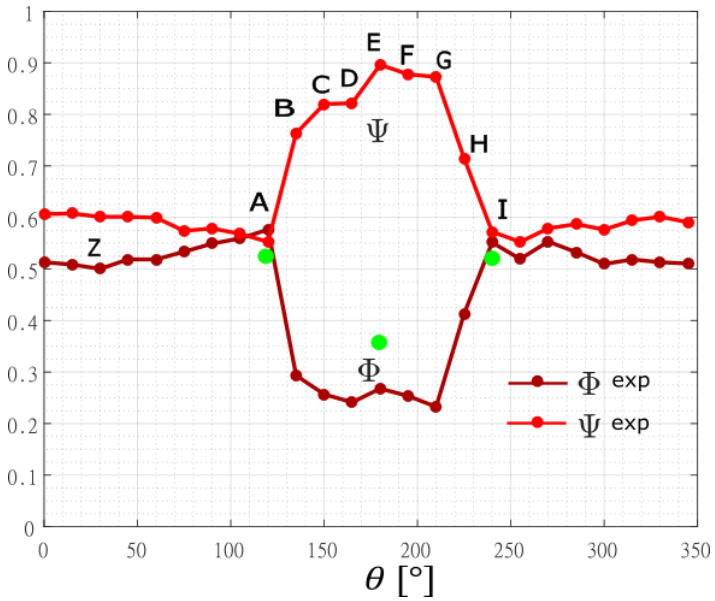

Figure 6-17 : flow coefficient and pressure rise at the last stable point as a function of θ for the 120° grid with porosity 0.23; the green marker are the values of ϕ extracted from PIV fields. Point from A to I are measured behind the grid and correspond to the same points in figure 6-16.

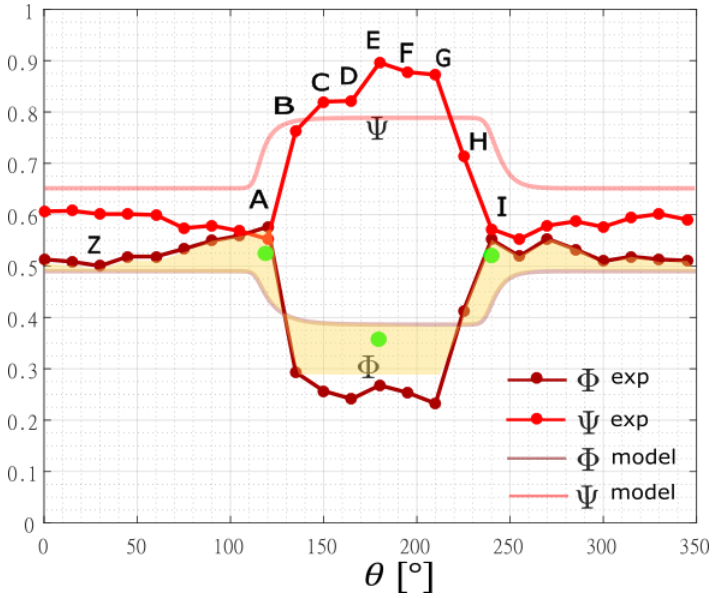

Figure 6-18 comparison between the experimental profiles and the profiles measured with Hynes Greitzer at the last stable point. In yellow are highlighted the areas marking the surplus of ϕ at the edges of the grid and the ϕ deficit behind the grid.

The effects of the stronger flow redistribution caused by the grid are reflected in the location of points A and I. They are at higher flow rate than point Z chosen far from the grid. From the velocity profiles (figure 6-17) it is clear that closer to the edges of the grid the flow rate is higher than far from the grid (point Z) and the lower is the ψ. This is due to a solid body type effect as schematized in figure 6-2 and it is not present as clearly in figure 6-5 for the 120° grid with porosity 0.5. The ϕ measured with PIV is also shown in figure 6-17.

The differences between the ϕ measured with PIV and estimated with the pressure rakes are consistent with the effect of upstream redistribution tending to decrease the velocity distortion in front of the compressor.

6.2.2 COMPARISON WITH MODEL

A comparison with the ψ and ϕ profiles calculated with Hynes Greitzer model shows more clearly the effect of the edges of the grid on the shape of the ϕ. In figure 6-18 the experimental profiles of figure 6-17 are compared to the profiles calculated with the model. The comparison shows that compared to the calculated flow coefficient ϕ, the experimental value has a surplus closer to the edges of the grid and a deficit behind the grid, and the two are almost balanced. In the model, in fact, no upstream redistribution is modelled in the basic flow, thus the shape of ϕ cannot take into account the effect of the edges of the grid which appears in the real flow. The consequences of the upstream redistribution on the ψ lead to a lower pressure rise compared to the model predicted pressure rise. The higher flow rate close to the grid edges causes a lower pressure rise locally (figure 6-18) and on the other hand, the low flow rate behind the grid does not cause a substantial increase in pressure rise, because locally the compressor operates closer to the peak, where the slope of the compressor is mild and losses are higher, so that a decrease of ϕ causes a smaller increase of ψ compared to when the compressor works at higher flow rates. Thus the average experimental pressure rise is lower than the one calculated with the model, as it is also seen comparing the experimental compressor characteristic curve with the one calculated by the model (figure 6-19).

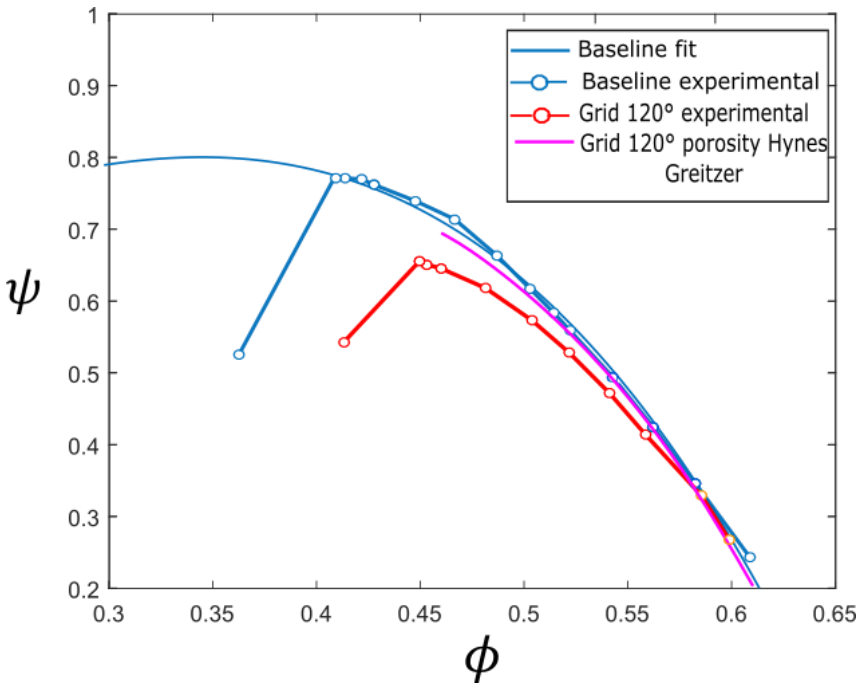

Figure 6-19: comparison of the experimental compressor curves of the baseline without the grid and the 120° with porosity 0.23 (both experimental and numerical).

The comparison between the experimental flow coefficient profiles and the ones calculated with the model, shows that the effects induced by the upstream redistribution of the grid are important and influence the pressure rise achieved by the compressor substantially. With weakly porous grids, the solid body type effects of flow redistribution lead to a different ϕ profile, which is linked to a different effect on the pressure rise of the compressor compared to the pressure rises estimated by mathematical models where no upstream redistribution is modelled. On the other hand, this does not prevent the models, as was seen in the previous chapter, to capture the instability at the correct mass flow rate. In the following we concentrate on the PIV fields to show some features of the flow in the regions A, E, I.

6.2.3 FLOW FIELDS IN THE BLADE CHANNELS

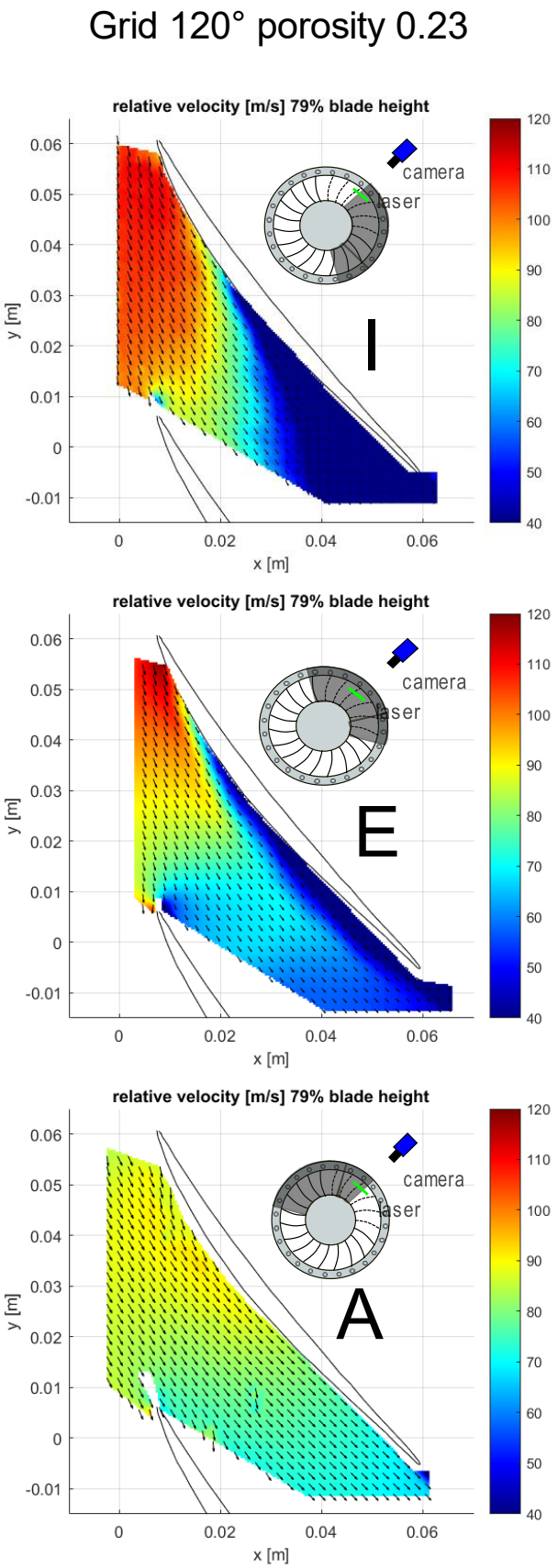

Figure 6-20 PIV fields (79% blade span) in the three positions A,E,I (figure 6-18) for the 120° grid with porosity 0.23 at the last stable point?

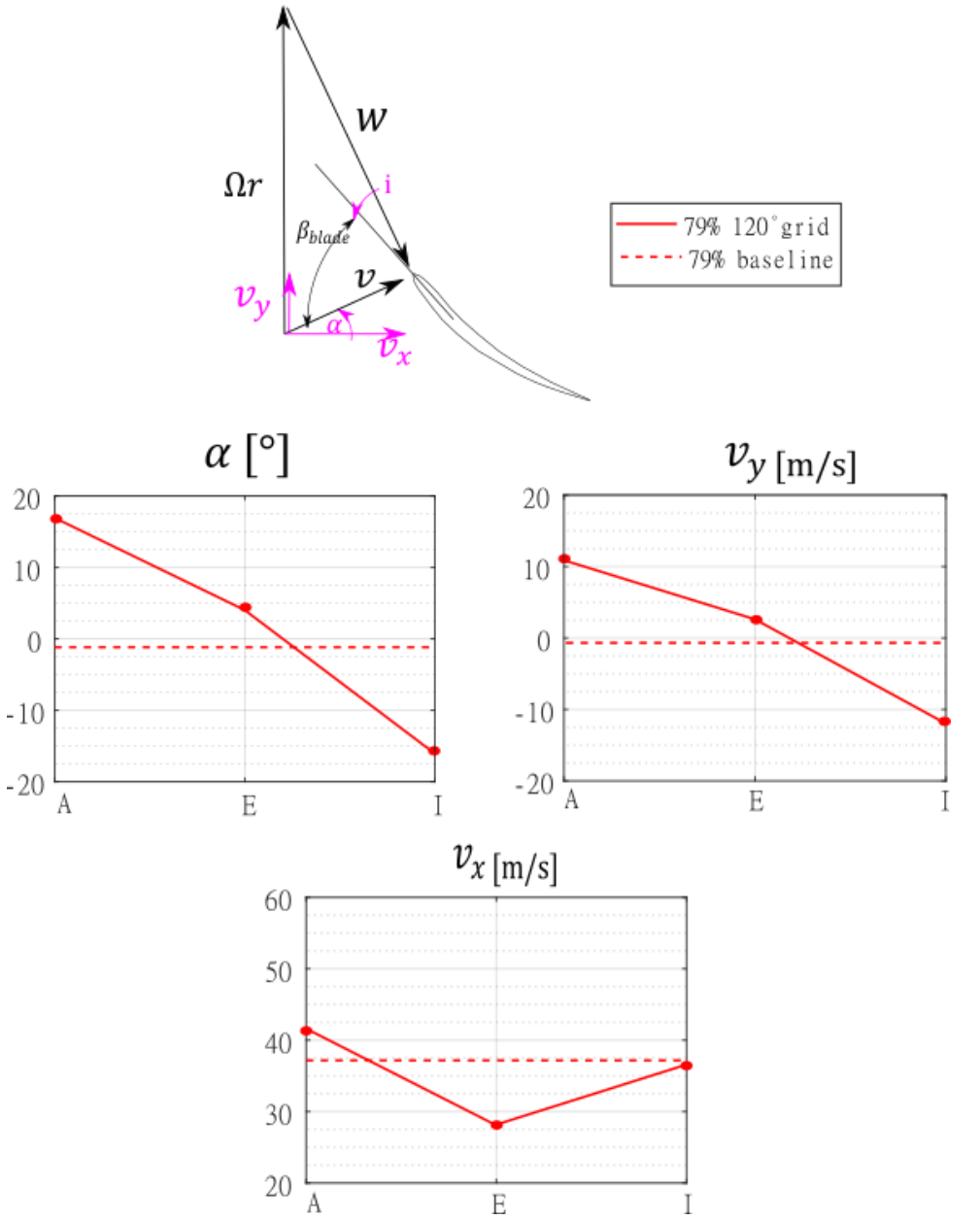

Figure 6-21: average calculated at the leading edge of PIV fields in figure 6-20 on the left of : absolute flow angle (α), tangential component of velocity (vy), axial component of velocity (vx)

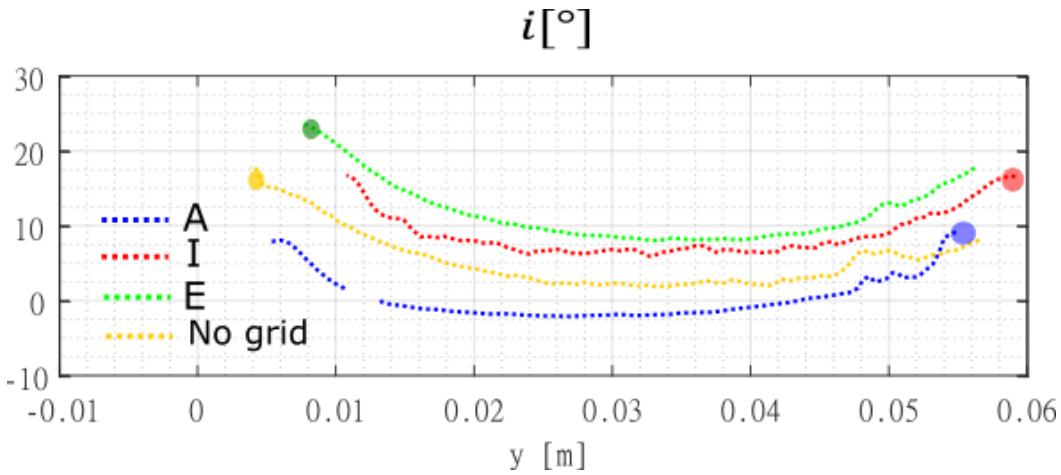

Figure 6-22 profiles of the incidence angle as a function of y extracted at the leading edge for the four PIV f fields in figure 6-20

In figure 6-20, the PIV fields at the radial plane at 79% of the blade span for the three positions laser/grid are presented. The asymmetry between A and I that was remarked in figure 6-8 in the case of porosity 0.5, is now dramatic. In A, the flow is clean from separation , and instead in I a strong separation is present. In figure 6-21, the averaged values of the angles and velocities corresponding to PIV fields in figure 6-20 are shown. The values in I have to be interpreted carefully because the flow is locally unsteady, and the values are extracted from the mean flow field.

As for the grid with porosity 0.5, one effect contributing to the asymmetry between A and I is the angle distortion and is linked to a similar pattern in the velocity triangles as the one shown in figure 6-11. The effect of angle distortion in A and I is stronger than for the porosity 0.5. The tangential velocities created by the tangential pressure gradients in A and I are of the order of 10 m/s, twice the value for porosity 0.5. The amplitude of the pressure loss on the other hand is around 3.5 times the pressure loss with porosity 0.5. These components of tangential velocity have an effect on the incidence on the blades. Figure 6-22 shows the incidence profiles at the leading edge. The incidence in A is reduced (the average on the channel is 0), consistently with the sign of tangential velocity. The low level of loading is clear in figure 6-20 by the weak diffusion of the relative velocity in the blade channel. On the other hand, higher incidence is met in E because of the axial velocity deficit (figure 6-21) and in I, helped by the tangential velocity component. Especially in E, the incidence is high and far beyond the stalling incidence for the non-distorted case. Stall of the blade would be expected, but the blade loading is preserved as it is clear observing figure 6-20 in the field E.

6.2.4 UNSTEADY ENERGY CONTENT

As for the case with porosity 0.5, the POD can provide further information on the level of unsteadiness in the flow. The cumulative energy in POD modes is shown in figure 6-23 for the three fields in figure 6-20, and compared to the energy without grid. Figure 6-23 shows that the most part of the energy content in the field is contained in the mean flow for positions E and A. On the other hand, in I, the flow contains high unsteadiness, as just 82% of the total energy is contained in the first POD mode.

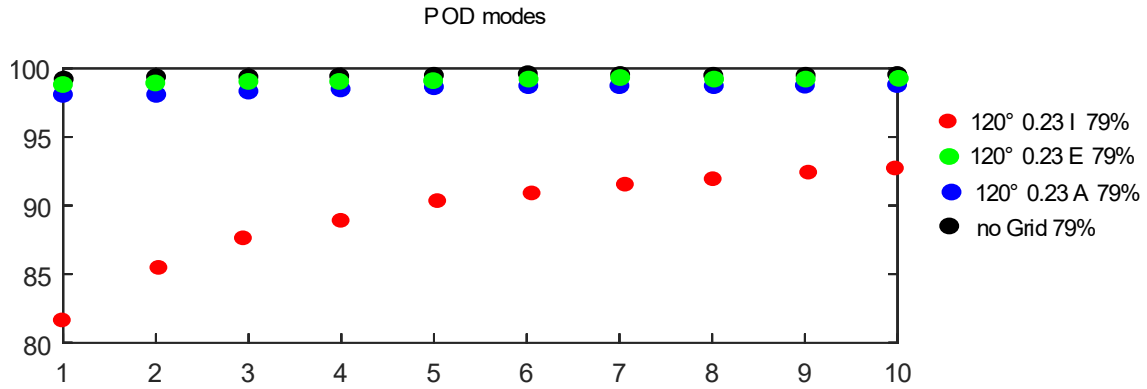

Figure 6-23 cumulative energy content in POD modes; comparison between the three fields in figure 6-20 and the baseline at the last stable point.

One element can help the interpretation of the flow in the different cases A, E, I: when blades are subjected to a strong change of incidence such as to go beyond the static stalling incidence of the blade, it is known (Ericsson and Reding, 1969) that the formation of large scale vortical structures is delayed in time from the moment when the peak stalling limit is reached, and for some time, the blade can operate at higher incidences. If we imagine that the peak incidence is reached behind the grid where the axial flow is at its minimum, since the blades are rotating, a delay of stall in time corresponds a delay in space, and the formation of vortical structures can be thus expected not exactly behind the grid at the peak of incidence, but towards the exit of the distorted region. This can partly explain why a strong separation is encountered in I and not in E, where incidence is maximum.

In the following, the POD modes and some instantaneous fields are shown for positions E and I, to show further differences in the flow fields. In figure 6-24, the POD modes for position E are shown. The bigger differences between the modes are encountered close to the suction surface. The second and third modes have alternated regions of low and high speed close to the suction surface, especially closer to the leading edge. The instantaneous fields shown in figure 6-25 show in fact that the first part of the suction surface closer to the leading edge is occupied by the separated region at some instants (instantaneous fields at $t_0 + 0.2\ s$ and $t_0 + 0.8\ s$) and at some other instants ($t_0 + 0.4\ s$ and $t_0 + 1\ s$) the separation region is occupying a region downstream, as if the separation region oscillates back and forth close to the leading edge. These phenomena are at the origin of the POD modes 2 and 3.

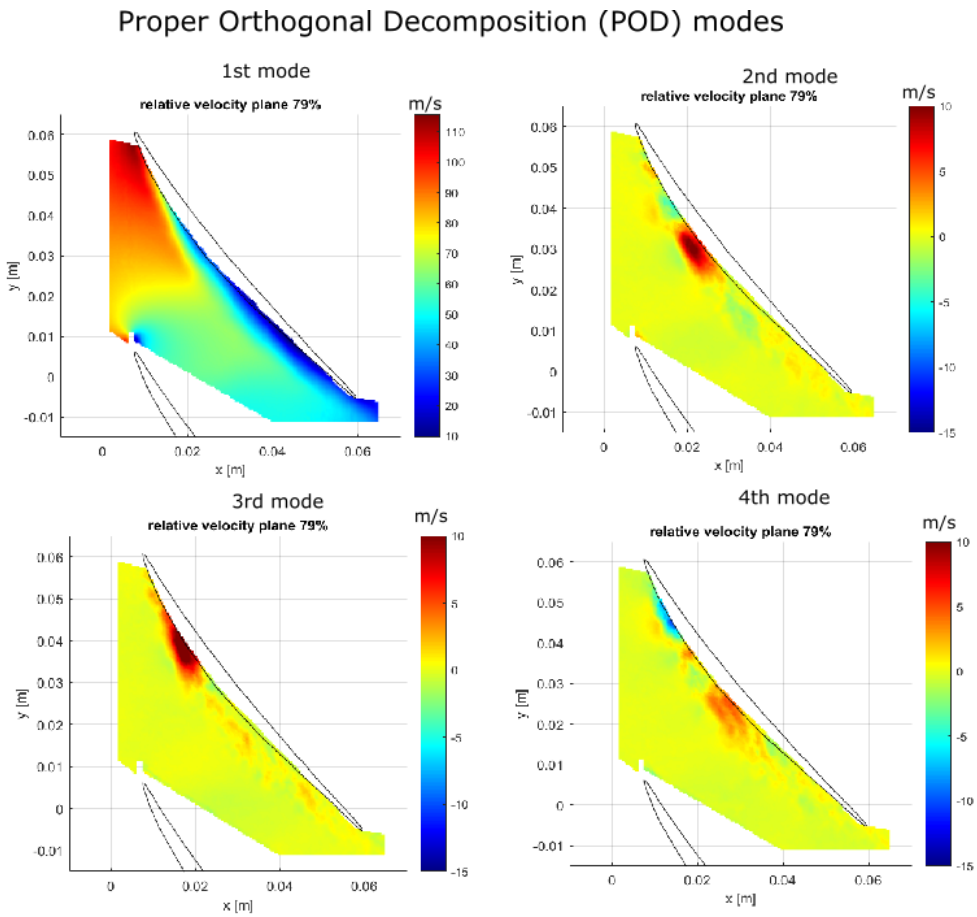

Figure 6-24: POD modes for the flow field in position E in figure 6-20

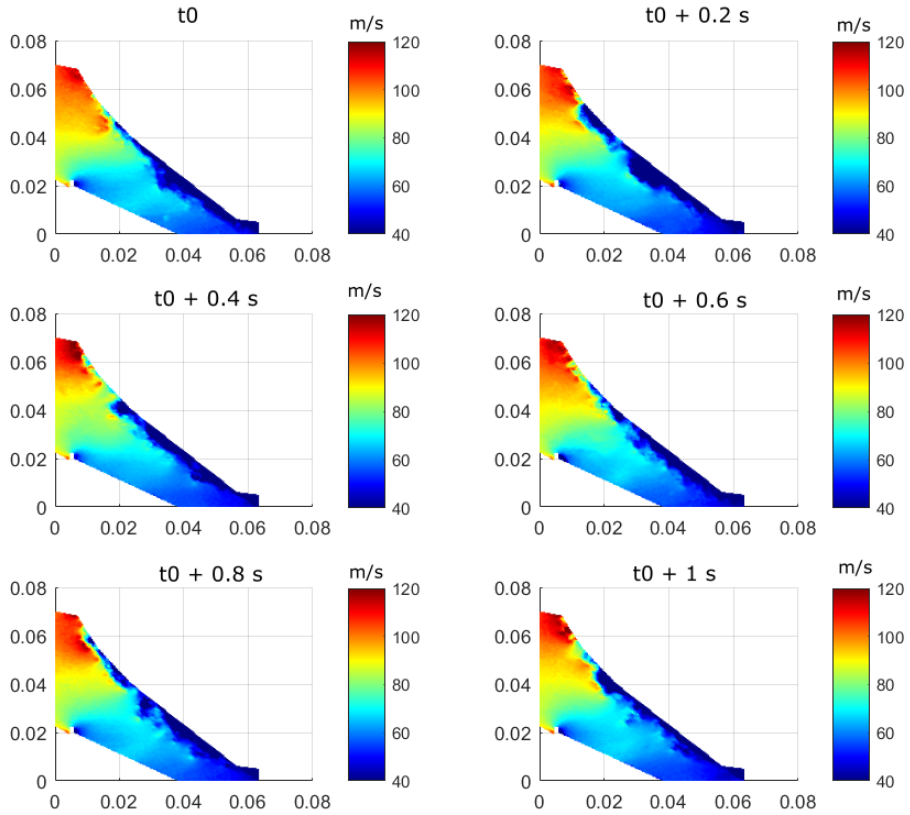

Figure 6-25 consecutive instantaneous flow fields in position E in figure 6-20

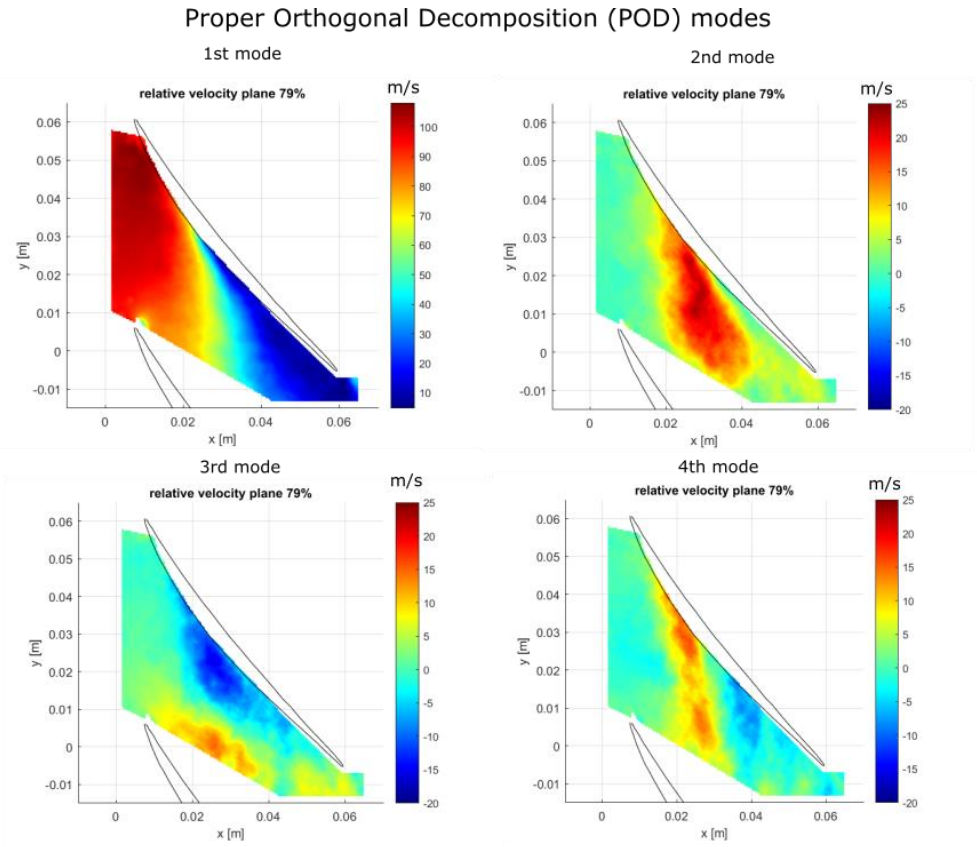

Figure 6-26 POD modes for the flow field in position I in figure 6-20

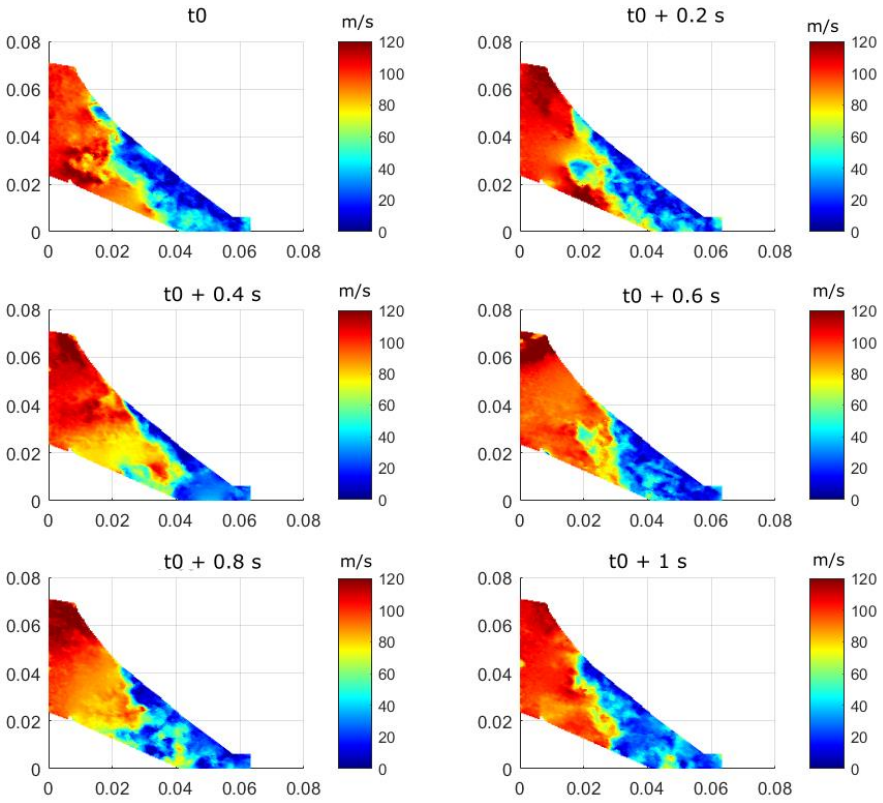

Figure 6-27 consecutive instantaneous flow fields in position I in figure 6-20

The POD modes for the field I were already shown in figure 4-32 , but have been replotted in figure 6-26 and compared to the instantaneous fields in figure 6-27. The oscillating modes (third and fourth) show that larger portions of flow oscillate back and forth in the channel compared to field E where just small portions close to the suction surface were involved. Some fields where the separation approaches the leading edge (t_0) alternates with fields where the separation is more concentrated over the second half of the channel closer to the trailing edge ($t_0 + 0.6\ s$).

6.2.5 3D FLOW

The flow in A and E in the other radial planes does not present very different flow features from the plane at 79% of the blade height. The occlusion of the blade channel at the exit of the distortion region, however, is not encountered at lower radial positions, indicating that the presence of the blockage towards the tip deviates the flow towards lower radial positions, generating strong radial gradients. In figure 6-28 the fields at the exit of the distortion region at different radii are shown. A strong radial flow is expected since the flow approaching the tip finds the channel occluded and must be redirected to lower radii. Such a kind of flow with a separation on the upper portion of the channel is expected also in other positions of the annulus more far from the exit of the distortion region, as it is suggested by the unsteady casing static pressure signals that were shown in the previous chapter. The signals indicate that a separation of flow is likely to exist on a significant extent of the annulus of the order of 90° and thus, strong three dimensional flow is expected in blade channels in those regions.

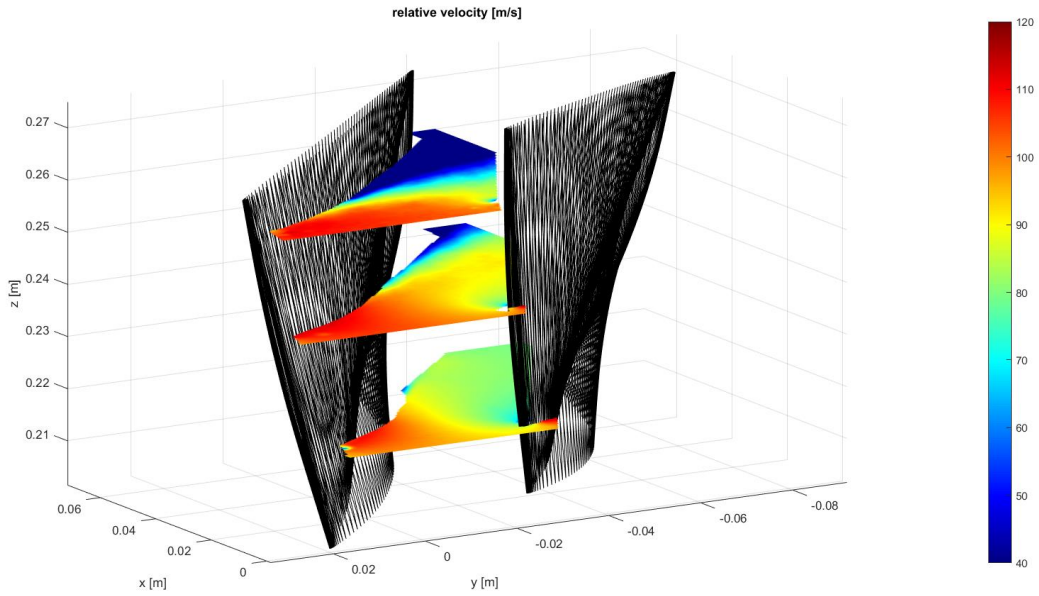

Figure 6-28: PIV fields at the 3 radial heights in position I at the exit of the distortion region.

6.3 CONCLUSIONS

To summarise, the grid with lower porosity creates a total pressure loss of about 3.5 times the pressure loss with the grid of porosity 0.5. The low porosity introduces a flow redistribution similar to the one that is found downstream of solid bodies that modifies the profile of ϕ usually encountered behind highly porous mediums, in particular leads to a flow deficit behind the grid, and flow surplus at the edges of the grid. The effect on the compressor pressure rise is a lower mean pressure rise compared to a pressure loss of the same amplitude but represented by a simple square wave as in the models like Hynes Greitzer and that can be typical of a highly porous medium. Another effect of the stronger distortion compared to porosity 0.5, is the presence of flow separation at the exit of the distortion region, which causes a three dimensional flow redistribution on a substantial part of the annulus.

Concerning the gird with porosity 0.23, a final consideration can be done: even if the upstream redistribution is influenced by the edge effect of the grid and flow separation and 3D flow is present, simplified models (as Hynes Greitzer) capture the arising of the instability at the correct mass flow rate (previous chapter). This suggests that these effects that are captured in the experiments and are missed in the model are not of leading order to determine the onset of the instability. Figure 5-2 in the previous chapter shows unsteady signals in which in a consistent part of the annulus a separation perturbation appears; the same separation cannot be captured by the Hynes Greitzer model, since the compressor is represented as an actuator disc with infinite blades and no separation can happen. Thus, since in both experiments and model the compressor stalls at the same flow rate, we can imagine that the presence of three dimensional flow and separation is not determinant (for the 120° grid) for the growth of the instability. The comparison suggests that also the modification of the shape of the ϕ profile due to the edge of the grid (figure 6-18) is not of primary importance and the main effect is due to the total pressure distortion induced by the grid.

7 CONCLUSIONS AND FUTURE PERSPECTIVES

In this work, a study of the effects of azimuthal inlet flow distortion on the performance and stability of an axial compressor has been performed. Various grids of different porosity and angular extension have been installed in front of a compressor stage, and the impact of the various grids on the performance of the machine has been measured. PIV measurements have also been performed with some grids of interest and have allowed to identify flow structures that would have been very hard to identify without, due to the complexity of distorted flow and the requirement of high spatial resolution. Unsteady pressure measurements at the casing were also used, to capture the flow dynamic, especially during transient operation.

The range of grid porosity was very wide compared to other studies previously performed in literature, and allows to enrich the description of the physics of grid distorted flows capturing some physics that was missed when the range of porosity was restricted. In particular the experiments show evidence of very different types of flow behind the grids, which result in different behaviour of the compressor. The performance of the compressor has been characterised in terms of stall margin, which is an important parameter for the machine performance. In the following, the main conclusions of the study are summarized:

- Identification of 4 regimes of flow and 4 regimes of stall.

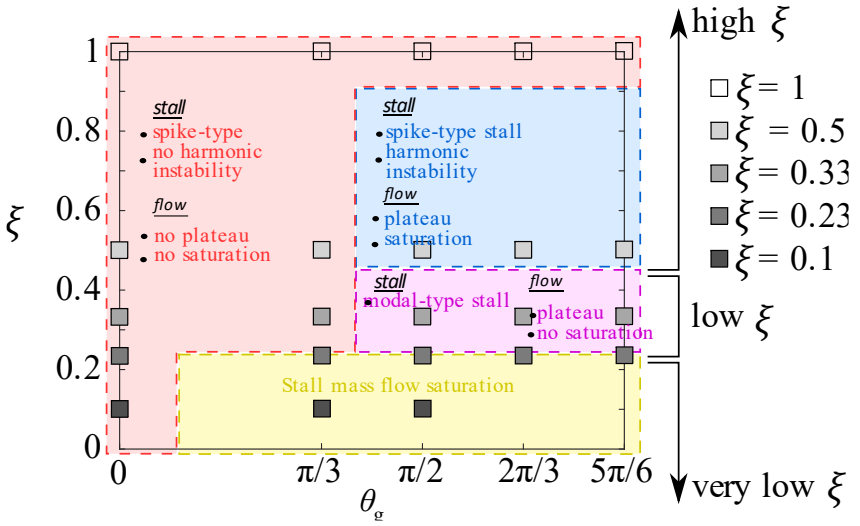

Figure 7-1 : four flow regimes and four stall regimes summarized in the same plot as a function of porosity and grid sector extension

The analysis of the effect of the various grid distorsions on the stall margin has proven the existence of four different flow regimes, some of them not described in previous studies, due to the use of very high grid porosities. For high porosities, the stall margin is seen to saturate when the extent of the grid increases beyond a specific angle called ‘’critical angle”, consistently with previous studies as Reid (1969). Thus this study confirms the existence of two regimes of behaviour separated by the critical angle for highly porous grids. On the other hand, the experiments on the moderately low porosity grids (0.33 , 023) have shown that no saturation of the stall margin is observed when the angular sector of the grid is increased, and no critical angle is identified. This represent a novelty and introduces a new regime for wide grids and low porosity. The results further demonstrated that the effect of saturation of the stall margin for high porosities is connected to the saturation of the total pressure loss of the grid when the angular extension is increased, and this is an

effect related to the high porosity of the grid. In fact, for lower porosities, no saturation of the total pressure loss is observed increasing the extension, and no saturation of the stall margin is thus observed.
A fourth new regime was identified at very low porosities (<0.23). In this range, the stall mass flow rate saturates and reducing further the porosity does not decrease the stall margin further, no matter the angular extent of the grid. The saturation of the stall flow rate for this last regime was explained by the saturation of the upstream flow redistribution following severe blockages in the blade channels.

The analysis of unsteady pressure signals at the last stable point and during the transition towards stall, have then allowed to extract information about the stall mechanism. It has been seen that corresponding to the four flow regimes, four stall regimes exist. For low angular extensions (below the critical angle), the stall mechanism is of spike type, as in the undistorted case. For higher angular extensions it depends on the porosity. High porosity grids introduce harmonic perturbations, but finally the stall mechanism is of spike type, while lower porosities are characterised by modal stall. For the fourth regime at very low porosity (<0.23) the mechanism is not clear since the flow separation strongly influences the physics.
The correspondence between the flow regimes and the stall regimes suggest that the stall mechanism is very much determined by the type of flow upstream of the compressor.

- Distortion scaling

In two of the identified regimes, a new scaling of the stall margin has been provided, based on physical arguments derived from models existing in literature (Hynes Greitzer). The non existence of the critical angle for low porosities, questions the use of the well known DC60 index used to correlate the distortion with the stall margin. The hypothesis on which is based this index (the existence of a critical angle) is met just for a restricted range of high porosities. Following Hynes Greitzer model, a physical based scale of the flow can be identified in an ‘’interaction angle” which characterises the interaction between the distorted and undistorted regions. It can be defined analytically and, in the case of a squared pressure perturbation, is equal to:

$$\theta_{int} = \frac{2\pi\lambda}{a\sqrt{\psi_m + \psi_g - R_L}}$$

and can be calculated numerically knowing the compressor geometry and the distortion pattern.

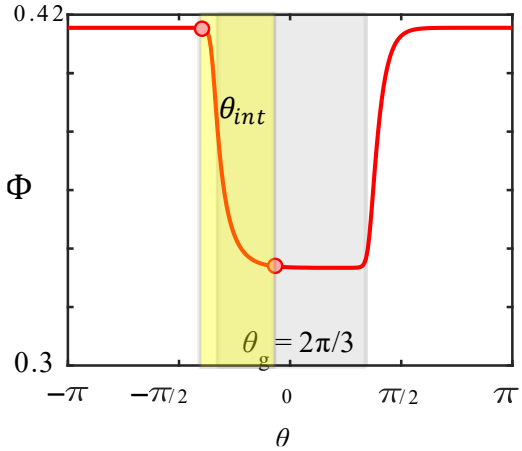

Figure 7-2 : profile of flow coefficient in the annulus $\phi(\theta)$for a grid extent θ_g of 120° ; θ_{int} scale in yellow ;

With reference to figure 7-2, θ_{int} describes the extension of the interaction region where the flow coefficient $\phi(\theta)$ changes from its value in the distorted region and outside of it. When the grid extension is smaller or equal to twice the interaction angle, the full flow is dominated by the interaction of the distorted and

undistorted regions. When the grid extension is bigger than twice the interaction angle, a low speed flow weakly influenced by the undistorted flow can establish, leading to a topologically different flow. Thus $2\theta_{int}$ separates the first regime (red in figure 7-1) from the second and third (blue and purple in figure 7-1).
Based on this interaction scale, a new index is built, which allows to scale the stall margin for the wide grids (more than twice the interaction angle) of high and moderate porosities. This scaling is based on an angle characteristic of the grid and interaction scales:

$$\theta_{avg} = \frac{\theta_{int} + \theta_g}{2}$$

where θ_g is the angular extent of the grid. The definition is chosen such as the window in which the total pressure drop is integrated corresponds as an order of magnitude to the plateau of the flow coefficient ϕ itself, accounting at the same time the two scales θ_{int} and θ_g (figure 7-3).

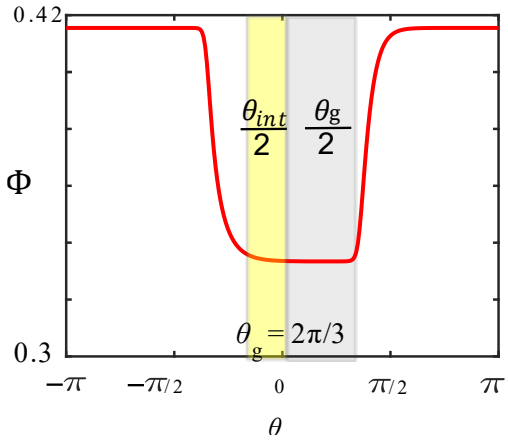

Figure 7-3 : interpretation of the definition of θ_{avg}

The distortion index in then inroduced:

$$DC\theta_{Avg} = \frac{\Delta p_t^*}{\bar{p_t}}$$

with Δp_t^* the difference between the integral pressure drop of the grid averaged on θ_{avg} and $\bar{p_t}$, the average of the pressure drop of the grid. The advantage of the scaling is that it does not rely on the definition of a critical angle, but intrisically captures the boundary between the regimes by the definition of the interaction angle, which is universal and can be caluclated for every compressor. A different scaling must on the other hand be found for narrow grids, and for the very low porousity regime. In these regimes in fact the flow cannot be characterized by the interaction scale.

- Detailed flow analysis

Finally, a detailed analysis of the flow has been conducted for two particular flow regimes with a 120° of high pororisty (0.5) and low porosity (0.23). For the first regime, it was observed that the flow is not very different than without the grid, consistently with the low level of distortion generated. An asymmetry in the flow behind the two edges of the grid has been observed, caused by the tangential pressure gradient between distorted and undistorted regions. This gradients modifies locally the velocity triangles, creating co-swirl and counter-swirl behind the two edges of the grid.
For the second regime, the effect of the stronger distortion is evident on the flow. In particular, the flow redistribution behind the grid is more similar to the one created by a solid object blockage, due to the low

porosity of the grid. The asymmetry in the flow that was observed in the previous regime is increased and at the exit of the distortion region, blade stall, leading to separated flow in the blade channels.
The flow coefficient profiles $\phi(\theta)$ have been compared to the profiles calculated with the Hynes Greitzer model. A square pattern pressure profile was given as an input to the model. The pressure drop was of the same amplitude as the one generated by the grid in the experiments. The deviations of $\phi(\theta)$ are bigger for grid of lower porosity and the comrpessor pressure rise calculated with the model is inaccurate, but still, the calculated stall mass flow is well predicted. This is remarkable, especially considering the complexity of the flow appearing from PIV measurements and the simplified model hypothesis. This confirms the relevance of the model as prelimiary predictive tool.

Some future perspectives can be drawn:

- Some CFD simulations are going to be performed by ONERA on the same configurations that have been tested experimentally. This is an opportunity to refine the flow analysis; in particular:
    - It will be possible to analyse the velocity flow fields in the other regions where PIV has not been performed.
    - It will be instructive to compare the onset of rotating stall in the numerical case and in the experimental case, in order to confirm and investigate further the richness in stalling behaviours encountered with different grids.
- It would be interesting to enrich the experimental study especially:
    - Performing PIV with 60° grids where the flow is dominated by the interaction region.
    - Testing more complex distortion patterns (example in figure 7-4) and exploring the validity of the correlations in those cases. It could be interesting to test radial pattern of distortion, especially to investigate their effect on the stall mechanism, which has been seen in this study to be dependent on the distortion pattern. The investigations could be also extended to swirl distortion, that lacks until today a theoretical basis.
- Correlations should be developed in the two following regimes:
    - $\frac{\theta_{int}}{\theta_g} \leq 0.4$. A new scaling is needed due to the different type of flow, dominated by the interaction of the distorted and undistorted flow. A better knowledge of mixing layers is needed, especially in the presence of internal flow where pressure gradients play a substantial role.
    - In the very low porosity regime, where the stall mass flow rate saturates. A starting point could be to define a criterion to identify for which intensities of distortion, channel blockage is encountered, in order to base the boundary of this fourth regime on a more physical ground.

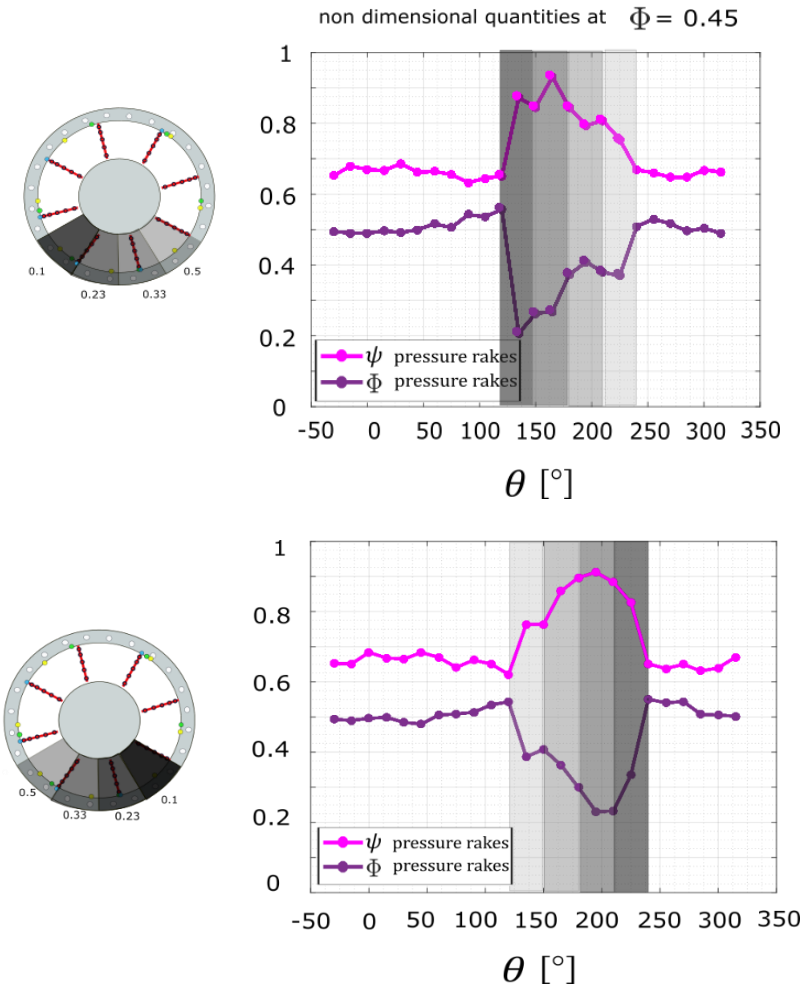

Figure 7-4 examples of distortion patterns that can be tested in the future to extend the present study

REFERENCES

AIR1419C: Inlet Total-Pressure-Distortion Considerations for Gas-Turbine Engines - SAE International." 2017 https://www.sae.org/standards/content/air1419c/.

Arntz, Aurélien, Olivier Atinault, Daniel Destarac, and Alain Merlen. 2014. "Exergy-Based Aircraft Aeropropulsive Performance Assessment: CFD Application to Boundary Layer Ingestion." In *32nd Applied Aerodynamics Conference*, *AIAA Aviation 2014*, Atlanta. https://doi.org/10.2514/6.2014-2573.

ARP1420: Gas Turbine Engine Inlet Flow Distortion Guidelines - SAE International." 2017 https://www.sae.org/standards/content/arp1420/.

Baretter, Alberto, Benjamin Godard, Pierric Joseph, Olivier Roussette, Francesco Romanò, Raphael Barrier, and Antoine Dazin. 2021. "Experimental and Numerical Analysis of a Compressor Stage under Flow Distortion." *International Journal of Turbomachinery, Propulsion and Power* 6 (November): 43. https://doi.org/10.3390/ijtpp6040043.

Beale, David, Kevin Cramer, and Peter King. 2002. "Development of Improved Methods for Simulating Aircraft Inlet Distortion in Turbine Engine Ground Tests ." In *22nd AIAA Aerodynamic Measurement Technology and Ground Testing Conference,* St.Louis. https://doi.org/10.2514/6.2002-3045.

Bissinger, Norbert C., and Thomas Breuer. 2010. "Basic Principles – Gas Turbine Compatibility – Intake Aerodynamic Aspects." In *Encyclopedia of Aerospace Engineering*. John Wiley & Sons, Ltd. https://doi.org/10.1002/9780470686652.eae487.

Bobula, George A., Ronald H. Soeder, and Leo A. Burkardt. 1983. "Effect of Variable Guide Vanes on the Performance of a High-Bypass Turbofan Engine." *Journal of Aircraft* 20 (4): 306–11. https://doi.org/10.2514/3.44868.

Braithwaite, W., JR. E. Graber, and C. Mehalic. 1973. "The Effect of Inlet Temperature and Pressure Distortion on Turbojet Performance." In *9th Propulsion Conference,* Las Vegas ; American Institute of Aeronautics and Astronautics. https://doi.org/10.2514/6.1973-1316.

Bruce, E. 1971 "Design and Evaluation of Screens to Produce Multi-Cycle plus or Minus 20% Amplitude Sinusoidal Velocity Profiles." In *8th Aerodynamic Testing Conference,* Bethesda, USA. American Institute of Aeronautics and Astronautics. https://doi.org/10.2514/6.1974-623.

Bucalo, Tamara Guimaraes, K. Todd Lowe, and Walter F. O'Brien. 2013 "An Overview of Recent Results Using the StreamVane Method for Generating Tailored Swirl Distortion in Jet Engine Research." In *54th AIAA Aerospace Sciences Meeting*. San Diego, California. American Institute of Aeronautics and Astronautics. https://doi.org/10.2514/6.2016-0534.

Burstadt, Paul L., J. E. Calogeras, and C. M. Mehalic. 1971. "Experimental Investigation of the Effect of Screen Induced Total Pressure Distortion on Turbojet Stall Margin." NASA Technical Memorandum ; Lewis Research center ; Cleveland, Ohio.

Camp, T. R., and I. J. Day. 1998. "1997 Best Paper Award—Turbomachinery Committee: A Study of Spike and Modal Stall Phenomena in a Low-Speed Axial Compressor." *Journal of Turbomachinery* 120 (3): 393–401. https://doi.org/10.1115/1.2841730.

Carta, Franklin O. 1967. "Unsteady Normal Force on an Airfoil in a Periodically Stalled Inlet Flow." *Journal of Aircraft* 4 (5): 416–21. https://doi.org/10.2514/3.43861.

Chue, R., T. P. Hynes, E. M. Greitzer, C. S. Tan, and J. P. Longley. 1989. "Calculations of Inlet Distortion Induced Compressor Flow Field Instability." *International Journal of Heat and Fluid Flow* 10 (3): 211–23. https://doi.org/10.1016/0142-727X(89)90040-4.

Conrad, E. William, and Adam E. Sobolewski. 1950. "Investigation of Effects of Inlet-Air Velocity Distortion on Performance of Turbojet Engine." Report. UNT Digital Library. September 13, 1950. https://digital.library.unt.edu/ark:/67531/metadc58625/m1/13/.

Cousins, William T., Dmytro Voytovych, Gregory Tillman, and Eric Gray. 2017 "Design of a Distortion-Tolerant Fan for a Boundary-Layer Ingesting Embedded Engine Application." In *53rd AIAA/SAE/ASEE Joint Propulsion Conference*. Atlanta, Georgia. American Institute of Aeronautics and Astronautics. Accessed March 2, 2022. https://doi.org/10.2514/6.2017-5042.

Cumpsty, Nicholas, and Andrew Heyes. 2015. *Jet Propulsion: A Simple Guide to the Aerodynamics and Thermodynamic Design and Performance of Jet Engines*. 3rd edition. Cambridge, United Kingdom: Cambridge University Press.

Day, I. J. 1993. "Stall Inception in Axial Flow Compressors." *Journal of Turbomachinery* 115 (1): 1–9. https://doi.org/10.1115/1.2929209.

———. 2015. "Stall, Surge, and 75 Years of Research." *Journal of Turbomachinery* 138 (1). https://doi.org/10.1115/1.4031473.

Ehrich, Fredric. 1957. "Circumferential Inlet Distortions in Axial Flow Turbomachinery." *Journal of the Aeronautical Sciences* 24 (6): 413–17. https://doi.org/10.2514/8.3870.

Elder, J. W. 1959. "Steady Flow through Non-Uniform Gauzes of Arbitrary Shape." *Journal of Fluid Mechanics* 5 (3): 355–68. https://doi.org/10.1017/S0022112059000258.

Emmons, H. W. 1955. "Compressor Surge and Stall Propagation." *Trans. of the ASME* 77 (4): 455–67.

Ericsson, L. E., and J. P. Reding. 1969. "Unsteady Airfoil Stall." NASA-CR-66787. https://ntrs.nasa.gov/citations/19690022782.

Fidalgo, V. Jerez, C. A. Hall, and Y. Colin. 2012. "A Study of Fan-Distortion Interaction Within the NASA Rotor 67 Transonic Stage." *Journal of Turbomachinery* 134 (5). https://doi.org/10.1115/1.4003850.

Florea, Razvan V., Claude Matalanis, Larry W. Hardin, Mark Stucky, and Aamir Shabbir. 2015. "Parametric Analysis and Design for Embedded Engine Inlets." *Journal of Propulsion and Power* 31 (3): 843–50. https://doi.org/10.2514/1.B34804.

Geiselhart, Karl A., David L. Daggett, Ron Kawai, and Doug Friedman. 2003. "Blended Wing Body Systems Studies: Boundary Layer Ingestion Inlets with Active Flow Control." NASA/CR-2003-212670

Gong, Yifang. 1999. "A Computational Model for Rotating Stall and Inlet Distortions in Multistage Compressors." PhD Thesis, Massachusetts Institute of Technology. https://dspace.mit.edu/handle/1721.1/9733.

Graf, M. B., T. S. Wong, E. M. Greitzer, F. E. Marble, C. S. Tan, H.-W. Shin, and D. C. Wisler. 1998. "Effects of Nonaxisymmetric Tip Clearance on Axial Compressor Performance and Stability." *Journal of Turbomachinery* 120 (4): 648–61. https://doi.org/10.1115/1.2841774.

Guimarães, Tamy, K. Todd Lowe, and Walter O'Brien. 2018. « Particle Image Velocimetry for Distorted Turbofan Engine Inlet Applications ». In *19th International Symposium on the Application of Laser and Imaging Techniques to Fluid Mechanics,* Lisbon Portugal.

Gunn, Ewan J., Sarah E. Tooze, Cesare A. Hall, and Yann Colin. 2013. "An Experimental Study of Loss Sources in a Fan Operating With Continuous Inlet Stagnation Pressure Distortion." *Journal of Turbomachinery* 135 (5). https://doi.org/10.1115/1.4007835.

Gunn, E. J., and C. A. Hall. 2014. "Aerodynamics of Boundary Layer Ingesting Fans." In . American Society of Mechanical Engineers Digital Collection. https://doi.org/10.1115/GT2014-26142.

Hewkin-Smith, M., G. Pullan, S. D. Grimshaw, E. M. Greitzer, and Z. S. Spakovszky. 2019. "The Role of Tip Leakage Flow in Spike-Type Rotating Stall Inception." *Journal of Turbomachinery* 141 (6). https://doi.org/10.1115/1.4042250.

Hoopes, Kevin M., and Walter F. O'Brien. 2015 "The StreamVane Method: A New Way to Generate Swirl Distortion for Jet Engine Research." In *49th AIAA/ASME/SAE/ASEE Joint Propulsion Conference*. San Jose, California. American Institute of Aeronautics and Astronautics. https://doi.org/10.2514/6.2013-3665.

Hynes, T. P., and E. M. Greitzer. 1987. "A Method for Assessing Effects of Circumferential Flow Distortion on Compressor Stability." *Journal of Turbomachinery* 109 (3): 371–79. https://doi.org/10.1115/1.3262116.

Idelchik, I. E. 1986. *Handbook of Hydraulic Resistance (2nd Revised and Enlarged Edition)*. *Washington*. https://ui.adsabs.harvard.edu/abs/1986wdch.book.....I.

Iura, Toru, and W. Duncan Rannie. 1953. "Observations of Propagating Stall in Axial-Flow Compressors." CALIFORNIA INST OF TECH PASADENA MECHANICAL ENGINEERING LAB. Technical Report 51754

Jahnen, Werner, Thomas Peters, and Leonhard Fottner. 2014. "Stall Inception in a 5-Stage HP-Compressor With Increased Load Due to Inlet Distortion." In . *ASME International Gas Turbine and Aeroengine*

Congress and Exhibition, Indianapolis, USA. American Society of Mechanical Engineers Digital Collection. https://doi.org/10.1115/99-GT-440.

Jardin, T. 2017. "Coriolis Effect and the Attachment of the Leading Edge Vortex." *Journal of Fluid Mechanics* 820 (June): 312–40. https://doi.org/10.1017/jfm.2017.222.

Katz, Robert. 1958. "Performance of Axial Compressors with Asymmetric Inlet Flows." Report or Paper. Pasadena, CA: California Institute of Technology. June 1958. https://resolver.caltech.edu/CaltechAUTHORS:20151105-165306203.

Kawai, Ronald T., Douglas M. Friedman, and Leonel Serrano. 2006. "Blended Wing Body (BWB) Boundary Layer Ingestion (BLI) Inlet Configuration and System Studies."NASA/CR-2006-214534

Koo, J.-K., and David F. James. 1973. "Fluid Flow around and through a Screen." *Journal of Fluid Mechanics* 60 (3): 513–38. https://doi.org/10.1017/S0022112073000327.

Laws, E., and J. Livesey. 1978."Flow Through Screens." In *Annual Review of Fluid Mechanics* 10(1)https://doi.org/10.1146/

Lesser, Andreas, and Reinhard Niehuis. 2014. "Transonic Axial Compressors With Total Pressure Inlet Flow Field Distortions." In ASME Turbo Expo 2014, Düsseldorf, Germany. American Society of Mechanical Engineers Digital Collection. https://doi.org/10.1115/GT2014-26627.

Lin, Feng, Meilin Li, and Jingyi Chen. 2005. "Long-to-Short Length-Scale Transition: A Stall Inception Phenomenon in an Axial Compressor With Inlet Distortion." *Journal of Turbomachinery* 128 (1): 130–40. https://doi.org/10.1115/1.2098808.

Lin, Peng, Cong Wang, and Yong Wang. 2017. "A High-Order Model of Rotating Stall in Axial Compressors with Inlet Distortion." *Chinese Journal of Aeronautics* 30 (3): 898–906. https://doi.org/10.1016/j.cja.2017.03.014.

Malavasi, Stefano, Gianandrea Messa, Umberto Fratino, and Alessandro Pagano. 2012. "On the Pressure Losses through Perforated Plates." *Flow Measurement and Instrumentation* 28 (December): 57–66. https://doi.org/10.1016/j.flowmeasinst.2012.07.006.

Margalida, Gabriel. 2019. "Analyse Expérimentale et Contrôle Actif de l'écoulement Dans Un Compresseur Axial Mono-Étagée Durant La Transition Vers Le Décrochage Tournant." These de doctorat, ENSAM. https://www.theses.fr/2019ENAM0039.

Margalida, Gabriel, Pierric Joseph, Olivier Roussette, and Antoine Dazin. 2020. "Comparison and Sensibility Analysis of Warning Parameters for Rotating Stall Detection in an Axial Compressor." *International Journal of Turbomachinery, Propulsion and Power* 5 (3): 16. https://doi.org/10.3390/ijtpp5030016.

McCarthy, J. H. 1964. "Steady Flow Past Non-Uniform Wire Grids." *Journal of Fluid Mechanics* 19 (4): 491–512. https://doi.org/10.1017/S0022112064000866.

Melick, H. C., 1973. " Analysis of Inlet Flow Distortion and Turbulence Effects on Compressor Stability." NASA_NTRS_Archive_19730012966.

Miller D.S. 1990. "Internal flow systems." Bedford, UK :Cranfield

Moore, F. K. 1984. "A Theory of Rotating Stall of Multistage Axial Compressors: Part I—Small Disturbances." *Journal of Engineering for Gas Turbines and Power* 106 (2): 313–20. https://doi.org/10.1115/1.3239565.

Moore, F. K., and E. M. Greitzer. 1986. "A Theory of Post-Stall Transients in Axial Compression Systems: Part I—Development of Equations." *Journal of Engineering for Gas Turbines and Power* 108 (1): 68–76. https://doi.org/10.1115/1.3239887.

Ochs, Stuart S., Gregory Tillman, Jongwook Joo, and Dmytro M. Voytovych. 2017. "Computational Fluid Dynamics-Based Analysis of Boundary Layer Ingesting Propulsion." *Journal of Propulsion and Power* 33 (2): 522–30. https://doi.org/10.2514/1.B36069.

Overall, B., and R. Harper. 1977. "The Airjet Distortion Generator System - A New Tool for Aircraft Turbine Engine Testing." In *13th Propulsion Conference*. Joint Propulsion Conferences. Orlando, Florida. American Institute of Aeronautics and Astronautics. https://doi.org/10.2514/6.1977-993.

Page, James H., Paul Hield, and Paul G. Tucker. 2018. "Effect of Inlet Distortion Features on Transonic Fan Rotor Stall." *Journal of Turbomachinery* 140 (7). https://doi.org/10.1115/1.4040030.

Pearson, H., and A. B. McKenzie. 1959. "Wakes in Axial Compressors." *The Aeronautical Journal* 63 (583): 415–16. https://doi.org/10.1017/S0368393100071273.

Perovic, D., C. A. Hall, and E. J. Gunn. 2015. “Stall Inception in a Boundary Layer Ingesting Fan.” *J. Turbomach*. Sep 2019, 141(9): https://doi.org/10.1115/GT2015-43025.

Pinker, R. A., and M. V. Herbert. 1967. “Pressure Loss Associated with Compressible Flow through Square-Mesh Wire Gauzes.” *Journal of Mechanical Engineering Science* 9 (1): 11–23. https://doi.org/10.1243/JMES_JOUR_1967_009_004_02.

Plourde, G., Roberts, F. and Smakula, F. 1968. “Insights into Axial Compressor Response to Distortion.” In *4th Propulsion Joint Specialist Conference*. Cleveland, USA. American Institute of Aeronautics and Astronautics.. https://doi.org/10.2514/6.1968-565.

Pullan, G., A. M. Young, I. J. Day, E. M. Greitzer, and Z. S. Spakovszky. 2015. “Origins and Structure of Spike-Type Rotating Stall.” *Journal of Turbomachinery* 137 (5). https://doi.org/10.1115/1.4028494.

Rannie, W. Duncan, and Frank E. Marble. 1957. “Unsteady Flows in Axial Turbomachines.” Report or Paper. 19680066466 Caltech. 1957. https://resolver.caltech.edu/CaltechAUTHORS:20110204-111252490.

Reid, C. 1969. “The Response of Axial Flow Compressors to Intake Flow Distortion.” In *ASME Gas Turbine Conference and Products Show*, Cleveland, Ohio.

Royce, Rolls. 2015. *The Jet Engine*. John Wiley & Sons.

Schneck, William, Anthony Ferrar, Justin Bailey, Kevin Hoopes, and Walter O’Brien. 2013 “Improved Prediction Method for the Design of High-Resolution Total Pressure Distortion Screens.” In *51st AIAA Aerospace Sciences Meeting Including the New Horizons Forum and Aerospace Exposition*. Grapevine, Texas. American Institute of Aeronautics and Astronautics. https://doi.org/10.2514/6.2013-1133.

Sciacchitano, A. 2019. “Uncertainty Quantification in Particle Image Velocimetry.” *Measurement Science and Technology* 30 (9): 092001. https://doi.org/10.1088/1361-6501/ab1db8.

Sears, W. R. 1953. “On Asymmetric Flow in an Axial-Flow Compressor Stage.” *Journal of Applied Mechanics* 20 (1): 57–62. https://doi.org/10.1115/1.4010594.

Sears, William R. 1955. “Rotating Stall in Axial Compressors.” *Zeitschrift Für Angewandte Mathematik Und Physik ZAMP* 6 (6): 429–55. https://doi.org/10.1007/BF01600530.

Stenning, A. H., Barry Stanley Seidel, and Yasutoshi Senoo. 1959. “Effect of Cascade Parameters on Rotating Stall.”NASA-MEMO-3-16-59W

Stenning, Alan Hugh. 1955. “Stall Propagation in Axial Compressors.” PhD Thesis, Massachusetts Institute of Technology.

Tan, C.S., I. Day, S. Morris, and A. Wadia. 2010. “Spike-Type Compressor Stall Inception, Detection, and Control.” *Annual Review of Fluid Mechanics* 42 (1): 275–300. https://doi.org/10.1146/annurev-fluid-121108-145603.

Taylor, G.I., 1963. *In The Scientific papers of G.I. Taylor,* (3): 383–386.

Uranga, Alejandra, Mark Drela, Edward Greitzer, Neil Titchener, Michael Lieu, Nina Siu, Arthur Huang, Gregory M. Gatlin, and Judith Hannon. 2014. “Preliminary Experimental Assessment of the Boundary Layer Ingestion Benefit for the D8 Aircraft.” In *52nd Aerospace Sciences Meeting*. National Harbor, Maryland. American Institute of Aeronautics and Astronautics. https://doi.org/10.2514/6.2014-0906.

Vegliò, M., 2015 ‘’Etude expérimentale des écoulements dans un étage de compresseur axial à basse vitesse en régime de fonctionnement instable ‘’ PhD Thesis, ENSAM

Vo, Huu Duc, Choon S. Tan, and Edward M. Greitzer. 2008. “Criteria for Spike Initiated Rotating Stall.” *Journal of Turbomachinery* 130 (1). https://doi.org/10.1115/1.2750674.

Wieghardt, K. E. G. 1953. “On the Resistance of Screens.” *Aeronautical Quarterly* 4 (2): 186–92. https://doi.org/10.1017/S0001925900000871.

Yao, Jixian, Steven E. Gorrell, and Aspi R. Wadia. 2010. “High-Fidelity Numerical Analysis of Per-Rev-Type Inlet Distortion Transfer in Multistage Fans—Part I: Simulations With Selected Blade Rows.” *Journal of Turbomachinery* 132 (4). https://doi.org/10.1115/1.3148478.

Yeh, Hsuan. 1959. “An Actuator Disc Analysis of Inlet Distortion and Rotating Stall in Axial Flow Turbomachines.” *Journal of the Aerospace Sciences* 26 (11): 739–53. https://doi.org/10.2514/8.8286.

Zachos, Pavlos K., David G. MacManus, Daniel Gil Prieto, and Nicola Chiereghin. 2016. “Flow Distortion Measurements in Convoluted Aeroengine Intakes.” *AIAA Journal* 54 (9): 2819–32. https://doi.org/10.2514/1.J054904.

Zheng, Shaokai, P. J. K. Bruce, J. M. R. Graham, and J. C. Vassilicos. 2018. “Weakly Sheared Turbulent Flows Generated by Multiscale Inhomogeneous Grids.” *Journal of Fluid Mechanics* 848 (August): 788–820. https://doi.org/10.1017/jfm.2018.387.

APPENDIX A: CHARACTERISTIC CURVES

GRID 15°

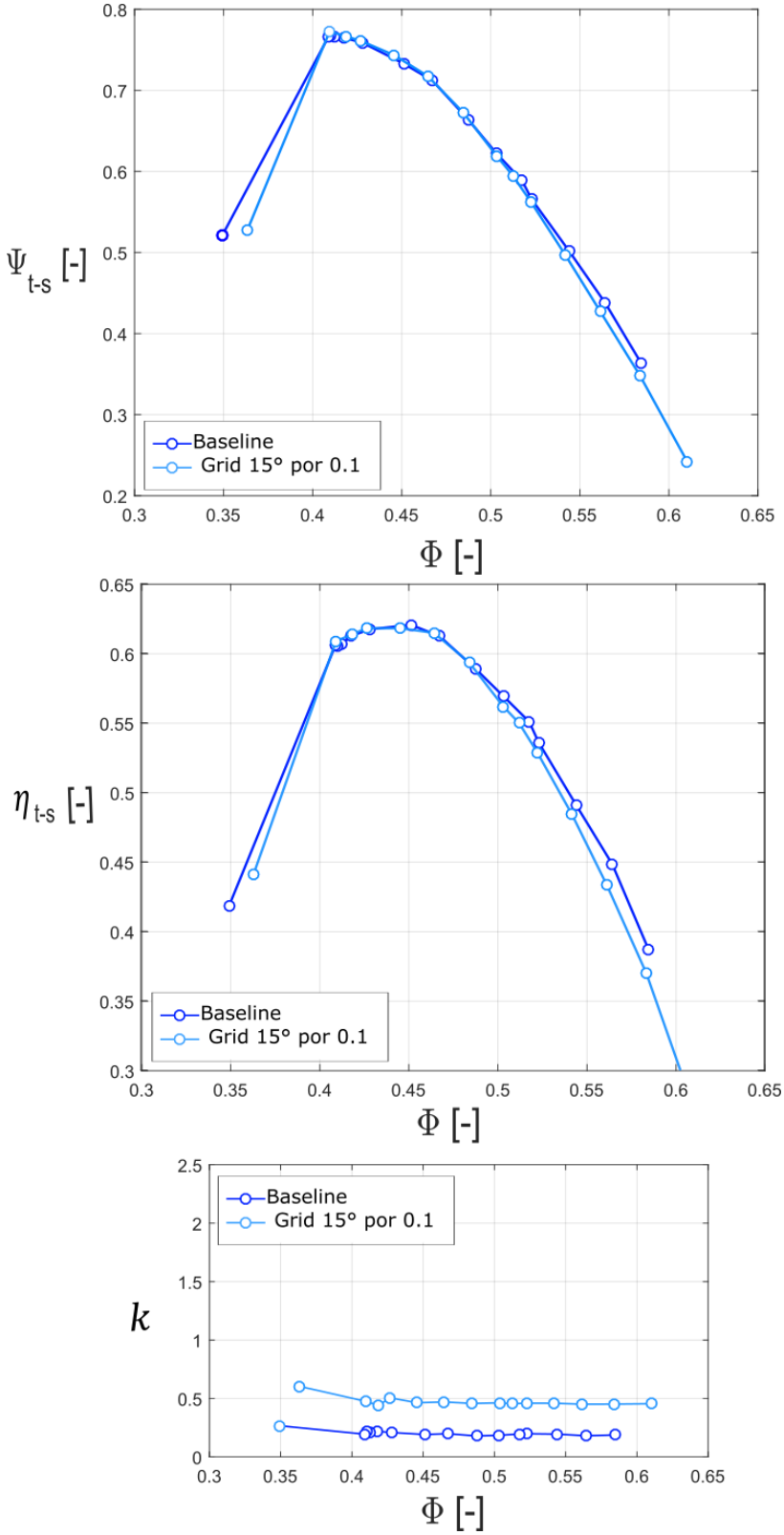

Figure A-1 : characteristic curves for 15° grid; from the top: pressure rise vs flow rate curve; efficiency vs flow rate curve; minimum total pressure behind the grid measured at the plane of the total pressure rakes. All the values are non-dimensional.

GRID 30°

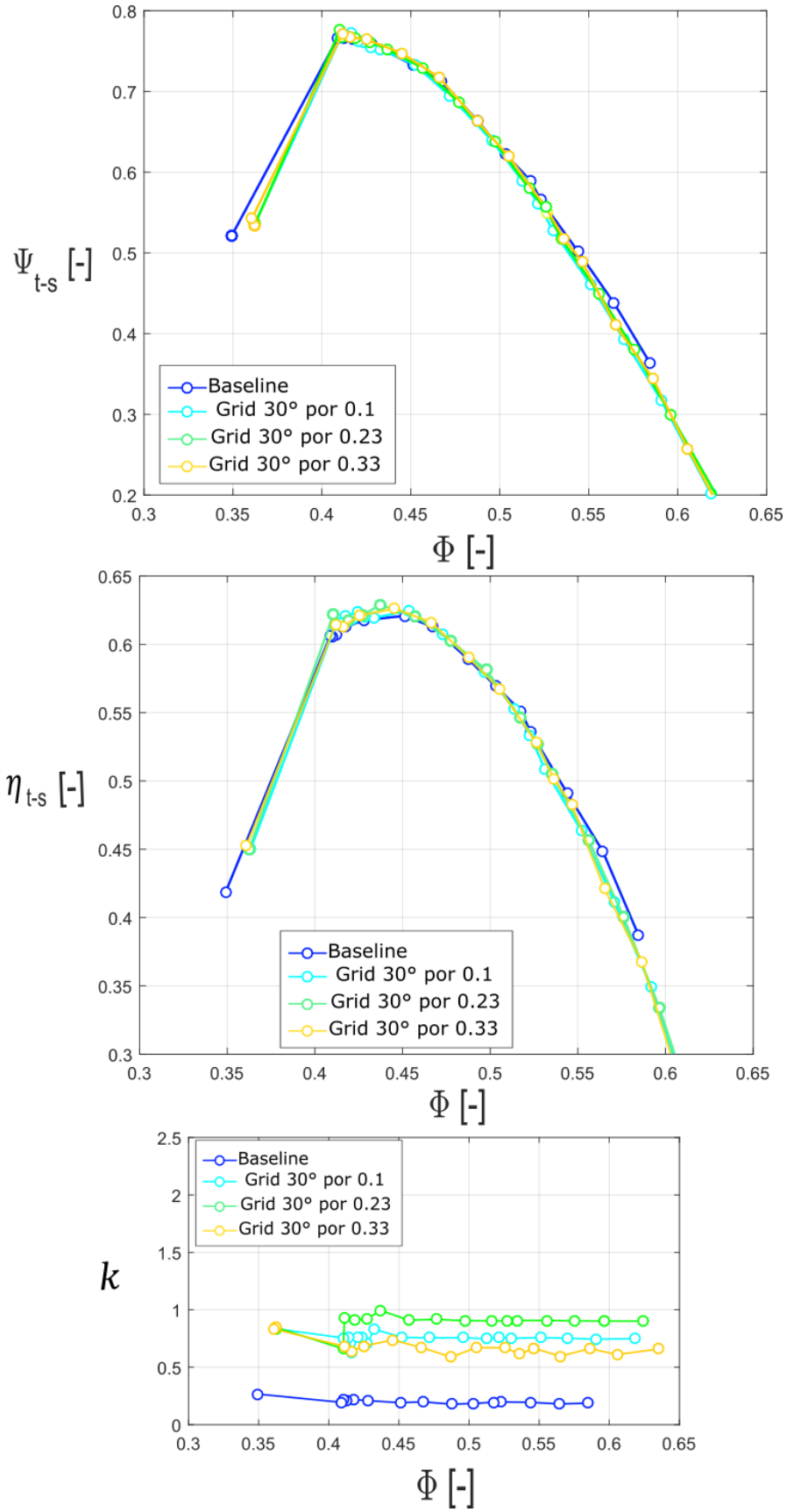

Figure A-2 characteristic curves for 30° grids; from the top: pressure rise vs flow rate curve; efficiency vs flow rate curve; minimum total pressure behind the grid measured at the plane of the total pressure rakes. All the values are non-dimensional.

GRID 60°

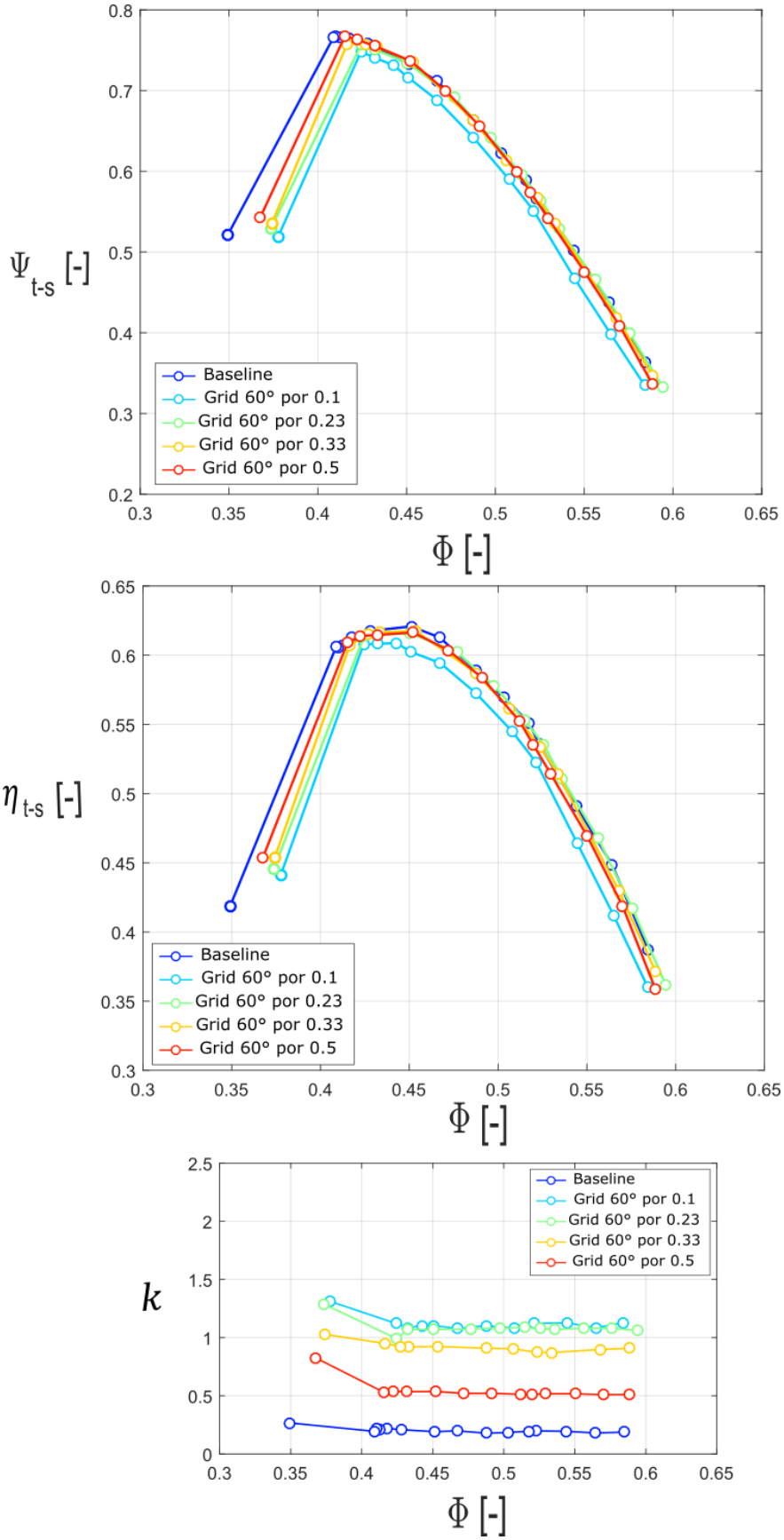

Figure A-3 : characteristic curves for 60° grid; from the top: pressure rise vs flow rate curve; efficiency vs flow rate curve; minimum total pressure behind the grid measured at the plane of the total pressure rakes. All the values are non-dimensional.

GRID 90°

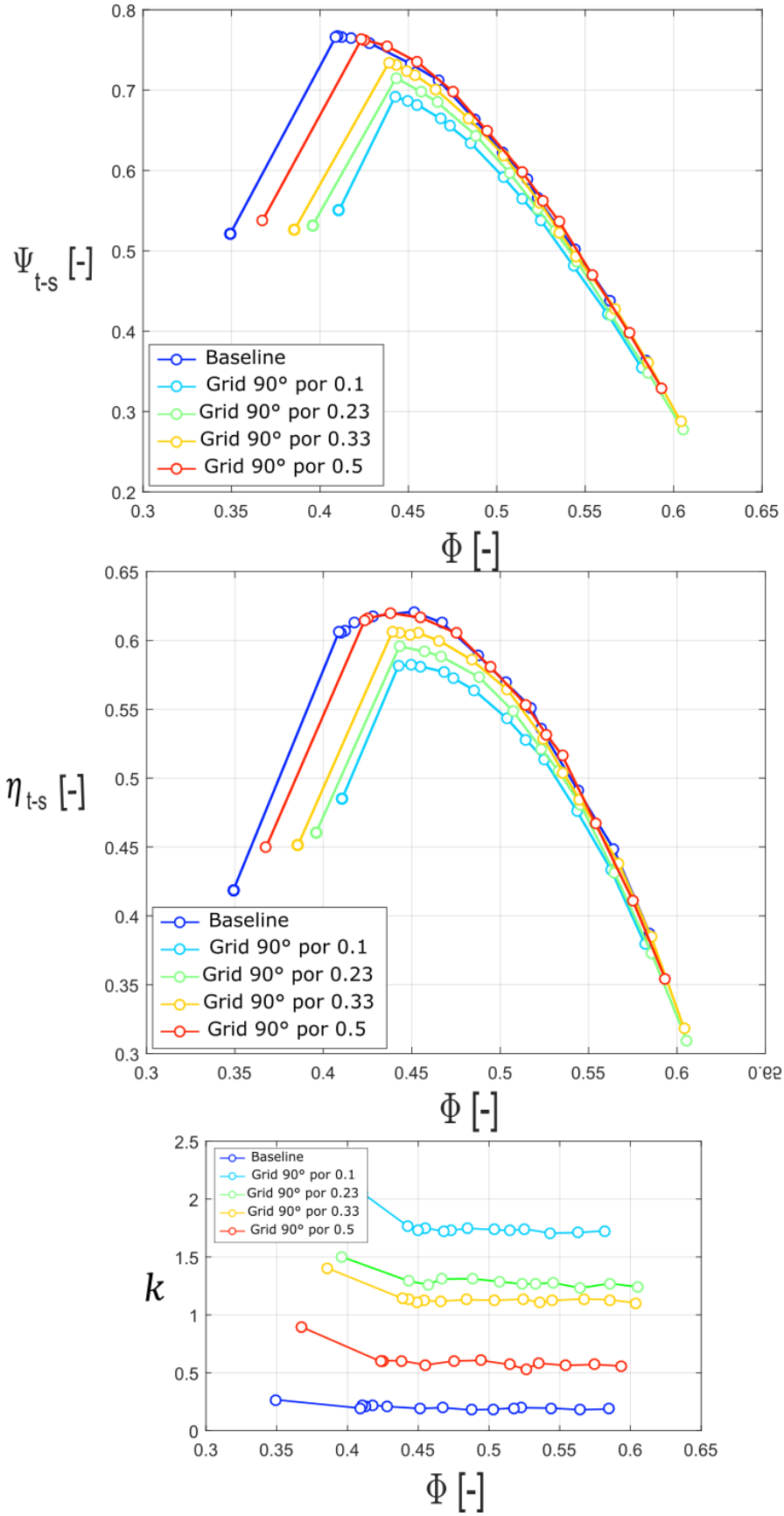

Figure A-4 : characteristic curves for 90° grid; from the top: pressure rise vs flow rate curve; efficiency vs flow rate curve; minimum total pressure behind the grid measured at the plane of the total pressure rakes. All the values are non-dimensional

GRID 120°

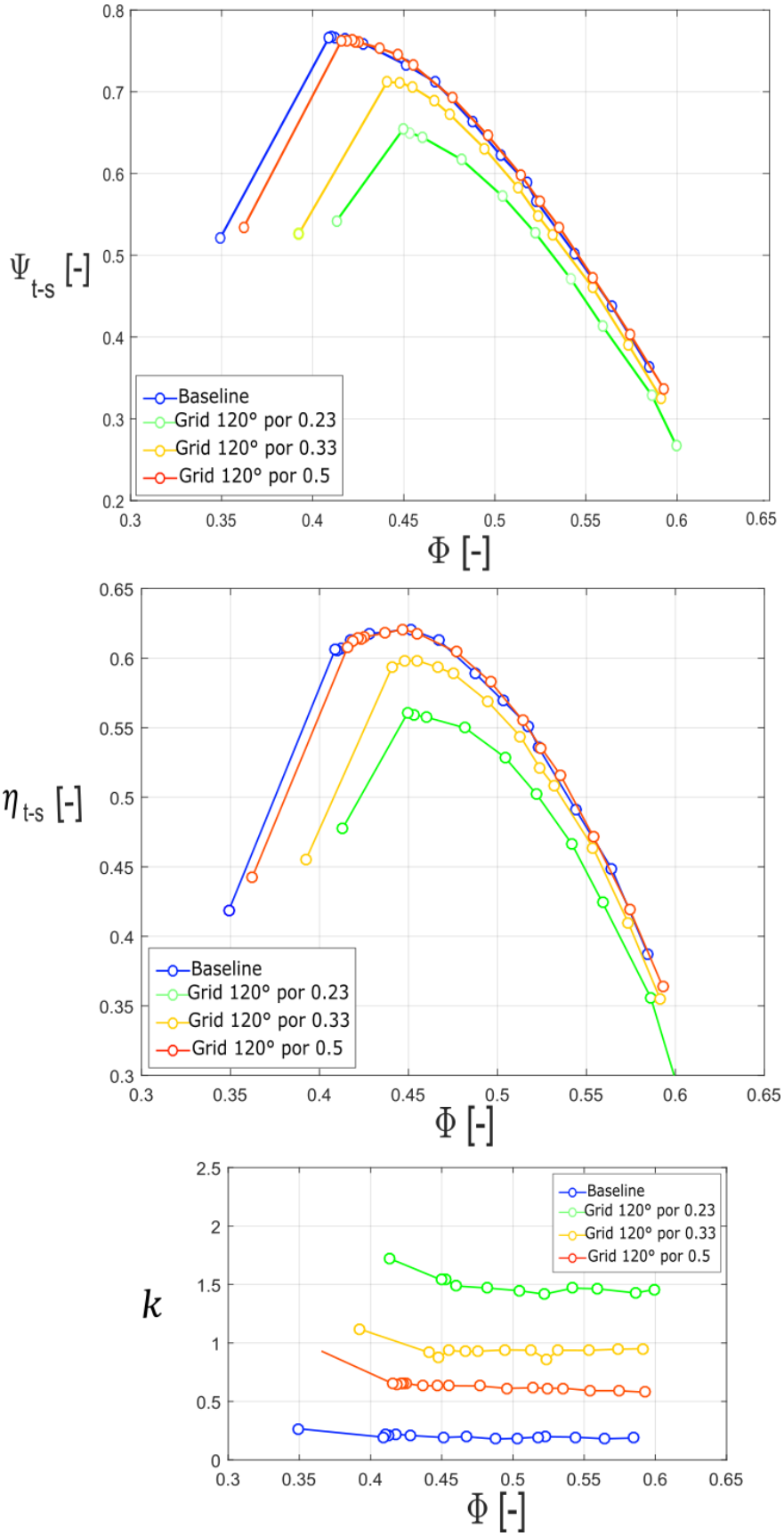

Figure A-5 : characteristic curves for 120° grid; from the top: pressure rise vs flow rate curve; efficiency vs flow rate curve; minimum total pressure behind the grid measured at the plane of the total pressure rakes. All the values are non-dimensional.

GRID 150°

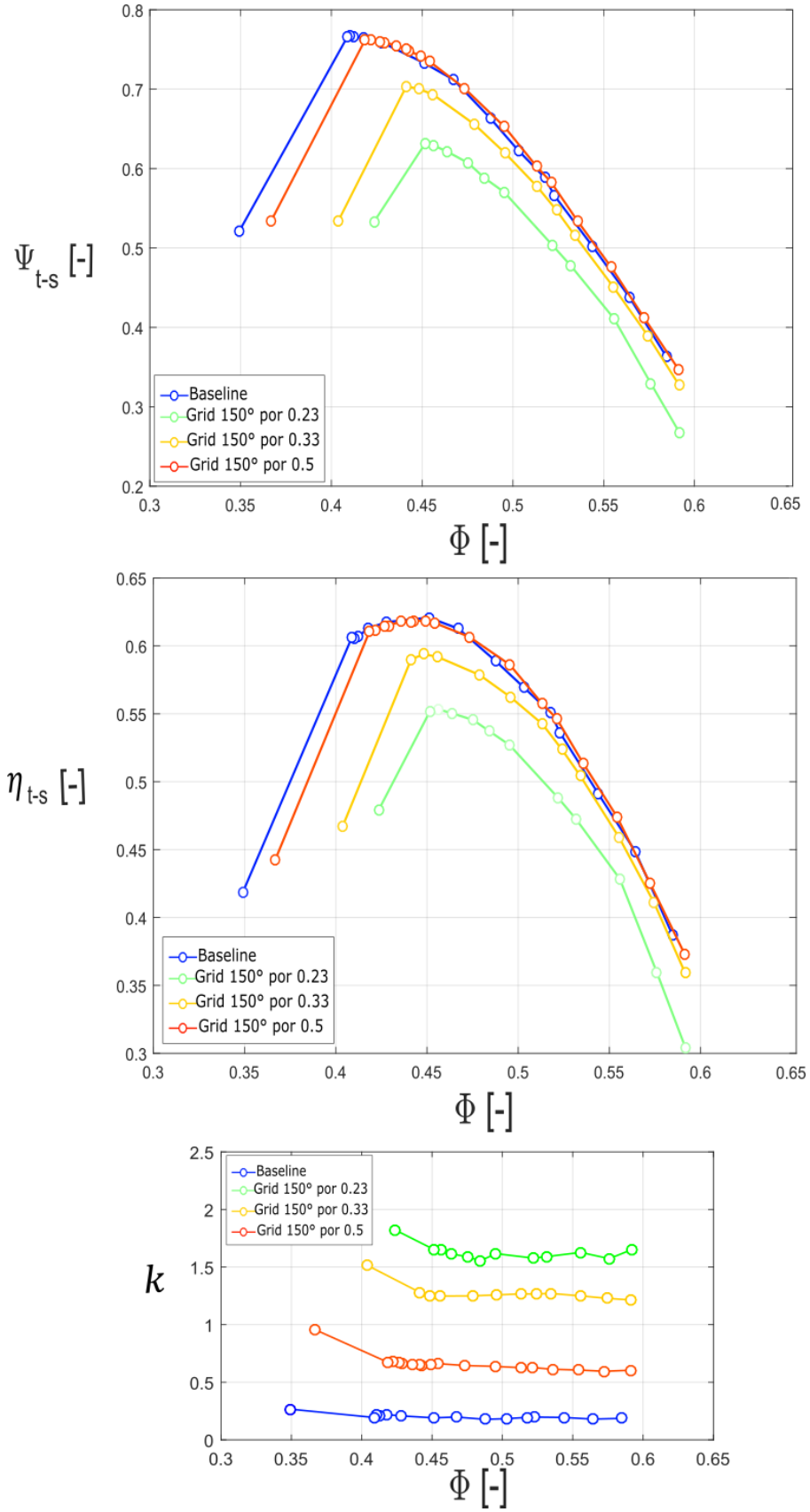

Figure A-6 : characteristic curves for 150° grid; from the top: pressure rise vs flow rate curve; efficiency vs flow rate curve; minimum total pressure behind the grid measured at the plane of the total pressure rakes. All the values are non-dimensional.

APPENDIX B: RELATIONSHIP BETWEEN $\Delta\alpha$ AND $\Delta\phi$

To demonstrate the result

$$-\Delta\alpha^2 \approx \Delta\phi$$

we make reference to figure B1, which defines the various quantities used in the following.

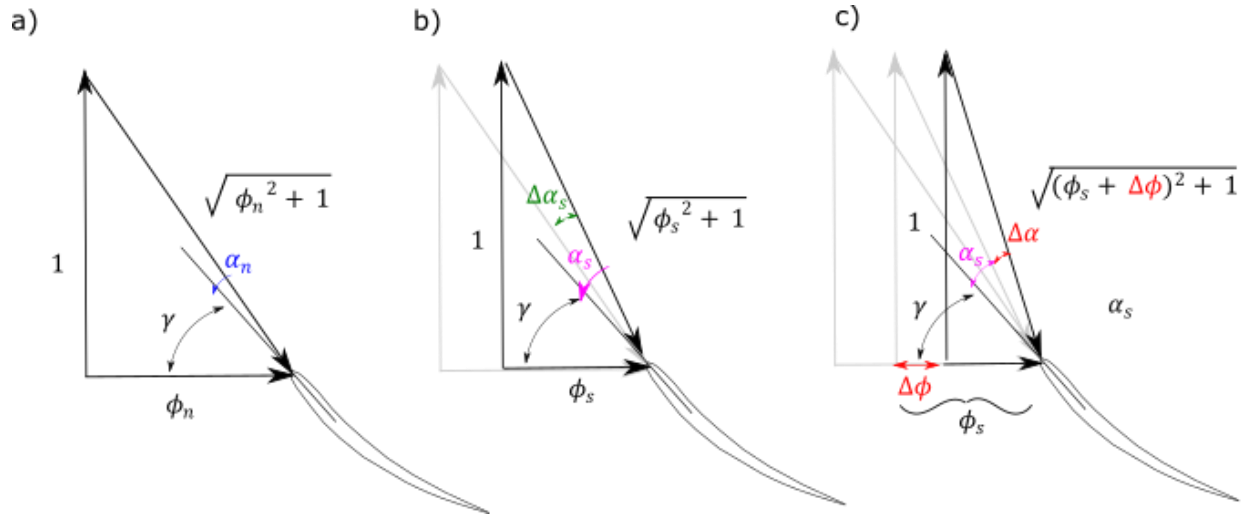

Figure B-1. left : velocity triangle at nominal point (ϕ_n) ; centre : velocity triangle at stall point (ϕ_s) ; right : velocity triangle with deviation $\Delta\phi$ from stall conditions

If the flow coefficient at stall ϕ_s is perturbed by a $\Delta\phi$, the angle α_s changes accordingly by a $\Delta\alpha$ (figure B-1c):

$$\cos(\alpha_s+\Delta\alpha)-\cos(\alpha_s) = \cos(\alpha_s)\cos(\Delta\alpha)-\sin(\alpha_s)\sin(\Delta\alpha)-\cos(\alpha_s) \quad \text{(B1)}$$

$$= \cos(\alpha_s)\left(1-\frac{\Delta\alpha^2}{2}+O(\Delta\alpha^4)\right)-\sin(\alpha_s)\left(\Delta\alpha+O(\Delta\alpha)^3\right)-\cos(\alpha_s) \quad \text{(B2)}$$

$$= -\cos(\alpha_s)\frac{\Delta\alpha^2}{2}-\sin(\alpha_s)\,\Delta\alpha+O(\Delta\alpha^3) \quad \text{(B3)}$$

To relate this change to a change in ϕ we consider figure B-2 that helps calculating $\cos(\alpha_s)$ in terms of ϕ .

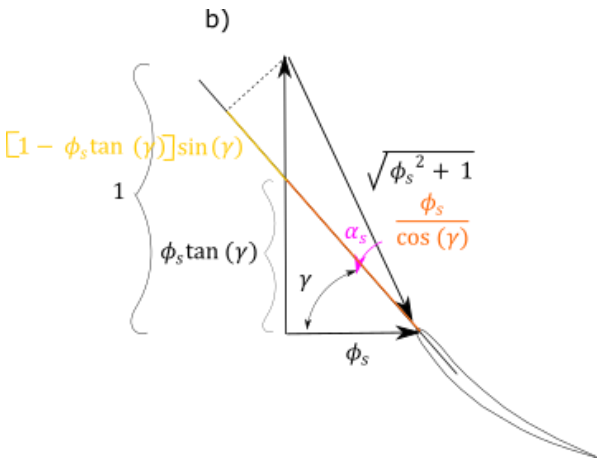

Figure B-2 :calculations to express $\cos(\alpha_s)$ as a function of ϕ_s

With reference to figure B-2, it is possible to write:

$$\sqrt{\phi_s^2+1}\cos(\alpha_s) = [1-\phi_s\tan(\gamma)]\sin(\gamma) + \frac{\phi_s}{\cos(\gamma)} = \cos(\gamma)\,(\tan(\gamma)+\phi_s) \tag{B4}$$

Thus

$$\cos(\alpha_s) = \frac{\cos(\gamma)\,(\tan(\gamma)+\phi_s)}{\sqrt{\phi_s^2+1}} \tag{B5}$$

Similarly it is possible to write

$$\cos(\alpha_s+\Delta\alpha) = \frac{\cos(\gamma)\,(\tan(\gamma)+\phi_s+\Delta\phi)}{\sqrt{(\phi_s+\Delta\phi)^2+1}} \tag{B6}$$

Thus combining equation B3, B5 and B6 we obtain

$$-\cos(\alpha_s)\frac{\Delta\alpha^2}{2} - \sin(\alpha_s)\,\Delta\alpha + O(\Delta\alpha^3) = \frac{\cos(\gamma)\,(\tan(\gamma)+\phi_s+\Delta\phi)}{\sqrt{(\phi_s+\Delta\phi)^2+1}} - \frac{\cos(\gamma)\,(\tan(\gamma)+\phi_s)}{\sqrt{\phi_s^2+1}} \tag{B7}$$

Expanding in Taylor series the denominator yields:

$$\sqrt{(\phi_s+\Delta\phi)^2+1} = \sqrt{\phi_s^2+1} + \frac{\phi_s\Delta\phi}{\sqrt{\phi_s^2+1}} + O(\Delta\phi^2) \tag{B8}$$

Hence we can write

$$\frac{\phi_s+\Delta\phi}{\sqrt{\phi_s^2+1}+\frac{\phi_s\Delta\phi}{\sqrt{\phi_s^2+1}}+O(\Delta\phi^2)} = \frac{\phi_s}{\sqrt{\phi_s^2+1}} + \frac{\Delta\phi}{(\phi_s^2+1)\sqrt{\phi_s^2+1}} + O(\Delta\phi^2) \tag{B9}$$

And thus, skipping some passages:

$$-\cos(\alpha_s)\frac{\Delta\alpha^2}{2} - \sin(\alpha_s)\,\Delta\alpha + O(\Delta\alpha^3) = \frac{\cos(\gamma)\,\Delta\phi[1+\phi_s\tan(\gamma)]}{(\phi_s^2+1)\sqrt{\phi_s^2+1}} + O(\Delta\phi^2) \tag{B10}$$

Expanding the left hand side in Taylor series with respect to nominal conditions yields:

$$\cos(\alpha_s) = \cos(\alpha_n+\Delta\alpha_s) = \cos(\alpha_n) - \Delta\alpha_s\sin(\alpha_n) + O(\Delta\alpha_s^2)$$

$$\sin(\alpha_s) = \sin(\alpha_n+\Delta\alpha_s) = \sin(\alpha_n) - \Delta\alpha_s\cos(\alpha_n) + O(\Delta\alpha_s^2)$$

where

$$\Delta\alpha_s = \alpha_s - \alpha_n$$

Thus we can re-write the left hand side of B10:

$$-\cos(\alpha_s)\frac{\Delta\alpha^2}{2} - \sin(\alpha_s)\,\Delta\alpha + O(\Delta\alpha^3) = -[\cos(\alpha_n) - \Delta\alpha_s \sin(\alpha_n) + O(\Delta\phi^2)]\frac{\Delta\alpha^2}{2} \tag{B11}$$

$$-[\sin(\alpha_n) - \Delta\alpha_s \cos(\alpha_n) + O(\Delta\phi^2)]\,\Delta\alpha + O(\Delta\alpha^3)$$

$$= -\cos(\alpha_n)\frac{\Delta\alpha^2}{2} - \sin(\alpha_n)\,\Delta\alpha + \sin(\alpha_n)\frac{\Delta\alpha_s\Delta\alpha^2}{2}$$
$$+ \cos(\alpha_n)\,\Delta\alpha_s\Delta\alpha + O(\Delta\alpha_s^2, \Delta\alpha^3)$$

At nominal conditions α_n, $\cos(\alpha_n) \gg \sin(\alpha_n)$, since the angle of attack is small, and thus we can write

$$\cos(\alpha_n)\left(-\frac{\Delta\alpha^2}{2} + \Delta\alpha_s\Delta\alpha\right) \approx \frac{\cos(\gamma)\,\Delta\phi[1 + \phi_s\tan(\gamma)]}{(\phi_s^2+1)\sqrt{\phi_s^2+1}} \tag{B12}$$

For CME2, the $\Delta\alpha_s$ is around 4° in unperturbed conditions. Assuming that in stall conditions the deviation $\Delta\alpha$ is 20°, the first term $-\frac{\Delta\alpha^2}{2}$ dominates on $\Delta\alpha_s\Delta\alpha$, so that at leading order

$$-\Delta\alpha^2 \approx \Delta\phi$$

HESAM UNIVERSITÉ

Alberto BARETTER

Arts et Métiers

Analysis of the performance and stability of an axial compressor operating under inlet flow distortion

Résumé

Pendant les derniers décennies, prescriptions sur la consommation de carburant plus strictes ont étés imposées à l'industrie aéronautique afin de limiter les émissions de produit de la combustion, suivant la croissante prise de conscience concernant la problématique environnementale. Cela a obligé les constructeurs à investiguer des nouvelles conceptions de moteurs, d'intégration moteur-fuselage et système de propulsion pour atteindre l'objective de la réduction d'émissions. Certains entre ces nouvelles conceptions pourraient exploiter une intégration moteur-fuselage non conventionnelle pour améliorer la performance globale de l'avion mais nécessitent d'une meilleure connaissance du fonctionnement des turbomachines quand l'écoulement à l'entrée du moteur est non-uniforme, une condition appelée distorsion d'entrée. La distorsion d'entrée est en effet une source de mauvaise performance du moteur. Des indications et règles de nature empirique existent pour estimer les effets négatifs de la distorsion dans le moteurs, mais la compréhension de la physique associée a ces écoulements est encore limitée, et nécessite d'être renforcée avant que des nouvelles conceptions puissent être proposées.

Cette thèse a comme objectif d'investiguer plus en détail la physique d'un distorsion d'entrée et ces effets sur la performance et la stabilité d'un compresseur axial. Pour le faire, un étude expérimental avec des grilles de distorsion a été mené, et des modèles mathématiques existants ont été utilisé pour interpréter les résultats de cet étude.

Mots clé : compresseurs axiaux , distorsion d'entrée, décrochage tournant

Résumé en anglais

During the last decades, stricter requirements on fuel consumption have been imposed to the aircraft industry in order to limit the emissions of combustion products, such as CO_2, following the increased awareness concerning the environmental problem. This has led manufacturers to investigate new engine designs, airframe-engine integration and propulsion techniques to achieve the goal of emission reduction. Some of these designs could take advantage of an unconventional engine-airframe integration to improve the global performance of the aircraft, but require an increased knowledge of the working of the turbomachines when non-uniform flow enters into the engine, a condition known as inlet distortion. Inlet distortion is known in fact to negatively affect the performance of the engine. Some empirical guidelines and rules exist to estimate the negative effects of a distortion on engines but the comprehension of the physics of such flows is still limited, and needs to be improved before new engine designs can be proposed.

This thesis is aimed at investigating more in depth the physics of an inlet distortion and its effects on the operation and stability of axial compressors. This is done by performing an experimental study on grid distortion on an axial compressor and by using existing mathematical models to help the interpretation of experimental results.

Keywords : axial compressors, inlet distortion, rotating stall